PET-MR imaging of hypoxia and vascularity in breast cancer

Dr Julia Carlota Carmona Bozo

This dissertation is submitted for the degree of Doctor in Philosophy

Darwin College

January 2021

DECLARATION

This thesis is the result of my own work and includes nothing which is the outcome of work done in collaboration except as declared in the preface and specified in the text.
It is not substantially the same as any work that I have submitted, or that have already been submitted before for any degree or other qualification at the University of Cambridge or other University, except as declared in the preface and specified in the text.
It does not exceed the prescribed word limit for the Degree Committee for Clinical Medicine and Veterinary Medicine.

Dr Julia C. Carmona Bozo

PET-MR Imaging of hypoxia and vascularity in breast cancer

ABSTRACT

Breast cancer is the most common cancer in the UK and in women globally. Imaging methods like mammography, ultrasound (US) and magnetic resonance imaging (MRI) play an important role in the diagnosis and management of breast cancer; they are generally utilised to provide anatomical or structural description of tumours in the clinical setting. It is widely accepted that the tumour microenvironment influences the phenotype, progression and treatment of breast cancer. This gave the impetus to move beyond tumour visualization in images to radiomics in order to provide additional disease characterisation and early biomarkers of tumour response.

Due to their ability to assess physiological processes *in vivo*, positron emission tomography (PET) and MRI can provide non-invasive characterisation of the tumour microenvironment, including perfusion, vascular permeability, cellularity and hypoxia, which is associated with poor clinical outcome and metastasis. Clinical imaging studies in breast tumours have hitherto assessed tumour physiological parameters separately, with only few directly comparing data from these modalities. To this end, hybrid PET-MRI represents an attractive option as it can allow examination of functional processes and features of tumours simultaneously, while also conferring methodological advantages to the way imaging information is combined.

The main aim of this thesis is to provide a better understanding of breast cancer pathophysiology using simultaneous PET and multi-parametric MRI. In particular, this work aims to explore relationships between imaging biomarkers of tumour vascularity measured by dynamic contrast-enhanced (DCE) MRI, cellularity using diffusion-weighted imaging (DWI) and hypoxia using ^{18}F-fluoromisonidazole (^{18}F-FMISO) PET. Correlations between functional PET-MRI parameters and immunohistochemical (IHC) biomarkers of hypoxia and vascularity as well as MRI morphological tumour descriptors are also presented. The thesis concludes with an investigation of the utility of MRI markers of perfusion and surrogate markers of hypoxia to quantitatively monitor and predict pathological response in patients undergoing neo-adjuvant chemotherapy (NACT) and provides projections for future work.

ACKNOWLEDGEMENTS

Since the beginning of my PhD, I have received support from lots of people. Some of them have left the Department during the course of my research; however, I am indebted to every person who provided me with his/her time and support.

Undoubtedly, I would like to first give special thanks to my supervisor, Professor Fiona J. Gilbert, for accepting me as her student and giving me the opportunity of studying in a country and at a University where I could receive high quality research skills. At the beginning of my course, Prof Gilbert also invited me to join meetings at the Cambridge Breast Unit in which she and her breast radiologist colleagues discussed different cases and another time, she also invited me to observe a breast biopsy performed by her. Thank you, Fiona (how she allows me to call her), these are unforgettable experiences, and I will always feel grateful to you. This PhD was challenging sometimes, but also rewarding and enjoyable. I deeply appreciate your trust and confidence in me even during challenging times.

Thanks, will never be enough to express all my gratitude to Roie, my PhD advisor and friend during the hardest times of my PhD. Roie, I am indebted to you for the huge amount of time you dedicated to either explain to me anything related to PET and statistics or to correct my work. I also would like to thank you for listening to me in moments when I felt unwell because of difficulties or home sick. I know that beyond the responsibilities of an advisor, you offered me your real friendship, which I hope it remains after the PhD (I know it will). You honestly cared about me in a heart-touching way, and I will always be grateful to you for this.

To my College tutor, Dr Duncan Needham (Dean of Darwin College): since the beginning of my PhD and beyond the end of the course your support was always present like your wise advice. When my grant finished, both, you and Prof Gilbert assisted me in being awarded the University's Hardship grant for postgraduate students. I am also deeply grateful with you for offering me a student job in College which I especially liked because I could collaborate with my College in keeping students safe or advising them during the COVID-19 second wave.

To the research team in both the NHS and University Departments of Radiology: none of the work here would have been possible without your continual support. In particular: Dr Corradina Caraco, Dr Elena Provenzano, Sarah Hilborne, Jackie Mason, Amy Frary, Dr Ramona Woitek, Gabrielle Baxter, Dr Andrew Patterson, Dr Martin Graves, Dr Andrew Priest,

Dr Reem Bedair, Gavin Mortimer, Carlos Coutinho, Ralph Ball, Ilse Patterson, Richard Black, Candice Anderson, Sarah Perkins, and Dr Andrew Gill.

To Dr Turid Torheim, thank you for your time and patience while providing me training in the software used for the pharmacokinetic analysis of DCE-MRI.

To all the staff of the Wolfson Brain Imaging Centre (WBIC), without the time and energy of all the radiographers and the people working at the Radiopharmaceutical Unit (RPU), the PET/MRI scans would have never occurred. Special thanks to Laura Nicoll, Karen Welsh, Vicky Lupson, Dr Tim Fryer, and each one of the radiochemists who synthesised ^{18}F-FMISO for our patients.

I would also like to express my gratitude to the NIHR Cambridge Biomedical Research Centre, the Cambridge Cancer Research UK Institute for funding this research, and the Vargas Scholarship offered by Darwin College for supporting me financially during my studies.

To Laura, my best friend in Cambridge and housemate, thank you for your great company and for being always there for me. Also, thank you for inviting me many times to your home in Germany since mine was far away. It was a pleasure to meet you.

To all my colleagues, acquaintances, and new friends that I met in Cambridge while doing my PhD, I am glad for having met such nice people and for the moments we spent laughing together: Lorena Escudero, Doreen Ai Lao, Bala Attili, Leonardo Rundo, Arnold Benjamin, Maria Delgado and Hao Li.

Last but not least, thank you to all my family members. You were always giving me emotional support and love from wherever you were in the world. Thank you for your advices, encouragement and as always, for your love.

PUBLICATIONS ARISING FROM THIS THESIS

Carmona-Bozo J, Manavaki R, Woitek R, Torheim T, Baxter G, Caraco C, Provenzano E, Graves M, Fryer T, Patterson A, Gilbert FJ. Hypoxia and perfusion in breast cancer: simultaneous assessment using PET/MR imaging. European Radiology. (Published)[1].

Carmona-Bozo J, Manavaki R, Provenzano E, Caraco C, Fryer T, Baxter G, Graves M, Gilbert FJ. Correlations between imaging biomarkers and immunohistochemistry biomarkers of hypoxia and vascularity in breast cancer. (In preparation).

PRESENTATIONS ARISING FROM THIS THESIS

Poster

2017

'Hypoxia and Perfusion in ER positive breast cancer: A study using combined PET-MR imaging'. British Society of Breast Radiology (BSBR), Dublin, Ireland. (Prize for best poster awarded).

Oral

2018

'PET-MR imaging of the hypoxic microenvironment in breast cancer'. European Congress of Radiology (ECR), Vienna, Austria.

2019

'Is ADC a predictor of hypoxia in ER+ breast cancer? A study using ^{18}F-FMISO-PET-MRI'. European Congress of Radiology (ECR), Vienna, Austria.

'Can the number of tumour feeding vessels predict hypoxia in breast cancer? A study using ^{18}F-FMISO-PET-MRI'. Annual Congress of the European Association of Nuclear Medicine (EANM), Barcelona, Spain.

TABLE OF CONTENTS

LIST OF TABLES

LIST OF FIGURES

COMMONLY USED ABBREVIATIONS

PET-MR: Positron Emission Tomography- Magnetic Resonance Imaging
AJCC: American Joint Committee on Cancer
TNM: Tumour-Node-Metastasis
HER2: Human epidermal growth factor 2 receptor
WHO: World Health Organisation
TDLU: Terminal duct lobular unit
NST: No special type
IHC: Immunohistochemistry
ER: Oestrogen receptor
PR: Progesterone receptor
Ki-67: Protein presented in proliferating cells. Hence, it is used as tumour proliferation marker.
TNBC: Triple negative breast cancer
ECM: Extracellular matrix
IFP: Interstitial fluid pressure
TCA: Tricarboxylic acid cycle
ETC: Electron transport chain
ATP: Adenosine triphosphate
AMPK: 5' AMP-activated protein kinase
HIF: Hypoxia inducible factor
HREs: Hypoxia-response elements
PHD: Prolyl hydroxylase-domain protein
pVHL: Von Hippel-Lindau protein
GLUT: Glucose transporter
LDHA: Lactate dehydrogenase A
PDK1: Pyruvate dehydrogenase kinase 1
MXI1: MAX interactor 1
VEGF: Vascular Endothelial Growth Factor
EPCs: Endothelial progenitor cells
ECs: Endothelial cells
BCAAs: Branched-chain amino acids

HbO_2: Oxy haemoglobin

CXCL 12: C-X-C motif chemokine 12

EMT: Epithelial mesenchymal transition

ERS: Endoplasmic reticulum stress

pHe: Extracellular pH

pHi: Intracellular pH

CEM: Contrast-enhanced mammography

CEDM: Contrast-enhanced digital mammography

CET: Contrast-enhanced tomosynthesis

CT: Tomography

DCE-MRI: Dynamic Contrast enhanced magnetic resonance imaging

TME: Tumour microenvironment

Mp-MRI: Multiparametric magnetic resonance imaging

ROI: Region of interest

Gd: Gadolinium

EES: Extravascular-extracellular space

AIF: Arterial Input Function

NAC: Neoadjuvant chemotherapy

iAUC: Initial area under the curve

TTP: Time to peak

BI-RADS: Breast Imaging Reporting and Data System

ACR: American College of Radiology

DCIS: Ductal carcinoma in-situ

DWI: Diffusion weighted imaging

DW-MRI: Diffusion weighted magnetic resonance imaging

ADC: Apparent Diffusion Coefficient

DWIBS: Body background signal suppression

Dt: Tissue diffusion coefficient

Dp: Pseudo-diffusion coefficient

F: Microvascular volume fraction

DKI: Diffusion weighted Kurtosis

IVIM: Intravoxel Incoherent motion

DTI: Diffusion Tensor Imaging

FA: Fractional Anisotropy

BOLD-MRI: Blood oxygen level-dependent magnetic resonance imaging

Oxy-hb: Oxygenated haemoglobin

Deoxy-hb: Deoxygenated haemoglobin

OE-MRI: Oxygen-enhanced magnetic resonance imaging

ΔR_1: Change of R_1

NSCLC: Non-small cell lung cancer

MRS: Magnetic Resonance Spectroscopy

^{1}H-MRS: Proton Magnetic Resonance Spectroscopy

tCho: Total choline peak

SNR: Signal to noise ratio

TE: Echo time

LDH-A: Lactic dehydrogenase A

HP ^{13}C-MRI: Hyperpolarized carbon-13 Magnetic Resonance Imaging

PET: Positron Emission Tomography

$T_{1/2}$: Half-life

^{18}F-FDG: ^{18}Fluoro-2-deoxy-glucose

GLUT: Glucose transporter

SUV: Standardized uptake value

^{15}O-H_2O: ^{15}O-labelled water

TBF: Tumour Blood Flow

^{82}Rb: ^{82}Rubidium

^{18}F-FMISO: ^{18}Fluorine-Fluoromisonidazole

^{18}F-FLT: ^{18}F-Fluorothymidine

PET-MRI: Positron emission tomography – Magnetic Resonance Imaging

ERα: Oestrogen receptor-α

HIF-1α: Hypoxia-inducible factor 1$^{\alpha}$

CAIX: Carbonic anhydrase nine

TOF-OSEM: Time-of-flight ordered-subsets expectation-maximisation

MIP: Maximum-intensity projection

SE: Standard errors

MBq: Megabecquerel

HF: Hypoxic fractions

IDC: Invasive ductal carcinoma

ILC: Invasive lobular carcinoma

IMC: Invasive mucinous carcinoma

IC: Invasive carcinoma

KEY COLLABORATOR CONTRIBUTIONS

The research nurses, Ms. Sarah Hillborne and Ms. Jackie Mason from the Department of Radiology and I, recruited and consented patients for the PET/MRI study (Chapters 3, 4 and 5).

I performed the qualitative and quantitative analysis of the DCE-MRI and DWI datasets used in Chapters 3 – 6 of this thesis. Similarly, tumour regions of interest were manually delineated by me, and inspected by Prof. Fiona Gilbert and Dr Ramona Woitek. Dr Andrew Patterson and Ms Gabrielle Baxter provided the MATLAB code used in the analysis of the DCE-MRI information. Dr Roido Manavaki provided the MATLAB code for the evaluation of tumour enhancing volumes (Chapter 6). Dr Turid Torheim provided training in the software used for the pharmacokinetic analysis of DCE-MRI data and also critical feedback on initial results.

Dr Corradina Caraco and I performed the qualitative evaluation of the ^{18}F-FMISO-PET images, and with Dr Roido Manavaki, we performed the analysis of PET images arising from the PET/MRI study (Chapters 3 – 5). Extraction of quantitative PET information was performed jointly by Dr Roido Manavaki and I, based on the MATLAB code she developed. Dr Tim Fryer provided a population-based arterial input function for PET.

Dr Elena Provenzano and Dr Jodi Miller performed the pathological and immunohistochemical analysis of tumour specimens arising from the PET/MRI study (Chapter 5). Dr Corradina Caraco and I visually evaluated digital immunohistochemistry images of tumour samples.

Statistical analysis was performed jointly by Dr. Roido Manavaki and I, for chapters 3-6.

References

1. Carmona-Bozo JC, Manavaki R, Woitek R, et al. Hypoxia and perfusion in breast cancer: simultaneous assessment using PET/MR imaging. *Eur Radiol*. 2020. doi:10.1007/s00330-020-07067-2

Chapter 1. The clinical problem: Breast cancer

Breast cancer is the most common cancer in women worldwide and the second most common cancer overall[1]. It is a leading cause of cancer death in less developed countries and the second leading cause of cancer death in British women, exceeded only by lung cancer[2]. The chance that a woman will die from breast cancer is about 1 in 37 (about 2.7%)[3]. Over 50,000 women are diagnosed with breast cancer each year in the UK and one in eight women will develop breast cancer at some point in their lifetime[4].

Breast tumours are very heterogeneous cancers exhibiting diverse metabolic and functional phenotypic characteristics that determine the risk of cancer progression and therapeutic resistance[5]. As with all solid tumours, malignant breast tumour cells can vary both genotypically and phenotypically within a primary tumour (intra-tumoural heterogeneity), between the primary tumour and its metastases or between tumours of the same histopathological sub-type (inter-tumoural heterogeneity)[6,7]. This heterogeneity confers different biological properties to breast tumours (vascularity, metabolism, proliferation rate, etc.)[7] amplifying the complexity of breast disease. Despite technological advances like whole-genome sequencing and functional viability screens, the impact of this heterogeneity and the microenvironment of breast cancer on tumour evolution remains poorly understood[5,8] and the translation of knowledge from research into clinical practice remains a challenge.

1.1 Background

1.1.1 Breast cancer anatomic staging

The American Joint Committee on Cancer (AJCC) has published eight editions of the tumour-node-metastasis (TNM) system for cancer anatomic staging. The last edition, published in 2017, included many new changes for breast cancer[9]. A major change was the incorporation of breast cancer biomarkers (tumour grade, hormone receptor status, HER2 expression and multigene panels) into the anatomic TNM staging[10].

This 8th edition of the AJCC staging system of breast cancer is available online[11] and magnificent reviews of this new staging system of breast cancer have been published by Jieun and Min Jung Kim in 2019[10] and by A. Giuliano et al[9] in 2017.

1.1.2 Breast cancer histological types

In August 2019 the World Health Organization (WHO) published a new classification of breast tumours in the second volume of the fifth edition of the WHO books on the classification of human tumours[12]. Breast carcinomas are divided into non-invasive or *in-situ* carcinoma and invasive carcinoma, when tumour cells have disseminated beyond the breast epithelium to the stroma[13]. Morphologically, breast carcinomas are originated from the epithelium of the ducts or the lobules that supply milk to the ducts and, according to where the tumour arises, breast carcinomas (in-situ and/or invasive breast carcinoma) are called ductal or lobular[13,14]. Both types, ductal and lobular, arise from the terminal duct lobular unit (TDLU)[13], see figure 1.1. However, it was suggested that cytoarchitectural features should be considered to classify the tumour as either ductal or lobular[15].

According to the latest version of the WHO classification, invasive breast carcinomas should be categorized into the following subtypes: *Invasive breast carcinoma of no special type* (NST); including carcinomas with medullary features which for clinical purposes are now considered one end of the spectrum of the tumour infiltrating lymphocytes- rich invasive breast cancer-NST (TIL-rich IBC-NSTs) rather than a distinct morphological subtype. It is recommended to use the term “IBC-NST with medullary pattern”. In addition, oncocytic, lipid-rich, glycogen-rich clear cell, sebaceous carcinomas, which are rarely encountered, are also now recognized as special patterns of NST along with carcinoma with osteoclast-like stromal giant cells, pleomorphic carcinoma, choriocarcinomatous and melanotic patterns. The second WHO category of invasive breast carcinomas is *invasive breast carcinomas of special type* such as microinvasive carcinoma, invasive lobular carcinoma, tubular carcinoma, cribriform carcinoma, mucinous carcinoma, invasive micropapillary carcinoma, carcinoma with apocrine differentiation and metaplastic carcinoma[16]. Special typemeans that when the pathologist observes the cells under a microscope, they will show certain features. The WHO classification of tumour editorial board also stated that if the invasive breast carcinoma has mixed components, both subtypes present need to be reported and percentages of each one be given.

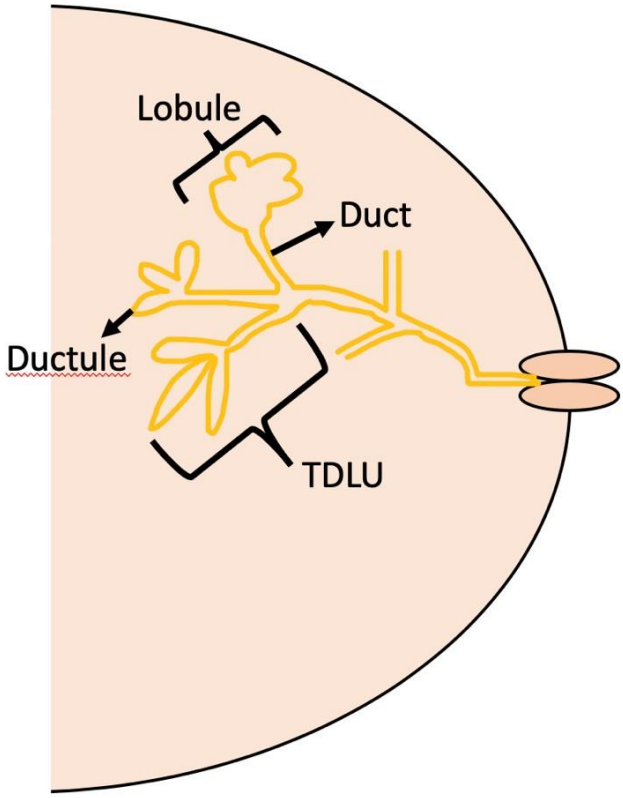

Figure 1.1 Anatomy of the breast; the terminal duct lobular unit (TDLU) is shown.

1.1.3 Breast cancer molecular sub-types

Current molecular subtype classification of breast cancer is based on expression of a small number of genes which is quantified using DNA microarray technique[17,18]. This classification which is also based on immunohistochemistry (IHC) markers of breast cancer such as estrogen receptor (ER), progesterone receptor (PR), human epidermal growth factor 2 receptor (HER2) and Ki-67[19], was suggested by the St. Gallen International Expert Consensus in 2011 and approved again in 2013[20]. According to the St. Gallen International Expert Consensus recommendations breast cancers can fall into 5 categories: luminal A, luminal-B/HER2 negative, luminal-B/HER2 positive, HER2 type and triple negative.

Luminal A breast cancers are hormone receptor positive (oestrogen and/or progesterone receptor positive) and HER2 negative. They produce low levels of Ki-67 (lower than 14%) - a protein which is associated to tumour cell proliferation and growth[18] - and have the best prognosis among breast cancer molecular sub-types.

Luminal -B/HER2 negative breast cancers are also hormone receptor positive (estrogen and/or progesterone receptor positive) and HER2 negative. They usually show higher levels ofKi-67 than luminal A breast cancers (equal or higher than 14%).
Luminal -B/HER2 positive breast cancers are hormone receptor positive (estrogen and/or progesterone receptor positive) and HER2 positive. Their expression of Ki-67 varies.
Luminal types of breast cancer express high amounts of luminal cytokeratins and genetic markers of luminal epithelial cells of the normal breast tissue[21].
Her2-enriched breast cancers are hormone receptor negative (do not have neither estrogen nor progesterone receptors) and HER2 positive. They can be treated with chemotherapeutic drugs which target the HER2 protein. Their expression of Ki-67 also varies.
Triple negative (TNBC) or basal-like breast tumours[22] are hormone-receptor negative and HER2 negative. This type of breast cancer is related to mutations of the BRCA1 gene[23]. These breast cancers tend to be more aggressive than luminal type breast cancers and they do not express genetic markers of luminal cytokeratins, smooth-muscle-specific markers and integrins[24].

1.1.4 Breast cancer grading

It has been widely accepted that the morphological appearances of tumour cells can be correlated with the degree of tumour malignancy[25,26]. The grade of a breast cancer identifies how different tumour cells are from normal epithelial breast cells, therefore, it depicts the aggressive potential of the tumour and it can be considered a prognostic factor[27].

Many scoring systems are available for determining the grade of breast cancers[27]. The Department of Breast Pathology of Addenbrookes' University hospital in Cambridge, UK, utilizes the Elston-Ellis modification of Scarff-Bloom-Richardson grading system which is used in this thesis. This grading method applies only to invasive breast carcinomas, in-situ carcinomas are not suitable for being graded with this technique[27].

Three morphological parameters are taken into consideration by pathologists while using the Elston-Ellis grading technique: the amount of tubule formation, nuclear pleomorphism and mitotic activity[27]. Each parameter is scored 1-3 and then to obtain the overall tumour grade the scores for each parameter are added to provide a final score ranging from 3 to 9[27]. Grade 1 or

well-differentiated breast cancers have a total score of 3-5, grade 2 or moderately differentiated cancers have a total score of 6-7 and grade 3 or poorly differentiated tumours have a total score of 8-9[27].

1.1.5 Breast Cancer microenvironment

A malignant solid tumour does not only consist of neoplastic cells but also stromal cells. Stromal cells have different origin, they can be mesenchymal cells, fibroblasts, myofibroblasts, endothelial cells, pericytes and inflammatory cells associated with the immune system[28]. Tumour cells are constantly interacting with the stromal cells and the extracellular matrix (ECM) which encircles the tumour[29]. The tumour microenvironment is composed by these numerous stromal cell types and the ECM surrounding the tumour[30].

The microenvironment of solid tumours is known to have hostile conditions, usually reflecting poor perfusion, oxygen deprivation, nutrient deficiency, severe acidity and elevated interstitial fluid pressure (IFP)[31].

1.1.5.1 Tumour metabolism in breast cancer

Tumour metabolism is known to be different from metabolism in normal tissues[32]. Table 1.1 displays the main differences between cell metabolism in normal cells and in tumour cells.

Tumour cells grow rapidly forming solid tumour masses. To grow more than 2 mm^3 in size, new vessel formation occurs (neo-angiogenesis) comprising of a chaotic immature vascular system. As the new tumour mass grows, compression and obstruction of these immature blood vessels arises. This results in poor oxygen supply especially at the centre of the mass[33,34] where tumour cells have to adapt to the new hypoxic conditions[34].

Under low levels of O_2 alternative metabolic pathways are activated in malignant tumours to fulfil nutrient demands of growing tumour cells using glycolytic intermediates[35] (Figure 1.2). Tricarboxilic acid (TCA) cycle intermediates are also used by cancer cells for the synthesis of macromolecules[36].

Table 1.1 Differences between normal tissue and tumour metabolism[37]

Normal Tissue Metabolism	Tumour Metabolism
TCA* and ETC* with normal O_2 concentration to derive energy (Normal mitochondrial function)	↑Glycolysis to derive energy (↓ mitochondrial function)
90% ATP from glycolysis	50% ATP from glycolysis
Normal programming	Metabolic reprograming- ↑glucose uptake, ↑Lactate production- ↑tumour cell survival (activation of "anaplerotic" pathways)
Glycolysis-dependant on hypoxia	Glycolysis independent of hypoxia[36]

*TCA: Tricarboxilic Acid cycle; ETC: Electron Transport Chain.

Cells respond to short-term hypoxia (oxygen deficiency) by inducing adaptive reactions through the AMP-activated protein kinase (AMPK) pathway, which increases glycolysis by the up regulation of catalytic enzymes, such as phosphofructokinase-1 and pyruvate kinase[38]. If the lack of O_2 remains, cells stimulate a hypoxia-inducible factor 1 (HIF-1), a heterodimer oxygen-sensitive transcription factor composed of alpha and beta subunits that can bind to hypoxia-response elements (HREs) activating the transcription of many genes[39]. Under adequate O_2 levels, HIF-1 activity decreases by the prolyl hydroxylase-domain protein (PHD) which hydroxylates the HIF-1 alpha subunit and enables the interaction with the Von Hippel-Lindau protein (pVHL), a tumour suppressor[34].

The net result of HIF-1 activation in a hypoxic environment is to shift energy production by increasing glycolysis and decreasing mitochondrial function[40]. HIF-1 increases glycolysis by transactivating genes that are able to stimulate the production of glucose transporters, such as GLUT1 and GLUT3, responsible for glucose import into the cell and the activation of glycolytic enzymes[41]. Lactate dehydrogenase A (LDHA), responsible for the conversion of pyruvate to lactate, is also influenced by HIF-1 alpha[41]. HIF-1 decreases mitochondrialfunction by transactivating genes such as pyruvate dehydrogenase kinase 1 (PDK1)[42,43,44] andMAX interactor 1 (MXI1) [43,45]. Another mechanism by which HIF-1 controls mitochondrial

function in hypoxia is de-activating cytochrome c oxidase in the Electron Transport Chain cycle (ETC)[44].

HIF-1 alpha stimulation also activates new blood vessel formation in tumours (neo-angiogenesis) regulating Vascular Endothelial Growth Factor (VEGF) and its receptors (VEGF-R1 and R2). This also promotes the recruitment of endothelial progenitor cells (EPCs) from the bone marrow and its differentiation into endothelial cells (ECs) [46,47,48]. Both, metabolic reprogramming and neo-vessel formation are tumour cell responses to adapt to hypoxic conditions[49,50].

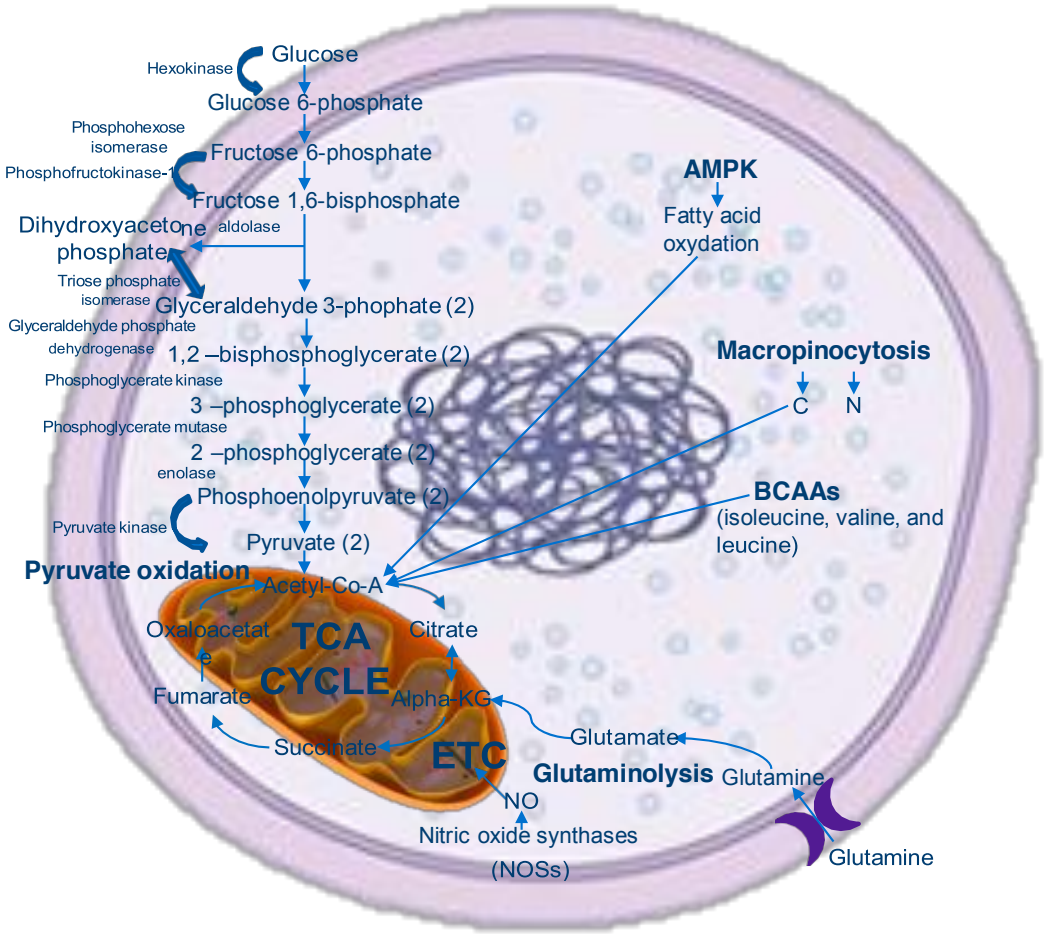

Figure 1.2 Alternative metabolic pathways in the tumour cell activated under hypoxic conditions. Firstly, glycolysis increases by the up-regulation of catalytic enzymes participating in this process by the activation of the AMP-activated protein kinase (AMPK) pathway, which also stimulates the oxidation of fatty acids. HIF-1 alpha can up-regulate glycolytic enzymes. Anaplerotic pathways (pathways that refill the cycle) generate TCA cycle intermediates used as precursors for the synthesis of molecules: Glutaminolysis, which produces alpha-

ketoglutarate from glutamine, pyruvate carboxylation which produces oxaloacetate from glucose/pyruvate and the oxidation of branched-chain amino acids (BCAAs) like isoleucine, valine and leucine. Carbon from macropinocytosis can also enter the TCA cycle and be oxidized to CO_2, producing ATP through oxidative phosphorylation. Nitric Oxide is a well-known surrogate of oxygen for the activation of cytochrome c oxidase in the electron transport chain (ETC).

1.1.5.2 Breast cancer vascularity

Angiogenesis, the formation of new blood vessels, is a requirement of neoplastic growth, proliferation and metastasis from early stages of progression[51,52,53]. As a general rule, tumours do not grow beyond a size of 1 to 2 mm without producing new blood vessels[54]. New blood vessel formation is associated to a process termed "angiogenic switch", a vascular remodelling process which allows cancer cells to invade and grow out their primary niche[55]. Tumour blood vessels display structural and functional abnormalities compared with the normal vasculature due to an imbalance between pro and anti-angiogenic factors making them tortuous and leaky[56]. They tend to be elongated, tortuous and have contour irregularities, aberrant branching and blind ends[31]. Similarly, their vascular density is abnormal, and their permeability is high which allows significant plasma leakage[31].

Angiogenesis is a consequence of microenvironmental factors and the newly formed blood vessels are inadequate to meet the demands of the tumour mass[55]. Angiogenesis is considered a target for new cancer treatment strategies because vascular endothelial cells are more genetically stable than tumour cells[57].

Breast tumours are characterized by an altered general vascular supply, a prominent feeding vessel, and increased regional vascularity[58]. The features and location of the breast tumour are factors which influence on the tumour's vascular supply[58]. Non-invasive imaging techniques of the breasts can monitor the functional fluctuations of tumour vascularity.

1.1.5.3 Hypoxia in breast cancer

Hypoxia, a deficiency of oxygen resulting from an imbalance between oxygen supply and consumption, was firstly described in tumours by Thomlinson and Gray in 1955[59]. Hypoxia plays a crucial role in the progression of cancer and can adversely affect patient prognosis. It has been shown that hypoxia negatively impacts tumour response to treatment as well as reducing patient survival rate[60,61,62,63]. Tumours that contain large regions of hypoxia are more likely to metastasize[64-65], a feature that appears to be mediated by several mechanisms, including changes in gene expression, inactivation and or activation of genes, and enhanced genomic instability[64-66].

Hypoxia is a characteristic pathophysiological feature of locally advanced solid tumours, including tumours of the breast[67 68,69,70,71,72,73], which may exhibit hypoxic areas that are heterogeneously distributed within the tumour mass[74].

Oxygen is transported to tissues as oxyhemoglobin (HbO_2) in the erythrocytes contained in the blood, together with other nutrients through blood vessels. Tumour cells are continuously growing and they can easily outgrow their vascular supply[69,75]. Hypoxia can result when the diffusion distance of the tumour cells from the nutrient blood vessel is >70 μm (*diffusion-limited or chronic hypoxia*)[67,75,76]. Furthermore, the characteristic disorganized vascular network of cancers with "leaky" fragile capillaries, containing porous fenestrations along the endothelial lining, further contributes to the poor delivery of oxygen and nutrients (*perfusion-limited or acute hypoxia*)[69]. Under these conditions, malignant cells stop growing as quickly as before and adapt their growing rate to the new lower levels of oxygen[76]. Acute hypoxia is often called "transient" because tumour blood flow tends to fluctuate in time although, other terms are often used, including cyclic, intermittent, repetitive or fluctuating[31,77]. However, bothchronic and acute hypoxia can co-exist in tumours[62]. While cancer cells adapt to hypoxia, theymay present heterogeneities in O_2 distribution[78].

1.1.5.3.1 Pathophysiology of hypoxia in breast cancer

Hypoxia inducible factor 2 (HIF-2 alpha) is a protein structurally similar to HIF-1 alpha which also activates the transcription of many genes distinct from those regulated by HIF-1 alpha[79]. The two hypoxia-inducible factors, HIF-1α and 2α, have been associated with a poor outcome

and treatment resistance in the vast majority of cancers, including the breast[80]. HIF-1α levels are not increased in benign fibrocystic disease, but aggressive breast tumours often exhibit increased levels of HIF-1α[81].

HIF-1α has been associated with an aggressive breast cancer phenotype which includes a large tumour size, high grade and levels of proliferation, and lymph-node metastasis[81]. HIF-1 alpha can positively stimulate tumour growth, vascularization, hematogenous and lymphatic dissemination of the cancer[75]. Vascularization is promoted by an increase in the regulation of angiogenic factors such as, VEGF, stromal-derived factor 1 (CXCL12), and stem cell factor which promotes the migration of bone marrow-derived angiogenic cells to the circulation[82].

All breast cancer molecular subtypes have been shown to upregulate HIF-1α and related proteins[75,83,84]. HIF-1 regulates genes implicated in every step of the breast cancer metastatic cascade[75,85] which can be deconvoluted into a series of discrete steps beginning with the epithelial mesenchymal transition (EMT), in which cells lose cell-to-cell contact, become motile and locally invade the surrounding stroma[85]. Local tissue invasion, which requires extracellular matrix (ECM) degradation, leads to intravasation that occurs when cancer cells penetrate the wall of a blood or lymphatic vessel[85]. Once breast cancer cells have intravasated, they survive within the circulation during transit to distant organs where they have the potential to extravasate by repenetrating the vessel wall. The metastatic site must be primed so that it presents a suitable microenvironment for cancer cells survival (premetastatic niche)[85].

Hypoxia induces activation of unoccupied estrogen receptor alpha in breast cancer cells and modulates the level of the receptor expression[86,87], which is intimately associated with the biology of breast carcinomas. Triple negative breast cancers, one of the most aggressive types of breast cancers and thus with worse prognosis[88], are associated with basal endoplasmic reticulum stress (ERS) which cooperates with hypoxia signaling to promote tumour progression and relapse[49].

1.1.5.4 Other parameters affecting the breast cancer microenvironment

1.1.5.4.1 Interstitial Fluid Pressure (IFP)

Tumour blood vessels fenestrations, which cause leakiness, and the abnormal lymphatic

system of cancers[89] result on an increased flow of free fluid to the interstitial space. This accumulation of fluid in the ECM of the cancer leads to a rise of the interstitial pressure[90,91,92]. Fibrosis and contraction of the ECM can also cause interstitial hypertension[93]. Values from 50 to 100 mmHg of IFP have been reported in tumours[94]. This increase of IFP blocks transcapillary transport which affects the uptake of cancer therapeutic agents[93]. Interstitial fluid pressure varies within the same tumour and from one tumour to the other[94]. It has been shown that the centre of tumours usually presents a higher IFP than the periphery[95].

1.1.5.4.2 PH

The increase of glycolysis in tumours leads to a rise of lactate production and consequently, to tumour acidosis[96]. In order to maintain homeostasis tumour cells develop mechanisms for exporting protons outside the cell, through the cell membrane, which makes the extracellular pH (pHe) lower than the intracellular pH (pHi)[97,98] whereas, in normal cells, the extracellular pH (pHe) is higher than the intracellular pH (pHi)[99,100]. PH values from 6.5 to 6.9 have been reported in the extracellular cancer microenvironment and, by contrast, normal tissues pHe values range between 7.2 and 7.5[101]. In mouse breast cancer models, lower pHe tumour values have been found in the range of 6.3-6.9, which may suggest high degree of malignancy[102].

Extracellular tumour acidosis has been associated to an increase of tumour aggressiveness[103], metastasis[104,105], chromosomal rearrangements[106], and angiogenesis[107]. Some studies have linked low tumour pHe to resistance to cancer therapy[108,109].

1.2 Importance of understanding the tumour microenvironment

As it was previously described, the tumour microenvironment can enhance tumour progression and metastasis. Similarly, many factors such as tumour hypoxia, acidosis and interstitial hypertension can create resistance to cancer treatment, radiation and/or chemotherapy. A better understanding of the microenvironment of breast cancer will guide us towards the development of treatment capable of destroying tumour cells in an attempt to improve patient prognosis, by increasing disease free survival and overall survival rates.

For decades, imaging methods have helped scientists and physicians gain insight into the tumour micromilieu and since these methods are non-invasive, patients are able to tolerate them more than invasive tissue biopsies.

The next chapter offers an overview of the imaging methods used to assess breast cancer microenvironment.

References

1. Ferlay J, Soerjomataram I, Dikshit R, et al. Cancer incidence and mortality worldwide: Sources, methods and major patterns in GLOBOCAN 2012. *Int J Cancer*. 2015. doi:10.1002/ijc.29210
2. WHO. Breast Cancer: Prevention and Control. https://www.who.int/cancer/detection/breastcancer/en/index1.html. Published 2020. Accessed April 12, 2020.
3. Anonimous. Breast Cancer Research Foundation. Breast Cancer Statistics. https://www.bcrf.org/breast-cancer-statistics. Accessed February 2, 2018.
4. Anonimous. Breast Cancer NOW. About breast cancer. http://breastcancernow.org/about-breast-cancer. Published 2018. Accessed February 2, 2018.
5. Polyak K. Heterogeneity in breast cancer. *J Clin Invest*. 2011. doi:10.1172/JCI60534
6. Badve S. Tumor heterogeneity in breast cancer. In: *Molecular Pathology of Breast Cancer*. ; 2016. doi:10.1007/978-3-319-41761-5_9
7. Fisher R, Pusztai L, Swanton C. Cancer heterogeneity: Implications for targeted therapeutics. *Br J Cancer*. 2013. doi:10.1038/bjc.2012.581
8. Lim B, Woodward WA, Wang X, Reuben JM, Ueno NT. Inflammatory breast cancer biology: the tumour microenvironment is key. *Nat Rev Cancer*. 2018. doi:10.1038/s41568-018-0010-y
9. Giuliano AE, Connolly JL, Edge SB, et al. Breast Cancer-Major changes in the American Joint Committee on Cancer eighth edition cancer staging manual. *CA Cancer J Clin*. 2017. doi:10.3322/caac.21393
10. Koh J, Kim MJ. Introduction of a new staging system of breast cancer for radiologists: An emphasis on the prognostic stage. *Korean J Radiol*. 2019. doi:10.3348/kjr.2018.0231
11. Cancer AJC on. *AJCC Cancer Staging Manual, Eighth Edition*. 8th ed. (Office AE, ed.). Chicago, IL; 2018.
12. WHO. No Title. IARC publications. http://publications.iarc.fr/Book-And-Report-Series/Who-Classification-Of-Tumours/Breast-Tumours-2019. Published 2020. Accessed April 13, 2020.
13. Makki J. Diversity of breast carcinoma: Histological subtypes and clinical relevance.

Clin Med Insights Pathol. 2015. doi:10.4137/CPath.s31563

14. Eheman CR, Shaw KM, Ryerson AB, Miller JW, Ajani UA, White MC. The changing incidence of in situ and invasive ductal and lobular breast carcinomas: United States, 1999-2004. *Cancer Epidemiol Biomarkers Prev*. 2009. doi: 10.1158/1055-9965.EPI-08-1082
15. Feldman AL, Yi ES. Rosai and Ackerman's Surgical Pathology. *JAMA*. 2012. doi:10.1001/jama.2011.1993
16. Board WC of TE. *Breast Tumours*. *WHO Classification of Tumours*.; 2019.
17. Rouzier R, Perou CM, Symmans WF, et al. Breast cancer molecular subtypes respond differently to preoperative chemotherapy. *Clin Cancer Res*. 2005. doi:10.1158/1078-0432.CCR-04-2421
18. Li LT, Jiang G, Chen Q, Zheng JN. Predic Ki67 is a promising molecular target in the diagnosis of cancer (Review). *Mol Med Rep*. 2015. doi:10.3892/mmr.2014.2914
19. Hennigs A, Riedel F, Gondos A, et al. Prognosis of breast cancer molecular subtypes in routine clinical care: A large prospective cohort study. *BMC Cancer*. 2016. doi:10.1186/s12885-016-2766-3
20. Goldhirsch A, Wood WC, Coates AS, Gelber RD, Thürlimann B, Senn HJ. Strategies for subtypes-dealing with the diversity of breast cancer: Highlights of the St Gallen international expert consensus on the primary therapy of early breast cancer 2011. *Ann Oncol*. 2011. doi:10.1093/annonc/mdr304
21. Rakha EA, El-Sayed ME, Green AR, et al. Biologic and clinical characteristics of breast cancer with single hormone receptor-positive phenotype. *J Clin Oncol*. 2007. doi:10.1200/JCO.2007.12.2747
22. Perou CM, Sørile T, Eisen MB, et al. Molecular portraits of human breast tumours. *Nature*. 2000. doi:10.1038/35021093
23. Esteller M. Promoter Hypermethylation and BRCA1 Inactivation in Sporadic Breast and Ovarian Tumors. *J Natl Cancer Inst*. 2000. doi:10.1093/jnci/92.7.564
24. Sotiriou C, Pusztai L. Gene-expression signatures in breast cancer. *N Engl J Med*. 2009. doi:10.1056/NEJMra0801289
25. Broders AC. Squamous-cell epithelioma of the lip: A study of five hundred and thirty-seven cases. *J Am Med Assoc*. 1920. doi:10.1001/jama.1920.02620100016007
26. Broders AC. SQUAMOUS-CELL EPITHELIOMA OF THE SKIN A STUDY OF 256 CASES. *Ann Surg*. 1921. doi:10.1097/00000658-192102000-00001
27. ELSTON CW, ELLIS IO. pathological prognostic factors in breast cancer. I. The

value of histological grade in breast cancer: experience from a large study with long-term follow-up. *Histopathology*. 1991. doi:10.1111/j.1365-2559.1991.tb00229.x

28. Yuan Y, Jiang YC, Sun CK, Chen QM. Role of the tumor microenvironment in tumor progression and the clinical applications (Review). *Oncol Rep*. 2016. doi:10.3892/or.2016.4660
29. Wang M, Zhao J, Zhang L, et al. Role of tumor microenvironment in tumorigenesis. *J Cancer*. 2017. doi:10.7150/jca.17648
30. Place AE, Jin Huh S, Polyak K. The microenvironment in breast cancer progression: Biology and implications for treatment. *Breast Cancer Res*. 2011. doi:10.1186/bcr2912
31. Horsman MR, Vaupel P. Pathophysiological basis for the formation of the tumor microenvironment. *Front Oncol*. 2016. doi:10.3389/fonc.2016.00066
32. Alberti KGMM. The biochemical consequences of hypoxia. *J Clin Pathol*. 1977;(S3-11):14-20. doi:10.1136/jcp.s3-11.1.14
33. Denko NC. Hypoxia, HIF and metabolism in the solid tumour. *Nat Rev Cancer*. 2008;8(SePTeMBeR):705-713. doi:10.1038/nrc2468
34. Masoud GN, Li W. HIF-1α pathway: Role, regulation and intervention for cancer therapy. *Acta Pharm Sin B*. 2015. doi:10.1016/j.apsb.2015.05.007
35. DeBerardinis RJ, Chandel NS. Fundamentals of cancer metabolism. *Sci Adv*. 2016;2(5):e1600200. doi:10.1126/sciadv.1600200
36. Koppenol WH, Bounds PL, Dang C V. Otto Warburg's contributions to current concepts of cancer metabolism. *Nat Rev Cancer*. 2011;11(5):325-337. doi:10.1038/nrc3038
37. Weinhouse S, Warburg O, Burk D, Schade AL. On respiratory impairment in cancer cells. *Science (80-)*. 1956. doi:10.1126/science.124.3215.267
38. Viollet B. AMPK: Lessons from transgenic and knockout animals. *Front Biosci*. 2009;Volume(14):19. doi:10.2741/3229
39. Solaini G, Baracca A, Lenaz G, Sgarbi G. Hypoxia and mitochondrial oxidative metabolism. *Biochim Biophys Acta*. 2010;1797(6-7):1171-1177. doi:10.1016/j.bbabio.2010.02.011
40. Ke Q, Costa M. Hypoxia-inducible factor-1 (HIF-1). *Mol Pharmacol*. 2006. doi:10.1124/mol.106.027029
41. Semenza GL. HIF-1 and tumor progression: Pathophysiology and therapeutics. *Trends Mol Med*. 2002. doi:10.1016/S1471-4914(02)02317-1
42. Papandreou I, Cairns RA, Fontana L, Lim AL, Denko NC. HIF-1 mediates adaptation

to hypoxia by actively downregulating mitochondrial oxygen consumption. *Cell Metab*. 2006;3(3):187-197. doi:10.1016/j.cmet.2006.01.012

43. Kim JW, Tchernyshyov I, Semenza GL, Dang C V. HIF-1-mediated expression of pyruvate dehydrogenase kinase: A metabolic switch required for cellular adaptation to hypoxia. *Cell Metab*. 2006;3(3):177-185. doi:10.1016/j.cmet.2006.02.002
44. Fukuda R, Zhang H, Kim J whan, Shimoda L, Dang C V., Semenza GLL. HIF-1 Regulates Cytochrome Oxidase Subunits to Optimize Efficiency of Respiration in Hypoxic Cells. *Cell*. 2007;129(1):111-122. doi:10.1016/j.cell.2007.01.047
45. Semenza GL, Wang GL. A nuclear factor induced by hypoxia via de novo protein synthesis binds to the human erythropoietin gene enhancer at a site required for transcriptional activation. *Mol Cell Biol*. 1992;12(12):5447-5454. doi:10.1128/MCB.12.12.5447
46. Muz B, de la Puente P, Azab F, Azab AK. The role of hypoxia in cancer progression, angiogenesis, metastasis, and resistance to therapy. *Hypoxia*. 2015:83. doi:10.2147/HP.S93413
47. Conway EM, Collen D, Carmeliet P. Molecular mechanisms of blood vessel growth. *Cardiovasc Res*. 2001;49(3):507-521. doi:10.1016/S0008-6363(00)00281-9
48. Carmeliet P. Angiogenesis in life, disease and medicine. *Nature*. 2005;438(7070):932-936. doi:10.1038/nature04478
49. Bertout JA, Patel SA, Simon MC. The impact of O2 availability on human cancer. *Nat Rev Cancer*. 2008;8(12):967-975. doi:10.1038/nrc2540
50. Boidot R, Branders S, Helleputte T, Rubio LI, Dupont P, Feron O. A generic cycling hypoxia-derived prognostic gene signature: application to breast cancer profiling. *Oncotarget*. 2014;5(16):6947-6963. doi:10.18632/oncotarget.2285
51. Brem S, Brem H, Folkman J, Finkelstein D, Patz A. Prolonged Tumor Dormancy by Prevention of Neovascularization in the Vitreous. *Cancer Res*. 1976.
52. Folkman J. How is blood vessel growth regulated in normal and neoplastic tissue?—G. H. A. clowes memorial award lecture. *Cancer Res*. 1986.
53. Hahnfeldt P, Panigrahy D, Folkman J, Hlatky L. Tumor development under angiogenic signaling: A dynamical theory of tumor growth, treatment response, and postvascular dormancy. *Cancer Res*. 1999.
54. Sherwood LM, Parris EE, Folkman J. Tumor Angiogenesis: Therapeutic Implications. *N Engl J Med*. 1971. doi:10.1056/NEJM197111182852108
55. Consolino L, Longo DL, Dastrù W, et al. Functional imaging of the angiogenic switch

in a transgenic mouse model of human breast cancer by dynamic contrast enhanced magnetic resonance imaging. *Int J Cancer*. 2016;139(2):404-413. doi:10.1002/ijc.30073

56. Bergers G, Benjamin LE. Tumorigenesis and the angiogenic switch. *Nat Rev Cancer*. 2003. doi:10.1038/nrc1093
57. Rajendran JG, Krohn KA. Imaging hypoxia and angiogenesis in tumors. *Radiol Clin North Am*. 2005. doi:10.1016/j.rcl.2004.08.004
58. Grubstein A, Yepes M, Kiszonas R. Magnetic resonance imaging of breast vascularity in medial versus lateral breast cancer. *Eur J Radiol*. 2010;75(2). doi:10.1016/j.ejrad.2009.10.020
59. Thomlinson RH, Gray LH. The histological structure of some human lung cancers and the possible implications for radiotherapy. *Br J Cancer*. 1955. doi:10.1038/bjc.1955.55
60. Busk M, Horsman MR, Jakobsen S, et al. Can hypoxia-PET map hypoxic cell density heterogeneity accurately in an animal tumor model at a clinically obtainable image contrast? *Radiother Oncol*. 2009;92(3):429-436. doi:10.1016/j.radonc.2009.08.026
61. Spence AM, Muzi M, Swanson KR, et al. Regional Hypoxia in Glioblastoma Multiforme Quantified with [18F]Fluoromisonidazole Positron Emission Tomography before Radiotherapy: Correlation with Time to Progression and Survival. *Clin Cancer Res*. 2008;14(9):2623-2630. doi:10.1158/1078-0432.CCR-07-4995
62. Vaupel P, Mayer A. The Clinical Importance of Assessing Tumor Hypoxia: Relationship of Tumor Hypoxia to Prognosis and Therapeutic Opportunities. *Antioxid Redox Signal*. 2015;22(10):878-880. doi:10.1089/ars.2014.6155
63. Mortensen LS, Busk M, Nordsmark M, et al. Accessing radiation response using hypoxia PET imaging and oxygen sensitive electrodes: A preclinical study. *Radiother Oncol*. 2011;99(3):418-423. doi:10.1016/j.radonc.2011.06.034
64. Travers RGB and S. Hypoxia: Targeting the Tumour. *Anticancer Agents Med Chem*. 2006;6(4):281-286. doi:http://dx.doi.org/10.2174/187152006777698169
65. Måseide K, Kalliomäki T, Hill RP. Microenvironmental Effects on Tumour Progression and Metastasis. In: Meadows GG, ed. *Integration/Interaction of Oncologic Growth*. Dordrecht: Springer Netherlands; 2005:1-22. doi:10.1007/1-4020-3414-8_1
66. Lal A, Peters H, St. Croix B, et al. Transcriptional Response to Hypoxia in Human Tumors. *J Natl Cancer Inst*. 2001;93(17):1337-1343. doi:10.1093/jnci/93.17.1337
67. Vaupel P, Mayer A. Hypoxia in cancer: Significance and impact on clinical outcome.

Cancer Metastasis Rev. 2007. doi:10.1007/s10555-007-9055-1

68. Vaupel P, Thews O, Hoeckel M. Treatment resistance of solid tumors: Role of hypoxia and anemia. *Med Oncol*. 2001. doi:10.1385/MO:18:4:243
69. Osinsky S, Zavelevich M, Vaupel P. Tumor hypoxia and malignant progression. In: *Experimental Oncology*. ; 2009.
70. Brown JM. Tumor Hypoxia in Cancer Therapy. *Methods Enzymol*. 2007. doi:10.1016/S0076-6879(07)35015-5
71. Vaupel P, Briest S, Höckel M. Hypoxia in breast cancer: Pathogenesis, characterization and biological/therapeutic implications. *Wiener Medizinische Wochenschrift*. 2002. doi:10.1046/j.1563-258X.2002.02032.x
72. Clarke H, Pallister CJ. The impact of anaemia on outcome in cancer. *Clin Lab Haematol*. 2005. doi:10.1111/j.1365-2257.2004.00664.x
73. Vaupel P, Höckel M, Mayer A. Detection and Characterization of Tumor Hypoxia Using pO $_2$ Histography. *Antioxid Redox Signal*. 2007. doi:10.1089/ars.2007.1628
74. Jiang L, Greenwood TR, Artemov D, et al. Localized hypoxia results in spatially heterogeneous metabolic signatures in breast tumor models. *Neoplasia (United States)*. 2012. doi:10.1593/neo.12858
75. Semenza GL. The hypoxic tumor microenvironment: A driving force for breast cancer progression. *Biochim Biophys Acta - Mol Cell Res*. 2016;1863(3):382-391. doi:https://doi.org/10.1016/j.bbamcr.2015.05.036
76. Oyen WJG, Kaanders JHAM, Bussink J. Molecular imaging of hypoxia. *Q J Nucl Med Mol Imaging*. 2013;57(3):217-218. doi:10.2967/jnumed.110.075663
77. Brown JM. Evidence for acutely hypoxic cells in mouse tumours, and a possible mechanism of reoxygenation. *Br J Radiol*. 1979. doi:10.1259/0007-1285-52-620-650
78. Bristow RG, Hill RP. Hypoxia and metabolism: Hypoxia, DNA repair and genetic instability. *Nat Rev Cancer*. 2008;8(3):180-192. doi:10.1038/nrc2344
79. Lau KW, Tian YM, Raval RR, Ratcliffe PJ, Pugh CW. Target gene selectivity of hypoxia-inducible factor-α in renal cancer cells is conveyed by post-DNA-binding mechanisms. *Br J Cancer*. 2007. doi:10.1038/sj.bjc.6603675
80. Semenza GL. Defining the role of hypoxia-inducible factor 1 in cancer biology and therapeutics. *Oncogene*. 2010;29(5):625-634. doi:10.1038/onc.2009.441
81. Bos R, Zhong H, Hanrahan CF, et al. Levels of Hypoxia-Inducible Factor-1 During Breast Carcinogenesis. *JNCI J Natl Cancer Inst*. 2001;93(4):309-314. doi:10.1093/jnci/93.4.309

82. Schito L, Rey S, Tafani M, et al. Hypoxia-inducible factor 1-dependent expression of platelet-derived growth factor B promotes lymphatic metastasis of hypoxic breast cancer cells. *Proc Natl Acad Sci*. 2012;109(40):E2707-E2716. doi:10.1073/pnas.1214019109
83. Giatromanolaki A, Koukourakis MI, Simopoulos C, et al. c-erbB-2 related aggressiveness in breast cancer is hypoxia inducible factor-1α dependent. *Clin Cancer Res*. 2004. doi:10.1158/1078-0432.CCR-04-1068
84. Generali D, Berruti A, Brizzi MP, et al. Hypoxia-inducible factor-1α expression predicts a poor response to primary chemoendocrine therapy and disease-free survival in primary human breast cancer. *Clin Cancer Res*. 2006. doi:10.1158/1078-0432.CCR-05-2690
85. Liu Z ji, Semenza GL, Zhang H feng. Hypoxia-inducible factor 1 and breast cancer metastasis. *J Zhejiang Univ Sci B*. 2015. doi:10.1631/jzus.B1400221
86. Cho J, Bahn JJ, Park M, Ahn WS, Lee YJ. Hypoxic activation of unoccupied estrogen-receptor-alpha is mediated by hypoxia-inducible factor-1 alpha. *J Steroid Biochem Mol Biol*. 2006. doi:10.1016/j.jsbmb.2006.03.002
87. Ryu K, Park C, Lee Y. Hypoxia-inducible factor 1 alpha represses the transcription of the estrogen receptor alpha gene in human breast cancer cells. *Biochem Biophys Res Commun*. 2011. doi:10.1016/j.bbrc.2011.03.119
88. Montagner M, Enzo E, Forcato M, et al. SHARP1 suppresses breast cancer metastasis by promoting degradation of hypoxia-inducible factors. *Nature*. 2012;487(7407):380-384. doi:10.1038/nature11207
89. Fukumura D, Jain RK. Tumor microenvironment abnormalities: Causes, consequences, and strategies to normalize. *J Cell Biochem*. 2007. doi:10.1002/jcb.21187
90. Leunig M, Jain RK, Goetz AE, Messmer K, Kastenbauer E. Interstitial Hypertension in Head and Neck Tumors in Patients: Correlation with Tumor Size. *Cancer Res*. 1992.
91. Jain RK, Boucher Y, Wolmark N. Interstitial Hypertension in Human Breast and Colorectal Tumors. *Cancer Res*. 1992.
92. Milosevic M, Fyles A, Hedley D, et al. Interstitial fluid pressure predicts survival in patients with cervix cancer independent of clinical prognostic factors and tumor oxygen measurements. *Cancer Res*. 2001.
93. Heldin CH, Rubin K, Pietras K, Östman A. High interstitial fluid pressure - An

obstacle in cancer therapy. *Nat Rev Cancer*. 2004. doi:10.1038/nrc1456

94. Vaupel P. Pathophysiology of Solid Tumors. In: ; 2009. doi:10.1007/978-3-540-74386-6_4
95. Boucher Y, Baxter LT, Jain RK. Interstitial Pressure Gradients in Tissue-isolated and Subcutaneous Tumors: Implications for Therapy. *Cancer Res*. 1990.
96. Gatenby RA, Gillies RJ. Why do cancers have high aerobic glycolysis? *Nat Rev Cancer*. 2004. doi:10.1038/nrc1478
97. Tannock IF, Rotin D. Acid pH in Tumors and Its Potential for Therapeutic Exploitation. *Cancer Res*. 1989.
98. Stubbs M, McSheehy PMJ, Griffiths JR, Bashford CL. Causes and consequences of tumour acidity and implications for treatment. *Mol Med Today*. 2000. doi:10.1016/S1357-4310(99)01615-9
99. Vaupel P. Physiological properties of malignant tumours. *NMR Biomed*. 1992. doi:10.1002/nbm.1940050505
100. Gerweck LE. Tumor pH: Implications for treatment and novel drug design. *Semin Radiat Oncol*. 1998. doi:10.1016/S1053-4296(98)80043-X
101. Gatenby RA, Gawlinski ET, Gmitro AF, Kaylor B, Gillies RJ. Acid-mediated tumor invasion: A multidisciplinary study. *Cancer Res*. 2006. doi:10.1158/0008-5472.CAN-05-4193
102. Chen M, Chen C, Shen Z, et al. Extracellular pH is a biomarker enabling detection of breast cancer and liver cancer using CEST MRI. *Oncotarget*. 2017. doi:10.18632/oncotarget.17404
103. Estrella V, Chen T, Lloyd M, et al. Acidity generated by the tumor microenvironment drives local invasion. *Cancer Res*. 2013. doi:10.1158/0008-5472.CAN-12-2796
104. White KA, Grillo-Hill BK, Barber DL. Cancer cell behaviors mediated by dysregulated pH dynamics at a glance. *J Cell Sci*. 2017. doi:10.1242/jcs.195297
105. Gillies RJ, Gatenby RA. Hypoxia and adaptive landscapes in the evolution of carcinogenesis. *Cancer Metastasis Rev*. 2007. doi:10.1007/s10555-007-9065-z
106. Morita T, Nagaki T, Fukuda I, Okumura K. Clastogenicity of low pH to various cultured mammalian cells. *Mutat Res - Fundam Mol Mech Mutagen*. 1992. doi:10.1016/0027-5107(92)90235-T
107. Shi Q, Le X, Wang B, et al. Regulation of vascular endothelial growth factor expression by acidosis in human cancer cells. *Oncogene*. 2001. doi:10.1038/sj.onc.1204500

108. Bix G, Castello R, Burrows M, et al. Endorepellin in vivo: Targeting the tumor vasculature and retarding cancer growth and metabolism. *J Natl Cancer Inst*. 2006. doi:10.1093/jnci/djj441

109. Mahoney BP, Raghunand N, Baggett B, Gillies RJ. Tumor acidity, ion trapping and chemotherapeutics: I. Acid pH affects the distribution of chemotherapeutic agents in vitro. *Biochem Pharmacol*. 2003. doi:10.1016/S0006-2952(03)00467-2

Chapter 2. Imaging the breast cancer microenvironment with MRI and PET

Mammography is the most common screening tool to detect breast cancer at an early stage, often in conjunction with breast ultrasound, particularly in women under the age of 40 years for whom mammography alone is less sensitive due to the abundant fibro-glandular tissue[1]. These conventional imaging modalities have well-documented pitfalls, particularly in missing small lesions and measuring tumours while distinguishing them from surrounding breast parenchyma[2,3,4,5,6]. The density of the adjacent parenchyma also poses a major challenge for mammography, limiting its overall sensitivity and specificity[7,8,9,10,11]. The latter has been overcome by Tomosynthesis, in which thin slices or images of a volume of tissue are used to reconstruct a pseudo 3D image of the breast, to detect breast cancer[6,12]. Some studies have shown that the addition of tomosynthesis to conventional or digital mammography can increase detection rates of breast cancer[6,13] , whereas tomosynthesis in combination with ultrasound is better than mammography alone for the determination of cancer morphology[14]. Alternative methods for imaging breast cancer include breast MRI, which has demonstrated higher sensitivity than all other breast imaging techniques for the diagnosis of breast malignancies regardless of the density of the parenchyma[15,16]. Currently, MRI is recognised as a valuable addition to the diagnostic work-up of breast mammography and ultrasound[1,16,17].

The injection of contrast material to enhance the visualisation of tumours with respect to the rest of the breast tissue, is being used in all imaging modalities. In mammography it is known as contrast-enhanced mammography (CEM) or digital mammography (CEDM); in tomosynthesis as contrast-enhanced tomosynthesis (CET), in tomography (CT) as contrast-enhanced CT or angio-CT and in MRI as dynamic contrast-enhanced (DCE) MRI. All contrast modalities have higher diagnostic accuracy than non-contrast modalities[18]. In a study by Chen-Pin et al. the diagnostic performance of CEDM with or without CET was equivalent to DCE-MRI for breast cancer[18]. Diagnosis of breast cancer is confirmed with image-guided core biopsy and/or fine needle aspiration cytology.

Beyond cancer diagnosis, the interest in visualizing the tumour microenvironment (TME) has been increasing not only for the clinical relevance (influence on carcinogenesis and treatment resistance) but also because the TME is abundant in comparison to cancer cells and it may contribute up to 90% of the tumour volume[19]. Many imaging techniques have been developed

to visualize, quantify and characterise the TME[20,21,22,23,24]. The most frequently used imaging techniques will be reviewed and discussed in this chapter.

2.1 Breast Magnetic Resonance Imaging (MRI) techniques available for imaging breast cancer microenvironment

MR imaging allows identification of the presence and progression (or regression) of disease, as well as the morphology of the breast lesion. Breast MRI is a non-invasive imaging technique that combines excellent soft tissue contrast with cross-sectional anatomical detail, allowing imaging with high spatial resolution and sensitivity[25]. Unaffected by breast density, MRI can show much more accurate delineation of lesion morphology and extent. It offers superiority in terms of image acquisition, as volumetric data can be acquired for both breasts simultaneously and in any desired plane, typically with sub-millimetre resolution. MRI has improved cancer treatment planning and reduced unnecessary biopsy procedures[26,27,28,29].

In addition to evaluating the morphological aspect of the breast lesion, MRI can simultaneously assess multiple cancer-biological processes or hallmarks of cancer such as vascularity, metabolism, hypoxia and cellularity[30]. The combined assessment of different functional (because they are indirect markers of the cancer physiological processes) MRI parameters is known as multiparametric resonance imaging (mpMRI) which offers high specificity to image the hallmarks of cancer[25,30,31,32].

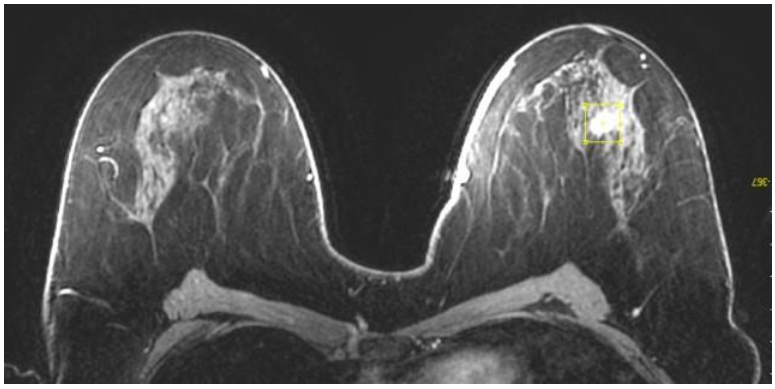

Figure 2.1 T1 post-contrast weighted image of a female patient of 70 years old. The yellow square illustrates an NST carcinoma on the right breast, ER and PR-positive, HER2-negative.

2.1.1 Dynamic Contrast Enhanced Magnetic Resonance Imaging (DCE-MRI) for imaging tumour vascularity and hypoxia

DCE-MRI provides high spatial resolution of tumour vascular organization, perfusion and permeability. DCE-MRI refers to a serial acquisition of images at the same spatial location before, during and after intravenous administration (preferably by a power injector) of an extracellular contrast agent. By observing the uptake and washout of a contrast agent through a region-of-interest (ROI) placed on the most enhancing part of the lesion, the behavior and extent of the disease can be accurately assessed together with the vasculature. The primary effect of administering gadolinium chelates (Gd) is to shorten the T_1 relaxation time of the hydrogen nuclei where the contrast medium accumulates[33]. This results in signal hyperintensity on T1-weighted images. By subtracting pre-contrast from the post-contrast images, the heart, blood vessels and lesions (and their vasculature) are hyper-intense compared to tissues that have little or no uptake of contrast. Information from DCE-MRI can be measured qualitatively, semi-quantitatively or quantitatively.

The tumour signal intensity information can be converted to contrast agent concentration, elucidating key physiological metrics of vascular function such as blood flow and capillary permeability, by performing pharmacokinetic modelling. Quantitative analysis of tumour vascular function using DCE-MRI is based on these mathematical pharmacokinetic models which provide measurements of the distribution of the contrast agent between the intravascular

and the interstitial space[34]. The Tofts' model (or standard Tofts' model) and extended Tofts' model have become a standard for the analysis of DCE-MRI[35]. A study by Sourbron et al[35] suggests that the Tofts' model should be used in tissues with weak vascularization or low blood flow whereas the extended Tofts' model results more accurate in highly perfused tissues. In tissues with intermediate vascularity, neither model offers a good fit to the tissue concentrations. The standard Tofts' model has been recommended for DCE- MRI of the breast because it estimates quantitative parameters within an error margin of 20%[36].

DCE-MRI quantitative analysis provides a range of pharmacokinetic parameters characterizing the movement of the contrast agent across the endothelium, between the intravascular and the extravascular space. Such parameters are: K^{trans} (min^{-1}), the volume transfer constant of contrast agent from the blood plasma to the extravascular-extracellular space (EES); $k_{ep,}$ (min^{-1}) the transfer rate constant of contrast reflux from the EES to the blood plasma; v_p, total blood plasma volume, and v_e, total EES volume fraction[37,38]. Owing to the hyperpermeability of the tumour vasculature, it is hypothesized that these parameters will be different in pathologic vessels like tumour capillaries. Some studies have reported reliable K^{trans} values (0.50-0.56[39,40]), k_{ep} (2.59[39]) and v_e (0.15[39]) values for characterizing benign and malignant breast lesions with sensitivity, specificity and accuracy over 80%. Huang et al[41] demonstrated that low K^{trans} values could differentiate malignant from benign breast lesions. Other authors have found higher K^{trans}, k_{ep} and v_e values in malignant breast tumours in comparison to normal breast parenchyma or benign tumours[42,43]. Pharmacokinetic analysis requires measurement of an arterial input function (AIF), which refers to the concentration of the contrast agent in a vesselentering the tissue over time[38].

Different investigators have demonstrated that K^{trans} and k_{ep} can differentiate between benign and malignant breast lesions and discriminate different breast cancer subtypes[25,44]. Other authors found that percentage changes of K^{trans} after the first cycle of NAC, were a good predictor of tumour pathological response[45].

When the DCE-MRI analysis method does not require characterization of the AIF, it is considered *semi-quantitative*. Semi-quantitative metrics are derived from the time-signal intensity (SI) curve[38], and examples include the initial area under the curve (iAUC), time to peak (TTP) and slope of the washout curve[37].

The Breast Imaging Reporting and Data System (BI-RADS) lexicon which was developed by the American College of Radiology (ACR) in order to standardize breast MRI reports, in addition to the evaluation of the lesion morphological features (shape, size and margins), includes MRI enhancement characteristics of the tumour such as internal and peripheral enhancement (also denominated rim enhancement, a sign of central hypoxia in the tumour[46]) and the analysis of the time-signal intensity curve of the cancer, known as well as tumour kinetic curve.

Semi-quantitative methods used in DCE-MRI are based on describing the shape of this time-signal intensity curve of Gd-concentration in the lesion[47]. The tumour enhancement curve helps to differentiate malignant tumours from benign lesions[48,49,50]. The enhancement kinetics curve is obtained by plotting the signal intensity values in breast tissue intensity over time after contrast material injection. It has two phases, which are assessed separately, an initial phase and a delayed phase (Figure 2.2). The initial phase or initial slope occurs within the first2 mins after contrast injection or when the time-signal intensity curve starts to increase. It is slow if there is a signal increase of less than 50% compare to the un-enhanced baseline, mediumif the signal intensity increases from 50 to 100%, and fast if the signal intensity increases morethan 100%. This enhancement rate is calculated according to the following enhancement formula: % Enhancement rate = $[(SI_{post} - SI_{pre})/SI_{pre}] \times 100$[51] where SI refers to signal intensity.

The delayed phase occurs after the first 2 mins post-contrast or after the curve has peaked. A persistent increase in signal intensity after contrast injection is considered a type 1 kinetic curve and is correlated to tumour benignity. A type 2 kinetic curve has a plateau pattern where there is initial contrast uptake followed by a plateau phase and indicates malignancy (however, the lesion could be benign or malignant). Type 3 curves are characterized by initial rapid uptake followed by rapid signal washout and it is strongly suggestive of malignancy[47]. Small cancers and DCIS usually present with a type 1 kinetic curve or steady enhancement in DCE-MRI whereas large tumours present type 3 kinetic curves or washout of the signal enhancement because of their increased vasculature.[52]

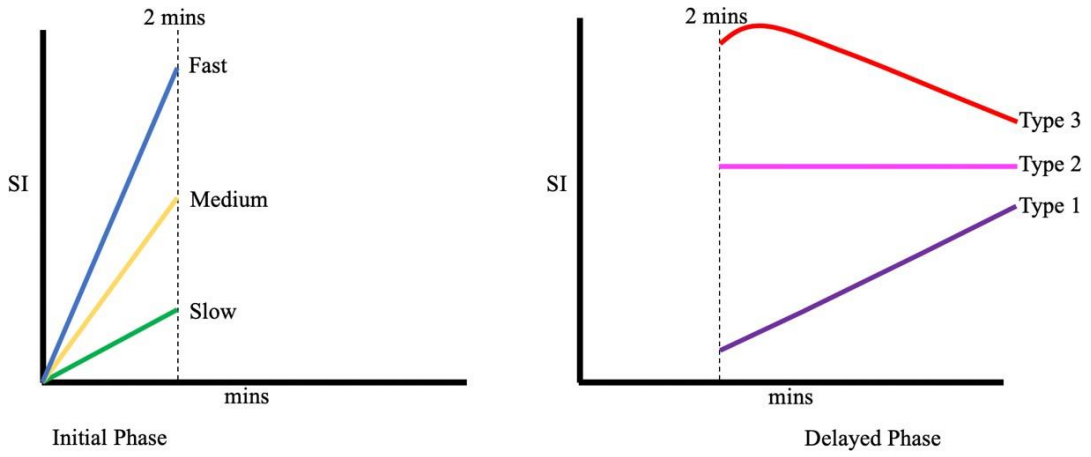

Figure 2.2 Phases of the time-signal kinetic curve of breast lesions. SI: Signal Intensity, mins: Minutes. A slow initial slope usually precedes a delayed phase of persistent enhancement (type 1 curve) whereas medium or fast initial slopes tend to be followed by plateau or washout curves (type 2 or 3, respectively).

DCE-MRI qualitative analysis consists of examining the internal enhancement features of the cancer which according to the fifth and last BI-RADS edition[53] are as follows: homogeneous enhancement, heterogeneous enhancement and rim enhancement[49]. In routine clinical practice, the data from DCE-MRI is analyzed qualitatively, using the BI-RADS lexicon, and semi-quantitatively (analysis of the enhancement curves of the lesions). The calculation of DCE-MRI quantitative parameters is reserved for breast cancer research, perhaps due to the time this analysis takes.

DCE-MRI is an evolving tool for determining breast disease and an excellent imaging modality to monitor treatment response in breast cancer patients receiving neoadjuvant chemotherapy (NAC), allowing visualization of the extent of disease and lesion heterogeneity, detection of changes in angiogenic properties before morphological alterations, and prediction of the overall response early during treatment. Likewise, gadolinium diethylene-triamine penta- acetic acid-based (DTPA or gadolinium-pentetate) DCE-MRI has been useful measuring hypoxia: Egeland et al[54] observed that xenografted tumours of human melanomas showing

high K^{trans} and v_e values had low fractions of hypoxic cells on pimonidazole stained specimens, whereas tumours showing low K^{trans} and v_e values had high hypoxic fractions. DCE-MRI has also provided measures of tumour hypoxia and IFP in cervical carcinoma[55]. These studies support the current attempts to establish DCE-MRI as an indirect method for assessing the presence and extent of hypoxia in human tumours.

2.1.2 Diffusion weighted Imaging (DWI) for imaging tumour perfusion and cellularity

In biological tissues, diffusion of water molecules follows a pattern according to the biophysical characteristics of the tissue such as tissue structure, cell membrane integrity and cell density[34]. In some pathological conditions like cancer, this diffusion pattern is disturbed[56]. Diffusion-weighted MRI (DW-MRI) or DWI is a non-invasive technique that visualizes the microstructural characteristics of water diffusion in biological tissues without the administration of contrast. The microscopic motion includes blood microcirculation in capillary networks, therefore, both, diffusion of water and perfusion are assessed by DWI. DWI-MRI has a short acquisition time of 2-3 minutes and it is available on most commercial scanners[57]. The sensitivity of DWI-MRI mainly depends on the degree of diffusion weighting, described by the b-value (s/mm^2).

To measure the diffusivity of the tissue, the Apparent Diffusion Coefficient (ADC, calculated in mm^2/s) is generated for each voxel in the image and presented as ADC maps[58]. The ADC can be calculated using two or multiple b-values varying between 0 and 1000 mm^2/s[57,58,59]. In malignant breast tumours, due to the high cellular density and abundance of intra and intercellular membranes, there is a more restricted diffusion and lower ADC in comparison to the normal breast parenchyma and benign lesions[60,61,62]. There is controversy with respect to a cut-off value of ADC to differentiate malignant from benign breast lesions, however, studies' cut-off values of ADC range between 1.1 and 1.3 x 10^{-3} mm^2/s[59,63]. Recently, body background signal suppression (DWIBS) has been added to DWI because it is superior to conventional DWI for the visualization of malignant and benign breast lesions[64,65,66].

DWI-MRI may reduce false positives and unnecessary biopsies[25]. It also enables the differentiation of breast cancer subtypes, including invasive versus non-invasive carcinomas[67,68]. DWI-MRI together with DCE-MRI of the breast provide higher diagnostic

accuracy than DCE-MRI alone[69,70]. Likewise, DWI is a useful tool for the assessment of tumour response after NAC. It has been reported that changes in ADC occur earlier than changes in vascularity (DCE-MRI parameters) or tumour size[71,72]. ADC can be used to identify metastatic breast cancer in axillary lymph nodes, and it has shown good correlations with prognostic factors of breast cancer (tumour grade and molecular markers such as oestrogen receptors and progesterone receptors)[73].

2.1.2.1 Intravoxel Incoherent motion Diffusion (IVIM)

IVIM results from the "pseudo-perfusion effect" caused by blood flow within a random capillary network[58,74,75]. Intravoxel Incoherent motion DWI is obtainedfrom multiple b-values without the injection of contrast material[76]. It provides measurements of diffusion and perfusion separately. Pure diffusion is acquired as tissue diffusion coefficient(D_t)[77]. Pseudo-diffusion coefficient (D_p) and microvascular volume fraction (f) are the perfusion parameters[78]. All these parameters allow a non-invasive assessment of the tumour microenvironment.

Many researchers have been able to correlate IVIM parameters with prognostic factors of breast cancer and DCE-MRI parameters[79,80,77]. In those studies, (D_t) values were positively correlated to hormonal expression[79,80] and Ki-67 expression[77]. Similarly, Sung et al[76]demonstrated positive correlations between IVIM-derived ADC and perfusion fraction (*f*) andDCE-MRI tumour kinetic features.

2.1.2.2 Diffusion Tensor Imaging (DTI)

Water molecules move in different directions within biological tissues (anisotropy)[88]. Obstacles likecell membranes, can block the movement of molecules going in some directions causing molecular displacements[89] (the molecule changes its original orientation). Another factor which can influence on these molecular displacements is the application of diffusion gradientsin multiple directions during the MRI examination to improve the analysis of diffusionanisotropy[90]. DTI-MRI detects and visualizes these molecular displacements[90]. DTI-derived parameters mean diffusivity (MD, an estimate of the average anisotropy) and fractional anisotropy (FA, a measure of the directionality of diffusion anisotropy) correlate well with tissue cellularity[91] and they can provide information about tumour aggressiveness in breast cancer[92].

A lower diffusion anisotropy has been found in breast cancers in comparison to the normal breast parenchyma[91]. Other researchers have successfully used DTI to differentiate malignant from benign breast tumours[93,94]. Kim et al[92] reported associations between DTI- derived metrics, MD and FA, and breast cancer histological prognostic factors. Specifically, they reported that lower MD and FA values were significantly associated with larger tumour size (>2 cm), nuclear grade 3 and lymph node metastasis. In the same study, significant differences in MD were observed between invasive breast carcinoma and DCIS.

2.1.2.3 Diffusion weighted Kurtosis (DKI)

Water molecules usually diffuse without any restrictions (with a "Gaussian pattern"), however, as previously mentioned, in biological tissues water molecules follow the tissue microstructure which restricts their free movement and diffusion (non-Gaussian diffusion)[81,82]. DKI quantifies the deviation of water diffusion from a Gaussian pattern[83]. In 2005, Jensen et al[83] proposed a DKI model from which parameters such as kurtosis and diffusion coefficients were derived.

DKI has demonstrated higher sensitivity than conventional DWI in the diagnosis of different types of cancer, including breast[84,85,86,87]. These studies have revealed that high grade cancers show more heterogeneity in their microstructure than low grade cancers. In a different study[82], DKI showed higher specificity than conventional DWI for differentiating malignant from benign breast lesions. High kurtosis values and low diffusivity coefficients were observed in grade 3 breast cancers and cancers with high Ki-67 expression.

There are two known limitations to DKI[1]: The first one is the long image acquisition time compared with that of Diffusion Tensor Imaging (DTI); a minimum of two nonzero b-values and 15 diffusion directions need to be acquired to calculate the diffusion and kurtosis tensor. This long image acquisition time increases susceptibility to patient motion and decreases throughput. Clinically feasible imaging protocols of 7–10 minutes have been suggested for DKI[2,3]. Another limitation of DKI is that the model is more complex (21 independent parameters) than DTI (six independent parameters)[4].

2.1.3 BOLD-MR for imaging tumour hypoxia and perfusion

This functional MRI technique has been traditionally used to measure tumour oxygenation, however, in brain tumours, it has proved to be able to assess tumour perfusion as well[34,95]. Blood oxygen level-dependent MRI (BOLD-MRI) can show the hemodynamic fluctuations which lead to oxygenation changes[95,96,97].BOLD-MRI distinguishes oxygenated hemoglobin (oxy-Hb) from deoxygenated hemoglobin (deoxy-Hb) which is paramagnetic (causes signal increase on T1-weighted images) and produces a change in the T_2*-relaxation rate of the tissue (see figure 2.3), therefore, signal loss is observed in T_2* weighted images[98]. Because of this, T_2*-weighted sequences are used to detect changes in deoxy-Hb which are small and typically range between 1-5%. Although T_2* weighted images are preferred in most cases to detect endogenous deoxy-Hb as contrast agent, a study deriving BOLD contrast from T_2 weighted images (T2WI) proved that T2WI are trustworthy to detect BOLD contrast in the breast[99]. Since blood flow in tumours is related to a response of the body to oxygen and carbon dioxide levels in tissues, BOLD-MRI R_2* ($1/T_2$*, apparent relaxation rate or decay rate) could be considered an indirect marker of hypoxia[100]. Interestingly, Li et al[101] reported that R_2* in treatment-naïve breast cancers may be a marker of perfusion whereas in treated breast cancers R_2* by contrast, seems to be a marker of tumour hypoxia. This is explained by the fact that before NAC, the authors observed a relationship between R_2*, relative blood flow and relative blood volume which it was not observed after NAC treatment.

There have been many reports of BOLD-MRI in the breast: Jiang et al[102] used an oxygen-breathing challenging BOLD technique in patients with locally advanced breast cancer. A preliminary observation was that a greater BOLD response was correlated with better treatment response. More recently, Wallace et al[103] investigated stimuli combinations for inducing BOLD contrast in healthy volunteers and breast cancer patients. Oxygen vs. 5% carbon was found to be the most robust stimulus for BOLD imaging in the breast, with heterogeneous results in malignant tissue.

BOLD-MRI can provide a non-invasive approach to assess breast tumour physiology, nevertheless, there are number of limitations for BOLD imaging: (1) blood flow is only an indirect marker of hypoxia; (2) T2*-sequences are susceptible to field inhomogeneity due to bone-air interfaces (particularly in the brain), hemosiderin/blood products, rapid flow in large veins and metal; (3) even small movement artefacts can lead to poor quality images[102].

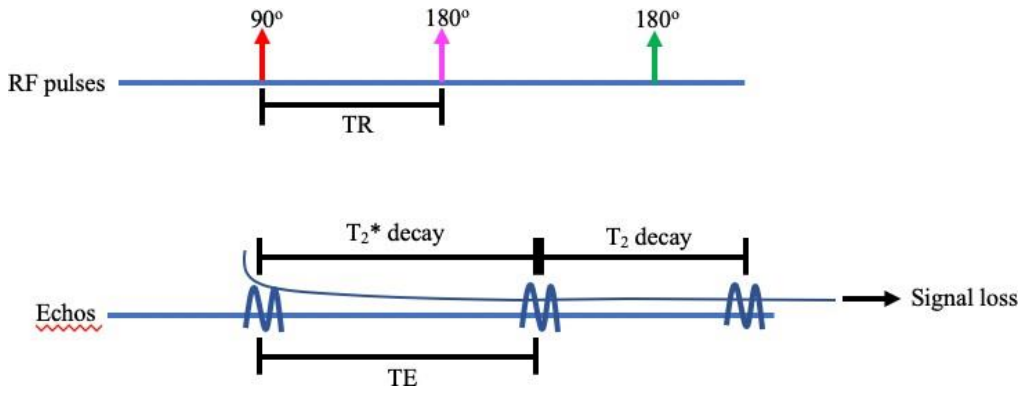

Figure 2.3 Physics behind BOLD-MRI[98]. After termination of the radiofrequency pulse transmission, the receiver coil detects a decrease or decay of the T2* and T2 relaxation times of the tissues due to signal loss. This T2* decay is detected and measured by BOLD-MRI. RF: Radiofrequency; TR: Repetition time (time between one pulse and the next one); TE: Echo time (time between consecutive echos).

2.1.4 Oxygen-Enhanced MRI (OE-MRI) for imaging tumour hypoxia

An emerging imaging technique is oxygen-enhanced MRI (OE-MRI). This method is based on measuring the increase of the longitudinal relaxation rate of protons (R_1) after the inhalation of oxygen. Since oxygen levels are normally adequate to satisfy mitochondrial demands, excess oxygen remains dissolved in plasma and interstitial fluid[104]. The change of R_1 (ΔR_1) is sensitive to oxygen concentration in the interstitial fluid and plasma and the relationship between ΔR_1 and pO_2 has been also shown by a research group[105,106]. As ΔR_1 is not dependent upon haemoglobin saturation, haemo-dynamic effects of hyperoxic gas breathing would not influence on it[107]. R_1 changes produce intensity changes on MRI T1 weighted images which typically are ≤5%[108]. Other biomarkers of OE-MRI, when used together with DCE-MRI, are Oxy-R (or perfused Oxy-R) which highlights the regions of the lesion that are perfused but lack oxygen enhancement and Oxy-E, which refers to tumour perfused areas with oxygen enhancement[109]. Oxy-R has provided utility distinguishing hypoxic tumour areas from well-oxygenated areas[107].

O'Connor et al[110] demonstrated that OE-MRI accurately quantifies tumour hypoxia non-invasively and that this technique could be translatable to the clinic. Similarly, Salem et al[111] showed that OE-MRI could be a good imaging modality to monitor hypoxia changes in non-

small cell lung cancer (NSCLC), to predict tumour response to immunotherapy in patients with hypoxic tumours and to guide radiotherapy by mapping regional hypoxia. OE-MRI could bear potential utility in radiotherapy: This modality was capable to distinguish radiation necrosis from high-grade gliomas in mouse models[112]. The value of OE-MRI continues to be investigated by several research groups.

2.1.5 Proton Magnetic Resonance Spectroscopy (^{1}H-MRS) for imaging tumour metabolism and pH

Magnetic Resonance Spectroscopy (MRS) provides spatially localized signal spectra of tissues in which the structure and concentration of chemical compounds in a certain region of interest (ROI) are shown as spectral peaks[34]. The position of each peak is determined by the chemical structure, and the area under each peak is determined by the chemical concentration[113]. Many studies using ^{1}H-MRS in the breast have identified high levels of the metabolite Choline in malignant breast tumours compared with benign and normal breast tissue[114,115,116]. Choline is needed to synthesize major phospholipids vital for cell membranes, hence, choline is a well-known marker of cell density and proliferation. The Choline peak (tCho, total Choline peak) that is located at 3.2 ppm (parts per million), represents different choline-containing compounds (free choline, phosphocholine and glycerophospho-choline)[25] which can be detectable in the normal breast parenchyma as well but at higher signal to noise ratio (SNR) levels[113,117].

Proton MRS can be very useful to detect cellular anaerobic metabolism since lactate is one of the more important compounds assessed on MR spectroscopy. Lactate resonates at 1.3 ppm with a characteristic double peak at long echo times (TE)[118]. It is elevated in necrotic areas which are commonly observed in higher grade tumours and infections[119]. Breast cancers can show high concentration of lactate[120]. Serganova *et al*[121] investigated lactic dehydrogenase A (LDH-A) regulation in primary breast cancer. The high lactate levels in small primary tumours of the breast were associated with intense pimonidazole staining (an immunohistochemical marker of hypoxia). The same authors recommended Lactate-MRS to monitor LDH-A targeted therapy and for the surveillance of patients who are at high risk of developing metastasis.

^{1}H-MRS can be performed as single or multi-voxel proton MRS. Single proton MRS is the most widely used acquisition approach[25] and it produces a single chemical spectrum from a 3-dimensional cuboid volume (or voxel) placed on the centre of a lesion[25,34]. On the other hand, multivoxel proton MRS produces a spatially resolved grid of spectra from a larger volume of voxels using multiple phase-encoding steps[25,34]. Breast MRS analysis is done qualitatively, semi-quantitatively or quantitatively[113]. The qualitative analysis consists of visually detecting the peak of total Choline (tCho). Semi-quantitative analysis focuses on measuring tCho SNR, peak height or peak integral. A threshold of tCho SNR >2 is commonly used to distinguish malignant from benign breast lesions[25]. The quantitative analysis of tCho is based on the calculation of its concentration using internal referencing to unsuppressed water signal (MRI scanners detect and localize the signals from hydrogen nuclei in water and lipids whose peaks dominate in-vivo spectra) or external referencing to a phantom with a known chemical concentration[113].

^{1}H-MRS improves the diagnosis of breast cancer. ^{1}H-MRS Choline concentration has shown high specificity for differentiating benign breast lesions from cancers[122,123,124]. Other researchers have reported a high sensitivity and accuracy of ^{1}H-MRS for breast cancer detection[32,125]. On the other hand, different investigators observed low sensitivity of proton MRS for detecting choline levels in small breast cancers (<10 mm)[113]. Choline levels in breast cancer may be an early predictive marker of tumour response after treatment since they reflect treatment-induced alterations in cell proliferation prior to changes in tumour size[126,127,128].

2.1.6 Hyperpolarized carbon-13 Magnetic Resonance Imaging (HP ^{13}C-MRI) for imaging tumour metabolism and hypoxia

Hyperpolarized (HP) carbon-13 (^{13}C) MRI is another non-invasive imaging modality which allows real-time in-vivo evaluation of cancer metabolism[129]. Naturally, the MRI signal of endogenous ^{13}C nuclei is low due to its low abundance in the human body (only 1.1% of carbon in the body is ^{13}C) and to its low nuclear spin polarization (the spins of ^{13}C nuclei are not well aligned to the external magnetic field)[130]. In order to observe ^{13}C alone or labelled to substrates such as pyruvate (the most widely used ^{13}C-labelled substrate[131,132,133]) using MRI, the MRI signal needs to be increased by a process called hyperpolarization[129], which increases the signal

of ^{13}C by more than 10,000 fold[134]. The basic principle of hyperpolarization is that electrons have a high level of polarization (most of the electrons are aligned in the same direction) at low temperatures and in high magnetic fields[129]. This high level of polarization can be transferred to ^{13}C-metabolic substrates (increasing their MRI signal) by mixing free electrons with the ^{13}C-labelled substrates[135]. The mixture needs to be placed in a polarizer at a high magnetic field (3.0-5.0 T) and at a low temperature. Lastly, the high electron spin polarization is transferred to the ^{13}C nuclear spins by microwave irradiation, and then the sample is ready to be injected into patients[34].

Pyruvate is converted into lactate by the enzyme lactate dehydrogenase (LDH) through a catalytic reaction. In tumours, the isoform A of the enzyme is predominantly presented[136]. HP ^{13}C-MRI affords high sensitivity to image in real time the spatial distribution of intravenous (i.v) hyperpolarized ^{13}C-pyruvate and the hyperpolarized ^{13}C-lactate formed from it[137]. The level of hyperpolarized-^{13}C lactate produced from the metabolism of ^{13}C pyruvate increases with cancer grade, reflecting disease aggressiveness[130,138], and can provide a rapid assessment of treatment response. The latter has been suggested by multiple studies demonstrating an early reduction in ^{13}C lactate following therapy[139,140]. Gallagher et al[138], demonstrated the feasibility of hyperpolarized ^{13}C MRI in patients with breast cancer. In their study, ^{13}C-pyruvate metabolism displayed tumour metabolic heterogeneity in breast cancers where lactate labelling correlated with tumour volume, MCT-1 expression (a protein which facilitates the transport of lactate across the plasma membrane[141]) and HIF-1 alpha. Similarly, different authors have considered that hyperpolarized ^{13}C-pyruvate may be a useful MRI biomarker of MCT-1 regulation and malignant transformation in breast cancer cells[142].

2.2 Positron Emission Tomography (PET) for the evaluation of breast cancer microenvironment

Pathological conditions often begin with molecular or biochemical changes occurring in an organ or tissue at a cellular level. Positron Emission Tomography (PET) is a highly sensitive and accurate nuclear medicine technology which identifies changes in the tissues at an earlier stage, before anatomical or structural changes[143]. PET can detect diseases in early onset although it is also used for the functional or metabolic assessment of normal tissues. PET detects the gamma-rays from positron-emitting isotopes. Some of

the most frequently used radioisotopes are carbon-11 (half-life, $T_{1/2}$ = 20 min), nitrogen-13 ($T_{1/2}$ = 10 min), fluorine-18 ($T_{1/2}$ = 110 min), copper-64 ($T_{1/2}$ =12.7 h), and iodine-124 ($T_{1/2}$ = 4.2 days)[143], among others.

The physics behind PET can be summarized as follows (see Figure 2.4)[144]. When the positron-emitting radiotracer is administered to patients, the nucleus emits a positron which travels a short distance, up to a few millimeters (mean positron range), to meet an electron in the tissue. This process is called annihilation (the positron annihilates with the electron). This annihilation event produces a pair of 511-KeV photons that are emitted in opposite directions,with an angle between them of approximately 180º. The resulting gamma rays (photons with the highest level of energy) are the signals detected by the PET scanner and converted to images. PET provides images of the quantitative uptake of the injected radiotracer from which the concentration of radiotracer can be calculated in becquerels per milliliter (Bq/mL). Radiotracer uptake can also be measured semi-quantitatively by calculation of the standardized uptake value (SUV) in a static PET image, this means a single point in time. The SUV is calculated by a formula, see Figure 2.5[145].

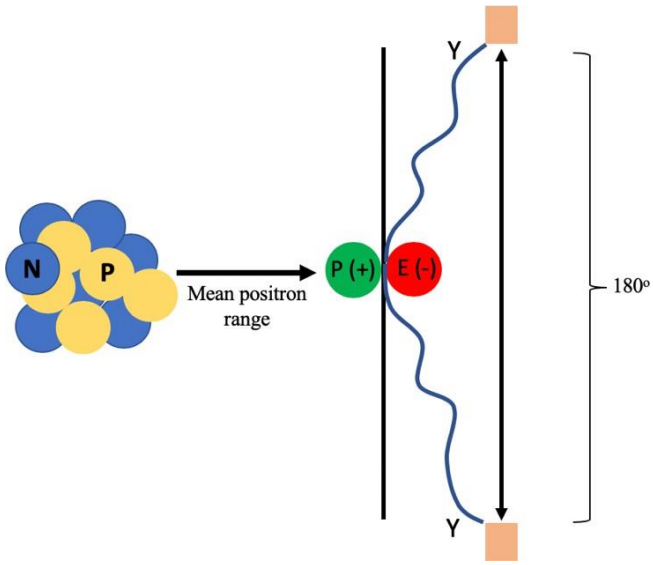

Figure 2.4 Annihilation reaction[144]. This image illustrates the nucleus of the radiotracer containing N=neutrons (blue circles) and P=protons (yellow circles) from which the positron is emitted after travelling a small distance called the mean positron range. The positron, which is positively charged, annihilates with a negatively charged electron while being in motion and then, 2 photons are emitted with an angle between them of 180º. This angle may vary 0.5º. The gamma rays from the two photons will hit the detectors (sand colour squares) of the PET scanner ring.

Positron Emission Tomography uses a broad range of radiotracers (molecules or radiopharmaceutical drugs labelled with different radioisotopes) which offer many advantages for the in-vivo and real-time evaluation of functional processes related to cancer pathophysiology. In the area of oncology, PET is being utilized for cancer staging, assessing treatment strategies and monitoring the effects of cancer therapy. The most commonly used oncologic PET radiotracer is ^{18}Fluoro-2-deoxy-glucose (^{18}F-FDG) and it is the only one approved by the Food and Drug Administration (FDA) for routine clinical use.

By combining PET with CT, functional and anatomic images are obtained from the same patient. PET-CT is required for differentiating normal from abnormal radiotracer uptake because PET provides poor anatomic detail which CT affords.

$$SUV\ (g/mL) = \frac{\text{Tissue radioactivity concentration (Bq/mL)}}{\text{injected radiotracer acitivity (Bq)} \ \div \ \text{patient weight (g)}}$$

Figure 2.5 SUV equation. Tracer concentration in the tissue is expressed in becquerels per milliliter (Bq/mL), injected radiotracer activity is in becquerels (Bq) and patient weight in grams (g).

2.2.1 PET for imaging tumour metabolism

Like other cells, tumour cells take up the glucose by facilitated transport via glucose transporters (GLUTs) and, later through glycolysis, pyruvate is derived from glucose under aerobic conditions. However, under anaerobic conditions (under the absence of oxygen), pyruvate is converted to lactate by LDHA[146]. Cancer cells have an increased glucose uptake due to upregulation of hexokinase activity[146]. ^{18}F-fluoro-2-deoxy-D-glucose (^{18}F-FDG) is a radiopharmaceutical analogue of glucose that is transported through cell membranes by GLUTs, in the same way that glucose. ^{18}F-FDG is then phosphorylated to ^{18}F-FDG-6-phosphate which cannot undergo glycolysis, unlike glucose-6 phosphate, and hence it is trapped within metabolically active cells[147]. The rate of ^{18}F-FDG uptake by cancer cells is proportional to their metabolic activity.

Since most tumour cells have an increased glucose metabolism, ^{18}F-FDG is trapped by all types

of cancer including most types of lymphoma, melanoma, breast cancers, ovarian, cervical, head and neck, stomach, oesophageal, colorectal, lung, etc[148]. Many studies have reported that changes in ^{18}F-FDG uptake predict tumour response to therapy and that further information regarding tumour grade and proliferative status may also be derived from ^{18}F-FDG scans[149]. ^{18}F-FDG-positron emission tomography (^{18}F-FDG-PET) is being utilized in breast cancer for the detection and differentiation of primary breast tumours, lymph node staging, detection of residual and metastatic disease and for the follow-up of patients after surgery, chemotherapy and/or external radiotherapy[150,151,152].

According to a meta-analysis involving 2,460 breast cancer patients, ^{18}F-FDG-PET sensitivities range between 20-100% and specificities between 65-100%[153]. Another study[154] reported that the sensitivity of ^{18}F-FDG-PET-CT in small breast lesions (<5mm) was 53% whereas in large lesions (>20mm) the sensitivity was 92%. The uptake of ^{18}F-FDG may be influenced by the phenotype, mitotic index and grade of the primary breast tumour[155]. ^{18}F-FDG has proved to be helpful predicting and monitoring response to neo-adjuvant chemotherapy, even early in the course of treatment[156,157,158]. Some authors[157] demonstrated a decrease of more than 40% in ^{18}F-FDG SUV_{max} in responding tumours after NAC, whereas non-responding tumours showed an increase, no change, or only a small decrease (of about 24%) in ^{18}F-FDG SUV_{max}. As for lymph node metastases, ^{18}F-FDG-PET is not sensitive enough to detect microscopic metastases in non-pathologically enlarged lymph nodes. However, in lymph node metastases larger than 3 cm, the sensitivity and specificity of ^{18}F-FDG-PET-CT at 97% and 100% has been reported[159,160].

Recent studies have shown the advantage of delayed or dual-time point imaging (DTPI) with ^{18}F-FDG-PET to distinguish malignant from benign ^{18}F-FDG uptake[161,162]. Delayed scan time-points may improve ^{18}F-FDG-PET image quality due to the greater tumour to background contrast[163,164].

2.2.2 PET for imaging tumour perfusion

For years ^{15}O-labeled water (^{15}O-H_2O)-PET has been considered the gold standard method to quantify blood flow in humans[165]. However, not many imaging centres can perform these PET studies because an on-site cyclotron to produce ^{15}O-H_2O is required. Since the half-life of ^{15}O is so short (only 122 seconds[165]), the radioactive activity of ^{15}O-H_2O would decay shortly after the radiotracer is produced. ^{15}O-H_2O-PET is a promising diagnostic tool for the assessment of tumour aggressiveness[166]. In prostate cancer, absolute quantification values of tumour perfusion measured by ^{15}O-H_2O-PET have been highly correlated to post-prostatectomy tumour Gleason grades[167]. In breast cancer patients, ^{15}O-H_2O-PET has proved to be effective for the early detection and quantitative analysis of sub-clinical post-radiotherapy changes in heart perfusion[168,169].

Different PET radiotracers produced with other radioisotopes are being used to quantify tumour blood flow. Since 1989, when the FDA allowed its use in clinical studies, ^{82}Rubidium (^{82}Rb)-PET has proved to accurately quantify myocardial (MBF) blood flow[166,170]. ^{82}Rubidium, is a potassium analogue which is trapped within cells in metabolically active tissues at a rate proportional to tissue blood flow[170,171] and as it is retained longer than ^{15}O in the tissues, ^{82}Rb allows quantitative measurements of blood flow using kinetic modelling and semi-quantitative measurements using SUV in late uptake images[166]. Few years ago, ^{82}Rb's potential to measure tumour blood flow (TBF) started to be evaluated. Mads R Jochumsen et al[166] demonstrated that ^{82}Rb-PET-CT was a diagnostic tool for quantitative tumour blood flow imaging after comparing its performance with the one of the gold standard method ^{15}O-H_2O-PET-CT. Likewise, they proved that ^{82}Rb-PET SUV was associated with prostate cancer aggressiveness and they could also show its potential to estimate TBF in this type of cancer. The same authors observed higher uptake of ^{82}Rb in the cancer than in the normal prostate tissue. Ali Shafiq et al[172]. reported a case of a male old patient in whom ^{82}Rb- cardiac PET helped to diagnose breast cancer metastasis in the lungs. The potential of ^{82}Rb-PET to diagnose breast cancer metastasis in the brain has also been explored by Lu et al[173]. In his study, ^{82}Rb-PET-MRI showed better tumour-to-noise ratio than ^{18}F-FDG-PET-MRI. The lesion was positive in both, ^{18}F-FDG and ^{82}Rb PET brain studies. To my knowledge, no studies have been done with ^{82}Rb-PET on primary breast cancers.

2.2.3 PET for imaging tumour hypoxia

Positron Emission Tomography can directly quantify oxygen levels by employing radiotracer labelled molecules which allow the non-invasive and three-dimensional evaluation of oxygen levels within the tumour in a more direct manner[174]. ^{18}F-FDG can be upregulated under hypoxic conditions, however, it is not specific for hypoxia. Therefore, since the1980s a great number of PET tracers have been developed for the identification of hypoxia in living tissues and solid tumours, starting with the 2-nitroimidazole family of compounds[175,174,176]. Only few of these compounds have been used to study breast cancer.

^{18}Fluorine-Fluoromisonidazole (^{18}F-FMISO) is a radiolabelled analogue of the hypoxic radio sensitizer drug, misonidazole. ^{18}F-FMISO is the predominant PET tracer among the tracers of the 2-nitroimidazoles group and it has been extensively investigated for noninvasively detecting hypoxia *in vivo* using PET imaging[177]. It freely diffuses into cells and under normal oxidative conditions, freely exits. When entering hypoxic cells, ^{18}F-FMISO is reduced and retained through accumulation of the 2-nitroimidazole metabolites and irreversibly bound to intracellular thiol-rich proteins[178] (Figure 2.6). ^{18}F-FMISO accumulation in hypoxic tumours increases over a period of approximately four hours, while the efflux from normoxic tissues starts at 30 minutes post-injection. Imaging times suggested range from 2 to 4 hours post injection[179].

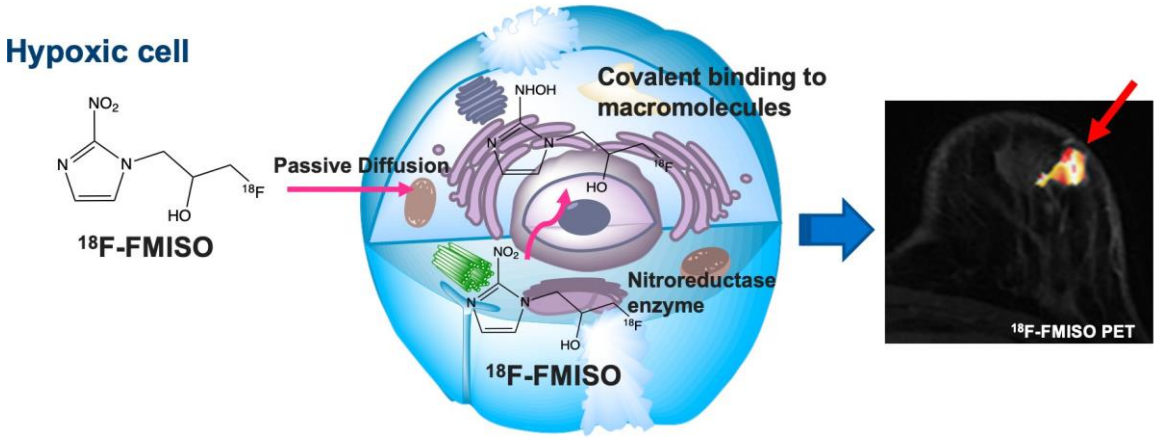

Figure 2.6 ^{18}F-FMISO metabolism under hypoxic conditions: ^{18}F-FMISO enters the cell by passive diffusion and under a hypoxic environment ($pO_2 \leq 10$ mmHg) it is reduced by the nitro reductase enzyme and becomes irreversibly trapped by intracellular proteins.

^{18}F-FMISO-PET is a highly sensitive and specific non-invasive technique for the evaluation of the hypoxic breast tumour microenvironment[180,181] and it has demonstrated potential in treatment selection and treatment response prediction[182,183]. By using ^{18}F-FMISO PET, Yamane et al (2016)[183] demonstrated that tumour hypoxia may play an important role in the differentiation of breast cancer subtypes[183]. Sorace et al[182] showed the potential of ^{18}F-FMISO-PET in predicting response to anti-HER2 therapy. In a recent study, baseline ^{18}F-FMISO-PET showed that HER2-negative breast cancers do not benefit from neo-adjuvant Nintedanib[184] (a potent multityrosine kinase receptor inhibitor and also VEGF receptor inhibitor[185]). Furthermore, ^{18}F-FMISO was studied in a triple negative human breast cancer xenograft where it could detect hypoxic status in TNBC cells at a macroscopic level[186].

Based on published information, ^{18}F-FMISO is the only nitroimidazole compound that has been used for the assessment of hypoxia in clinical research of breast cancer. Other non-nitroimidazole compounds like for example, ^{64}Cu-diacetyl-bis (N4-methylthiosemicarbazone) (^{64}Cu-ATSM) have been examined in different tumour types which do not include breast cancer[175]. Lopci et al (2014)[175] in their work about PET radiopharmaceuticals for imaging tumour hypoxia stated that evidence-based data favours the use of ^{18}F-FMISO, but the issue of sub-optimal tumour to background ratio persists.

Despite its high hypoxic selectivity, ^{18}F-FMISO suffers from a slow kinetic profile and limited clearance from normoxic tissue and blood which may result in moderate hypoxic-to-normoxic tissue contrast. However, very recently a new method to improve the tumour to background ratio of ^{18}F-FMISO imaging was published by Goos et al[187]. This method consists of pH responsive polymers designed for improving the delivery and retention of ^{18}F-FMISO into hypoxic cells.

PET imaging using ^{18}F-FMISO has been shown to identify hypoxic tumour sub-volumes and track spatiotemporal dynamics[188]. Efforts have been made to develop fluorinated hypoxia markers with improved pharmacokinetic properties. Examples include: ^{18}F- fluoroazomycin arabinoside (^{18}F-FAZA), ^{18}F- fluoroerythronitroimidazole (^{18}F-FETNIM), and flortanidazole, 3-[^{18}F] fluoro-2-(4-((2-nitro-1H-imidazol-1-yl) methyl)-1H-1,2,3-triazol-1-yl)-propan-1-ol) ^{18}F-HX4. Nevertheless, none of these compounds have been used to study breast cancer.

One study[5] comparing ^{18}F-HX4 with ^{18}F-FMISO and ^{18}F-FAZA for PET imaging of hypoxia found higher tissue clearance for ^{18}F-HX4 than for ^{18}F-FMISO. The absolute tracer activity in

tissue 4 hours post injection was highest for ^{18}F-FMISO and lowest for ^{18}F-HX4. Simulated contrast at four hours post injection was highest for ^{8}F-HX4 (2.39), while ^{8}F-FMISO and ^{18}F-FAZA were comparable (1.67 and 1.75, respectively). Currently, ^{18}F-FAZA and ^{18}F-HX4 are not available in the UK.

2.2.4 PET for imaging tumour proliferation

^{18}F-Fluorothymidine (^{18}F-FLT)-PET enables the quantification of cell proliferation in tumours[189,190,191,192]. ^{18}F-FLT is a structural analogue of the DNA constituent thymidine. It enters proliferating cells by active transport and partly via passive and/or facilitative diffusion[190]. Within the intracellular space, ^{18}F-FLT is phosphorylated by the enzyme thymidine kinase 1 (TK1), which is a key enzyme in DNA precursor synthesis[193,194]. The presence of TK1 in cells is an indicator of active cell proliferation because TK1 is upregulated during the S phase of the cell cycle[194]. Phosphorylation of ^{18}F-FLT into ^{18}F-FLT-phosphate leads to the intracellular retention of the radiotracer (^{18}F-FLT-phosphate forms undergo minimal incorporation into DNA). As phosphorylation by TK1 is the rate limiting step in the ^{18}F-FLT metabolic pathway, ^{18}F-FLT accumulation in cells is proportional to the activity of TK1 and therefore, to sustained cellular proliferation[195]. The accumulation of ^{18}F-FLT in tumours has shown good correlations with cell proliferation measurements from in vitro assays[196], pre-clinical animal studies[197] and human studies[198,199,200,201]. Furthermore, ^{18}F-FLT-PET has shown high specificity in the diagnosis of primary tumours[199, 202] and it can also depict response to chemotherapy.[203,204]

In breast cancer, ^{18}F-FLT-PET SUV and tumour-to-reference tissue ratios have been correlated to the histochemical proliferation index Ki-67 in preliminary studies[205,206,207]. A recent systematic review and meta-analysis about ^{18}F-FLT-PET imaging in which the association between Ki-67 expression and ^{18}F-FLT-PET SUV was examined in various types of cancer, confirmed significant correlations overall and particularly in breast cancer[208]. In a study included in this meta-analysis[209], the sensitivity and specificity of ^{18}F-FLT to predict chemotherapy response in breast cancer was shown. ^{18}F-FLT-PET has also demonstrated specificity in the diagnosis of primary breast tumours and loco-regional metastases[210,211]. ^{18}F-FLT SUV measurements have been reported highly reproducible in the breast (test-retest correlation co-efficient ≥ 0.97[205]) and changes in ^{18}F-FLT SUV measured early after the initiation of treatment were found to be potentially predictive of eventual response to chemotherapy[189,190,212].

There are many other PET radiotracers that are currently being used for the evaluation of other physiological processes such as neuroinflammation, angiogenesis, etc. Every day scientists strive to develop new radiotracers by labelling new molecules or the same molecules with other radioisotopes until finding a radiotracer that proves to be safe and reliable to be used in clinical studies. All of this with the purpose of continuing exploring the cancer microenvironment through the in-vivo assessment by PET.

2.3 Positron Emission Tomography - Magnetic Resonance Imaging (PET-MRI)

Positron emission tomography – Magnetic Resonance Imaging (PET-MRI) is a hybrid imaging technology that incorporates MRI and PET information acquired simultaneously. The most relevant fields where PET-MRI is being used are oncology[213,214,215], cardiology[216] and neurology[217]. The technique emerged as a result of the limited soft-tissue contrast resolutionof CT, especially in the pelvis, head and neck, even when full-dose radiation exposure and contrast medium are employed. As it is well recognized, MRI provides higher soft tissue contrast and spatial resolution than CT[218]. The use of breast PET-MRI combined with other MRI parameters has shown promise in reducing unnecessary breast biopsies that would be recommended based on DCE-MRI examinations[219].

This hybrid technique is highly specific for the diagnosis of nodal breast cancer metastasis compared to conventional imaging methods[220,221]. The added clinical value of hybrid ^{18}F-FDG-PET-MRI compared to conventional imaging in breast cancer management has been assessed by Goorts *et al* (2017)[221]. They reported that PET-MRI results helped to prolong or reduce treatment in 8/40 (20%) patients with breast cancer by identifying more or fewer malignant lymph nodes and distant metastasis. In another study, PET-MRI outperformed PET-CT at a lower radiation dose for breast cancer patients in need of whole-body staging or post-treatment surveillance[222].

PET-MRI is unlikely to become part of the breast clinical routine due to cost, radiation dose, imaging post-processing, and exam reading times. PET-MRI may be more relevant in breast cancer research especially before and during NAC treatment, where all the MRI and PET parameters can be converted into radiomics that may lend increased precision to breast cancer treatment.

Fusion of MR and PET images (fused or combined PET-MRI) may confer clinical advantages over PET-CT; however, it also carries out some limitations.

The following are some of the advantages combined PET-MRI has over PET-CT:

- Simultaneous acquisition of PET and MRI provides an insight into the structural and biochemical features of the cancer in only one exam per patient, shortening the diagnostic cycle of neoplastic diseases (it is only one exam instead of many others).
- PET-MRI provides better methodological analysis of the tumour characterization than PET-CT and MRI separately, currently done only for research. Since the patient is in the exact same position for thePET and MRI scanning, it is easier to correlate imaging parameters extracted from thesame ROI (region of interest) than from two different ROIs located in two different studies (on the PET-CT and the MRI).
- Combined PET-MRI affords more reliable correlations between imaging biomarkers depicting different physiological processes (like for example, correlations between imaging biomarkers of tumour vascularity and hypoxia). Because tissue blood flow and oxygenation may vary over time (seconds and/or minutes), hybrid PET-MRI can help avoiding the confounding effects of intermittent hypoxia or fluctuating perfusion in the analysis of radiomics.
- The availability of sophisticated MRI sequences, such as diffusion and DCE-MRI or MRI spectroscopy, which can provide important information additionally to the information extracted from PET.

Limitations of PET-MRI:

- Attenuation correction[223]: Even though the attenuation of PET photons by biological tissues allows the generation and differentiation of contrasts (scale of grays) on PET-CT images, it also affects adequate quantification of PET parameters because photon attenuation (less photon detection by the detectors of the scanner) may cause underestimation of actual radiotracer activity in lesions or normal tissues. Therefore, to perform attenuation correction of PET images is required. MRI is unable to measure attenuation since there is no relation between MRI signal intensity and photon synthesis or absorption. Different methods of attenuation, like Dixon resonance sequence that is the most commonly used, are used to create attenuation maps from MR images.

- PET-MRI studies are usually longer and more uncomfortable than PET-CT studies. Hence, they are less acceptable for patients and more expensive as fewer studies can be performed per day.

The contraindications of PET/MRI are the same as those of MRI and PET (metallic devices incompatible with magnetic field, claustrophobia and pregnancy or breastfeeding, respectively.)

2.3.1 PET-MRI as a method of measuring hypoxia in breast cancer

Simultaneous PET and MRI assessment of the breast cancer micromilieu has been limited in human studies, perhaps, because of the low availability of PET-MRI systems which may be product of the higher costs of PET-MRI scanners in comparison to PET-CT scanners[224].

Combined PET-MRI scans can avoid spatial and temporal shifts in the hypoxic status of the cancer (cycling hypoxia) due to fluctuations of the tumour blood flow[225]. Similarly, the molecular and phenotypic diversity demonstrated between same breast cancer subtypes and within each cancer (intra-tumoral and inter-tumoral heterogeneity)[226] illustrates the potential role of simultaneous multi-modality imaging in detecting or examining hypoxic breast cancers, improving therefore breast cancer treatment selection and efficacy.

The main aim of this thesis was to provide a better understanding of breast cancer pathophysiology using simultaneous PET and multi-parametric MRI. In particular, this work aimed to explore relationships between imaging biomarkers of tumour vascularity measured by dynamic contrast-enhanced (DCE) MRI, cellularity using diffusion-weighted imaging (DWI) and hypoxic status using ^{18}F-fluoromisonidazole (^{18}F-FMISO) PET.

References

1. Saslow D, Boetes C, Burke W, et al. American cancer society guidelines for breast screening with MRI as an adjunct to mammography. *Obstet Gynecol Surv*. 2007. doi:10.1097/01.ogx.0000269073.50925.38
2. Gruber I V., Rueckert M, Kagan KO, et al. Measurement of tumour size with mammography, sonography and magnetic resonance imaging as compared to histological tumour size in primary breast cancer. *BMC Cancer*. 2013;13. doi:10.1186/1471-2407-13-328
3. Hieken TJ, Harrison J, Herreros J, Velasco JM. Correlating sonography, mammography, and pathology in the assessment of breast cancer size. In: *American Journal of Surgery*. ; 2001. doi:10.1016/S0002-9610(01)00726-7
4. Shoma A, Moutamed A, Ameen M, Abdelwahab A. Ultrasound for accurate measurement of invasive breast cancer tumor size. *Breast J*. 2006. doi:10.1111/j.1075-122X.2006.00249.x
5. Bosch AM, Kessels AGH, Beets GL, et al. Preoperative estimation of the pathological breast tumour size by physical examination, mammography and ultrasound: A prospective study on 105 invasive tumours. *Eur J Radiol*. 2003. doi:10.1016/S0720-048X(03)00081-0
6. Ciatto S, Houssami N, Bernardi D, et al. Integration of 3D digital mammography with tomosynthesis for population breast-cancer screening (STORM): A prospective comparison study. *Lancet Oncol*. 2013. doi:10.1016/S1470-2045(13)70134-7
7. Merritt CRB. Diagnostic accuracy of mammography, clinical examination, US, and MR imaging in preoperative assessment of breast cancer. *Breast Dis*. 2005. doi:10.1016/S1043-321X(05)80190-0
8. Nazari SS, Mukherjee P. An overview of mammographic density and its association with breast cancer. *Breast Cancer*. 2018. doi:10.1007/s12282-018-0857-5
9. Boyd NF, Guo H, Martin LJ, et al. Mammographic density and the risk and detection of breast cancer. *N Engl J Med*. 2007. doi:10.1056/NEJMoa062790
10. Fletcher SW, Elmore JG. Mammographic Screening for Breast Cancer. *N Engl J Med*. 2003;348(17):1672-1680. doi:10.1056/NEJMcp021804
11. Kolb TM, Lichy J, Newhouse JH. Comparison of the performance of screening mammography, physical examination, and breast US and evaluation of factors that influence them: An analysis of 27,825 patient evaluations. *Radiology*. 2002.

doi:10.1148/radiol.2251011667

12. Y.LoPhD A links open overlay panelJay AB. Breast Tomosynthesis: State-of-the-Art and Review of the Literature. *Acad Radiol*. 2011;18(10):1298-1310. doi:https://doi.org/10.1016/j.acra.2011.06.011
13. Friedewald SM, Rafferty EA, Rose SL, et al. Breast cancer screening using tomosynthesis in combination with digital mammography. *JAMA - J Am Med Assoc*. 2014. doi:10.1001/jama.2014.6095
14. Förnvik D, Zackrisson S, Ljungberg O, et al. Breast tomosynthesis: Accuracy of tumor measurement compared with digital mammography and ultrasonography. *Acta radiol*. 2010. doi:10.3109/02841850903524447
15. Mariscotti G, Houssami N, Durando M, et al. Accuracy of mammography, digital breast tomosynthesis, ultrasound and MR imaging in preoperative assessment of breast cancer. *Anticancer Res*. 2014.
16. National Collaborating Centre for Cancer (UK). Familial breast cancer, classification and care of people at risk of familial breast cancer. *Natl Collab Cent Cancer*. 2013.
17. Lord SJ, Lei W, Craft P, et al. A systematic review of the effectiveness of magnetic resonance imaging (MRI) as an addition to mammography and ultrasound in screening young women at high risk of breast cancer. *Eur J Cancer*. 2007. doi:10.1016/j.ejca.2007.06.007
18. Chou CP, Lewin JM, Chiang CL, et al. Clinical evaluation of contrast-enhanced digital mammography and contrast enhanced tomosynthesis - Comparison to contrast-enhanced breast MRI. *Eur J Radiol*. 2015. doi:10.1016/j.ejrad.2015.09.019
19. Conklin MW, Keely PJ. Why the stroma matters in breast cancer: Insights into breast cancer patient outcomes through the examination of stromal biomarkers. *Cell Adhes Migr*. 2012. doi:10.4161/cam.20567
20. Fukumura D, Jain RK. Imaging angiogenesis and the microenvironment. *APMIS*. 2008. doi:10.1111/j.1600-0463.2008.01148.x
21. Narunsky L, Oren R, Bochner F, Neeman M. Imaging aspects of the tumor stroma with therapeutic implications. *Pharmacol Ther*. 2014. doi:10.1016/j.pharmthera.2013.10.003
22. Kobayashi H, Longmire MR, Ogawa M, Choyke PL. Rational chemical design of the next generation of molecular imaging probes based on physics and biology: Mixing modalities, colors and signals. *Chem Soc Rev*. 2011. doi:10.1039/c1cs15077d
23. Ramamonjisoa N, Ackerstaff E. Characterization of the tumor microenvironment and tumor-stroma interaction by non-invasive preclinical imaging. *Front Oncol*. 2017.

doi:10.3389/fonc.2017.00003

24. LeBleu VS. Imaging the Tumor Microenvironment. *Cancer J*. 2015;21(3):174-178. doi:10.1097/PPO.0000000000000118
25. Rahbar H, Partridge SC. Multiparametric MR Imaging of Breast Cancer. *Magn Reson Imaging Clin N Am*. 2016. doi:10.1016/j.mric.2015.08.012
26. Polanec SH, Pinker-Domenig K, Brader P, et al. Multiparametric MRI of the prostate at 3 T: limited value of 3D 1H-MR spectroscopy as a fourth parameter. *World J Urol*. 2016. doi:10.1007/s00345-015-1670-9
27. Ueno Y, Tamada T, Bist V, et al. Multiparametric magnetic resonance imaging: Current role in prostate cancer management. *Int J Urol*. 2016. doi:10.1111/iju.13119
28. Kim JH, Choi SH, Ryoo I, et al. Prognosis prediction of measurable enhancing lesion after completion of standard concomitant chemoradiotherapy and adjuvant temozolomide in glioblastoma patients: Application of dynamic susceptibility contrast perfusion and diffusion-weighted imaging. *PLoS One*. 2014. doi:10.1371/journal.pone.0113587
29. Turkbey B, Mani H, Aras O, et al. Prostate cancer: Can multiparametric mr imaging help identify patients who are candidates for active surveillance? *Radiology*. 2013. doi:10.1148/radiol.13121325
30. Marino MA, Helbich T, Baltzer P, Pinker-Domenig K. Multiparametric MRI of the breast: A review. *J Magn Reson Imaging*. 2018;47(2):301-315. doi:10.1002/jmri.25790
31. Pinker K, Baltzer P, Bogner W, et al. Multiparametric MR imaging with high-resolution dynamic contrast-enhanced and diffusion-weighted imaging at 7 T improves the assessment of breast tumors: A feasibility study. *Radiology*. 2015. doi:10.1148/radiol.15141905
32. Pinker K, Bogner W, Baltzer P, et al. Improved diagnostic accuracy withmultiparametric magnetic resonance imaging of the breast using dynamic contrast- enhanced magnetic resonance imaging, diffusion-weighted imaging, and 3-dimensionalproton magnetic resonance spectroscopic imaging. *Invest Radiol*. 2014. doi:10.1097/RLI.0000000000000029
33. DH1. L. Mechanisms of contrast enhancement in magnetic resonance imaging. *JCancer*. 1991;42:6-12. https://pubmed.ncbi.nlm.nih.gov/2001531/.
34. Marino MA, Helbich T, Baltzer P, Pinker-Domenig K. Multiparametric MRI of the breast: A review. *J Magn Reson Imaging*. 2018. doi:10.1002/jmri.25790
35. Sourbron SP, Buckley DL. On the scope and interpretation of the Tofts models for DCE-

MRI. *Magn Reson Med*. 2011. doi:10.1002/mrm.22861

36. Litjens GJS, Heisen M, Buurman J, Ter HaarRomeny BM. Pharmacokinetic models in clinical practice: What model to use for DCE-MRI of the breast? In: *2010 7th IEEE International Symposium on Biomedical Imaging: From Nano to Macro, ISBI 2010 - Proceedings*. ; 2010. doi:10.1109/ISBI.2010.5490382
37. Yankeelov T, Gore J. Dynamic Contrast Enhanced Magnetic Resonance Imaging in Oncology:Theory, Data Acquisition,Analysis, and Examples. *Curr Med Imaging Rev*. 2007. doi:10.2174/157340507780619179
38. Gordon Y, Partovi S, Müller-Eschner M, et al. Dynamic contrast-enhanced magnetic resonance imaging: fundamentals and application to the evaluation of the peripheral perfusion. *Cardiovasc Diagn Ther*. 2014. doi:10.3978/j.issn.2223-3652.2014.03.01
39. Jena A, Taneja S, Singh A, Negi P, Mehta SB, Sarin R. Role of pharmacokinetic parameters derived with high temporal resolution DCE MRI using simultaneous PET/MRI system in breast cancer: A feasibility study. *Eur J Radiol*. 2017. doi:10.1016/j.ejrad.2016.11.029
40. Amarnath J, Sangeeta T, Mehta S. Role of quantitative pharmacokinetic parameter (transfer constant: K trans) in the characterization of breast lesions on MRI. *Indian J Radiol Imaging*. 2013. doi:10.4103/0971-3026.113614
41. Huang W, Tudorica LA, Li X, et al. Discrimination of Benign and Malignant Breast Lesions by Using Shutter-Speed Dynamic Contrast-enhanced MR Imaging. *Radiology*. 2011;261(2):394-403. doi:10.1148/radiol.11102413
42. Kim SG, Freed M, Leite APK, Zhang J, Seuss C, Moy L. Separation of benign and malignant breast lesions using dynamic contrast enhanced MRI in a biopsy cohort. *J Magn Reson Imaging*. 2017. doi:10.1002/jmri.25501
43. Fan WX, Chen XF, Cheng FY, et al. Retrospective analysis of the utility of multiparametric MRI for differentiating between benign and malignant breast lesions in women in China. *Med (United States)*. 2018. doi:10.1097/MD.0000000000009666
44. Helbich TH, Roberts TPL, Gossmann A, et al. Quantitative gadopentetate-enhanced MRI of breast tumors: Testing of different analytic methods. *Magn Reson Med*. 2000. doi:10.1002/1522-2594(200012)44:6<915::AID-MRM13>3.0.CO;2-S
45. Ashraf A, Gaonkar B, Mies C, et al. Breast DCE-MRI kinetic heterogeneity tumor markers: Preliminary associations with neoadjuvant chemotherapy response. *Transl Oncol*. 2015;8(3):154-162. doi:10.1016/j.tranon.2015.03.005
46. Van Dijke CF, Brasch RC, Roberts TPL, et al. Mammary carcinoma model: Correlation

of macromolecular contrast-enhanced MR imaging characterizations of tumor microvasculature and histologic capillary density. *Radiology*. 1996. doi:10.1148/radiology.198.3.8628876

47. Yang SN, Li FJ, Chen JM, Zhang G, Liao YH, Huang TC. Kinetic curve type assessment for classification of breast lesions using dynamic contrast-enhanced mr imaging. *PLoS One*. 2016. doi:10.1371/journal.pone.0152827
48. Kuhl CK, Mielcareck P, Klaschik S, et al. Dynamic breast MR imaging: Are signal intensity time course data useful for differential diagnosis of enhancing lesions? *Radiology*. 1999. doi:10.1148/radiology.211.1.r99ap38101
49. Helbich TH. Contrast-enhanced magnetic resonance imaging of the breast. *Eur J Radiol*. 2000;34(3):208-219. https://doi.org/10.1016/S0720-048X(00)00200-X.
50. Kaiser WA, Zeitler E. Mr imaging of the breast: Fast imaging sequences with and without Gd-DTPA. Preliminary observations. *Radiology*. 1989. doi:10.1148/radiology.170.3.2916021
51. Cheng L, Li X. Breast magnetic resonance imaging: kinetic curve assessment. *Gland Surg*. 2013. doi:10.3978/j.issn.2227-684X.2013.02.04
52. Mayrhofer RM, Ng HP, Putti TC, Kuchel PW. Magnetic Resonance in the Detection of Breast Cancers of Different Histological Types. *Magn Reson Insights*. 2013. doi:10.4137/mri.s10640
53. Rao AA, Feneis J, Lalonde C, Ojeda-Fournier H. A pictorial review of changes in the BI-RADS fifth edition. *Radiographics*. 2016. doi:10.1148/rg.2016150178
54. Egeland TAM, Gulliksrud K, Gaustad JV, Mathiesen B, Rofstad EK. Dynamic contrast-enhanced-MRI of tumor hypoxia. *Magn Reson Med*. 2012;67(2):519-530. doi:10.1002/mrm.23014
55. Simonsen TG, Lund K V., Hompland T, Kristensen GB, Rofstad EK. DCE-MRI–Derived Measures of Tumor Hypoxia and Interstitial Fluid Pressure Predict Outcomes in Cervical Carcinoma. *Int J Radiat Oncol Biol Phys*. 2018. doi:10.1016/j.ijrobp.2018.04.035
56. Chilla GS, Tan CH, Xu C, Poh CL. Diffusion weighted magnetic resonance imaging and its recent trend—a survey. *Quant Imaging Med Surg*. 2015;5(3):407-422. doi:10.3978/j.issn.2223-4292.2015.03.01
57. Partridge SC, Nissan N, Rahbar H, Kitsch AE, Sigmund EE. Diffusion-weighted breast MRI: Clinical applications and emerging techniques. *J Magn Reson Imaging*. 2017. doi:10.1002/jmri.25479

58. Le Bihan D, Breton E, Lallemand D, Aubin ML, Vignaud J, Laval-Jeantet M. Separation of diffusion and perfusion in intravoxel incoherent motion MR imaging. *Radiology*. 1988. doi:10.1148/radiology.168.2.3393671

59. Pereira FPA, Martins G, Figueiredo E, et al. Assessment of breast lesions with diffusion-weighted MRI: Comparing the use of different b values. *Am J Roentgenol*. 2009. doi:10.2214/AJR.09.2522

60. Thomassin-Naggara I, De Bazelaire C, Chopier J, Bazot M, Marsault C, Trop I. Diffusion-weighted MR imaging of the breast: Advantages and pitfalls. *Eur J Radiol*. 2013. doi:10.1016/j.ejrad.2012.03.002

61. Woodhams R, Matsunaga K, Iwabuchi K, et al. Diffusion-weighted imaging of malignant breast tumors: The usefulness of apparent diffusion coefficient (ADC) value and ADC map for the detection of malignant breast tumors and evaluation of cancer extension. *J Comput Assist Tomogr*. 2005;29(5):644-649. doi:10.1097/01.rct.0000171913.74086.1b

62. Yabuuchi H, Matsuo Y, Okafuji T, et al. Enhanced mass on contrast-enhanced breast MR imaging: Lesion characterization using combination of dynamic contrast-enhanced and diffusion-weighted MR images. *J Magn Reson Imaging*. 2008;28(5):1157-1165. doi:10.1002/jmri.21570

63. Bozkurt TB, Koç G, Sezgin G, Altay C, Gelal MF, Oyar O. Value of apparent diffusion coefficient values in differentiating malignant and benign breast lesions. *Balkan Med J*. 2016. doi:10.5152/balkanmedj.2016.141007

64. Bickelhaupt S, Laun FB, Tesdorff J, et al. Fast and noninvasive characterization of suspicious lesions detected at breast cancer X-ray screening: Capability of diffusion-weighted MR imaging with MIPs. *Radiology*. 2016. doi:10.1148/radiol.2015150425

65. Stadlbauer A, Salomonowitz E, Bernt R, et al. Diffusion-weighted MR imaging with background body signal suppression (DWIBS) for the diagnosis of malignant and benign breast lesions. *Eur Radiol*. 2009. doi:10.1007/s00330-009-1426-2

66. Telegrafo M, Rella L, Stabile Ianora AA, Angelelli G, Moschetta M. Unenhanced breast MRI (STIR, T2-weighted TSE, DWIBS): An accurate and alternative strategy for detecting and differentiating breast lesions. *Magn Reson Imaging*. 2015. doi:10.1016/j.mri.2015.06.002

67. Martincich L, Deantoni V, Bertotto I, et al. Correlations between diffusion-weighted imaging and breast cancer biomarkers. *Eur Radiol*. 2012. doi:10.1007/s00330-012-2403-8

68. Bickel H, Pinker-Domenig K, Bogner W, et al. Quantitative apparent diffusion coefficient as a noninvasive imaging biomarker for the differentiation of invasive breast cancer and ductal carcinoma in situ. *Invest Radiol*. 2015. doi:10.1097/RLI.0000000000000104

69. El Khouli RH, Jacobs MA, Mezban SD, et al. Diffusion-weighted imaging improves the diagnostic accuracy of conventional 3.0-T breast MR imaging. *Radiology*. 2010. doi:10.1148/radiol.10091367

70. Bogner W, Gruber S, Pinker K, et al. Diffusion-weighted MR for differentiation of breast lesions at 3.0 T: How does selection of diffusion protocols affect diagnosis? *Radiology*. 2009. doi:10.1148/radiol.2532081718

71. Park SH, Moon WK, Cho N, et al. Diffusion-weighted MR imaging: Pretreatment prediction of response to neoadjuvant chemotherapy in patients with breast cancer. *Radiology*. 2010. doi:10.1148/radiol.10092021

72. Pickles MD, Gibbs P, Lowry M, Turnbull LW. Diffusion changes precede size reduction in neoadjuvant treatment of breast cancer. *Magn Reson Imaging*. 2006. doi:10.1016/j.mri.2005.11.005

73. Hasanzadeh F, Faeghi F, Valizadeh A, Bayani L. Diagnostic Value of Diffusion Weighted Magnetic Resonance Imaging in Evaluation of Metastatic Axillary Lymph Nodes in a Sample of Iranian Women with Breast Cancer. *Asian Pac J Cancer Prev*. 2017;18(5):1265-1270. doi:10.22034/APJCP.2017.18.5.1265

74. Koh DM, Collins DJ, Orton MR. Intravoxel incoherent motion in body diffusion-weighted MRI: Reality and challenges. *Am J Roentgenol*. 2011. doi:10.2214/AJR.10.5515

75. Suo S, Lin N, Wang H, et al. Intravoxel incoherent motion diffusion-weighted MR imaging of breast cancer at 3.0 tesla: Comparison of different curve-fitting methods. *J Magn Reson Imaging*. 2015. doi:10.1002/jmri.24799

76. Song SE, Cho KR, Seo BK, et al. Intravoxel incoherent motion diffusion-weighted MRI of invasive breast cancer: Correlation with prognostic factors and kinetic features acquired with computer-aided diagnosis. *J Magn Reson Imaging*. 2019. doi:10.1002/jmri.26221

77. Kim Y, Ko K, Kim D, et al. Intravoxel incoherent motion diffusion-weighted MR imaging of breast cancer: Association with histopathological features and subtypes. *Br J Radiol*. 2016. doi:10.1259/bjr.20160140

78. D. LB, E. B, D. L, et al. Contribution of Intravoxel Incoherent Motion (IVIM) imaging

to neuroradiology. *J Neuroradiol*. 1987.

79. Cho GY, Moy L, Kim SG, et al. Evaluation of breast cancer using intravoxel incoherent motion (IVIM) histogram analysis: comparison with malignant status, histological subtype, and molecular prognostic factors. *Eur Radiol*. 2016. doi:10.1007/s00330-015-4087-3
80. Lin N, Chen J, Hua J, Zhao J, Zhao J, Lu J. Intravoxel incoherent motion MR imaging in breast cancer: Quantitative analysis for characterizing lesions. *Int J Clin Exp Med*. 2017.
81. Coutu JP, Chen JJ, Rosas HD, Salat DH. Non-Gaussian water diffusion in aging white matter. *Neurobiol Aging*. 2014. doi:10.1016/j.neurobiolaging.2013.12.001
82. Sun K, Chen X, Chai W, et al. Breast cancer: Diffusion kurtosis mr imaging-diagnostic accuracy and correlation with clinical-pathologic factors1. *Radiology*. 2015. doi:10.1148/radiol.15141625
83. Jensen JH, Helpern JA, Ramani A, Lu H, Kaczynski K. Diffusional kurtosis imaging: The quantification of non-Gaussian water diffusion by means of magnetic resonance imaging. *Magn Reson Med*. 2005. doi:10.1002/mrm.20508
84. Rosenkrantz AB, Sigmund EE, Johnson G, et al. Prostate cancer: Feasibility and preliminary experience of a diffusional kurtosis model for detection and assessment of aggressiveness of peripheral zone cancer. *Radiology*. 2012. doi:10.1148/radiol.12112290
85. Raab P, Hattingen E, Franz K, Zanella FE, Lanfermann H. Cerebral gliomas: Diffusional kurtosis imaging analysis of microstructural differences. *Radiology*. 2010. doi:10.1148/radiol.09090819
86. Rosenkrantz AB, Sigmund EE, Winnick A, et al. Assessment of hepatocellular carcinoma using apparent diffusion coefficient and diffusion kurtosis indices: Preliminary experience in fresh liver explants. *Magn Reson Imaging*. 2012. doi:10.1016/j.mri.2012.04.020
87. Nogueira L, Brandão S, Matos E, et al. 1197-1203Application of the diffusion kurtosis model for the study of breast lesions. *Eur Radiol*. 2014. doi:10.1007/s00330-014-3146-5
88. Beaulieu C. The basis of anisotropic water diffusion in the nervous system - A technical review. *NMR Biomed*. 2002. doi:10.1002/nbm.782
89. Sung HK, Eun SC, Hyeon SK, et al. Diffusion-weighted imaging of breast cancer: Correlation of the apparent diffusion coefficient value with prognostic factors. *J Magn*

Reson Imaging. 2009. doi:10.1002/jmri.21884

90. Le Bihan D, Mangin JF, Poupon C, et al. Diffusion tensor imaging: Concepts and applications. *J Magn Reson Imaging*. 2001. doi:10.1002/jmri.1076
91. Jiang R, Ma Z, Dong H, Sun S, Zeng X, Li X. Diffusion tensor imaging of breast lesions: Evaluation of apparent diffusion coefficient and fractional anisotropy and tissue cellularity. *Br J Radiol*. 2016. doi:10.1259/bjr.20160076
92. Kim JY, Kim JJ, Kim S, et al. Diffusion tensor magnetic resonance imaging of breast cancer: associations between diffusion metrics and histological prognostic factors. *Eur Radiol*. 2018. doi:10.1007/s00330-018-5429-8
93. Baltzer PAT, Schäfer A, Dietzel M, et al. Diffusion tensor magnetic resonance imaging of the breast: A pilot study. *Eur Radiol*. 2011. doi:10.1007/s00330-010-1901-9
94. Plaza MJ, Morris EA, Thakur SB. Diffusion tensor imaging in the normal breast: Influences of fibroglandular tissue composition and background parenchymal enhancement. *Clin Imaging*. 2016. doi:10.1016/j.clinimag.2015.12.001
95. Lüdemann L, Förschler A, Grieger W, Zimmer C. BOLD signal in the motor cortex shows a correlation with the blood volume of brain tumors. *J Magn Reson Imaging*. 2006. doi:10.1002/jmri.20530
96. Ogawa S, Menon RS, Tank DW, et al. Functional brain mapping by blood oxygenation level-dependent contrast magnetic resonance imaging. A comparison of signal characteristics with a biophysical model. *Biophys J*. 1993. doi:10.1016/S0006-3495(93)81441-3
97. Wallace TE, Patterson AJ, Abeyakoon O, et al. Detecting gas-induced vasomotor changes via blood oxygenation level-dependent contrast in healthy breast parenchyma and breast carcinoma. *J Magn Reson Imaging*. 2016. doi:10.1002/jmri.25177
98. Kim SG, Bandettini PA. Principles of BOLD functional MRI. In: *Functional Neuroradiology: Principles and Clinical Applications*. ; 2012. doi:10.1007/978-1-4419-0345-7_16
99. Rakow-Penner R, Daniel B, Glover GH. Detecting Blood Oxygen Level-Dependent (BOLD) contrast in the breast. *J Magn Reson Imaging*. 2010;32(1):120-129. doi:10.1002/jmri.22227
100. Logothetis NK. The underpinnings of the BOLD functional magnetic resonance imaging signal. *J Neurosci*. 2003;23(10):3963-3971. doi:23/10/3963 [pii]
101. Li SP, Padhani AR, Taylor NJ, et al. Imaging tumor hypoxia with BOLD MRI in primary breast cancer. *J Clin Oncol*. 2010;28(15_suppl):e13526-e13526.

doi:10.1200/jco.2010.28.15_suppl.e13526

102. Jiang L, Weatherall PT, McColl RW, Tripathy D, Mason RP. Blood oxygenation level-dependent (BOLD) contrast magnetic resonance imaging (MRI) for prediction of breast cancer chemotherapy response: A pilot study. *J Magn Reson Imaging*. 2013;37(5):1083-1092. doi:10.1002/jmri.23891
103. Wallace T. *PhD Thesis: Development of Functional Magnetic Resonance Techniques for Imaging Breast Cancer*. Cambridge; 2016.
104. Gray LH, Steadman JM. Determination of the oxyhaemoglobin dissociation curves for mouse and rat blood. *J Physiol*. 1964. doi:10.1113/jphysiol.1964.sp007509
105. Young IR, Clarke GJ, Baffles DR, Pennock JM, Doyle FH, Bydder GM. Enhancement of relaxation rate with paramagnetic contrast agents in NMR imaging. *J ComputTomogr*. 1981. doi:10.1016/0149-936X(81)90089-8
106. Cao-Pham TT, Joudiou N, Van Hul M, et al. Combined endogenous MR biomarkers to predict basal tumor oxygenation and response to hyperoxic challenge. *NMR Biomed*. 2017. doi:10.1002/nbm.3836
107. Dewhirst MW, Birer SR. Oxygen-enhanced MRI is a major advance in tumor hypoxia imaging. *Cancer Res*. 2016;76(4):769-772. doi:10.1158/0008-5472.CAN-15-2818
108. O'Connor JPB, Robinson SP, Waterton JC. Imaging tumour hypoxia with oxygen-enhanced MRI and BOLD MRI. *Br J Radiol*. 2019. doi:10.1259/bjr.20180642
109. Little RA, Jamin Y, Boult JKR, et al. Mapping hypoxia in renal carcinoma with oxygen-enhanced MRI: Comparison with intrinsic susceptibility MRI and pathology. *Radiology*. 2018. doi:10.1148/radiol.2018171531
110. O'Connor JPB, Boult JKR, Jamin Y, et al. Oxygen-enhanced MRI accurately identifies, quantifies, and maps tumor hypoxia in preclinical cancer models. *Cancer Res*. 2016;76(4):787-795. doi:10.1158/0008-5472.CAN-15-2062
111. Salem A, Little RA, Latif A, et al. Oxygen-enhanced MRI is feasible, repeatable, and detects radiotherapy-induced change in hypoxia in xenograft models and in patients with Non-small cell lung cancer. *Clin Cancer Res*. 2019. doi:10.1158/1078-0432.CCR-18-3932
112. Jost S, Garbow J. TH-C-204C-03: Radiation Necrosis and Its Characterization Using Advanced MRI. In: *Medical Physics*. ; 2010. doi:10.1118/1.3469505
113. Bolan PJ. Magnetic Resonance Spectroscopy of the Breast: Current Status. *Magn Reson Imaging Clin N Am*. 2013. doi:10.1016/j.mric.2013.04.008
114. Roebuck JR, Cecil KM, Schnall MD, Lenkinski RE. Human breast lesions:

Characterization with proton MR spectroscopy. *Radiology*. 1998. doi:10.1148/radiology.209.1.9769842

115. Cecil KM, Schnall MD, Siegelman ES, Lenkinski RE. The evaluation of human breast lesions with magnetic resonance imaging and proton magnetic resonance spectroscopy. *Breast Cancer Res Treat*. 2001. doi:10.1023/A:1017911211090
116. Gribbestad IS, Singstad TE, Nilsen G, et al. In vivo 1H MRS of normal breast and breast tumors using a dedicated double breast coil. *J Magn Reson Imaging*. 1998. doi:10.1002/jmri.1880080602
117. Zhao C, Bolan PJ, Royce M, et al. Quantitative mapping of total choline in healthy human breast using proton echo planar spectroscopic imaging (PEPSI) at 3 Tesla. *J Magn Reson Imaging*. 2012. doi:10.1002/jmri.23748
118. Ford TC, Crewther DP. A comprehensive review of the 1H-MRS metabolite spectrum in autism spectrum disorder. *Front Mol Neurosci*. 2016. doi:10.3389/fnmol.2016.00014
119. Blüml S. Magnetic resonance spectroscopy: Basics. In: *MR Spectroscopy of Pediatric Brain Disorders*. ; 2013:11-23. doi:10.1007/978-1-4419-5864-8_2
120. Jagannathan NR, Sharma U. Breast tissue metabolism by magnetic resonance spectroscopy. *Metabolites*. 2017. doi:10.3390/metabo7020025
121. Serganova I, Rizwan A, Ni X, et al. Metabolic imaging: A link between lactate dehydrogenase A, lactate, and tumor phenotype. *Clin Cancer Res*. 2011;17(19):6250-6261. doi:10.1158/1078-0432.CCR-11-0397
122. Bartella L, Morris EA, Dershaw DD, et al. Proton MR spectroscopy with choline peak as malignancy marker improves positive predictive value for breast cancer diagnosis: Preliminary study. *Radiology*. 2006. doi:10.1148/radiol.2393051046
123. Bartella L, Thakur SB, Morris EA, et al. Enhancing nonmass lesions in the breast: Evaluation with proton (1H) MR spectroscopy. *Radiology*. 2007. doi:10.1148/radiol.2451061639
124. Meisamy S, Bolan PJ, Baker EH, et al. Adding in vivo quantitative1H MR spectroscopy to improve diagnostic accuracy of breast MR imaging: Preliminary results of observer performance study at 4.0 T. *Radiology*. 2005. doi:10.1148/radiol.2362040836
125. Baltzer PAT, Dietzel M. Breast lesions: Diagnosis by using proton MR spectroscopy at 1.5 and 3.0 T - Systematic review and meta-analysis. *Radiology*. 2013. doi:10.1148/radiol.13121856
126. Haddadin IS, Mclntosh A, Meisamy S, et al. Metabolite quantification and high-field MRS in breast cancer. *NMR Biomed*. 2009. doi:10.1002/nbm.1217

127. Meisamy S, Bolan PJ, Baker EH, et al. Neoadjuvant chemotherapy of locally advanced breast cancer: Predicting response with in vivo 1H MR spectroscopy - A pilot study at 4 T. *Radiology*. 2004. doi:10.1148/radiol.2332031285
128. Shin HJ, Baek HM, Cha JH, Kim HH. Evaluation of breast cancer using proton MR spectroscopy: Total choline peak integral and signal-to-noise ratio as prognostic indicators. *Am J Roentgenol*. 2012. doi:10.2214/AJR.11.7292
129. Wang ZJ, Ohliger MA, Larson PEZ, et al. Hyperpolarized 13C MRI: State of the art and future directions. *Radiology*. 2019. doi:10.1148/radiol.2019182391
130. Albers MJ, Bok R, Chen AP, et al. Hyperpolarized 13C lactate, pyruvate, and alanine: Noninvasive biomarkers for prostate cancer detection and grading. *Cancer Res*. 2008;68(20):8607-8615. doi:10.1158/0008-5472.CAN-08-0749
131. Kurhanewicz J, Vigneron DB, Ardenkjaer-Larsen JH, et al. Hyperpolarized 13C MRI: Path to Clinical Translation in Oncology. *Neoplasia (United States)*. 2019. doi:10.1016/j.neo.2018.09.006
132. Haris M, Yadav SK, Rizwan A, et al. Molecular magnetic resonance imaging in cancer. *J Transl Med*. 2015;13(1). doi:10.1186/s12967-015-0659-x
133. Park I, Larson PEZ, Zierhut ML, et al. Hyperpolarized 13C magnetic resonance metabolic imaging: Application to brain tumors. *Neuro Oncol*. 2010;12(2):133-144. doi:10.1093/neuonc/nop043
134. Ardenkjær-Larsen JH, Golman K, Gram A, et al. Increase of signal-to-noise of more than 10,000 times in liquid state NMR. *Discov Med*. 2003.
135. Nelson SJ, Kurhanewicz J, Vigneron DB, et al. Metabolic imaging of patients with prostate cancer using hyperpolarized [1-13C]pyruvate. *Sci Transl Med*. 2013. doi:10.1126/scitranslmed.3006070
136. Dutta P, Le A, Vander Jagt DL, et al. Evaluation of LDH-A and glutaminase inhibition in vivo by hyperpolarized 13C-pyruvate magnetic resonance spectroscopy of tumors. *Cancer Res*. 2013. doi:10.1158/0008-5472.CAN-13-0465
137. Golman K, In 't Zandt R, Thaning M. Real-time metabolic imaging. *Proc Natl Acad Sci U S A*. 2006. doi:10.1073/pnas.0601319103
138. Gallagher FA, Woitek R, McLean MA, et al. Imaging breast cancer using hyperpolarized carbon-13 MRI. *Proc Natl Acad Sci U S A*. 2020. doi:10.1073/pnas.1913841117
139. Day SE, Kettunen MI, Gallagher FA, et al. Detecting tumor response to treatment using hyperpolarized 13C magnetic resonance imaging and spectroscopy. *Nat Med*. 2007.

doi:10.1038/nm1650

140. Witney TH, Kettunen MI, Hu DE, et al. Detecting treatment response in a model of human breast adenocarcinoma using hyperpolarised 1- 13 Cpyruvate and 1,4- 13 C 2 fumarate. *Br J Cancer*. 2010. doi:10.1038/sj.bjc.6605945
141. Halestrap AP. The monocarboxylate transporter family-Structure and functional characterization. *IUBMB Life*. 2012. doi:10.1002/iub.573
142. Harris T, Eliyahu G, Frydman L, Degani H. Kinetics of hyperpolarized 13C1-pyruvate transport and metabolism in living human breast cancer cells. *Proc Natl Acad Sci*. 2009. doi:10.1073/pnas.0909049106
143. Zhu A, Daniel Lee A, Shim H. Metabolic PET Imaging in Cancer Detection and Therapy Response. *Semin Oncol*. 2011. doi:10.1053/j.seminoncol.2010.11.012.Metabolic
144. Kapoor V, McCook BM, Torok FS. An introduction to PET-CT imaging. *Radiographics*. 2004. doi:10.1148/rg.242025724
145. Testanera Giorgio; Hogg Peter. Principles and Practice of PET/CT Part 1 A Technologist's Guide EAEA. *Eur Assoc Nucl Med*. 2010.
146. Anthony P. Robbins' Pathologic Basis of Disease. *J Clin Pathol*. 1990. doi:10.1136/jcp.43.2.176-a
147. Smith TA. FDG uptake, tumour characteristics and response to therapy: a review. *Nucl Med Commun*. 1998;19(2):97—105. doi:10.1097/00006231-199802000-00002
148. Rohren EM, Turkington TG, Coleman RE. Clinical Applications of PET in Oncology. *Radiology*. 2004. doi:10.1148/radiol.2312021185
149. Smith TAD. Fdg uptake, tumour characteristics and response to therapy a review. *Nucl Med Commun*. 1998. doi:10.1080/00006231-199802000-00002
150. Lind P, Igerc I, Beyer T, Reinprecht P, Hausegger K. Advantages and limitations of FDG PET in the follow-up of breast cancer. *Eur J Nucl Med Mol Imaging*. 2004;31 Suppl 1(June):S125-S134. doi:10.1007/s00259-004-1535-8
151. Basely MJ, Bernard P, Gisserot O, Maszelin P, Bussy E, de Jaureguiberry J-P. Umbilical Metastasis From Breast Cancer Detected by FDG PET. *Clin Nucl Med*. 2009;34(5). https://journals.lww.com/nuclearmed/Fulltext/2009/05000/Umbilical_Metastasis_From_Breast_Cancer_Detected.7.aspx.
152. Aukema TS, Straver ME, Valdés Olmos RA, Vogel W V. A different role for FDG PET/CT in axillary lymph node staging in breast cancer. *Eur J Nucl Med Mol Imaging*. 2009;36(11):1896. doi:10.1007/s00259-009-1211-0
153. Peare R, Staff RT, Heys SD. The use of FDG-PET in assessing axillary lymph node

status in breast cancer: A systematic review and meta-analysis of the literature. *Breast Cancer Res Treat*. 2010. doi:10.1007/s10549-010-0771-9

154. Çermik TF, Mavi A, Basu S, Alavi A. Impact of FDG PET on the preoperative staging of newly diagnosed breast cancer. *Eur J Nucl Med Mol Imaging*. 2008. doi:10.1007/s00259-007-0580-5
155. Tchou J, Sonnad SS, Bergey MR, et al. Degree of tumor FDG uptake correlates with proliferation index in triple negative breast cancer. *Mol Imaging Biol*. 2010;12(6):657-662. doi:10.1007/s11307-009-0294-0
156. Lebron L, Greenspan D, Pandit-Taskar N. PET imaging of breast cancer: Role in patient management. *PET Clin*. 2015;10(2):159-195. doi:10.1016/j.cpet.2014.12.004
157. Duch J, Fuster D, Muñoz M, et al. 18F-FDG PET/CT for early prediction of response to neoadjuvant chemotherapy in breast cancer. *Eur J Nucl Med Mol Imaging*. 2009;36(10):1551-1557. doi:10.1007/s00259-009-1116-y
158. Kumar A, Kumar R, Seenu V, et al. The role of 18F-FDG PET/CT in evaluation of early response to neoadjuvant chemotherapy in patients with locally advanced breast cancer. *Eur Radiol*. 2009;19(6):1347-1357. doi:10.1007/s00330-009-1303-z
159. Robertson IJ, Hand F, Kell MR. FDG-PET/CT in the staging of local/regional metastases in breast cancer. *Breast*. 2011. doi:10.1016/j.breast.2011.07.002
160. Straver ME, Aukema TS, Olmos RAV, et al. Feasibility of FDG PET/CT to monitor the response of axillary lymph node metastases to neoadjuvant chemotherapy in breast cancer patients. *Eur J Nucl Med Mol Imaging*. 2010;37(6):1069-1076. doi:10.1007/s00259-009-1343-2
161. Cheng G, Torigian DA, Zhuang H, Alavi A. When should we recommend use of dual time-point and delayed time-point imaging techniques in FDG PET? *Eur J Nucl Med Mol Imaging*. 2013;40(5):779-787. doi:10.1007/s00259-013-2343-9
162. Houshmand S, Salavati A, Segtnan EA, Grupe P, Høilund-Carlsen PF, Alavi A. Dual-time-point imaging and delayed-time-point fluorodeoxyglucose-PET/computed tomography imaging in various clinical settings. *PET Clin*. 2016;11(1):65-84. doi:10.1016/j.cpet.2015.07.003
163. Boerner AR, Weckesser M, Herzog H, et al. Optimal scan time for fluorine-18 fluorodeoxyglucose positron emission tomography in breast cancer. *Eur J Nucl Med*. 1999;26(3):226-230. doi:10.1007/s002590050381
164. Beaulieu S, Kinahan P, Tseng J, et al. SUV varies with time after injection in (18)F-FDG PET of breast cancer: characterization and method to adjust for time differences.

J Nucl Med. 2003;44(7):1044-1050. http://www.ncbi.nlm.nih.gov/pubmed/12843218.

165. Kramer G, Yaqub M, Bahce I, et al. CT-perfusion versus [O-15]H2O PET in lung tumors: Effects of CT-perfusion methodology. *Med Phys*. 2013;40:52502. doi:10.1118/1.4798560
166. Jochumsen MR, Tolbod LP, Pedersen BG, et al. Quantitative tumor perfusion imaging with 82Rb PET/CT in prostate cancer: Analytic and clinical validation. *J Nucl Med*. 2019. doi:10.2967/jnumed.118.219188
167. Tolbod LP, Nielsen MM, Pedersen BG, et al. Non-invasive quantification of tumor blood flow in prostate cancer using 15O-H2O PET/CT. *Am J Nucl Med Mol Imaging*. 2018.
168. Żyromska A, Małkowski B, Wiśniewski T, Majewska K, Reszke J, Makarewicz R. 15O-H2O PET/CT as a tool for the quantitative assessment of early post-radiotherapy changes of heart perfusion in breast carcinoma patients. *Br J Radiol*. 2018;91(1088):20170653. doi:10.1259/bjr.20170653
169. Bogdan Malkowski2,3, Agnieszka Żyromska1,7, Tomasz Wisniewski7, Rita Łopatto6, Karolina Majewska5, Łukasz Bałszewski3 JR and MW. 15O-H2O PET/CT confirms early postradiotherapy changes of heart perfusion in breast carcinoma patients. *J Nucl Med*. 2016;57(2):571. http://jnm.snmjournals.org/content/57/supplement_2/571.short?trendmd-shared=0&related-urls=yes&legid=jnumed;57/supplement_2/571.
170. Chatal JF, Rouzet F, Haddad F, Bourdeau C, Mathieu C, Guludec D Le. Story of rubidium-82 and advantages for myocardial perfusion PET imaging. *Front Med*. 2015. doi:10.3389/fmed.2015.00065
171. LOVE WD, ROMNEY RB, BURCH GE. A comparison of the distribution of potassium and exchangeable rubidium in the organs of the dog, using rubidium. *Circ Res*. 1954. doi:10.1161/01.RES.2.2.112
172. Shafiq A, Ammar KA, Gilles L, et al. Metastatic breast cancer diagnosed by rubidium-82 positron emission tomography myocardial perfusion imaging. *J Nucl Cardiol*. 2018. doi:10.1007/s12350-017-0838-7
173. Lu Y. FDG and 82Rb PET/MRI features of brain metastasis of breast cancer. *Clin Nucl Med*. 2015. doi:10.1097/RLU.0000000000000712
174. Fleming IN, Manavaki R, Blower PJ, et al. Imaging tumour hypoxia with positron emission tomography. *Br J Cancer*. 2015;112(2):238-250. doi:10.1038/bjc.2014.610
175. Lopci E, Grassi I, Chiti A, et al. PET radiopharmaceuticals for imaging of tumor

hypoxia: a review of the evidence. *Am J Nucl Med Mol Imaging*. 2014;4(4):365-384. doi:10.1038/bjc.2014.610

176. Chapman JD, Franko AJ, Sharplin J. A marker for hypoxic cells in tumours with potential clinical applicability. *Br J Cancer*. 1981;43(4):546-550. doi:10.1038/bjc.1981.79
177. Raleigh JA, Chou SC, Arteel GE, Horsman MR. Comparisons among pimonidazole binding, oxygen electrode measurements, and radiation response in C3H mouse tumors. *Radiat Res*. 1999;151(5):580-589. doi:10.2307/3580034
178. Masaki Y, Shimizu Y, Yoshioka T, et al. The accumulation mechanism of the hypoxia imaging probe "fMISO" by imaging mass spectrometry: Possible involvement of low-molecula metabolites. *Sci Rep*. 2015;5. doi:10.1038/srep16802
179. Thorwarth D, Eschmann SM, Holzner F, Paulsen F, Alber M. Combined uptake of [18F]FDG and [18F]FMISO correlates with radiation therapy outcome in head-and-neck cancer patients. *Radiother Oncol*. 2006;80(2):151-156. doi:10.1016/j.radonc.2006.07.033
180. Muzi M, Peterson LM, O'Sullivan JN, et al. 18F-fluoromisonidazole quantification of hypoxia in human cancer patients using image-derived blood surrogate tissue reference regions. *J Nucl Med*. 2015. doi:10.2967/jnumed.115.158717
181. Rajendran JG, Krohn KA. F-18 fluoromisonidazole for imaging tumor hypoxia: Imaging the microenvironment for personalized cancer therapy. *Semin Nucl Med*. 2015. doi:10.1053/j.semnuclmed.2014.10.006
182. Sorace AG, Syed AK, Barnes SL, et al. Quantitative [18F]FMISO PET Imaging Shows Reduction of Hypoxia Following Trastuzumab in a Murine Model of HER2+ Breast Cancer. *Mol Imaging Biol*. 2017;19(1):130-137. doi:10.1007/s11307-016-0994-1
183. Yamane T, Ueda S, Seto A, Matsunari I, Saeki T, Kuji I. Clinical impact of 18F-FMISO PET in the distinction of intrinsic subtypes of breast cancer. *J Nucl Med* . 2016;57(supplement 2):570. http://jnm.snmjournals.org/content/57/supplement_2/570.abstract.
184. Hilberg F, Roth GJ, Krssak M, et al. BIBF 1120: Triple angiokinase inhibitor with sustained receptor blockade and good antitumor efficacy. *Cancer Res*. 2008;68(12):4774-4782. doi:10.1158/0008-5472.CAN-07-6307
185. Teo QQ, Thng CH, Koh TS, Ng QS. Dynamic Contrast-enhanced Magnetic Resonance Imaging: Applications in Oncology. *Clin Oncol*. 2014;26(10):9-20. doi:10.1016/j.clon.2014.05.014

186. Nehmeh SA, Lee NY, Schröder H, et al. Reproducibility of Intratumor Distribution of 18F-Fluoromisonidazole in Head and Neck Cancer. *Int J Radiat Oncol Biol Phys*. 2008;70(1):235-242. doi:10.1016/j.ijrobp.2007.08.036

187. Goos JACM, Davydova M, Lengkeek N, et al. pH-Responsive Polymers for Improving the Signal-to-Noise Ratio of Hypoxia PET Imaging with [18F]Fluoromisonidazole. *Macromol Rapid Commun*. 2020. doi:10.1002/marc.202000061

188. Andrzejewski P, Wengert G, Helbich TH, et al. Sequential [18F]FDG-[18F]FMISO PET and Multiparametric MRI at 3T for Insights into Breast Cancer Heterogeneity and Correlation with Patient Outcomes: First Clinical Experience. *Contrast Media Mol Imaging*. 2019. doi:10.1155/2019/1307247

189. Woolf DK, Beresford M, Li SP, et al. Evaluation of FLT-PET-CT as an imaging biomarker of proliferation in primary breast cancer. *Br J Cancer*. 2014;110(12):2847-2854. doi:10.1038/bjc.2014.207

190. Pio BS, Park CK, Pietras R, et al. Usefulness of 3'-[F-18]fluoro-3'-deoxythymidine with positron emission tomography in predicting breast cancer response to therapy. *Mol Imaging Biol*. 2006;8(1):36-42. doi:10.1007/s11307-005-0029-9

191. Louise K, Hons B. Development of a PET radioligand targeting angiogenesis for oncology applications. 2016;(March).

192. Deng S-M, Zhang W, Zhang B, Wu Y-W. Assessment of tumor response to chemotherapy in patients with breast cancer using (18)F-FLT: a meta-analysis. *Chin J Cancer Res*. 2014;26(5):517-524. doi:10.3978/j.issn.1000-9604.2014.08.17

193. Dittmann H, Jusufoska A, Dohmen BM, et al. 3′-Deoxy-3′-[18F]fluorothymidine (FLT) uptake in breast cancer cells as a measure of proliferation after doxorubicin and docetaxel treatment. *Nucl Med Biol*. 2009;36(2):163-169. doi:10.1016/j.nucmedbio.2008.10.012

194. Jagarlamudi KK, Shaw M. Thymidine kinase 1 as a tumor biomarker: Technical advances offer new potential to an old biomarker. *Biomark Med*. 2018. doi:10.2217/bmm-2018-0157

195. Bading JR, Shields AF. Imaging of cell proliferation: status and prospects. *J Nucl Med*. 2008;49 Suppl 2(6):64S--80S. doi:10.2967/jnumed.107.046391

196. Seitz U, Wagner M, Neumaier B, et al. Evaluation of pyrimidine metabolising enzymes and in vitro uptake of 3′-[18F]fluoro-3′-deoxythymidine ([18F]FLT) in pancreaticcancer cell lines. *Eur J Nucl Med*. 2002;29(9):1174-1181. doi:10.1007/s00259-002- 0851-0

197. Bradbury MS, Hambardzumyan D, Zanzonico PB, et al. Dynamic Small-Animal PET Imaging of Tumor Proliferation with 3'-Deoxy-3'-18F-Fluorothymidine in a Genetically Engineered Mouse Model of High-Grade Gliomas. *J Nucl Med*. 2008;49(3):422-429. doi:10.2967/jnumed.107.047092

198. Francis DL, Freeman A, Visvikis D, et al. In vivo imaging of cellular proliferation in colorectal cancer using positron emission tomography. *Gut*. 2003;52(11):1602-1606. doi:10.1136/gut.52.11.1602

199. Buck AK, Hetzel M, Schirrmeister H, et al. Clinical relevance of imaging proliferative activity in lung nodules. *Eur J Nucl Med Mol Imaging*. 2005;32(5):525-533. doi:10.1007/s00259-004-1706-7

200. Buck AK, Herrmann K, Shen C, Dechow T, Schwaiger M, Wester HJ. Molecular imaging of proliferation in vivo: Positron emission tomography with [18F]fluorothymidine. *Methods*. 2009;48(2):205-215. doi:10.1016/j.ymeth.2009.03.009

201. Eckel F, Herrmann K, Schmidt S, et al. Imaging of proliferation in hepatocellular carcinoma with the in vivo marker 18F-fluorothymidine. *J Nucl Med*. 2009;50(9):1441-1447. doi:10.2967/jnumed.109.065896

202. Yap CS, Czernin J, Fishbein MC, et al. Evaluation of thoracic tumors with 18F-fluorothymidine and 18F-fluorodeoxyglucose-positron emission tomography. *Chest*. 2006;129(2):393-401. doi:10.1378/chest.129.2.393

203. Chen W, Cloughesy T, Kamdar N, et al. Imaging Proliferation in Brain Tumors with 18F-FLT PET: Comparison with 18F-FDG. *J Nucl Med*. 2005;46(6):945-952. doi:46/6/945 [pii]

204. Herrmann K, Ott K, Buck AK, et al. Imaging Gastric Cancer with PET and the Radiotracers 18F-FLT and 18F-FDG: A Comparative Analysis. *J Nucl Med*. 2007;48(12):1945-1950. doi:10.2967/jnumed.107.044867

205. Kenny LM, Vigushin DM, Al-Nahhas A, et al. Quantification of cellular proliferation in tumor and normal tissues of patients with breast cancer by [18F]fluorothymidine-positron emission tomography imaging: Evaluation of analytical methods. *Cancer Res*. 2005;65(21):10104-10112. doi:10.1158/0008-5472.CAN-04-4297

206. Contractor KB, Kenny LM, Stebbing J, et al. Biological basis of [11C]choline-positron emission tomography in patients with breast cancer: Comparison with [18F]fluorothymidine positron emission tomography. *Nucl Med Commun*. 2011;32(11):997-1004. doi:10.1097/MNM.0b013e328349567b

207. Czekierdowski A, Czekierdowska S, Czuba B, et al. Microvessel density assessment in

benign and malignant endometrial changes. *J Physiol Pharmacol*. 2008;59(SUPPL. 4):45-51.

208. Chalkidou A, Landau DB, Odell EW, Cornelius VR, O'Doherty MJ, Marsden PK. Correlation between Ki-67 immunohistochemistry and 18F-Fluorothymidine uptake in patients with cancer: A systematic review and meta-analysis. *Eur J Cancer*. 2012;48(18):3499-3513. doi:10.1016/j.ejca.2012.05.001
209. ACRIN Study 6689 Separation of FLT and FLT-glucuronide Process Manual. 2011:1-8.
210. Smyczek-Gargya B, Fersis N, Dittmann H, et al. PET with [18F]fluorothymidine for imaging of primary breast cancer: a pilot study. *Eur J Nucl Med Mol Imaging*. 2004;31(5):720-724. doi:10.1007/s00259-004-1462-8
211. Been LB, Elsinga PH, de Vries J, et al. Positron emission tomography in patients with breast cancer using 18F-3 `-deoxy-3 `-fluoro-L-thymidine (18F-FLT) - a pilot study. *EJSO*. 2006;32(1):39-43. doi:10.1016/j.ejso.2005.09.016
212. Kenny L, Coombes RC, Vigushin DM, Al-Nahhas A, Shousha S, Aboagye EO. Imaging early changes in proliferation at 1 week post chemotherapy: A pilot study in breast cancer patients with 3′-deoxy-3′-[18F]fluorothymidine positron emission tomography. *Eur J Nucl Med Mol Imaging*. 2007;34(9):1339-1347. doi:10.1007/s00259-007-0379-4
213. Buchbender C, Heusner TA, Lauenstein TC, Bockisch A, Antoch G. Oncologic PET/MRI, Part 1: Tumors of the Brain, Head and Neck, Chest, Abdomen, and Pelvis. *J Nucl Med*. 2012;53(6):928-938. doi:10.2967/jnumed.112.105338
214. Buchbender C, Heusner TA, Lauenstein TC, Bockisch A, Antoch G. Oncologic PET/MRI, Part 2: Bone Tumors, Soft-Tissue Tumors, Melanoma, and Lymphoma. *J Nucl Med*. 2012;53(8):1244-1252. doi:10.2967/jnumed.112.109306
215. Martinez-Möller A, Eiber M, Nekolla SG, et al. Workflow and scan protocol considerations for integrated whole-body PET/MRI in oncology. *J Nucl Med*. 2012. doi:10.2967/jnumed.112.109348
216. Rischpler C, Nekolla SG, Dregely I, Schwaiger M. Hybrid PET/MR imaging of the heart: potential, initial experiences, and future prospects. *J Nucl Med*. 2013;54(3):402-415. doi:10.2967/jnumed.112.105353
217. Dimou E, Booij J, Rodrigues M, et al. Amyloid PET and MRI in Alzheimers Disease and Mild Cognitive Impairment. *Curr Alzheimer Res*. 2009;6(3):312-319. doi:http://dx.doi.org/10.2174/156720509788486563
218. Kitajima K, Suenaga Y, Ueno Y, et al. Value of fusion of PET and MRI for staging of

endometrial cancer: Comparison with ^{18}F-FDG contrast-enhanced PET/CT and dynamic contrast-enhanced pelvic MRI. *Eur J Radiol*. 2013;82(10):1672-1676. doi:10.1016/j.ejrad.2013.05.005

219. Kong EJ, Chun KA, Bom HS, Lee J, Lee SJ, Cho IH. Initial experience of integrated PET/MR mammography in patients with invasive ductal carcinoma. *Hell J Nucl Med*. 2014. doi:10.1967/s002449910142
220. Botsikas D, Kalovidouri A, Becker M, et al. Clinical utility of 18F-FDG-PET/MR for preoperative breast cancer staging. *Eur Radiol*. 2016. doi:10.1007/s00330-015-4054-z
221. Goorts B, Vöö S, van Nijnatten TJA, et al. Hybrid18F–FDG PET/MRI might improve locoregional staging of breast cancer patients prior to neoadjuvant chemotherapy. *Eur J Nucl Med Mol Imaging*. 2017. doi:10.1007/s00259-017-3745-x
222. Melsaether AN, Raad RA, Pujara AC, et al. Comparison of whole-body 18F FDG PET/MR imaging and whole-body 18F FDG PET/CT in terms of lesion detection and radiation dose in patients with breast cancer. *Radiology*. 2016. doi:10.1148/radiol.2016151155
223. Delso G, Voert E Ter, Barbosa FDG, Veit-Haibach P. Pitfalls and Limitations in Simultaneous PET/MRI. *Semin Nucl Med*. 2015. doi:10.1053/j.semnuclmed.2015.04.002
224. Ehman EC, Johnson GB, Villanueva-Meyer JE, et al. PET/MRI: Where might it replace PET/CT? *J Magn Reson Imaging*. 2017. doi:10.1002/jmri.25711
225. Dewhirst MW, Cao Y, Moeller B. Cycling hypoxia and free radicals regulate angiogenesis and radiotherapy response (Nature Reviews Cancer (2008) 8, (425-437)). *Nat Rev Cancer*. 2008. doi:10.1038/nrc2438
226. Polyak K. Heterogeneity in breast cancer. *J Clin Invest*. 2011. doi:10.1172/JCI60534

Chapter 3. Relationship between hypoxia and vascularity in breast cancer by using PET-MRI

In Chapter 1 we introduced breast cancer as a clinical problem and in Chapter 2 imaging techniques for the detection and characterisation of breast tumours were presented. This Chapter investigates the breast cancer microenvironment with specific emphasis on relationships between imaging descriptors of vascularity and oxygenation in breast malignancies.

It is widely accepted that hypoxia is associated with poor clinical outcome and metastasis in breast cancer. However, temporal fluctuations in hypoxia (cycling hypoxia) and perfusion can confound interpretation of imaging results. To remove the confounding effect of temporal fluctuations in hypoxia and perfusion, the relationship between these two parameters was investigated using combined PET-MR imaging with ^{18}F-fluoromisonidazole (^{18}F-FMISO).

A large portion of this work has been recently published in European Radiology[1] and presented at national and international conferences.

3.1 Objective

To examine the association between hypoxia, perfusion and cellularity in treatment-naïve breast cancers using combined ^{18}F-FMISO-PET/MRI.

3.2 Hypothesis

It was hypothesised that breast cancers with poor perfusion, as measured by DCE-MRI, or high cellular density, as measured by DWI, will show hypoxia on ^{18}F-FMISO-PET.

3.3 Background

Hypoxia is a common characteristic of the microenvironment of solid tumours and arises as a consequence of a dysregulated metabolism and the structurally and functionally aberrant microcirculation found in cancers[2-4]. Adaptation to hypoxia is achieved by propagating molecular signalling cascades to promote metabolic reprogramming towards glycolysis and restore oxygen and nutrient supply to the tumour via the formation of new vessels

(angiogenesis). In breast cancer, the presence of hypoxia has been confirmed via pO_2 histography in both pre-invasive and invasive tumours and has been shown to occur regardless of histological type, molecular sub-type, grade, size or patient characteristics[3,4]. *In vitro* studies have shown that hypoxia promotes a dedifferentiated phenotype in ductal carcinoma *in situ* (DCIS)[5] and downregulates the expression and function of oestrogen receptor-α (ERα)[6,7]. Furthermore, several immunohistochemical studies of breast tumour specimens have demonstrated that overexpression of hypoxia-associated proteins, such as hypoxia-inducible factor 1α (HIF-1α) and carbonic anhydrase IX (CAIX) are associated with an aggressive phenotype[8], poor prognosis[9], increased risk of metastasis and resistance to treatment[10,11].
Though tumour hypoxia can be broadly categorised as chronic (diffusion-limited) or acute (perfusion-limited), it is generally accepted that the tumour microenvironment is a highly dynamic entity, exhibiting temporally-varying perfusion patterns and heterogeneous oxygen-tension gradients in neoplastic cell subpopulations[12]. Experimental evidence suggests that oxygenation levels in tumours continually fluctuate, with several cells oscillating between hypoxia and variable oxygenation states owing to transient changes in perfusion[13,14]. These perfusion and oxygenation abnormalities serve in inducing a variety of gene expression profiles and the definition of a unique microenvironment in tumours that is pivotal for growth and metastatic dissemination[15].

Imaging methods, like PET and MRI have been used to non-invasively probe pathophysiological aspects of the tumour microenvironment, including hypoxia and neovascularisation. As discussed in Chapter 2, DCE-MRI has an established role in the diagnosis and management of breast cancer and has demonstrated utility in the characterisation of tumour vascular features related to perfusion and vascular permeability in several clinical studies[16,17,18]. DWI-MRI has also been utilised to provide surrogate measures of breast cancer cellular density and information on the integrity of cell membranes[19,20]. On the other hand, PET with ^{18}F-labelled nitroimidazoles can provide specific measures of intracellular hypoxia. In breast cancer, ^{18}F-fluoromisonidazole (^{18}F-FMISO) – the most extensively studied PET hypoxia biomarker – has been used for the evaluation of response to anti-angiogenic and HER2-targetted treatment in both clinical studies[21,22] and preclinical models of disease[23,24,25] and shown potential utility as a predictor of response to primary endocrine therapy[26,27]. Additionally, high ^{18}F-FMISO uptake at baseline has been associated with shorter disease-free survival[28] and disease-specific death[29].

Despite *in vitro* evidence regarding the link between tumour hypoxia and vascular function, multi-modal imaging approaches for the characterisation of this aspect of the tumour microenvironment have been limited in the clinical setting[22,29,30]. Given the dynamic nature of processes like hypoxia and perfusion, sequential multi-modal imaging investigations may not be able to effectively assess relationships between these parameters, as similar tumour status cannot be guaranteed at different time points of the imaging sessions. Simultaneous assessment of the hypoxia and perfusion status in tumours can mitigate confounders associated with the dynamic character of these processes, and thus allow additional pathophysiological characterisation of breast cancer. To this end, imaging with a combined PET/MRI system presents an attractive option, as it can allow examination of tumours under the same physiologic conditions.

3.4 Methods

3.4.1 Patients

Between February 2017 and November 2018, a total of 32 women with treatment-naïve, pathologically confirmed primary breast cancer, were prospectively enrolled from Addenbrooke's Hospital, Cambridge, UK. Patients aged >18 years, with a tumour >10 mm diameter on mammography and/or ultrasound were considered eligible for the study. Pregnancy, lactation, history of serious breast trauma within three months prior to diagnosis, previous surgery or radiotherapy for cancer or benign breast disease, inadequate renal function, previously known allergies to gadolinium-based contrast agents and contraindications to MRI were exclusion criteria for the study.

All patients gave written, informed consent before participating in the study. The research was approved by a National Research Ethics Committee (14/EE/0145) and the Administration of Radioactive Substances Advisory Committee (ARSAC), UK.

3.4.2 PET/MRI acquisition

^{18}F-FMISO-PET/MR scans were performed on a SIGNA PET/MR scanner (GE Healthcare, Milwaukee, WI), University of Cambridge, UK. ^{18}F-FMISO was provided by the Radiopharmaceutical Unit, Wolfson Brain Imaging Centre, University of Cambridge, UK.

Participants underwent a 60-min simultaneous PET/MR scan of the breasts in the prone position, using a 16-channel bilateral breast array coil (RAPID Biomedical, Rimpar, Germany) 120 min (median [range]: 120.2 [119.8–127.5] min) after injection of 306 ± 14 MBq ^{18}F-FMISO. The uptake period post injection (p.i.) was used to enhance hypoxic-to-normoxic tissue-contrast and allow the free ^{18}F-FMISO concentrations in tissue and blood to reach equilibrium[23,24] a requirement for influx-rate constant (K_i) determination by Patlak analysis[25]. Participants were not required to fast before the PET/MR examination.

3.4.2.1 PET acquisition: Emission data from 120-180 min p.i. (12×5-min frames) were reconstructed into a 192×192×89 matrix with 3.12×3.12×2.78 mm voxels, using time-of-flight ordered-subsets expectation-maximisation (TOF-OSEM) with 4 iterations and 28 subsets. Corrections for normalisation, dead-time, random events, scatter, attenuation, sensitivity and isotope decay were applied as implemented on the scanner, together with an isotropic 4-mm FWHM Gaussian filter post reconstruction. Plasma radioactivity concentration from two venous blood samples, acquired immediately before and after the end of the PET/MR examination, were employed for scaling an ^{18}F-FMISO population-based arterial input function (AIF) derived from existing data (Appendix A-1 and appendix figure A-1), permitting calculation of the Patlak influx rate constant K_i, as previously reported[31].

3.4.2.2 MRI acquisition: The MRI protocol included: the manufacturer's 2-point Dixon sequence for PET attenuation correction, T_1 and T_2-weighted images, DWI, and a DCE series. Sequences for measuring B_1^+ transmission-field inhomogeneity (B_1-mapping), using a Bloch-Siegert method, and baseline T_1 (T_1 mapping), as required for pharmacokinetic analysis of DCE data were also acquired[32]. For DCE acquisition, a dose of 0.1 mmol/kg of bodyweight of Gadovist (Bayer Healthcare, Germany) was administered intravenously as a bolus with an automated injector at 3 mL/s followed by a saline flush. DCE acquisition involved five pre-contrast image volumes followed by 43 phases after contrast injection. Details of MR sequence acquisition parameters are presented in Table 3.1.

Table 3.1 MRI acquisition parameters

MR sequence parameters	T_1 mapping (VFA)	B_1^+ mapping (Bloch-Siegert)	DCE (VIBRANT-TRICKS)	DWI
Sequence	3D SPGR	2D SPGR	3D SPGR	2D SE-EPI
FOV diameter (mm)	350	350	350	360
Image Matrix	256×256	128×128	512×512	140×192
Slice thickness (mm)	2.8	7.0	2.8 (interpolated to 1.4)	4.0
No. of slices	112	22	112	26
b-values (s/mm^2)	n/a	n/a	n/a	0, 900
Pixel size	1.4×1.4	2.7×2.7	0.6×0.6	2.6×1.9
Fat suppression	No	No	Yes†	Yes‡
ASSET factor	2	n/a	2.5	2
TR (ms)	4.2	24	7.1	6.0
TE (ms)	2.1	13.7	3.8	94.9
RF excitation (degrees)	2, 3, 5, 10, 15	20	12	90
No. of averages	1	1	0.5	5
Bandwidth (kHz)	62.5	15.6	125	250
Acquisition time	33 s (per flip angle)	2 m 20 s	8 m 5 s	10 m 48 s

VFA: variable flip angle; VIBRANT-TRICKS: volume image breast assessment–time-resolved imaging of contrast kinetics; 3D SPGR: three-dimensional spoiled gradient recalled echo; 2D SPGR: two-dimensional spoiled gradient recalled echo; DWI: Diffusion weighted imaging; 2D SE-EPI: two-dimensional spin echo–echo-planar imaging; FOV: field-of-view; ASSET: array spatial sensitivity encoding technique; n/a: not applicable.
† Spatial-spectral water excitation
‡ Spatial-spectral water excitation with water spatial pre-saturation

3.4.3 Image analysis

Region-of interest delineation: Tumour regions of interest (ROIs) were manually delineated in OsiriX, version 8.0.2 (Pixmeo SARL, Switzerland) by three radiologists in consensus (one, three and >20 years of experience in breast MRI respectively). Regions were drawn on the peak-enhancing volumes of the DCE-MRI series (approximately corresponding to phase 19 of the DCE-MRI series) and included all consecutive axial sections encompassing the enhancing tumour mass and including multifocal/multicentric disease. For ROI delineation on the DCE images, care was taken to visually exclude normal breast parenchyma, fat, necrotic areas (void of signal within the tumour) and large vessels. To guide region definition, subtraction images were created in Osirix by subtracting pre-contrast images from the peak-enhancing phase of the DCE image series (~2 min from the start of enhancement). For the exclusion of large

vessels, maximum-intensity projection (MIP) images were also generated from the subtraction image-set and used as an additional reference for ROI delineation. In cases of multifocality or multicentricity on the MRI, region determination was based on the pathological review. Synchronous bilateral cancers were regarded as independent lesions[33].

For DWI analysis, whole tumour regions were demarcated on all axial slices encompassing the tumour on the b=900 s/mm^2 image, using the DCE post-contrast images as guidance, and subsequently imported on the corresponding apparent diffusion coefficient (ADC) map for each lesion. For ROI delineation, care was taken to avoid tumour boundaries, non-enhancing lesion voxels, necrotic and cystic areas[34]. Additionally, the ADC value of the darkest part of the tumour (dp-ADC) was measured, using a 5 mm circular ROI in the visually darkest (and most suspicious) region of the tumour[35,36] (Figure 3.1).

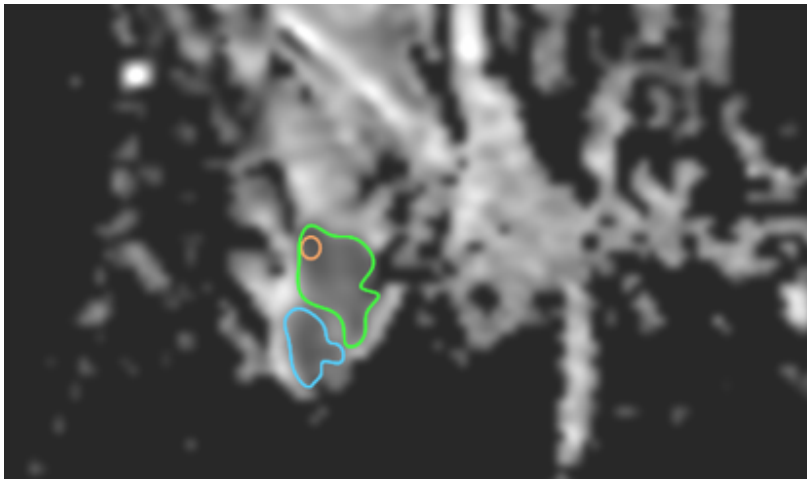

Figure 3.1 ADC map of 45-year-old female patient with an invasive ductal carcinoma (hormone receptor-positive/HER2-; grade 3) in the posterior aspect of the left breast. Regions of interest encompassing the entire lesion are shown in green and blue color and a small 5-mm diameter circular region encompassing the darkest area within the lesion is shown in orange color.

DCE-MRI: Pharmacokinetic analysis of the DCE-MRI series was performed in MIStar, version 3.2.63 (Apollo Medical Imaging, Melbourne, Australia) using the extended Tofts' model[37] to calculate the forward volume transfer constant, K^{trans}, efflux rate constant, k_{ep}, extracellular-extravascular volume fraction v_e and plasma volume fraction v_p. Modelling utilised the

modified Fritz-Hansen arterial input function[38,39]. During model fitting, thresholds were applied, and all parameters were restricted to positive values with $v_e \leq 1$. K^{trans} values >5 mL/cm^3/min were regarded as non-physiological[17].

Before pharmacokinetic analysis, a cuboid region encompassing the entire tumour across the DCE-MRI series was motion corrected using a 3D affine model implemented in MIStar, which utilised the peak-enhancing phase of the DCE image series as reference for the registration. Transmission-field inhomogeneity on DCE-MR images was corrected by generating B_1^+ correction maps, using in-house software implemented in Matlab R2016b (Mathworks Inc., Natick, MA). Computation of B_1^+ maps included smoothing by a 3×3×3 median filter. T_{10} maps were subsequently generated in MIStar, utilising the B_1^+-field maps to correct for spatial variations in flip angle[30].

K^{trans} values in the most vascularised area of the tumour (hotspot K^{trans}) were calculated by averaging pixel values within a 9-pixel square region of interest placed around the area exhibiting the highest K^{trans} value on the K^{trans} parametric maps[34]. The region encompassing the hotspot K^{trans} area was subsequently superimposed on the corresponding co-registered K_i map to calculate the mean K_i values within the hotspot area.

DWI-MRI: Calculation of ADC maps was performed in OsiriX, using *b*-values of 0 and 900 s/mm^2.

ADC maps were calculated using the following equation:

$$\mathrm{ADC} = \frac{\ln\left(\frac{S_0}{S_1}\right)}{(b_1 - b_0)} \quad (1)$$

where S_0 and S_1 are the signal intensities in images obtained with b_0=0 s/mm^2 and b_1=900 s/mm^2.

PET: To reduce the impact of patient motion during acquisition, ^{18}F-FMISO dynamic image series were non-rigidly registered to the first frame using the Advanced Normalization Tools (ANTs) package (http://stnava.github.io/ANTs/). Registered frames from 150–180 min p.i. were averaged, rigidly registered to the peak-enhancing phase of the DCE-MRI series and subsequently employed for the determination of ^{18}F-FMISO uptake as mean and maximum standardised uptake values normalised by body-weight (SUV_{mean}, SUV_{max}), maximum tumour-

to-plasma (T_{max}/P) and tumour-to-muscle (T_{max}/M) ratios within the tumour regions defined on the DCE-MRI. For T_{max}/M calculations, the mean radioactivity concentration in a bilateral region in the pectoral muscle was used to represent normoxic tissue. The quality of the registrations was visually inspected by a breast radiologist. In two cases where lesions were located directly adjacent to pectoral muscle, regions were only placed in the contralateral muscle. Given that increased tracer uptake may represent high tracer delivery to a region rather than trapping under hypoxic conditions, the influx rate of ^{18}F-FMISO (K_i) into the trapped tissue compartment was determined as a more specific measure of tumour hypoxia. K_i maps were produced by Patlak-plot analysis, using in-house software implemented in Matlab R2016b. Hypoxic fractions (%HF) in tumour ROIs were calculated as the percentage of voxels with K_i values >2×standard deviations (SD) of the mean K_i in the normoxic muscle. Image analysis was performed using Analyze 12.0 (AnalyzeDirect Inc.,).

3.4.4 Histology

Histopathological information including tumour histological subtype, grade, oestrogen receptor (ER), progesterone receptor (PR) and human epidermal growth factor receptor-2 (HER2) status were obtained from core biopsies or surgical tumour specimens. Cancers with positive ER or PR expression were classified as hormone-receptor (HR) positive. Histopathological classification of breast tumours was performed following the WHO classification for breast tumours[40]. Tumours were graded according to the Elston-Ellis scoring system[34].

3.4.5 Statistical analysis

Statistical analysis was performed in IBM SPSS Statistics for MacOS, v25.0 (IBM Corp.) or Matlab 2016b. Continuous data were assessed for normality using the Anderson-Darling test. Correlations between continuous variables were assessed using the Pearson correlation (r) or Spearman correlation (ρ) coefficients. t-tests were used for comparison between means of two groups, and ANOVA when more than two groups were compared. Where data was not normally distributed, or normality could not be assessed, Mann-Whitney U and Mood's median or Kruskal-Wallis H tests were employed for comparisons between two or more groups, respectively. p-values <0.05 were considered statistically significant, unless otherwise indicated.

3.5 Results

A total of 32 women were enrolled into the study. Two participants withdrew before the PET/MR examination. PET and MRI data from one participant were excluded owing to inadequate acquisition of the DCE-MRI series that did not permit delineation of a tumour ROI. Additionally, DCE-MRI from a further patient was excluded due to poor quality of the images. In total, data from 29 participants was analysed with 32 biopsy-confirmed primary breast cancers on PET-MRI and 31 on DCE-MRI. ADC calculations included data from 18 patients (19 lesions), who successfully completed the DWI examination. Clinical information about the patient cohort is provided in Table 3.2.

Table 3.2 Clinical characteristics of the patient population (*n*=29).

Characteristic	***n* (%)**
Age at diagnosis (years)[a]	57 [37-78]
Menopausal status	
Pre-menopausal	10 (35)
Post-menopausal	19 (65)
Clinical management	
Primary surgery	21 (72)
Neo-adjuvant therapy	8 (28)
Lesion presentation	
Unilateral	26 (90)
Unilateral (synchronous)	1 (3)
Bilateral (synchronous)	2 (7)
Lesion laterality[b] [*n*=32 lesions]	
Right breast	16 (50)
Left breast	16 (50)

[a]Data presented as median [range].

[b]Lesion numbers include synchronous bilateral carcinomas, which were regarded as independent lesions.

Two-thirds of the lesions (21/32; 66%) were invasive ductal cancers (IDC), while 6/32 (19%) were invasive lobular carcinomas (ILC). The majority of cancers (29/32; 91%) were either grade 2 or 3. HR-positive expression was noted for 31/32 (97%) lesions, with 24/32 (77%) cancers being HER2-negative. Tumour characteristics are summarised in Table 3.3. Of the 19

cancers included in comparisons with DWI, 14 (74%) were IDC, three (16%) ILC, and two were classified as mucinous and mixed cancers respectively. All tumours were HR-positive, with 13 (68%) lesions also being negative for HER2.

Table 3.3 Tumour characteristics (*n*=32).

Characteristic	***n* (%)**
Lesions	32
Pathological size (mm)[a,b]	26 [10-142]
Lesion longest diameter on MRI	
≤20 mm	10 (31)
>20 mm	22 (69)
Histopathological subtype	
Ductal (IDC)	21 (66)
Lobular (ILC)	6 (19)
Mucinous (IMC)	2 (6)
Mixed[c]	3 (9)
Histological grade[d]	
1	3 (9)
2	16 (50)
3	13 (41)
Hormone-receptor status[e]	
Positive (ER or PR)	31 (97)
Negative	1 (3)
HER2 status[f]	
Positive	7 (22)
Negative	25 (78)

[a]Data presented as median [range].

[b]Pathological size measured on tumor specimens from patients undergoing primary surgery (*n*=21).

[c]Invasive carcinomas with presence of both lobular and ductal components on histology.

[d]Nottingham combined histologic grade.

[e]Tumours classified as ER or PR-positive, if >10% of the cells demonstrated nuclear staining by immunohistochemistry.

[f]Tumours classified as HER2-positive, if they scored 3+ on immunohistochemistry, or if they carried gene amplification as detected by fluorescence *in situ* hybridization (FISH).

3.5.1 Correlation between clinical data and ^{18}F-FMISO-PET/MRI parameters

Linear regression analysis was used to investigate the effect of age, patient menopausal status and the interaction between age and menopausal status on ^{18}F-FMISO and DCE-MRI parameters. This analysis did not reveal any statistically significant association with the imaging parameters (Table 3.4). Menopausal status and the interaction of age and menopausal state showed statistically significant associations with both mean lesion ADC and dp-ADC (Table 3.4). However, the statistical significance of these associations was not upheld after false discovery rate (FDR) correction for multiple comparisons (Menopausal status: ADC: p=0.24 dp-ADC: p=0.28; Age*Menopausal Status: p=0.36 dp-ADC: p=0.36).

Injected activity did not significantly correlate with ^{18}F-FMISO hypoxia parameters (Table 3.5). Similarly, lesion laterality did not yield significant differences in DCE-MRI metrics (Table 3.6). Comparisons of mean lesion ADC and dp-ADC values between right and left-sided breast cancers trended towards statistical significance (p=0.05; Table 3.6). However, it should be noted that the group of right-breast cancers included a mucinous carcinoma. IMC have been demonstrated to yield higher ADC than cancers of other histologic subtypes or benign breast tumours[41]. Removing the one mucinous lesion from this analysis reduced the significance of this comparison (p=0.1).

Table 3.4 Linear regression coefficients (β) with standard errors (SE) and *p* values for age, menopausal status and an interaction effect between age and menopausal status as regressors for regional DCE-MRI and PET values.

Parameters	Age β, [SE], *p*	Menopausal status[a] β, [SE], *p*	Age*Menopausal status β, [SE], *p*
Lesions (*n*)		31	
K^{trans}	-0.028, [0.025], 0.27	-1.924, [1.340], 0.16	-0.043, [0.027], 0.13
k_{ep}	-0.004, [0.003], 0.25	0.028, [0.178], 0.88	0.001, [0.004], 0.80
v_e	-0.022, [0.011], 0.07	-1.351, [0.611], 0.37	0.029, [0.013], 0.27
$ln(v_p)$[b]	-0.085, [0.055], 0.14	-3.371, [3.002], 0.27	0.086, [0.061], 0.17
Lesions (*n*)		19	
ADC ($\times 10^{-3}$)	-0.016, [0.015], 0.31	-2.079, [0.848], 0.02*	0.039, [0.017], 0.03*
dp-ADC ($\times 10^{-3}$)	-0.016, [0.016], 0.33	-1.931, [0.884], 0.046*	0.035, [0.018], 0.06
Lesions (*n*)		32	
K_i ($\times 10^{-3}$)	-0.038, [0.037], 0.32	-2.200, [2.000], 0.27	-0.047, [0.041], 0.26
(1/%HF)[b]	1.058, [1.058], 0.32	108.1, [56.9], 0.09	-2.001, [1.173], 0.12
SUV_{max}	-0.016, [0.020], 0.42	0.180, [1.108], 0.87	0.007, [0.022], 0.75
SUV_{mean}	-0.016, [0.013], 0.25	-0.591, [0.732], 0.47	0.017, [0.016], 0.27
T_{max}/M	-0.016, [0.015], 0.31	-0.071, [0.844], 0.93	0.008, [0.017], 0.65
T_{max}/P	-0.015, [0.012], 0.23	-0.149, [0.673], 0.83	0.007, [0.014], 0.62

[a]0 = Pre-menopausal; 1 = Post-menopausal

[b]Due to the non-normality of residuals, as indicated by Shapiro-Wilk tests and Q-Q plots, v_e values were transformed using the natural logarithm, whereas the reciprocal of %HF was taken before linear regression.

Table 3.5 Spearman correlation coefficient (ρ) and *p* value between PET parameters and injected activity (MBq).

Parameter	Injected Activity (MBq) ρ	 *p*
Lesions (*n*)	32	
K_i ($\times 10^{-3}$)	0.07	0.73
HF (%)	-0.09	0.66
SUV_{max}	0.20	0.31
SUV_{mean}	0.01	0.95
T_{max}/M	0.15	0.44
T_{max}/P	0.19	0.34

Table 3.6 MRI and PET parameters with respect to lesion laterality. Data are presented as median [range] or mean ± standard deviation (SD) as appropriate.

	Laterality		
Parameters	**Right**	**Left**	***p***
Lesions (*n*)	16	15	
K^{trans}	0.60 [0.09-1.27]	0.35 [0.13-1.98]	0.13[a]
k_{ep}	0.24 ± 0.07	0.28 ± 0.04	0.08[a]
v_e	0.47 [0.09-1.27]	0.41 [0.13-1.98]	0.44[a]
v_p	0.11 [0-0.55]	0.06 [0-0.37]	0.19[a]
Lesions (*n*)	10	9	
ADC ($\times 10^{-3}$)	0.11 [0.83-2.46]	0.81 [0.42-1.28]	0.05[a]
dp-ADC ($\times 10^{-3}$)	0.88 [0.47-2.12]	0.65 [0.25-1.13]	0.13[a]
Lesions (*n*)	16	16	
K_i ($\times 10^{-3}$)	0.188 ± 0.566	0.085 ± 0.646	0.63
HF(%)	0 [0-2.19]	0 [0.-4.74]	0.41
SUV_{max}	1.61 ± 0.36	1.51 ± 0.36	0.45
SUV_{mean}	1.20 ± 0.36	1.13 ± 0.36	0.40
T_{max}/M	1.07 ± 0.20	1.08 ± 0.31	0.89
T_{max}/P	0.86 ± 0.21	0.85 ± 0.24	0.85

3.5.2 Relationship between ^{18}F-FMISO-PET and DCE-MRI parameters

Scatter plots indicating the relationships between DCE-MRI parameters and K_i or %HF are illustrated in Figure 3.2. An inverse relationship was observed between mean lesion K_i and K^{trans}, v_e, and v_p (Figure 3.2a-3.2d), which was statistically significant for K_i *vs*. K^{trans} (r=-0.38, p=0.04), but not for K_i *vs*. v_e (r=-0.30, p=0.10) or v_p (r=-0.28, p=0.12). Associations between %HF and DCE-MRI parameters followed similar trends, also indicating a decrease in hypoxia with increasing K^{trans}, v_e, and v_p (Figure 3.2e-3.2h). Similarly, a weak negative correlation was observed between K_i and K^{trans} in the hotspot area of the tumour (r=-0.16, p=0.40; Figure 3.3). Statistically significant correlations were observed between %HF and both K^{trans} (r=-0.33, p=0.04) and v_e (r=-0.38, p=0.03). No correlation was observed between k_{ep} and either K_i (r=0.08, p=0.65) or %HF (r=0.02, p=0.90).

Figure 3.4 presents axial slices through K_i and K^{trans} parametric maps of four tumours of different histological subtype, indicating heterogeneous spatial relationships between hypoxia and perfusion; other DCE-MRI parametric images are given in Figure 3.5.

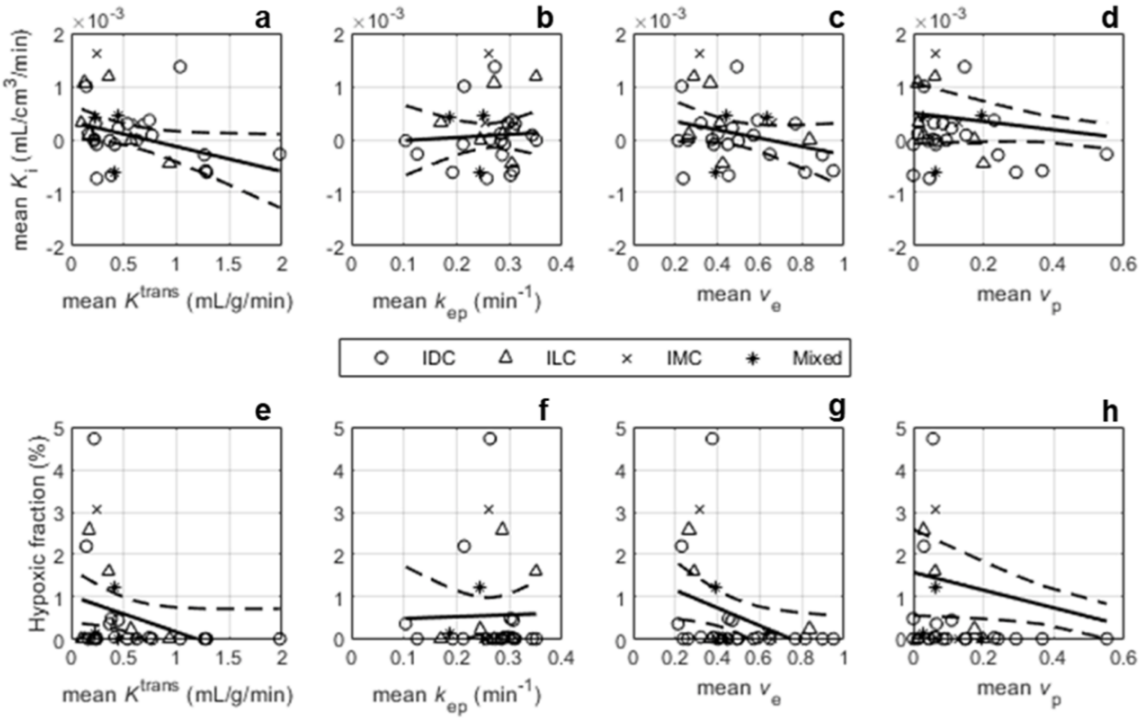

Figure 3.2 ^{18}F-FMISO-PET K_i and hypoxic fraction (%) *vs*. the following DCE-MRI parameters: (**a**,**e**) contrast influx rate, K^{trans} (mL/g/min); (**b**,**f**) contrast efflux rate, k_{ep} (min^{-1}); (**c**,**g**) fractional volume of extravascular-extracellular space, v_e; (**d**,**h**) plasma fractional volume, v_p. IDC: invasive ductal carcinoma; ILC: invasive lobular carcinoma; IMC: invasive mucinous carcinoma; Mixed: carcinoma of mixed ductal and lobular type.

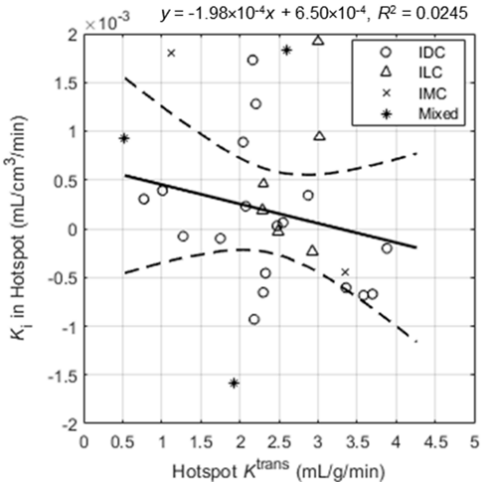

Figure 3.3 Scatterplot and regression line of K_i (mL/cm^3/min) *vs*. K^{trans} (mL/g/min) in the most vascularised area of the tumour (hotspot).

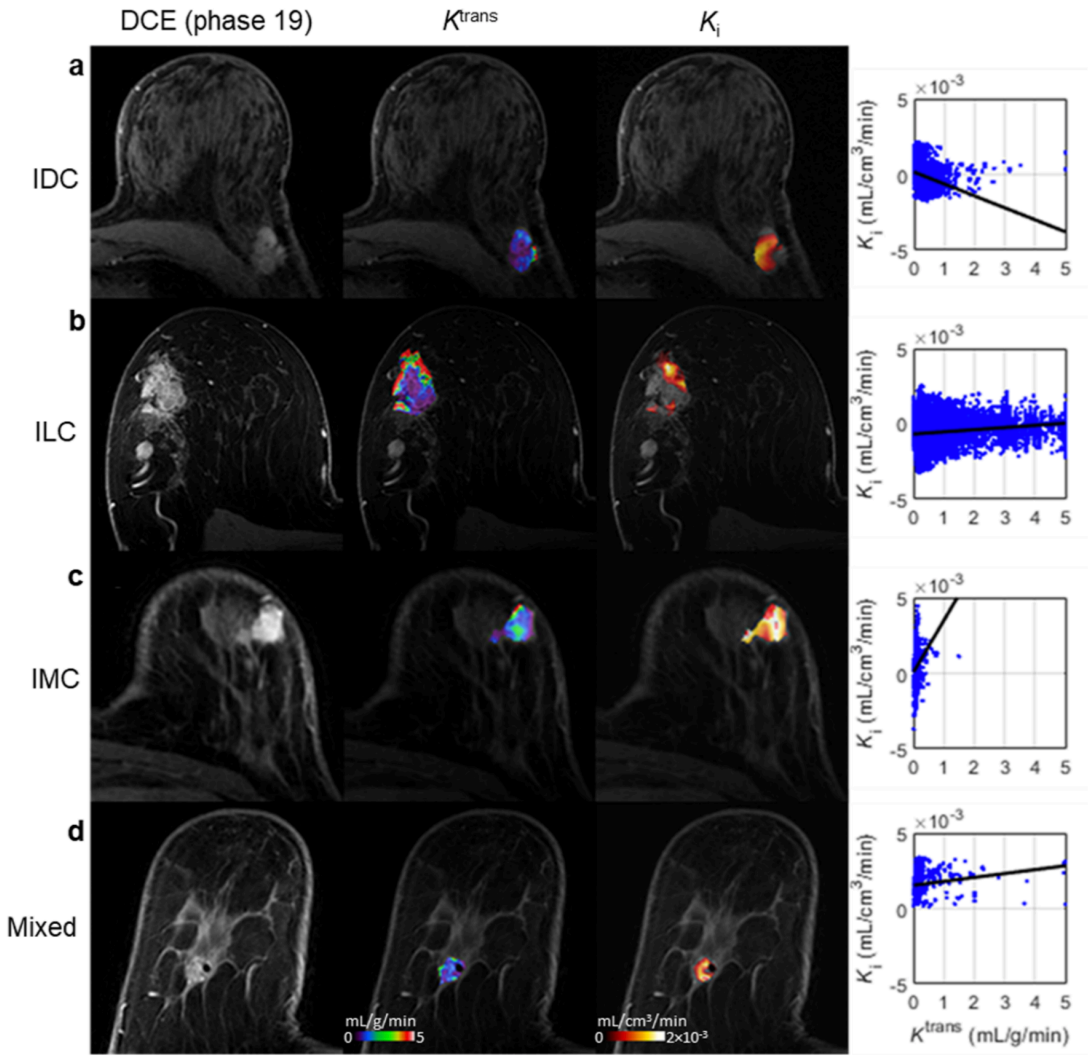

Figure 3.4 Axial images of four representative patients with: (**a**) invasive ductal carcinoma (IDC); (**b**) invasive lobular carcinoma (ILC); (**c**) invasive mucinous carcinoma (IMC); and (**d**) carcinoma of mixed ductal and lobular type (Mixed). (*Left-to-right*) DCE-MRI image at peak enhancement; K^{trans} map representing tumour perfusion for the lesion ROI overlaid on the peak enhancing DCE-MRI image; K_i map representing tumour hypoxia for the lesion ROI overlaid on the peak enhancing DCE-MRI image; scatter plot and regression line of K_i *vs*. K^{trans} voxel-values within the tumour. K^{trans}: contrast influx rate (mL/g/min); K_i: ^{18}F-FMISO influx rate (mL/cm^3/min); ADC: apparent diffusion coefficient (mm^2/s).

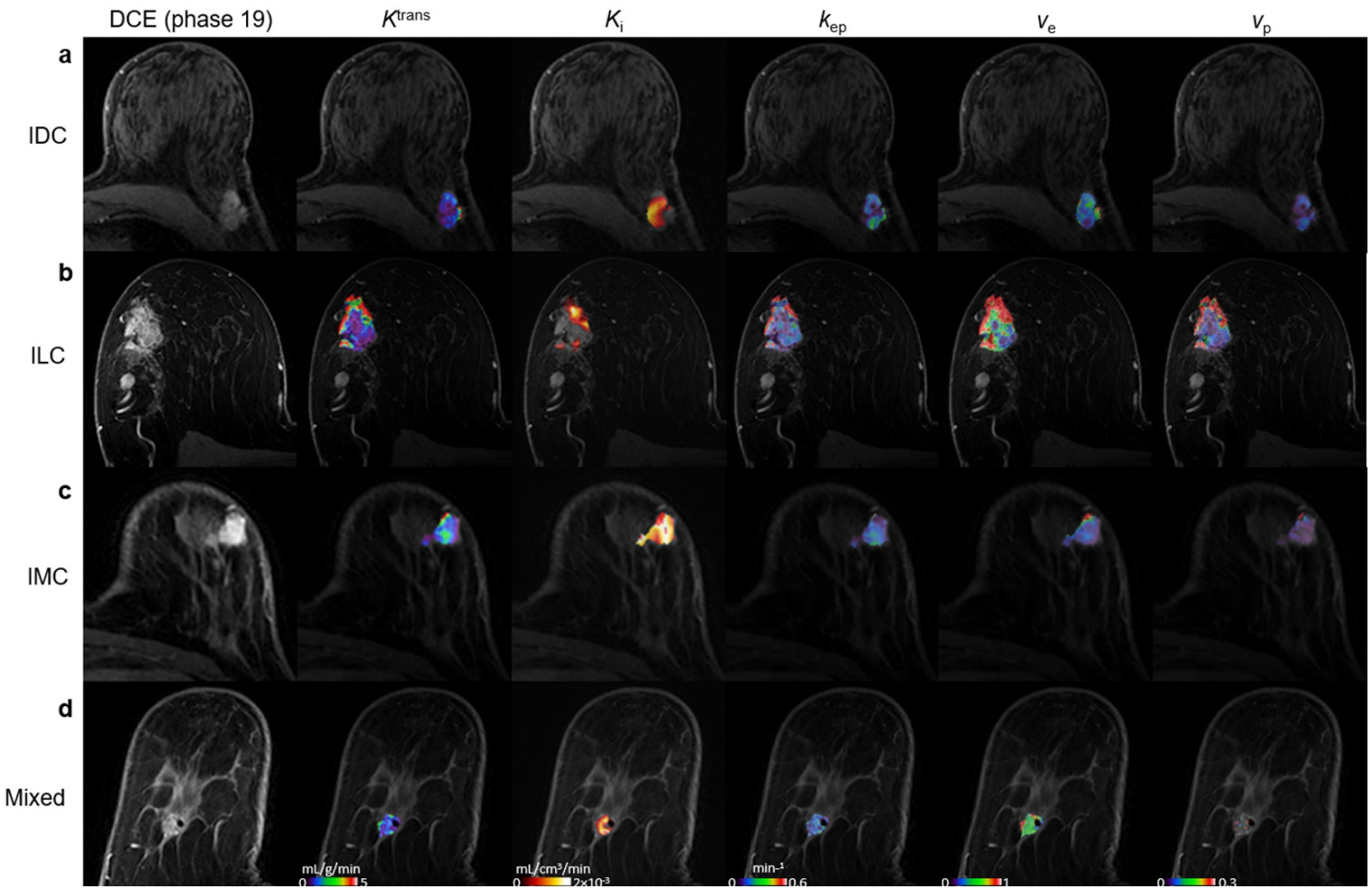

Figure 3.5 Axial images of the four representative patients shown in Fig. 3.4 with: (**a**) invasive ductal carcinoma (IDC); (**b**) invasive lobular carcinoma (ILC); (**c**) invasive mucinous carcinoma (IMC); and (**d**) carcinoma of mixed ductal and lobular type (Mixed). (*Left to right*) DCE-MRI image at peak enhancement, K^{trans}, K_i, k_{ep}, v_e and v_p maps. K^{trans}: contrast influx transfer rate (mL/g/min); k_{ep}: contrast efflux transfer rate (min^{-1}); v_e: fractional volume of extravascular-extracellular space; v_p: plasma fractional volume; K_i: ^{18}F-FMISO influx rate ($mL/cm^3/min$).

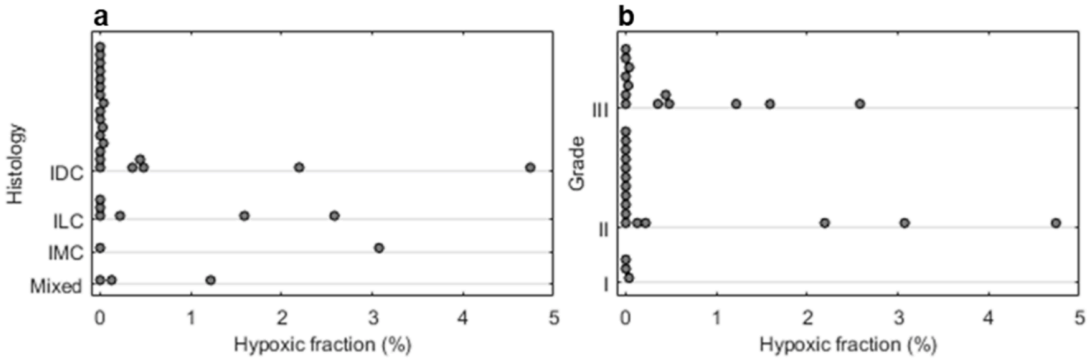

Figure 3.6 Dot plots of hypoxic fraction (%) by (**a**) histological type and (**b**) nuclear grade.

3.5.3 ^{18}F-FMISO-PET and DCE-MRI parameters vs. tumour histology and grade

Hypoxic fractions >1% were observed in 6/32 (19%) cancers with an additional 8/32 (25%) lesions displaying hypoxic fractions greater than zero but less than 1%; the remaining 18/32 (56%) tumours had no measurable %HF. Dot plots of %HF *vs*. tumour histological subtype and grade are presented in Figure 3.6. K_i, %HF and ^{18}F-FMISO uptake parameters showed no significant difference between different histological subtype or grade (Tables 3.7 and 3.8). Similarly, no significant differences were observed between histological groups or grades for the DCE-derived parameters (Tables 3.7 and 3.8), except for the efflux rate-constant k_{ep}, which displayed differences among grade 2 and 3 cancers that were trending towards statistical significance after FDR correction of p-values for multiple comparisons was done (median [range]: 0.25 [0.13-0.34] *vs*. 0.30 [0.10-0.35] min^{-1}; p_{unc}=0.009; p_{cor}=0.1). Furthermore, analysis of hypoxia and K^{trans} values in the most vascularised area of the tumour (hotspot on DCE-MRI) yielded no significant differences among different histological subtypes or grades (Tables 3.9 and 3.10).

Table 3.7 MRI and ^{18}F-FMISO-PET parameters with respect to tumour histology. Data are presented as median [range] or mean ± standard deviation (SD) as appropriate.

Parameter	Histology				*p*-value
	IDC	ILC	Mixed	IMC	
Lesions (*n*=31)	20	6	3	2	
K^{trans}	0.43 [0.14–1.97]	0.26 [0.10–0.94]	0.41 [0.23–0.45]	0.44 [0.25–0.64]	0.77[a]
k_{ep}	0.26 [0.10–0.35]	0.28 [0.17–0.35]	0.25 [0.19–0.25]	0.26 [0.25–0.26]	0.14[a]
v_e	0.46 [0.21–0.95]	0.39 [0.26–0.84]	0.44 [0.39–0.64]	0.49 [0.31–0.66]	0.30[a]
v_p	0.08 [0–0.55]	0.05 [0.01–0.2]	0.06 [0.03–0.19]	0.09 [0.06–0.13]	0.77[a]
Lesions (*n*=19)	14	3	1	1	
ADC ($\times10^{-3}$)	0.90 [0.42–1.55]	1.05 [0.84–1.28]	1.02 [--]	2.46 [--]	0.51[b]
dp-ADC ($\times10^{-3}$)	0.76 [0.25-1.09]	0.96 [0.64-1.12]	0.81 [--]	2.12 [--]	0.42[b]
Lesions (*n*=32)	21	6	3	2	
K_i ($\times10^{-3}$)	0.00 ± 0.52	0.37 ± 0.65	0.08 ± 0.61	0.97 ± 0.91	0.26[c]
%HF	0 [0–4.74]	0.10 [0–2.58]	0.13 [0–1.22]	1.54 [0–3.07]	0.63[a]
SUV_{max}	1.53 ± 0.41	1.77 ± 0.16	1.60 ± 0.21	1.25 ± 0.12	0.31[c]
SUV_{mean}	1.14 ± 0.26	1.27 ± 0.18	1.17 ± 0.16	1.07 ± 0.15	0.65[c]
T_{max}/M	1.02 ± 0.24	1.30 ± 0.29	1.09 ± 0.22	0.95 ± 0.02	0.12[c]
T_{max}/P	0.87 ± 0.22	0.83 ± 0.33	0.87 ± 0.09	0.84 ± 0.09	0.99[c]

[a]Mood's median test

[b]Mann-Whitney *U* test for malignancies of type IDC and ILC only (mixed and IMC lesions were not included in the comparison)

[c]One-way analysis of variance (ANOVA)

IDC: invasive ductal carcinoma; ILC: invasive lobular carcinoma; Mixed: invasive carcinoma with presence of lobular and ductal components; IMC: invasive mucinous carcinoma; K^{trans}: contrast influx rate (mL/g/min); k_{ep}: contrast efflux rate (min^{-1}); v_e: fractional volume of extravascular-extracellular space; v_p: plasma fractional volume; ADC: apparent diffusion coefficient (mm^2/s); dp-ADC: ADC (mm^2/s) in the darkest part of the tumour; K_i: ^{18}F-FMISO influx rate ($mL/cm^3/min$); %HF: percentage hypoxic fraction; SUV: standardised uptake value (g/mL); T_{max}/M: tumour-to-muscle ratio; T_{max}/P: tumour-to-plasma ratio.

Table 3.8 MRI and ^{18}F-FMISO-PET parameters with respect to nuclear grade. Data are presented as median [range] or mean ± standard deviation (SD) as appropriate.

Parameter	Grade 1	Grade 2	Grade 3	*p*-value
Lesions (*n*=31)	3	15	13	
K^{trans}	0.41 [0.24-0.54]	0.24 [0.10-1.98]	0.45 [0.17-1.27]	0.29[a]
k_{ep}	0.29 [0.26-0.31]	0.25[*c] [0.13-0.34]	0.30[*d] [0.10-0.35]	0.009[**a]
v_e	0.38 [0.24-0.77]	0.45 [0.23-0.84]	0.43 [0.21-0.95]	0.65[a]
v_p	0.06 [0.05-0.08]	0.06 [0.00-0.55]	0.09 [0.00-0.37]	0.46[a]
Lesions (*n*=19)	1	9	9	
ADC ($\times 10^{-3}$)	1.08 [--]	1.05 [0.42-2.46]	0.84 [0.70-1.28]	0.34[b]
dp-ADC ($\times 10^{-3}$)	0.76 [--]	0.93 [0.25-2.12]	0.70 [0.52-1.12]	0.22[b]
Lesions (*n*=32)	3	16	13	
K_i ($\times 10^{-3}$)	-0.18 ± 0.52	0.25 ± 0.58	0.06 ± 0.65	0.47[c]
%HF	0 [0-0.04]	0 [0-4.74]	0.04 [0-2.6]	0.35[a]
SUV_{max}	1.28 ± 0.29	1.55 ± 0.29	1.66 ± 0.46	0.28[c]
SUV_{mean}	0.98 ± 0.09	1.18 ± 0.19	1.18 ± 0.29	0.37[c]
T_{max}/M	0.96 ± 0.02	1.04 ± 0.17	1.56 ± 0.36	0.36[c]
T_{max}/P	0.78 ± 0.08	0.81 ± 0.20	0.85 ± 0.25	0.21[c]

[a]Kruskal-Wallis *H*

[b]Mann-Whitney *U* test for grade 1 and 2 cancers only (grade I lesions were not included in the comparison).

[c]One-way analysis of variance (ANOVA)

[d]Significant difference between grade 2 and 3 cancers (p=0.01). Pairwise multiple comparison analysis utilized the Dwass-Steel-Critchlow-Fligner method.

[*]p<0.05; [**]p<0.01

Table 3.9 Hotspot K^{trans} (mL/g/min) and ^{18}F-FMISO-PET parameters with respect to tumour histology. Data are presented as mean ± standard deviation (SD) or median [range] as appropriate.

Parameter[a]	Histology				*p*-value
	IDC	**ILC**	**Mixed**	**IMC**	
Lesions (*n*=31)	20	6	3	2	
Hotspot K^{trans}	2.50 ± 0.95	2.67 ± 0.35	1.68 ± 1.05	2.24 ± 1.58	0.46[a]
Hotspot K_i ($\times 10^{-3}$)	-0.03 ± 1.14	0.54 ± 0.79	0.69 ± 1.59	0.39 ± 1.77	0.65[a]
Hotspot SUV	0.90 ± 0.26	0.91 ± 0.41	0.90 ± 0.48	1.14 ± 0.75	0.68[a]
Hotspot T/P	0.49 [0.33-1.07]	0.42 [0.23-0.56]	0.53 [0.27-0.66]	0.75 [0.66-0.85]	0.38[b]

[a]One-way analysis of variance (ANOVA)

[b]Mood's median test

K^{trans}: contrast influx rate (mL/g/min); K_i: ^{18}F-FMISO influx rate (mL/cm^3/min); SUV: standardised uptake value (g/mL); T/P: tumour-to-plasma ratio.

Table 3.10 Hotspot K^{trans} (mL/g/min) and ^{18}F-FMISO-PET parameters in the hotspot area with respect to nuclear grade. Data are presented as median [range] or mean ± standard deviation (SD) as appropriate.

Parameter	Grade			*p*-value
	1	**2**	**3**	
Lesions (*n*=31)	3	15	13	
Hotspot K^{trans}	2.55 [2.30-3.58]	2.30 [0.53-4.26]	2.32 [1.75-3.70]	0.683[†]
Hotspot K_i ($\times 10^{-3}$)	-0.43 ± 0.42	0.57 ± 0.97	-0.16 ± 1.31	0.153[‡]
Hotspot SUV_{bw}	0.66 ± 0.09	0.96 ± 0.25	0.94 ± 0.27	0.168[‡]
Hotspot T/P	0.37 [0.35-0.48]	0.53 [0.23-0.90]	0.54 [0.32-1.07]	0.397[†]

[†] Kruskal-Wallis *H*

[‡] One-way analysis of variance (ANOVA)

3.5.4 Effect of tumour size on ^{18}F-FMISO-PET and DCE-MRI parameters

Table 3.11 presents correlations between imaging parameters and tumour size as measured by longest diameter on MRI or pathological size. No or weak negative correlations were observed between tumour size and DCE-MRI parameters. Conversely, ^{18}F-FMISO-PET parameters correlated positively with size; %HF significantly correlated with pathological size (r=0.63, p=0.001), while ^{18}F-FMISO-PET uptake metrics displayed associations of moderate strength with longest diameter on MRI.

Table 3.11 Pearson correlation coefficients r (p-value) between tumour size (obtained from MRI and pathological specimens) and ^{18}F-FMISO-PET/MRI parameters.

Parameter	Tumour size (mm)	
	Longest diameter on MRI	Pathological size
Lesions (n)	31	21
K^{trans}	-0.15 (0.42)	-0.16 (0.48)
k_{ep}	-0.04 (0.84)	-0.15 (0.48)
v_e	-0.04 (0.83)	-0.27 (0.22)
v_p	-0.13 (0.50)	-0.09 (0.70)
Lesions (n)	19	11
ADC ($\times10^{-3}$)	0.08 (0.72)	0.56 (0.07)
dp-ADC ($\times10^{-3}$)	0.06 (0.79)	0.23 (0.40)
Lesions (n)	32	21
K_i ($\times10^{-3}$)	0.15 (0.29)	0.21 (0.48)
HF (%)	0.26 (0.16)	0.63 (0.001**)
SUV_{max}	0.48 (0.02*)	0.26 (0.24)
SUV_{mean}	0.42 (0.006**)	0.39 (0.07)
T_{max}/M	0.45 (0.01*)	0.32 (0.14)
T_{max}/P	0.43 (0.02*)	0.49 (0.02*)

$^{*}p$<0.05; $^{**}p$<0.01.
[a]Pathological size as measured on tumour specimens from patients undergoing primary surgery (n=21).

3.5.5 ADC vs. ^{18}F-FMISO-PET and DCE-MRI parameters

Positive correlations were observed between mean lesion ADC and DCE-MRI indices (K^{trans}: r=0.24, p=0.34; v_e: r=0.29, p=0.25; v_p: r=0.20, p=0.43), except for k_{ep} which correlated negatively with mean lesion ADC (r=-0.15, p=0.56; Figure 3.7); none of which were

statistically significant. No correlations were observed between mean lesion ADC and K_i or %HF (K_i: r=0.05, p=0.84; %HF r=0.04, p=0.88; Figure 3.7). Representative ADC maps are given in Figure 3.8.

Similarly, mean ADC of the darkest part of the tumour (dp-ADC) showed weak positive correlations with K_i and %HF (Figure 3.9) which were not statistically significant. Similar to mean lesion ADC, dp-ADC correlated positively to DCE-MRI K^{trans} and negatively to $k_{ep.}$ No association was observed between dp-ADC, v_e and v_p (Figure 3.10). Correlations between dp-ADC and DCE-MRI parameters (K^{trans}, K^{ep}, V_e, V_p) were not statistically significant.

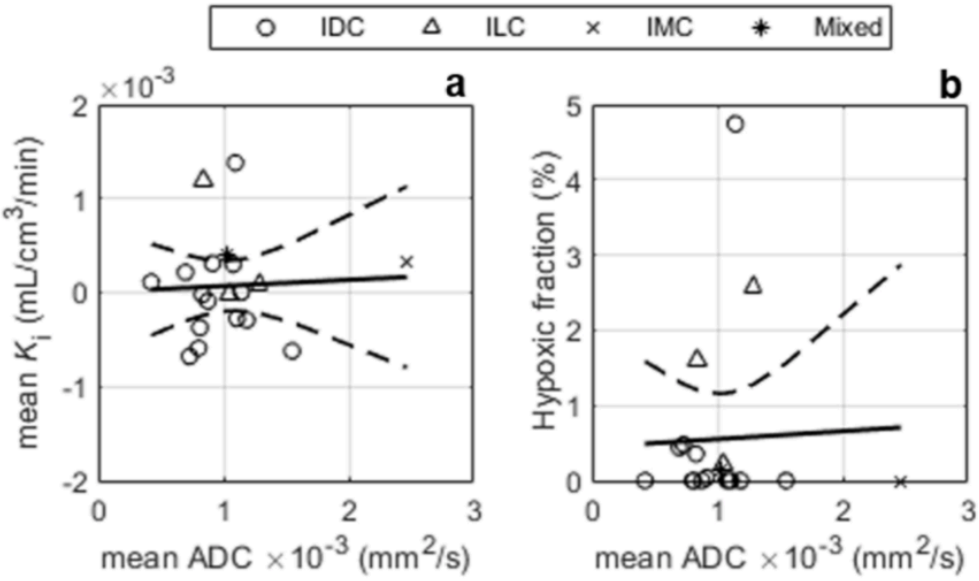

Figure. 3.7 ^{18}F-FMISO-PET parameters *vs*. mean whole tumour apparent diffusion coefficient (ADC): (**a**) influx rate K_i and (**b**) hypoxic fraction (%). IDC: invasive ductal carcinoma; ILC: invasive lobular carcinoma; IMC: invasive mucinous carcinoma; Mixed: carcinoma of mixed ductal and lobular type.

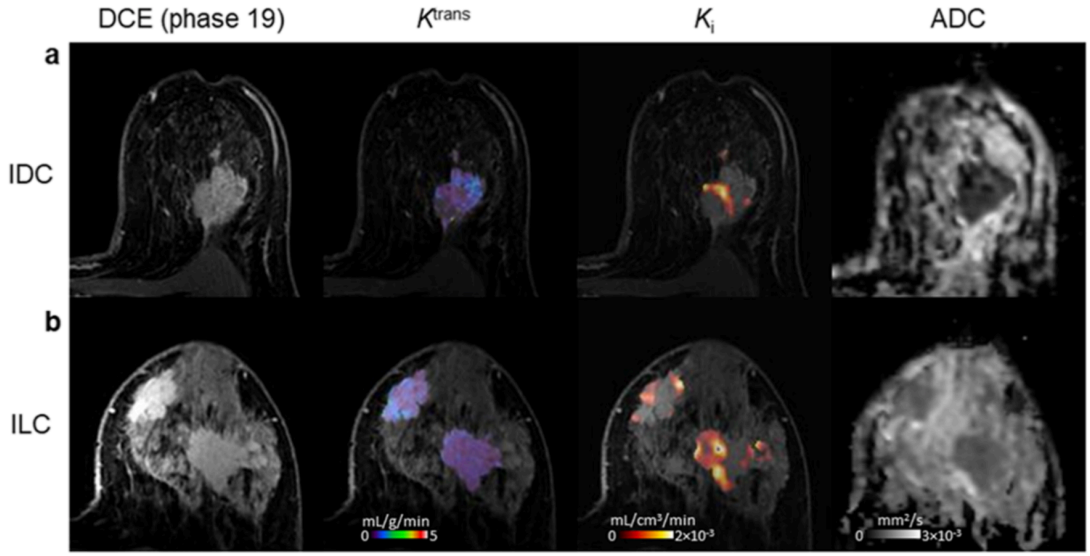

Figure 3.8 Axial images of two patients with: (**a**) invasive ductal carcinoma (IDC); (**b**) invasive lobular carcinoma (ILC). (*Left-to-right*) DCE-MRI image at peak enhancement; K^{trans} map representing tumour perfusion for the lesion ROI; K_i map representing tumour hypoxia for the lesion ROI; ADC map of the lesion. K^{trans}: contrast influx rate (mL/g/min); K_i: ^{18}F-FMISO influx rate (mL/cm^3/min); ADC: apparent diffusion coefficient (mm^2/s).

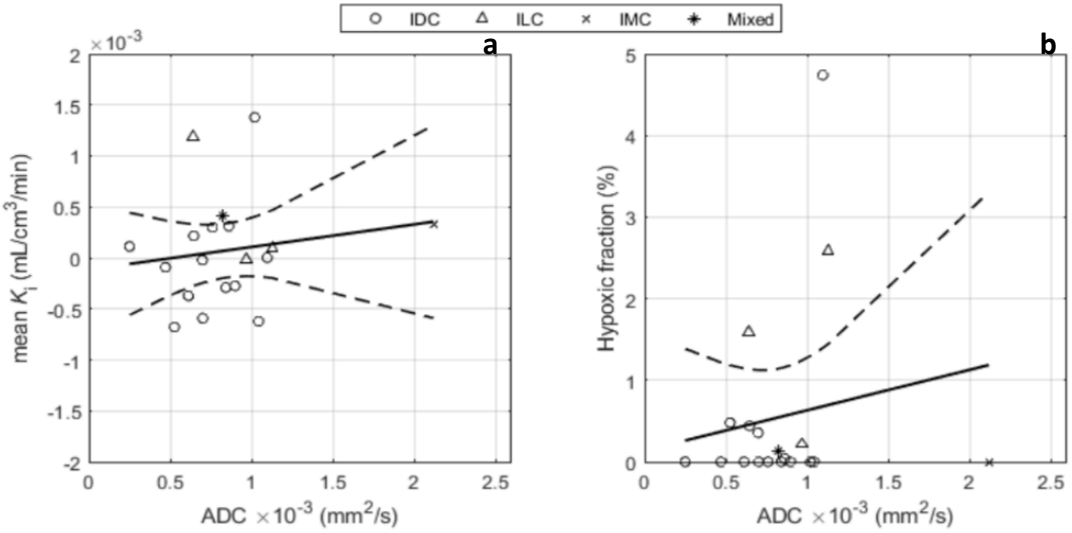

Figure 3.9 Scatterplot and regression line of (**a**) influx rate K_i (mL/cm^3/min) and (**b**) hypoxic fraction (%) *vs*. apparent diffusion coefficient of the darkest part of the tumour (dp-ADC) (mm^2/s).

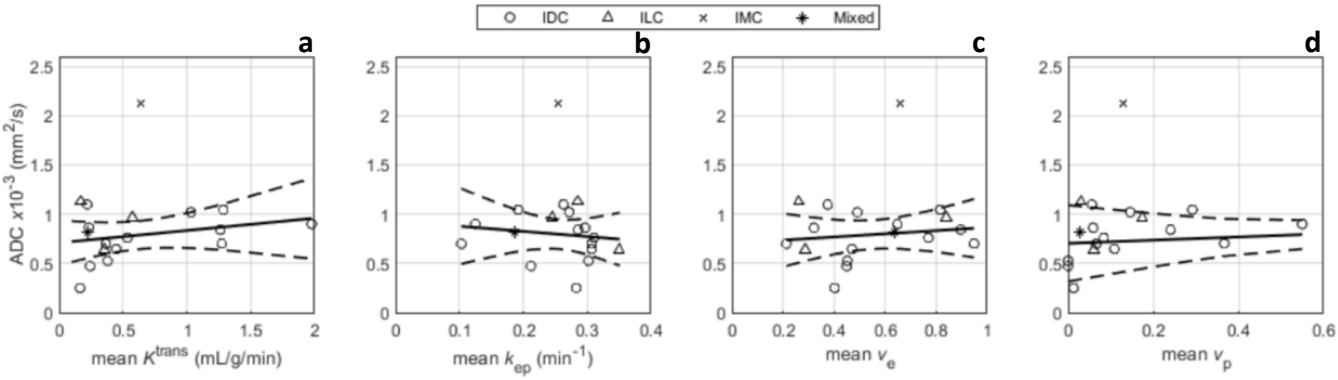

Figure 3.10 Scatterplot and regression line of DCE-MRI parameters *vs*. apparent diffusion coefficient of the darkest part of the tumour (dp-ADC [mm^2/s]): (**a**) contrast influx rate, K^{trans} (mL/g/min); (**b**) contrast efflux rate, k_{ep} (min^{-1}); (**c**) fractional volume of extravascular-extracellular space, v_e; (**d**) plasma fractional volume, v_p.

3.6 Discussion

This study explored the relationship between tumour hypoxia and vascular function in breast cancer using combined ^{18}F-FMISO-PET/MRI. Hypoxic fractions and K_i measured on ^{18}F-FMISO-PET showed inverse relationships with the DCE-MRI perfusion parameter K^{trans}, consistent with the generally accepted view that tumour hypoxia is a consequence of inadequate oxygen supply to the tumour[42]. Previous clinical studies in cervical and head-and-neck carcinomas have demonstrated significant negative correlations between contrast enhancement or pharmacokinetic parameters from DCE-MRI and polarographic pO_2 measurements or pimonidazole immunohistochemistry[41,43]. These findings are consistent with these results in breast cancer.

However, PET and DCE-MRI parametric images exhibited largely heterogeneous intra-tumoural patterns with hypoxic islands on K_i maps often colocalising with areas of increased K^{trans}. This spatially discrepant relationship between hypoxia and perfusion has been previously documented, with the co-existence of hypoxic and hyperperfused tumour sub-volumes[44]. Various biological mechanisms, including HIF-1α-induced angiogenesis, interstitial fluid pressure, a fluctuating haemodynamic response, increased oxygen diffusion distances from the microvasculature, and the presence of longitudinal oxygen gradients across tumour vessels have all been proposed to explain the occurrence of hypoxia in highly perfused areas[45,46]. Thus, although the general trend of our results would support the widely accepted view that hypoxia develops in hypo perfused breast tumours, the diverse relationships observed in individual tumour sub-volumes indicate heterogeneity in hypoxia-perfusion patterns and reflect the variety of pathophysiological mechanisms occurring in cancers.

The weak relationship between PET hypoxia parameters with k_{ep} suggests that the degree of tumour hypoxia is more strongly influenced by vascular flow rather than vessel permeability. Li *et al*[47] have previously suggested that k_{ep} is a much more sensitive measure of vessel permeability than K^{trans}, as the latter represents a combined measure of blood flow, vessel permeability and capillary-surface area. Our findings broadly agree with previous research in cervical and head-and-neck carcinomas, which illustrated weaker correlations between hypoxia and permeability-surface-area product than between hypoxia and blood flow[41,48]. The relationship between K^{trans} and regional hypoxia observed in our study suggests this is due to fluctuations in tumour vascular flow rather than capillary permeability.

No or weak positive correlations were found between static ^{18}F-FMISO parameters (SUV_{mean}, SUV_{max}, T_{max}/M, T_{max}/P) and DCE-MRI metrics. In contrast, in human head-and-neck cancer, where hypoxia is often marked, ^{18}F-FMISO SUV measurements were negatively correlated with both K^{trans} and k_{ep}[18]. A plausible explanation for this disparity is the higher level of hypoxia typically encountered in head-and-neck cancer, which will lead to uptake values being more dominated by hypoxia-specific ^{18}F-FMISO trapping rather than non-specific tracer accumulation. Due to the higher contribution of non-specific ^{18}F-FMISO accumulation at low hypoxia levels[49], the use of uptake values in cancers without marked hypoxia may not accurately reveal relationships between hypoxia and perfusion.

No significant correlation was observed between PET hypoxia parameters and tumour grade or subtype. Our sample size of non-IDC cases was small for evaluating the impact of histology on tumour hypoxic status, but the presence of non-zero hypoxic fractions was observed in all histological subtypes studied. Hypoxic fractions and higher K_i were noted in both grade 2 and 3 tumours, and less so in grade 1 cancers. These findings are concordant with previously reported small differences in hypoxia between low and high-grade breast malignancies[50].
Correlations between DCE-MRI functional parameters and pathological size or MR tumour diameter yielded moderate negative relationships and conversely positive associations between ^{18}F-FMISO-PET hypoxia parameters and size. The size-related hypoxia changes could be ascribed to diffusion-limited hypoxia, concomitant decreased perfusion or increased interstitial fluid pressure[51].

ADC has been shown to inversely correlate with cellular density[52], and therefore a reduction in whole tumour ADC should theoretically be accompanied by an increase in tumour hypoxia. Our findings indicated no association between mean whole tumour ADC and PET hypoxia parameters. This result could be explained by the molecular subtype of lesions in our sample, which predominantly consisted of ER-positive/HER2-negative cancers. Due to lower blood flow, ER-positive or HER2-negative lesions exhibit lower ADC values than ER-negative or HER2-positive cancers[53,54]. As ADC is affected not only by tissue cellularity but several pathophysiologic processes including blood flow, membrane permeability and the geometric architecture of the interstitial space[55,56] it is likely that the lack of association between the PET hypoxia parameters and mean whole tumour ADC is a consequence of the combined effect of cellularity, perfusion and micro-vessel structure on ADC. This assertion is further supported

by the weak correlations between DCE-MRI indices and ADC (mean WTu and Dptu) observed in this study. It should be noted however that inconsistent correlations between mean ADC and DCE-MRI parameters have been reported in tumours, including breast cancer[57,58,59].

ADC measurement approach using a small region of interest (ROI) in the visually assessed lowest ADC area of the tumour has been found to be the most practical and diagnostically accurate measurement in mass lesions in comparison to whole-lesion ROIs[36,60]. Likewise, small-ROI ADC measurement has been more frequently associated with tumour prognostic factors[60], although this study did not reveal significant correlations between tumour prognostic factors (such as histological tumour type, grade and size) and ADC measured in the darkest part of the lesion. In this study, mean ADC of the part of the tumour with more restricted diffusion presented poor positive correlations with PET hypoxia parameters and as previously mentioned, this may be due to the influence of other hallmarks of the cancer. Small-ROI ADC (from the part of the lesion with more restricted diffusion), like whole tumour ADC, correlated weakly to DCE-MRI quantitative parameters.

We calculated hypoxic fractions based on a specific parameter for hypoxia namely influx rate-constant K_i. Despite the higher variability associated with kinetic parameter estimates, our choice was based on two considerations. First, several authors have reported lack of correlation between ^{18}F-FMISO uptake ratios and pO_2 measurements casting doubt on the accuracy of thresholds derived from static PET imaging for hypoxic quantification[61,62]. Kinetic parameters, including K_i, have provided superior correlations with physiological measures of hypoxia from pO_2 histography and immunohistochemistry[61,62]. Second, these thresholds have mostly been defined on measurements from head-and-neck cancers and are not necessarily applicable to other tumour types, including breast cancer.

The main limitations of our study are the small sample size and that the majority of cancers were HR-positive ductal carcinomas. Though our findings cannot be generalised to the full spectrum of histological/molecular subtypes encountered in breast cancer, our study indicates the presence of hypoxia in all histological subtypes studied independent of nuclear grade. While the majority of lesions (56%) examined were found to be non-hypoxic, it should be noted that breast tumours are generally less hypoxic than cancers of the head-and-neck, cervix or lung and show greater variability in hypoxia among molecular subtypes, with basal-like subtypes being the most hypoxic[63].

3.7 Conclusion and clinical impact

Our demonstration of *in vivo* simultaneous measurement of perfusion and hypoxia is clinically important for three reasons. First, previous reports have indicated that tumours with a high hypoxia-perfusion ratio (i.e. hypoxia due to low perfusion) have a poorer prognosis and suboptimal treatment response[64,65]. In breast cancer, studies have described differences in the response to perfusion-related hypoxic exposure between molecular subtypes[66,67], emphasising the need for combined hypoxia-perfusion measurements to provide more accurate prognostic information or tailor treatment. Second, preoperative radiotherapy or radio-chemotherapy regimes in early or locally advanced breast cancer have reported beneficial clinical outcomes[68,69]. Hypoxia and hypoperfusion are known to reduce the effectiveness of radiotherapy and chemotherapy, therefore knowing the hypoxia-perfusion status of tumours at baseline could allow optimisation of these regimens. Third, tumour hypoxia can occur independently of hypoperfusion as evidenced in the oncology literature[44,45,64,65] and our findings. As such, the data presented here can be viewed as providing further indication of the benefit of non-invasive multi-modal assessment of the tumour microenvironment for disease characterisation.

In conclusion, we found a negative relationship between tumour hypoxia, measured by ^{18}F-FMISO-PET, and markers of perfusion and vascular function from DCE-MRI, endorsing the hypothesis of perfusion-driven hypoxia in breast cancer. No associations were observed between ^{18}F-FMISO-PET parameters and tumour histology or grade, but hypoxic fractions increased with lesion size. The intra-tumoral heterogeneity observed in hypoxia and perfusion images is consistent with the known complex relationship between perfusion and the hypoxic tumour micromilieu. The combined assessment of hypoxia-perfusion status of tumours may need to be considered in determining treatment efficacy or informing therapy selection in breast cancer patients, which could be achieved using simultaneous multi-modality imaging as reported here.

References

1. Carmona-Bozo, J. C. *et al.* Hypoxia and perfusion in breast cancer: simultaneous assessment using PET/MR imaging. *Eur. Radiol.* (2020). doi:10.1007/s00330-020-07067-2
2. Helczynska, K. *et al.* Hypoxia promotes a dedifferentiated phenotype in ductal breast carcinoma in situ. *Cancer Res.* (2003).
3. Cooper, C. *et al.* Intermittent hypoxia induces proteasome-dependent down-regulation of estrogen receptor α in human breast carcinoma. *Clin. Cancer Res.* (2004). doi:10.1158/1078-0432.CCR-04-1235
4. Semenza, G. L. The hypoxic tumor microenvironment: A driving force for breast cancer progression. *Biochimica et Biophysica Acta - Molecular Cell Research* (2016). doi:10.1016/j.bbamcr.2015.05.036
5. Chia, S. K. *et al.* Prognostic significance of a novel hypoxia-regulated marker, carbonic anhydrase IX, in invasive breast carcinoma. *J. Clin. Oncol.* (2001). doi:10.1200/JCO.2001.19.16.3660
6. Generali, D. *et al.* Hypoxia-inducible factor-1α expression predicts a poor response to primary chemoendocrine therapy and disease-free survival in primary human breast cancer. *Clin. Cancer Res.* (2006). doi:10.1158/1078-0432.CCR-05-2690
7. Dewhirst, M. W., Cao, Y. & Moeller, B. Cycling hypoxia and free radicals regulate angiogenesis and radiotherapy response. *Nature Reviews Cancer* **8**, 425–437 (2008).
8. Kimura, H. *et al.* Fluctuations in red cell flux in tumor microvessels can lead to transient hypoxia and reoxygenation in tumor parenchyma. *Cancer Res.* (1996).
9. Bristow, R. G. & Hill, R. P. Hypoxia and metabolism: Hypoxia, DNA repair and genetic instability. *Nature Reviews Cancer* **8**, 180–192 (2008).
10. Turnbull, L. W. Dynamic contrast-enhanced MRI in the diagnosis and management of breast cancer. *NMR in Biomedicine* **22**, 28–39 (2009).
11. Partridge, S. C., Nissan, N., Rahbar, H., Kitsch, A. E. & Sigmund, E. E. Diffusion-weighted breast MRI: Clinical applications and emerging techniques. *Journal of Magnetic Resonance Imaging* (2017). doi:10.1002/jmri.25479
12. Oyen, W. J. G., Kaanders, J. H. A. M. & Bussink, J. Molecular imaging of hypoxia. *Quarterly Journal of Nuclear Medicine and Molecular Imaging* **57**, 217–218 (2013).
13. Quintela-Fandino, M. *et al.* 18F-fluoromisonidazole PET and activity of neoadjuvant nintedanib in early HER2-negative breast cancer: A window-of-opportunity randomized

trial. *Clin. Cancer Res.* **23**, 1432–1441 (2017).

14. Ueda, S., Saeki, T., Osaki, A., Yamane, T. & Kuji, I. Bevacizumab induces acute hypoxia and cancer progression in patients with refractory breast cancer: Multimodal functional imaging and multiplex cytokine analysis. *Clin. Cancer Res.* (2017). doi:10.1158/1078-0432.CCR-17-0874
15. Cheng, J. *et al.* 18F-fluoromisonidazole PET/CT: A potential tool for predicting primary endocrine therapy resistance in breast cancer. *J. Nucl. Med.* (2013). doi:10.2967/jnumed.112.111963
16. Asano, A. *et al.* Intracellular hypoxia measured by 18F-fluoromisonidazole positron emission tomography has prognostic impact in patients with estrogen receptor-positive breast cancer. *Breast Cancer Res.* (2018). doi:10.1186/s13058-018-0970-6
17. Andrzejewski, P. *et al.* Sequential [18F]FDG-[18F]FMISO PET and Multiparametric MRI at 3T for Insights into Breast Cancer Heterogeneity and Correlation with Patient Outcomes: First Clinical Experience. *Contrast Media Mol. Imaging* (2019). doi:10.1155/2019/1307247
18. Jansen, J. F. A. *et al.* Noninvasive assessment of tumor microenvironment using dynamic contrast-enhanced magnetic resonance imaging and 18F- fluoromisonidazole positron emission tomography imaging in neck nodal metastases. *Int. J. Radiat. Oncol. Biol. Phys.* (2010). doi:10.1016/j.ijrobp.2009.07.009
19. Gerstner, E. R. *et al.* ACRIN 6684: Assessment of tumor hypoxia in newly diagnosed glioblastoma using 18F-FMISO PET and MRI. *Clin. Cancer Res.* (2016). doi:10.1158/1078-0432.CCR-15-2529
20. Pinker, K. *et al.* Multiparametric [18F]fluorodeoxyglucose/[18F]fluoromisonidazole positron emission tomography/ magnetic resonance imaging of locally advanced cervical cancer for the non-invasive detection of tumor heterogeneity: A pilot study. *PLoS One* (2016). doi:10.1371/journal.pone.0155333
21. Simoncic, U. *et al.* Comparison of DCE-MRI kinetic parameters and FMISO-PET uptake parameters in head and neck cancer patients. *Med. Phys.* (2017). doi:10.1002/mp.12228
22. Taylor, E. *et al.* Quantifying Reoxygenation in Pancreatic Cancer During Stereotactic Body Radiotherapy. *Sci. Rep.* (2020). doi:10.1038/s41598-019-57364-0
23. Rasey, J. S. *et al.* Characterization of Radiolabeled Fluoromisonidazole as a Probe for Hypoxic Cells. *Radiat. Res.* (1987). doi:10.2307/3576986
24. Muzi, M. *et al.* 18F-fluoromisonidazole quantification of hypoxia in human cancer

patients using image-derived blood surrogate tissue reference regions. *J. Nucl. Med.* (2015). doi:10.2967/jnumed.115.158717

25. Patlak, C. S., Blasberg, R. G. & Fenstermacher, J. D. Graphical evaluation of blood-to-brain transfer constants from multiple-time uptake data. *J. Cereb. Blood Flow Metab.* (1983). doi:10.1038/jcbfm.1983.1
26. Belton, M. *et al.* Hypoxia and tissue destruction in pulmonary TB. *Thorax* (2016). doi:10.1136/thoraxjnl-2015-207402
27. Koh, W. J. *et al.* Imaging of hypoxia in human tumors with [F-18]fluoromisonidazole. *Int. J. Radiat. Oncol. Biol. Phys.* (1992). doi:10.1016/0360-3016(92)91001-4
28. Rasey, J. S. *et al.* Quantifying regional hypoxia in human tumors with positron emission tomography of [18F]fluoromisonidazole: A pretherapy study of 37 patients. *Int. J. Radiat. Oncol. Biol. Phys.* (1996). doi:10.1016/S0360-3016(96)00325-2
29. Bruehlmeier, M., Roelcke, U., Schubiger, P. A. & Ametamey, S. M. Assessment of hypoxia and perfusion in human brain tumors using PET with 18F-fluoromisonidazole and 15O-H2O. *J. Nucl. Med.* (2004).
30. Bedair, R. *et al.* Effect of radiofrequency transmit field correction on quantitative dynamic contrastenhanced Mr imaging of the breast at 3.0 T1. *Radiology* (2016). doi:10.1148/radiol.2015150920
31. Banelli, B. *et al.* Pathological and molecular characteristics distinguishing contralateral metastatic from new primary breast cancer. *Ann. Oncol.* (2009). doi:10.1093/annonc/mdp470
32. Tofts, P. S. *et al.* Estimating kinetic parameters from dynamic contrast-enhanced T1-weighted MRI of a diffusable tracer: Standardized quantities and symbols. *Journal of Magnetic Resonance Imaging* (1999). doi:10.1002/(SICI)1522-2586(199909)10:3<223::AID-JMRI2>3.0.CO;2-S
33. Baltzer, P. *et al.* Diffusion-weighted imaging of the breast—a consensus and mission statement from the EUSOBI International Breast Diffusion-Weighted Imaging working group. *Eur. Radiol.* (2020). doi:10.1007/s00330-019-06510-3
34. Liney, G. P., Gibbs, P., Hayes, C., Leach, M. O. & Turnbull, L. W. Dynamic contrast-enhanced MRI in the differentiation of breast tumors: User-defined versus semi-automated region-of-interest analysis. *J. Magn. Reson. Imaging* (1999). doi:10.1002/(SICI)1522-2586(199912)10:6<945::AID-JMRI6>3.0.CO;2-I
35. Kuhl, C. K. Current status of breast MR imaging: Part 2. Clinical applications. *Radiology* (2007). doi:10.1148/radiol.2443051661

36. Avendano, D. *et al.* Limited role of DWI with apparent diffusion coefficient mapping in breast lesions presenting as non-mass enhancement on dynamic contrast-enhanced MRI. *Breast Cancer Res.* (2019). doi:10.1186/s13058-019-1208-y
37. Sourbron, S. P. & Buckley, D. L. On the scope and interpretation of the Tofts models for DCE-MRI. *Magn. Reson. Med.* (2011). doi:10.1002/mrm.22861
38. Fritz-Hansen, T. *et al.* Measurement of the arterial concentration of Gd-DTPA using MRI: A step toward quantitative perfusion imaging. *Magn. Reson. Med.* (1996). doi:10.1002/mrm.1910360209
39. Walker-Samuel, S., Leach, M. O. & Collins, D. J. Evaluation of response to treatment using DCE-MRI: The relationship between initial area under the gadolinium curve (IAUGC) and quantitative pharmacokinetic analysis. *Phys. Med. Biol.* (2006). doi:10.1088/0031-9155/51/14/021
40. Hoon Tan, P. *et al.* The 2019 WHO classification of tumours of the breast. *Histopathology* (2020). doi:10.1111/his.14091
41. Donaldson, S. B. *et al.* Perfusion estimated with rapid dynamic contrast-enhanced magnetic resonance imaging correlates inversely with vascular endothelial growth factor expression and pimonidazole staining in head-and-neck cancer: A pilot study. *Int. J. Radiat. Oncol. Biol. Phys.* (2011). doi:10.1016/j.ijrobp.2010.09.039
42. Vaupel, P., Kallinowski, F. & Okunieff, P. Blood Flow, Oxygen and Nutrient Supply, and Metabolic Microenvironment of Human Tumors: A Review. *Cancer Res.* (1989).
43. Cooper, R. A. *et al.* Tumour oxygenation levels correlate with dynamic contrast-enhanced magnetic resonance imaging parameters in carcinoma of the cervix. *Radiother. Oncol.* (2000). doi:10.1016/S0167-8140(00)00259-0
44. Grkovski, M. *et al.* Multiparametric imaging of tumor hypoxia and perfusion with 18F-fluoromisonidazole dynamic PET in head and neck cancer. *J. Nucl. Med.* (2017). doi:10.2967/jnumed.116.188649
45. Dewhirst, M. W., Navia, I. C., Brizel, D. M., Willett, C. & Secomb, T. W. Multiple etiologies of tumor hypoxia require multifaceted solutions. *Clinical Cancer Research* (2007). doi:10.1158/1078-0432.CCR-06-2629
46. Beaney, R. P., Jones, T., Lammertsma, A. A., Mckenzie, C. G. & Halnan, K. E. POSITRON EMISSION TOMOGRAPHY FOR IN-VIVO MEASUREMENT OF REGIONAL BLOOD FLOW, OXYGEN UTILISATION, AND BLOOD VOLUME IN PATIENTS WITH BREAST CARCINOMA. *Lancet* (1984). doi:10.1016/S0140-6736(84)90063-1

47. Li, S. P. *et al.* Vascular characterisation of triple negative breast carcinomas using dynamic MRI. *Eur. Radiol.* (2011). doi:10.1007/s00330-011-2061-2
48. Dickie, B. R. *et al.* The prognostic value of dynamic contrast-enhanced MRI contrast agent transfer constant Ktrans in cervical cancer is explained by plasma flow rather than vessel permeability. *Br. J. Cancer* (2017). doi:10.1038/bjc.2017.121
49. Nunn, A., Linder, K. & Strauss, H. W. Nitroimidazoles and imaging hypoxia. *European Journal of Nuclear Medicine* (1995). doi:10.1007/BF01081524
50. Vaupel, P., Schlenger, K., Knoop, C. & Hockel, M. Oxygenation of human tumors: Evaluation of tissue oxygen distribution in breast cancers by computerized O2 tension measurements. *Cancer Res.* **51**, 3316–3322 (1991).
51. Dadiani, M., Margalit, R., Sela, N. & Degani, H. High-Resolution Magnetic Resonance Imaging of Disparities in the Transcapillary Transfer Rates in Orthotopically Inoculated Invasive Breast Tumors. *Cancer Res.* (2004). doi:10.1158/0008-5472.CAN-03-2665
52. Surov, A., Meyer, H. J. & Wienke, A. Correlation between apparent diffusion coefficient (ADC) and cellularity is different in several tumors: A meta-analysis. *Oncotarget* (2017). doi:10.18632/oncotarget.17752
53. Jeh, S. K. *et al.* Correlation of the apparent diffusion coefficient value and dynamic magnetic resonance imaging findings with prognostic factors in invasive ductal carcinoma. *J. Magn. Reson. Imaging* (2011). doi:10.1002/jmri.22400
54. Martincich, L. *et al.* Correlations between diffusion-weighted imaging and breast cancer biomarkers. *Eur. Radiol.* (2012). doi:10.1007/s00330-012-2403-8
55. Bihan, D. Le. Molecular diffusion, tissue microdynamics and microstructure. *NMR Biomed.* (1995). doi:10.1002/nbm.1940080711
56. Bihan, D. Le. Apparent diffusion coefficient and beyond : What diffusion mr imaging can tell us about tissue structure. *Radiology* (2013). doi:10.1148/radiol.13130420
57. Chu, J. P. *et al.* Pilot study on evaluation of any correlation between MR perfusion (K trans) and diffusion (apparent diffusion coefficient) parameters in brain tumors at 3 tesla. *Cancer Imaging* (2012). doi:10.1102/1470-7330.2012.0001
58. Arlinghaus, L. R. *et al.* On the relationship between the apparent diffusion coefficient and extravascular extracellular volume fraction in human breast cancer. *Magn. Reson. Imaging* (2011). doi:10.1016/j.mri.2011.02.004
59. Yankeelov, T. E. *et al.* Integration of quantitative DCE-MRI and ADC mapping to monitor treatment response in human breast cancer: initial results. *Magn. Reson. Imaging* (2007). doi:10.1016/j.mri.2006.09.006

60. Arponent, O. *et al.* Diffusion-weighted imaging in 3.0 Tesla breast MRI: Diagnostic performance and tumor characterization using small subregions vs. whole tumor regions of interest. *PLoS One* (2015). doi:10.1371/journal.pone.0138702
61. Kelada, O. J. *et al.* Quantification of Tumor Hypoxic Fractions Using Positron Emission Tomography with [18F]Fluoromisonidazole ([18F]FMISO) Kinetic Analysis and Invasive Oxygen Measurements. *Mol. Imaging Biol.* (2017). doi:10.1007/s11307-017-1083-9
62. Shi, K. *et al.* Quantitative Analysis of [18F]FMISO PET for Tumor Hypoxia: Correlation of Modeling Results with Immunohistochemistry. *Mol. Imaging Biol.* (2017). doi:10.1007/s11307-016-0975-4
63. Bhandari, V. *et al.* Molecular landmarks of tumor hypoxia across cancer types. *Nat. Genet.* (2019). doi:10.1038/s41588-018-0318-2
64. Lehtiö, K. *et al.* Imaging perfusion and hypoxia with PET to predict radiotherapy response in head-and-neck cancer. *Int. J. Radiat. Oncol. Biol. Phys.* (2004). doi:10.1016/j.ijrobp.2003.12.014
65. Thorwarth, D., Eschmann, S. M., Scheiderbauer, J., Paulsen, F. & Alber, M. Kinetic analysis of dynamic 18F-fluoromisonidazole PET correlates with radiation treatment outcome in head-and-neck cancer. *BMC Cancer* (2005). doi:10.1186/1471-2407-5-152
66. Harrison, H. *et al.* Contrasting hypoxic effects on breast cancer stem cell hierarchy is dependent on er-a status. *Cancer Res.* (2013). doi:10.1158/0008-5472.CAN-12-2505
67. Von Minckwitz, G. *et al.* Neoadjuvant chemotherapy and bevacizumab for HER2-negative breast cancer. *N. Engl. J. Med.* (2012). doi:10.1056/NEJMoa1111065
68. Poleszczuk, J. *et al.* Neoadjuvant radiotherapy of early-stage breast cancer and long-term disease-free survival. *Breast Cancer Res.* (2017). doi:10.1186/s13058-017-0870-1
69. Brackstone, M. *et al.* Concurrent Neoadjuvant Chemotherapy and Radiation Therapy in Locally Advanced Breast Cancer. *Int. J. Radiat. Oncol. Biol. Phys.* (2017). doi:10.1016/j.ijrobp.2017.06.005

Appendix A: Chapter 3

Appendix A-1:

Measurement of ^{18}F-FMISO radioactivity concentration in blood samples and scaling of the population-based arterial input function (AIF)

The ^{18}F-FMISO population-based AIF used in this study was generated by averaging measured arterial input functions derived from six healthy volunteers scanned at the Wolfson Brain Imaging Centre, University of Cambridge as part of a study in stroke and normalised by body weight.

For each scan the ^{18}F-FMISO population-based AIF was scaled by two venous blood samples (~2 mL each) collected following arteriovenous equilibrium [29], prior to (107 ± 6.4 min p.i) and after the end (186.9 ± 6.5 min p.i) of the PET/MR acquisition. Immediately after collection, each blood sample was aliquoted into a sample tube and centrifuged (6000 rpm; 5 min) to separate plasma, of which ~0.5 mL was apportioned for measuring radioactivity using a Triathler gamma counter (HIDEX, Turku, Finland). The radioactivity concentration (Bq/mL) in each plasma sample was subsequently calculated accounting for radioisotope decay between the time of measurement and injection. Given the low levels of metabolism and protein binding of ^{18}F-FMISO in human plasma, no correction for ^{18}F-FMISO plasma metabolites or protein binding was performed [29-31]. To determine the scale factor applied to the ^{18}F-FMISO population-based AIF for each patient, the ratio between the measured ^{18}F-FMISO radioactivity concentration in each venous plasma sample and the population-derived AIF at the time of blood sampling was calculated and averaged across the two blood samples.

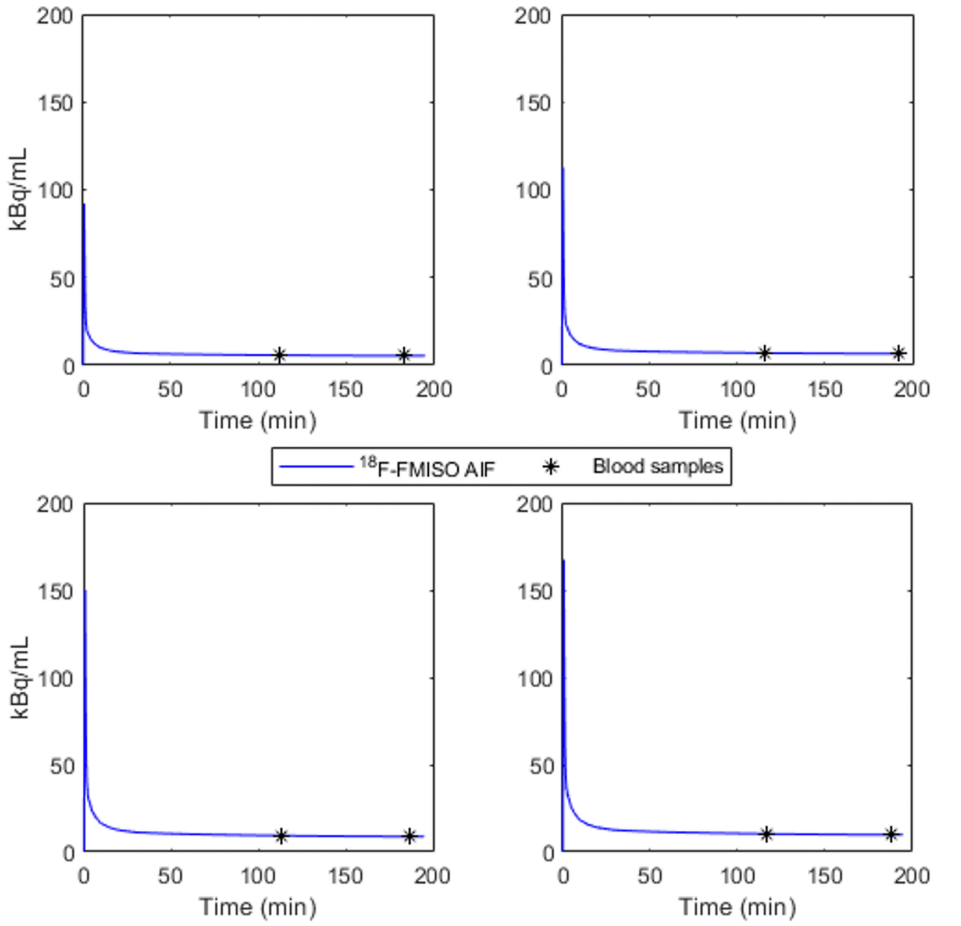

Appendix Figure A-1: ^{18}F-FMISO population-based arterial input functions (AIFs) for four representative patients, each scaled by two venous plasma samples.

Chapter 4. The relationship between tumour radiological features, whole-breast vascularity and PET/MR imaging parameters of hypoxia and vascular function

Chapter 3 examined the relationship between hypoxia and vascular function in treatment-naïve breast cancer using ^{18}FMISO-PET/MRI. At the tumour level, hypoxia as measured by ^{18}F-FMISO-PET was found to be negatively correlated with perfusion measured by DCE-MRI, supporting the hypothesis of perfusion-driven hypoxia in breast cancer.

This chapter aims to expand upon this finding by exploring associations between radiological descriptors of peri-tumoral and whole-breast vascularity, and quantitative metrics of hypoxia and perfusion derived from ^{18}F-FMISO-PET/MRI.

4.1 Background

Tumour enhancement kinetics obtained from dynamic contrast enhanced magnetic resonance imaging (DCE-MRI) have been important for breast cancer diagnosis and management[1,2]. These features of the lesion are included in the American College of Radiology Breast Imaging Reporting and Data system (BI-RADS) lexicon. This lexicon was initially developed in 1993 with the purpose of standardizing imaging reports and facilitating communication among physicians[3]. Likewise, it allows a better description of the morphological features of breast cancers (shape, margins and internal enhancement characteristics). The fifth and most recent BI-RADS edition, published in 2016, improved and expanded the lexicon for mammography, breast ultrasonography (US) and breast MRI[3]. The MR imaging lexicon of the fifth edition added for first time descriptors for the amount of fibro glandular tissue and background parenchymal enhancement. Additionally, terms used to describe mass and non-mass enhancements were consolidated in the new edition.

In addition to contrast enhancement kinetics of the cancer (quantitative vascular parameters and kinetic curve), other vascular features obtained from DCE-MRI have been extensively studied such as background parenchymal enhancement, whole breast vascularity, tumour internal enhancement and the adjacent vessel sign[4]. Blood-vessel analysis of breast cancers on contrast-enhanced magnetic resonance images (CE-MRI) dates back to 1997 when Siewert et

al[5] demonstrated the diagnostic value of the adjacent vessel sign to differentiate benign from malignant breast lesions. The adjacent vessel sign refers to the presence of one or more prominent vessels adjacent to a breast mass[6] and can be considered as an indicator of tumour vascularity. Previous reports have found a strong significant correlation between the total number of adjacent feeding vessels (AFV), tumour size and features from histopathology[7,8].

4.1.1 Local and whole breast vascularity assessment

Although most studies have focused on the vascular function and microcirculation properties of breast tumours, the vascularity of the ipsilateral breast has also been shown to increase in women with breast cancer[2,9]. Associations between breast cancer and increased vascularity of the cancer-bearing breast have been demonstrated with contrast-enhanced MRI[2,9,10], laser Doppler imaging[11], CT angiography[12] and PET[13], with studies also indicating an overall increase in the blood flow of the ipsilateral breast. Aside from the neo-angiogenesis stimulated by breast cancer, other reasons explaining this association could be the reduced flow resistance in the tumour neo-vessels as well as an increased tumour metabolism[14]. Prominent increased whole-breast vascularity has also been associated with poor prognosis.

Subtracted dynamic MR images or maximum-intensity-projection (MIP) reconstruction of subtracted dynamic MR images are often used to measure breast and cancer vascularity simultaneously. Breast vascularity is frequently assessed by visually analyzing the contrast enhancement of the breast parenchyma (background parenchymal enhancement) and grouping it into different categories according to the level of enhancement (minimal, mild, moderate or marked) and to its distribution (symmetric or asymmetric)[3]. However, Sardanelli et al[2]. proposed a different method for breast vascularity assessment which was used in this study. The method is based on counting the number of breast blood vessels, arteries and veins, with 3 cm long or longer and 2 mm or greater in maximal diameter.

Given the association between ipsilateral whole-breast vascularity and tumour blood flow and the negative association between tumour hypoxia and perfusion, it would be reasonable to hypothesise that vascular blood flow within the cancer-bearing breast may also be a surrogate marker of the perfusion and hypoxia status of tumours. This chapter evaluates the relationship between parameters of tumour hypoxia and perfusion from ^{18}FMISO-PET/MRI with

morphological features of the cancer and qualitative measures of whole breast and tumour vascularity, including the number of adjacent feeding vessels (AFV). To the best of our knowledge, DCE-MRI features of whole-breast and peritumoral vascularity, specifically, signal-intensity curve type and tumour adjacent feeding vessels have not been previously correlated to imaging parameters of tumour hypoxia.

4.2 Methods

4.2.1 Patients

The patient population for the study consisted of 29 women with 32 newly diagnosed and biopsy-confirmed primary breast cancers on PET-MRI and 31 on DCE-MRI. ADC calculations included data from 18 patients (19 lesions). The inclusion and exclusion criteria for the study, as well as further clinical information about the patient population are provided in Chapter 3, Section 3.4.1 and Table 3.1, respectively.

4.2.2 PET/MR acquisition

A detailed description of the PET/MR acquisition protocol is presented in Chapter 3, Section 3.4.2. MR sequence information is given in Chapter 3, Table 3.1.

4.2.3 Image analysis

4.2.3.1 Radiological evaluation

Three radiologists reviewed the MR images and identified lesions in each patient in consensus, using information from the post-contrast T_1-weighted and subtraction images. For each PET/MR examination, the following lesion characteristics were evaluated: location, size, morphology, and enhancement kinetics. The readers were blinded to the pathological findings at the time of image evaluation.

Lesion size: For size assessment, the longest diameter (LD) in the axial plane was taken as tumour size measurement. In cases of multifocality or multicentricity, all foci were measured, and the sum of all longest diameters was calculated[15]. In addition, total tumour ROI volume was calculated by summing tumour volumes across all slices encompassing the cancer and multiplying by the slice thickness (i.e. 1.4 mm).

Morphology and enhancement kinetics: Morphology and kinetic curve assessment used descriptors from the Fifth Edition of the ACR BI-RADS Atlas[3] and included the following:

i. Shape – oval, round, irregular
ii. Margins – circumscribed, not-circumscribed: irregular, spiculated
iii. Internal enhancement characteristics – homogeneous, heterogeneous, rim enhancement
iv. Signal intensity (S/I) curve description
    a. Initial phase – slow, medium, fast
    b. Delayed phase – persistent (Type 1), plateau (Type 2), washout (Type 3)

Breast vascularity assessment: Whole-breast vascularity was evaluated according to the method of Sardanelli *et al*[2] using axial and coronal maximum intensity projections (MIPs) from subtracted MR images. The total number of significant vessels, i.e. arteries or veins, which were ≥3 cm in length and ≥2 mm in maximal diameter, were recorded for each breast. A score ranging from 0 to 3, corresponding to low and high breast vascularity respectively, was assigned to each breast according to the following criteria:

i. Score 0 - Absence or very low vascularity: Complete absence of vessels ≥3 cm in length and ≥2 mm in maximal diameter or presence of vessels <3 cm in length and <2 mm in maximal diameter
ii. Score 1 – Low vascularity: Presence of 1 vessel ≥3 cm in length and ≥2 mm in maximal diameter
iii. Score 2 – Moderate vascularity: Presence of 2-4 vessels ≥3 cm in length and ≥2 mm in maximal diameter
iv. Score 3 – High vascularity: Presence of ≥5 vessels that were ≥3 cm in length and ≥2 mm in maximal diameter.

A vascularity score for each patient was subsequently calculated by averaging the vascularity scores for the two breasts. To facilitate statistical analysis, breast vascularity was further classified as either low (scores 0 and 1) or high (scores 2 and 3).

Asymmetries in breast vascularity were assessed by taking the difference in the number of significant vessels between the two breasts. Vascular asymmetry was considered present in cases where the difference in the number of vessels between the two breasts was ≥2. In women with unilateral disease and presence of vascular asymmetry (i.e. patients with one-sided increased vascularity), the side of vascular asymmetry (ipsilateral or contralateral) was recorded and also, the breast with the highest number of vessels (ipsilateral or contralateral).

Furthermore, the presence and number of enlarged vessels, defined as vessels ≥3 cm in length and ≥3 mm in maximal diameter, was also recorded for each breast in patients. For this analysis of whole-breast vascularity and comparisons between the ipsilateral and contralateral breast, women with bilateral cancers were excluded.

Tumour adjacent feeding vessel count: MIPs of subtraction images were used for counting adjacent feeding vessels (AFV) in tumours[16]. Either all vessels leading to the enhancing tumour mass or in contact with the edges of the lesion on the DCE-MR images were considered as AFV[17]. In cases of multifocal or multicentric breast cancers, the aggregate AFV count was calculated.

4.2.3.2 Quantitative analysis

Tumour region of interest delineation: Tumour regions were manually delineated in OsiriX, version 8.0.2 (Pixmeo SARL, Switzerland) by three radiologists in consensus as previously described (Chapter 3, Section 3.4.3). In brief, regions were drawn on the peak enhancing phase of the DCE-MRI series (phase 19) on all consecutive axial sections encompassing the enhancing mass and including multifocal/multicentric disease. Bilateral breast cancers were treated as individual lesions[18].

DCE-MRI: Pharmacokinetic analysis of DCE-MRI data was performed in MIStar, version 3.2.63 (Apollo Medical Imaging, Melbourne, Australia) using the extended Tofts' model to calculate the volume transfer constant, K^{trans}, efflux rate constant, k_{ep}, extravascular-extracellular volume fraction v_e, and plasma volume fraction, v_p. B_1^+ maps and T_1 maps were also computed as outlined in Chapter 3.4.2.2. In addition to pharmacokinetic analysis, the enhancing tumour volume (ETV) was calculated for each patient using the signal enhancement ratio method[19]. Early percent enhancement (PE_e) and signal-enhancement ratio (SER) maps for each lesion were derived from pre-contrast images (S_0), early post-contrast (S_E, phase 19 of the DCE series) and late post-contrast (S_L) images, phase 46 of the DCE series; using the following equations: $PE_e = 100\times(S_E - S_0)/S_0$ and $SER = 100\times(S_E - S_0)/(S_L - S_0)$ respectively. ETV was subsequently calculated by summing all image voxels within the tumour ROI above thresholds for PE and SER, followed by connectivity test to eliminate single voxels or exceedingly small regions. For ETV calculations, thresholds of 70% and 100% were used for PE and SER respectively[19].

DWI-MRI: Calculation of apparent diffusion coefficient (ADC) maps was performed in OsiriX, using *b*-values of 0 and 900 s/mm^2, as previously described in Chapter 3, Section 3.4.3. Aside from the whole lesion mean ADC, mean ADC from the darkest part of the tumour (dp-ADC) was measured, using a 5 mm circular region in the visually darkest area of the tumour[20,21] (Chapter 3, Section 3.4.3).

PET: Image frames from 120-180 min p.i were averaged, registered to the peak-enhancing phase of the DCE-MRI series and subsequently employed for the determination of ^{18}F-FMISO uptake as standardised uptake values normalised by body weight (SUV_{bw}), tumour-to-plasma (T_{max}/P) and tumour-to-muscle (T_{max}/M) ratios using the ROIs defined on DCE-MRI. The influx rate of ^{18}F-FMISO into the trapped (hypoxic) tissue compartment (K_i) was determined, as a more specific measure of tumour hypoxia. K_i maps were produced by using the Patlak-plot analysis, for which a population-based arterial input function was utilised. Hypoxic fractions (%HF) in tumour ROIs were calculated as the percentage of voxels with K_i values higher than 2×standard deviations (SD) of the mean K_i in the normoxic muscle.

4.2.3.3 Histology

Histopathological information including tumour type, grade, oestrogen receptors (ER), progesterone receptors (PR) and human epidermal growth factor receptor 2 (HER2) were obtained from core biopsies and/or surgical tumour specimens. Tumours were graded using the Elston-Ellis scoring system[22]. Cancers with positive ER or PR expression were classified as hormone-receptor (HR) positive. Expression of hormones and HER2 were measured by immunohistochemistry (Chapter 3. Section 3.4.4).

4.2.3.4 Statistical analysis

Statistical analysis was performed in IBM SPSS Statistics for MacOS, v25.0 (IBM Corp., Armonk, NY) or Matlab 2016b. Continuous data was assessed for normality using the Anderson-Darling test and is presented as mean ± SD or median [range] as appropriate.

Correlations between continuous variables were assessed using the Pearson (r) or Spearman (ρ) correlation coefficient, whereas Kendall's τ_b was used to measure correlations between ordinal variables. Associations between nominal variables were assessed using chi-squared (χ^2) tests and Cramer's V. t-tests were used for comparison between means of two groups, and

ANOVA when more than two groups were compared. Where data was not normally distributed, or normality could not be assessed, Mann-Whitney *U* and Mood's median or Kruskal-Wallis *H* tests were employed for comparisons between two or more groups respectively. Linear regression was utilised for assessing the relationships between continuous variables or between continuous and categorical variables, whereas associations between lesion and patient metrics were examined using mixed effects models with random intercepts for subjects. In cases where the ensuing residuals from linear regression or mixed models were not normally distributed as indicated by normality tests and Q-Q plots, dependent variables (i.e. quantitative PET and MRI parameters) were transformed using the natural logarithm to yield more normally distributed residuals. Factors affecting parameter associations were identified through separate univariate analyses and included into the models if p-values were ≤ 0.1. In all analyses, p-values <0.05 were considered statistically significant, unless otherwise indicated.

4.3 Results

Twenty-nine patients with 32 pathologically confirmed breast cancers were analysed. The majority of lesions were NST or invasive ductal carcinomas (21/32; 66%), grade 2 (16/32; 50%) and positive for hormone receptors (31/32; 97%). Clinical information about the patient population can be found in Table 4.1. Further clinical details can be found in Chapter 3, Table 3.2. Lesion histological characteristics are summarised in Table 4.2.

Table 4.1: Clinical characteristics for the patient population (n=29 patients).

Characteristic	***n* (%)**
Age at diagnosis (years)[a]	57 [37-78]
Menopausal status	
Pre-menopausal	10 (35)
Post-menopausal	19 (65)
Clinical management	
Primary surgery	21 (72)
Neo-adjuvant therapy	8 (28)
Lesion presentation	
Unilateral	27 (93)
Bilateral (synchronous)	2 (7)

[a]Data presented as median [range].

Table 4.2: Tumour characteristics (*n*=32 lesions).

Histological features	***n* (%)**
Lesions (*n*)	32
Histological sub-type	
Ductal (IDC)	21 (66)
Lobular (ILC)	6 (19)
Mixed[a]	3 (9)
Mucinous (IMC)	2 (6)
Histological Grade	
1	3 (9)
2	16 (50)
3	13 (41)
Molecular subtype	
HR+/HER2-	24 (75)
HR+/HER2+	7 (22)
HR-/HER2-	1 (3)
Lesion laterality[b]	
Right breast	16 (50)
Left breast	16 (50)

[a]Invasive carcinomas for which histology indicated the presence of both lobular and ductal components.
HR: hormone receptor; HER2: Human epidermal growth factor receptor 2.

A summary of the morphological and enhancement characteristics of the cancers in this sample is given in Table 4.3. The median lesion diameter on MRI was 24 [10 – 117] mm, with 22/32 (69%) cancers measuring >2 cm in the longest diameter, while the median tumour volume was 2.44 [0.29 – 27.74] cm^3. Thirty-one breast cancers (31/32; 97%) depicted irregular shape, whereas one cancer showed an oval shape (1/32; 3%). All 32 lesions had non-circumscribed margins, with 17/32 cancers (53%) presenting with irregular margins and 15/32 (47%) with spiculated margins.

All masses showed rim enhancement. Initial phase enhancement was classified as fast for all lesions, with 29/31 (93%) cancers showing either plateau (type 2) or washout (type 3) curves. Two breast tumours (2/31; 7%) displayed persistent enhancement (type 1), although they were malignant lesions. The median ETV was 2.29 [0.29 – 22.02] cm^3.

Table 4.3: Tumour morphological and enhancement characteristics (*n*=32 lesions).

Characteristic	***n* (%)**
Longest diameter (LD) on MRI (mm)[a]	24 [10 - 117]
≤20 mm	10 (31)
>20 mm	22 (69)
Adjacent feeding vessels (AFV)[a]	10.5 [1 – 58]
Volume (cm^3)[a]	2.44 [0.29 – 27.74]
Enhancing tumour volume (ETV; cm^3)[a]	2.29 [0.29 – 22.02]
Shape	
Oval	1 (3)
Irregular	31 (97)
Margins	
Non-circumscribed	32 (100)
Irregular	17 (53)
Spiculated	15 (47)
Internal enhancement characteristics[b]	
Rim enhancement	31 (100)
Signal intensity (S/I) curve description[b]	
Initial phase	
Fast	31 (100)
Delayed phase	
Persistent (Type 1)	2 (7)
Plateau (Type 2)	14 (45)
Washout (Type 3)	15 (48)

[a]Data presented as median [range].
[b]Internal enhancement characteristics and signal intensity curve descriptors were evaluated in *n*=31 cancers.

Table 4.4: Breast vascularity assessment for the patient population (*n*=29 patients).

Characteristic	*n* (%)
Breast vascularity	
Absent (score 0)	4 (14)
Low (score 1)	3 (10)
Moderate (score 2)	20 (69)
High (score 3)	2 (7)
Significant breast vessels (number)[a]	4 ± 3
Vascular asymmetry	
Absence	18 (62)
Presence	11 (38)
Vascular asymmetry side [*n*=27 patients][b]	
One-sided increased vascularity	9 (33)
Contralateral	2 (7)
Ipsilateral	7 (26)
No vascular asymmetry	18 (67)
Enlarged vessels [*n*=29 patients]	
Absence	14 (48)
Presence	15 (52)
Number[c]	0 [0 – 3]

[a]Data presented as mean ± standard deviation (SD).
[b]Data given for patients with unilateral disease (*n*=27), patients with bilateral disease (*n*=2) were excluded.
[c]Data presented as median [range].

4.3.1 Local and whole-breast vascularity assessment

The median number of tumour AFV was 11 [1 – 58] vessels (Table 4.3) in all patients, whereas the mean number of significant blood vessels in the breasts, vessels ≥ 3 cm in length and ≥ 2 mm in maximal diameter, was 4 ± 3 vessels (Table 4.4). Breast vascularity was characterised as moderate (score 2) or high (score 3) for 22/29 (76%) patients, with 11/29 (38%) women also exhibiting vascular asymmetry between the two breasts (Table 4.5). The median number of significant breast vessels in women with vascular asymmetry was 6 [3 – 9] vessels. Presence of enlarged vessels was noted in 52% (15/29) of all patients.

Among women with unilateral disease (*n*=27), vascular asymmetry was observed in 9/27 (33%) patients (Table 4.4). In general, there was a tendency for a higher number of significant

breast vessels (and subsequently a higher vascular score) in the ipsilateral rather than the contralateral breast (Table 4.5); however, differences in the number of significant breast vessels between the two breasts did not reach statistical significance (ipsilateral *vs* contralateral: 2 [0 – 7] *vs* 2 [0 – 5] vessels, p=0.08). The correlation between the number of significant breast vessels in the ipsilateral and contralateral breast was positive (ρ=0.5, p=0.01), like it was the correlation between ipsilateral and contralateral breast vascularity scores (τ_b=0.6, p<0.001).

Table 4.5: Individual breast vascularity assessment for patients with unilateral tumours (n=27 patients).

Characteristic	***n* (%)**
Ipsilateral breast	
Breast vascularity	
Absent (score 0)	4 (15)
Low (score 1)	4 (15)
Moderate (score 2)	17 (63)
High (score 3)	2 (7)
Significant breast vessels[a]	2 [0 – 7]
Enlarged breast vessels[a]	1 [1 – 3]
Contralateral breast	
Breast vascularity	
Absent (score 0)	6 (22)
Low (score 1)	7 (26)
Moderate (score 2)	13 (48)
High (score 3)	1 (4)
Significant breast vessels[a]	2 [0 - 5]
Enlarged breast vessels[a]	1 [1 - 3]

[a]Data presented as median [range].

Table 4.6: Ipsilateral *vs* contralateral breast vascularity scores for women with unilateral disease (n=27). Two patients with bilateral cancers were excluded from ipsilateral *vs* contralateral breast comparisons. Vascularity scores of 0 and 1 were classified as low vascularity, whereas vascularity scores of 2 and 3 were classified as high vascularity.

	Contralateral breast vascularity	
Ipsilateral breast vascularity	Low (n = 13)	High (n = 14)
Low (n = 8)	7	1
High (n = 19)	6	13

Notably, in approximately three-quarters of the patients (20/27; 74%), there was correspondence in the vascularity score between the two breasts (Table 4.6). Patient vascularity scores were significantly associated with the presence (Cramer's V=0.42, p=0.04) and number of enlarged breast vessels (τ_b=0.45, p=0.01). Analogous relationships were observed between the presence of vascular asymmetry and the presence (Cramer's V=0.33, p=0.13) or number of enlarged vessels (presence *vs* absence of vascular asymmetry: 0 [0 – 2] *vs* 1 [0 – 3] vessels, p=0.07), but these relationships did not achieve statistical significance. Additionally, there was no significant difference in the number of enlarged vessels between the ipsilateral and contralateral breast in patients with unilateral disease (ipsilateral *vs* contralateral: 1 [1 – 2] *vs* 1 [1 – 3] vessels, p=0.23).

The number of AFV in tumours did not significantly correlate with the number of breast significant vessels in either the ipsilateral (ρ=0.20, p=0.28) or contralateral breast[1] (ρ=-0.30, p=0.12). Similarly, weak associations were observed between whole-breast or patient vascularity scores and AFV (ipsilateral breast: τ_b=0.13, p=0.36; contralateral breast[1]: τ_b=-0.14, p=0.38; patient: τ_b=0.15, p=0.33). Additionally, no correlations were observed between AFV and the number of enlarged breast vessels (ρ=0.06, p=0.77). Patients with vascular asymmetry had a higher number of AFV than patients with no asymmetry (presence *vs* absence: 18 [4 – 32] *vs* 9 [1 - 58] vessels, p=0.045), while the presence or absence of enlarged breast vessels did not yield any statistically significant difference in the number of AFV (presence *vs* absence: 12 [1 – 37] vs 15 [4 - 58] vessels, p=0.65).

4.3.2 Correlations between clinical data and morphological DCE-MRI descriptors

There was no statistically significant correlation between patient age and tumour size, measured as the longest lesion diameter on MRI (ρ=-0.28, p=0.14). In contrast, the correlation between tumour volume and patient age was close to statistical significance (ρ=-0.37, p=0.05). No association was observed between tumour size metrics (LD and volume) with patient body mass index (LD: ρ=0.08, p=0.67; volume: ρ=0.08, p=0.67)[2], menopausal status (pre-

[1] Correlations between the number of AFV and significant breast vessels or breast vascularity scores in the contralateral breast excluded two patients with bilateral tumours.

[2]The Spearman correlation coefficients between BMI and tumour longest diameter or volume were 0.079 (p=0.669) and 0.078 (p=0.671) respectively. Both correlation coefficients and the respective p values were rounded to the second decimal point.

menopausal *vs* post-menopausal – LD: 20.5 [9.8 – 117] *vs* 24 [10 – 60] mm, p=0.71; volume: 2.12 [0.5 – 27.7] *vs* 2.4 [0.3 – 21.2] cm^3, p=0.74) or lesion laterality (right *vs* left breast – LD: 29.5 [10 – 117] *vs* 20 [9.8 – 71] mm, p=0.13; volume: 2.5 [0.5 – 27.8] *vs* 2.3 [0.4 – 22.3] cm^3, p=0.78). Additionally, the type of margins (irregular *vs* spiculated) was not associated with any of these clinical parameters (age: 56 ± 11 *vs* 61 ±13 years, p=0.28; BMI: 27.3 ± 4.9 *vs* 28.8 ± 5.8 kg/cm^2, p=0.28; lesion laterality: Cramer's V = 0.19, p=0.29).
In a similar manner, delayed phase patterns of the time-signal intensity tumour curve were not significantly associated with menopausal status (Cramer's V = 0.36, p=0.14) or lesion laterality (Cramer's V = 0.1, p=0.85). No statistically significant difference was found in the age (Type 1 *vs* Type 2 *vs* Type 3: 66 [66 – 66] *vs* 63 [37 – 78] *vs* 50 [37 – 75] years old, p=0.19) or BMI (Type 1 *vs* Type 2 *vs* Type 3: 27.5 [26.0 – 29] *vs* 29 [24 – 39] *vs* 24.5 [20 – 36] kg/cm^2, p=0.30) of patients with lesions presenting type 1, 2 or 3 kinetic curves. Tumour enhancing volumes showed similar correlations with clinical variables as other tumour size metrics, displaying a negative correlation with patient age that was close to statistical significance (ρ=-0.31, p=0.09); no association with patient BMI (ρ=0.04, p=0.83) and no difference between pre and post-menopausal women (1.3 [0.32 – 22.0] *vs* 2.4 [0.29 – 13.0] cm^3, p=0.98) .

With respect to local tumour vascularity, there was no significant correlation between the total number of tumour AFV and patient age (ρ=-0.04, p=0.83) or BMI (ρ=0.15, p=0.45). Likewise, no statistically significant difference in AFVs was observed between pre or post-menopausal women (pre-menopausal *vs* post-menopausal: 11 [2 – 58] vs 10 [1 - 31], p=0.84), and right or left-sided lesions (right *vs* left breast: 10 [4 – 32] *vs* 12 [1 – 58], p=0.91). In terms of whole breast vascularity, no significant association was found between breast vascularity scores and age (τ_b=0.09, p=0.55), BMI (τ_b =0.21, p=0.17), menopausal status (χ^2=1.48, p=0.69) or lesion laterality (χ^2=6.53, p=0.09). Furthermore, the presence of vascular asymmetry was not related to any of the aforementioned clinical characteristics (presence *vs* absence – age: 57 ± 13 *vs* 57 ± 11 years, p=1.0; BMI: 28.5 ± 6.8 vs 27.2 ± 4.2 years, p=0.79; menopausal status: Cramer's V = 0.18, p=0.33).

4.3.3 Relationships between tumour morphological and enhancement descriptors

Tumours with irregular margins were larger than those with spiculated boundaries, suggesting a potential interaction effect between margin type and tumour size (measured as either the longest diameter on MRI or volume) in this sample of cancers (Table 4.7.A). Similarly, there

was a statistically significant difference in ETV between cancers with irregular and spiculated margins (Table 4.7.B). Although relationships between tumour size and delayed-phase kinetic curve patterns were not statistically significant (LD: τ_b=0.27, p=0.07; volume: τ_b=0.20, p=0.18; ETV: τ_b=0.23, p=0.13), breast cancers with type 3 kinetic curves tended to be larger than those displaying type 1 or type 2 curves (Table 4.8.A).

Table 4.7: Size (A), enhancement (B) and vascularity (C) parameters according to the type of tumour margins (n=32 lesions). Data are presented as median [range]. Lesions included for DCE-MRI analysis (n=31).

		Margins		
	Parameter	**Irregular**	**Spiculated**	***p***
A. Size	Lesions (n=32)	17	15	
	LD	33.5 [14 – 117]	20 [9.8 – 38]	0.01*[a]
	Volume	5.6 [0.5 – 27.7]	1.7 [0.3 – 7.5]	0.02*[a]
B. Enhancement	Lesions (n=31)	16	15	
	ETV	3.4 [0.3 – 22.0]	1.7 [0.3 – 5.8]	0.03*[a]
	Kinetic curve type	3 [1 – 3]	2 [1 – 3]	0.02*[b]
C. Vascularity	Lesions (n=31)	16	15	
	AFV	15 [4 – 58]	10 [1 – 31]	0.38[a]

[a]Mann-Whitney U test
[b]Chi-squared (χ^2) test
*p<0.05; **p<0.01
LD: tumour longest diameter (LD, mm); volume: tumour volume (cm^3); ETV: enhancing tumour volume (cm^3); AFV: adjacent feeding vessels (count).

The association between kinetic curve delayed phase enhancement patterns and margin types was also statistically significant in this data set (χ^2=7.81, p=0.02), with 11/16 (69%) lesions with irregular margins displaying type 3 enhancement and 11/15 (73%) cancers with spiculated margins showing a type 2 curve pattern (Table 4.7.C).

4.3.4 Local and whole-breast vascularity *vs* tumour morphology and delayed phase enhancement patterns

There was a significant positive correlation between the number of AFV and tumour longest diameter (ρ=0.48, p=0.01), volume (ρ=0.37, p=0.04), or ETV (ρ=0.46, p=0.01), indicating a tendency for larger tumours or tumours with a larger enhancing component to display a higher number of feeding vessels. There was no statistically significant difference in the median number of AFV between cancers with irregular and spiculated margins (Table 4.7.C) or lesions displaying different delayed-phase enhancement patterns (Table 4.8.C).

Table 4.8: Size (A), enhancement (B) and vascularity (C) parameters with respect to delayed-phase enhancement patterns. Data are presented as mean [95% confidence interval]. Lesions included for DCE-MRI analysis (n=31).

		Delayed-phase enhancement			
	Parameter	Persistent (Type 1)	Plateau (Type 2)	Washout (Type 3)	***p***
A. Size	Lesions (n=31)	2	14	15	
	LD	18 [8 – 43]	21 [16 – 29]	32 [23 – 44]	0.15[a]
	Volume	1.97 [0.33 – 11.7]	2.00 [1.04 – 3.83]	4.02 [0.72 – 7.89]	0.30[a]
B. Enhancement	Lesions (n=31)	2	14	15	
	ETV	1.0 [0.18 – 5.54]	1.7 [0.91 – 3.17]	3.09 [1.62 – 5.89]	0.27[a]
C. Vascularity	Lesions (n=31)	2	14	15	
	AFV	11 [3 – 40]	10 [6 – 16]	10 [6 – 16]	0.98[a]

[a] p values were estimated using by linear regression of each parameter for the effect of delayed-phase enhancement type. Due to no non-normality of residuals, dependent variables were transformed using the natural logarithm before being inserted into the model. The table presents untransformed mean estimates and 95% confidence intervals of DCE-MRI parameters.
LD: tumour longest diameter (LD, mm); volume: tumour volume (cm^3); ETV: enhancing tumour volume (cm^3); AFV: adjacent feeding vessels (count).

Table 4.9: Fixed effects estimates (β), 95% confidence intervals [CI] and *p* values for the association of log-transformed values of the tumour longest diameter (LD; mm), volume (cm^3) and enhancing tumour volume (ETV; cm^3) with vascularity scores for the ipsilateral breast, contralateral breast and patient overall breast vascularity score.

	Vascularity score		
	Ipsilateral breast	Contralateral breast[a]	Overall
Parameter		β,[CI],*p*	
ln(LD)	0.15,[-0.02 – 0.32],0.13	0.11,[-0.18 – 0.40],0.13	0.18,[-0.11 – 0.46],0.24
ln(Volume)	0.39,[-0.05 – 0.82],0.11	0.08,[-0.49 – 0.65],0.79	0.25,[-0.33 – 0.83],0.41
ln(ETV)	0.47,[0.18 – 0.77],0.05	-0.04,[-0.62 – 0.54],0.90	0.19,[-0.39 – 0.76],0.53

[a]Associations between vascularity scores for the contralateral breast and DCE-MRI parameters were computed for patients with unilateral cancers (*n*=27). Two patients with bilateral lesions were excluded from these associations.

Table 4.10: Fixed effects estimates (β), 95% confidence intervals [CI] and *p* values for the association of log-transformed values of the tumour longest diameter (LD; mm), volume (cm^3) and enhancing tumour volume (ETV; cm^3) with the number of significant breast vessels for the ipsilateral and contralateral breast.

	Significant vessels	
	Ipsilateral breast	Contralateral breast[a]
Parameter	β,[CI], *p*	
ln(LD)	0.07,[-0.02 – 0.16],0.17	0.03,[-0.15 – 0.21],0.74
ln(Volume)	0.16,[-0.07 – 0.38],0.19	-0.01,[-0.37 – 0.34],0.94
ln(ETV)	0.23,[0.09 – 0.38],0.06	-0.09,[-0.45 – 0.27],0.63

[a]Associations between the number of significant vessels in the contralateral breast and DCE-MRI parameters were computed for patients with unilateral cancers (*n*=27). Two patients with bilateral lesions were excluded from these associations.

Table 4.11: Fixed effects estimates (β), 95% confidence intervals [CI] and *p* values for the association of log-transformed values of the tumour longest diameter (LD; mm), volume (cm^3) and enhancing tumour volume (ETV; cm^3) with the presence of vascular asymmetry, and the presence or number of enlarged vessels.

	Vascular asymmetry	**Enlarged vessels**	
	Presence	Presence	Number
Parameter	β,[CI], *p*	β,[CI], *p*	
ln(LD)	-0.02,[-0.02 – 0.32],0.13	0.54,[0.12 – 0.56],0.02*	0.27,[0.01 – 0.54],0.05
ln(Volume)	0.07,[-0.88 – 1.00],0.88	1.11,[0.29 – 0.94],0.01*	0.55,[0.02 – 1.07],0.05
ln(ETV)	0.16,[-0.79 – 1.11],0.74	0.91,[0.04 – 1.78],0.05	0.43,[-0.11 – 0.97],0.13

[a]Associations between vascular asymmetry and DCE-MRI parameters were computed for patients with unilateral cancers (*n*=27). Two patients with bilateral lesions were excluded from these associations.
$^{*}p<0.05$; $^{**}p<0.01$

The fixed-effect estimates together with confidence intervals and *p*-values for the association between whole-breast or patient vascularity scores with tumour LD, volume and ETV are presented in Tables 4.9 – 4.11. Vascularity scores, the number of significant vessels in each breast and presence of vascular asymmetry were positively associated with tumour LD or volume, but these associations were not significant (Tables 4.9 – 4.11 respectively). In contrast, the presence or number of enlarged vessels was significantly associated with larger cancers (Table 4.11). Furthermore, ETV displayed positive associations with the vascularity score and number of significant breast vessels for the ipsilateral breast (Tables 4.9 and 4.10 respectively). There was also a positive association between ETV and the number or presence of enlarged vessels (Table 4.11) which was close to statistical significance.

Table 4.12: Mean [95% confidence interval (CI)] for the association of tumour histology with the tumour longest diameter (LD; mm), volume (cm^3), enhancing tumour volume (ETV; cm^3) and number of adjacent feeding vessels (AFV). Lesions included for DCE-MRI analysis (*n*=31).

		Histology				
	Parameter	**IDC**	**ILC**	**Mixed**	**IMC**	***p***
A. Size	Lesions (*n*=32)	21	6	3	2	
	LD	23 [18 – 31]	35 [21 – 58]	26 [13 – 54]	20 [8 – 48]	0.53[a]
	Volume	2.19 [1.30 – 3.67]	6.73 [2.56 – 17.71]	3.94 [1.00 – 15.46]	0.87 [0.16 – 4.66]	0.11[a]
B. Enhancement	Lesions (*n*=31)	20	6	3	2	
	ETV	1.83 [1.07 – 3.14]	4.65 [1.75 – 12.39]	2.44 [0.61 – 9.75]	0.87 [0.16 – 4.73]	0.26[a]
C. Vascularity	Lesions (*n*=31)	20	6	3	2	
	AFV	10 [7 – 15]	15 [7 – 30]	6 [2 – 16]	5 [2 – 18]	0.33[b]

[a]*p* values were estimated using by linear regression of each parameter for the effect of tumour histological subtype. Due to no non-normality of residuals, dependent variables were transformed using the natural logarithm before linear regression analysis. IDC: invasive ductal carcinoma; ILC: invasive lobular carcinoma; IMC: invasive mucinous carcinoma; Mixed: invasive carcinomas for which histology indicated the presence of both ductal and lobular components.

4.3.5 The influence of tumour histology and grade on descriptors of tumour morphology, enhancement and vascularity

Tables 4.12, 4.13 and 4.14 present tumour morphology, enhancement, and vascularity parameters with respect to histological subtype, molecular subtype and nuclear grade, respectively. Regarding tumour size and ETV, no statistically significant differences were observed in tumours of different histology, molecular subtype or nuclear grade (Tables 4.12 – 4.14, respectively). Though size and ETV comparisons between HR+/HER2- and HR+/HER2+ lesions were not statistically significant[3], HR+/HER2- lesions were on average larger in size than HR+/HER2+ cancers, while also displaying a larger enhancing volume (Table 4.13). It should be noted however, HR+/HER2- cancers constituted the majority in this sample of tumours.

Table 4.13: Median [range] for the tumour longest diameter (LD; mm), volume (cm^3), enhancing tumour volume (ETV; cm^3) and number of adjacent feeding vessels (AFV) according to molecular subtype. Lesions included for DCE-MRI analysis (*n*=31).

		Molecular subtype			
	Parameter	HR+/HER2-	HR+/HER2+	HR-/HER2-	***p***
A. Size	Lesions (*n*=32)	24	7	1	
	LD	26 [10 – 117]	19 [10 – 34]	31 [–]	0.06[a,b]
	Volume	3.69 [0.39 – 27.74]	1.71 [0.29 – 2.46]	3.55 [–]	0.07[a,b]
B. Enhancement	Lesions (*n*=31)	24	6	1	
	ETV	3.13 [0.32 – 22.02]	1.50 [0.29 – 2.36]	2.29 [–]	0.07[a,b]
C. Vascularity	Lesions (*n*=31)	24	6	1	
	AFV	12 [1 – 58]	11 [4 – 18]	5 [–]	0.57[a,b]

[a]The single HR-/HER2- cancer was excluded from statistical comparisons.
[b]Mann-Whitney *U* test. HR: hormone receptor; HER2: human epidermal growth factor 2.

[3] The single triple-negative cancer in this dataset was excluded from statistical comparisons but is reported in Table 4.13 for completeness.

Overall, an increase in tumour size metrics, ETV and number of AFV could be observed with higher tumour grade (Table 4.14). Grade 3 cancers exhibited a larger size and ETV, and consequently a larger number of feeding vessels, than lower grade lesions. However, correlations between nuclear grade and tumour size or ETV did not reach statistical significance (LD: τ_b=0.19, p=0.20; volume: τ_b=0.24, p=0.10; ETV: τ_b=0.20, p=0.17; Table 4.15). Additionally, no significant association was observed between kinetic-curve types and tumour histology (χ^2=6.30, p=0.39), molecular subtype (χ^2=1.66, p=0.79) or grade (τ_b=0.26, p=0.13).

Associations between tumour prognostic factors and breast vascularity characteristics are given in Table 4.15 and Figure 4.1. Whole-breast and patient vascularity scores or the number of significant breast vessels in the cancer-bearing or contralateral breast were not associated with tumour histology, molecular subtype or grade (Table 4.15; Figure 4.1 (a), (c) and (e) respectively). Similarly, no differences were observed in the number of AFV between cancers of different histology (Table 4.12), molecular subtype (Table 4.13) or grade (Table 4.14).

Table 4.14: Mean [95% confidence interval] for the association of tumour grade with the tumour longest diameter (LD; mm), volume (cm^3), enhancing tumour volume (ETV; cm^3) and number of adjacent feeding vessels (AFV). Lesions included for DCE-MRI analysis (n=31).

		Grade			
	Parameter	1	2	3	***p***
A. Size	Lesions (n=32)	3	16	13	
	LD	22 [11 – 45]	23 [17 – 31]	29 [21 – 41]	0.54[a]
	Volume	1.77 [0.42 – 7.44]	2.12 [1.14 – 3.95]	3.99 [2.00 – 7.96]	0.32[a]
B. Enhancement	Lesions (n=31)	3	15	13	
	ETV	1.36 [0.33 – 5.57]	1.72 [0.92 – 3.23]	3.09 [1.57 – 6.07]	0.35[a]
C. Vascularity	Lesions (n=31)	3	15	13	
	AFV	8 [3 – 22]	10 [6 – 15]	11 [7 – 18]	0.84[a]

[a]p values were estimated using by linear regression of each parameter for the effect of tumour histological subtype. Due to no non-normality of residuals, dependent variables were transformed using the natural logarithm before linear regression analysis. $^{*}p<0.05$; $^{**}p<0.01$

Table 4.15: Associations and respective *p* values between whole breast and patient vascularity scores or number of significant breast vessels and tumour histology, molecular subtype, or grade. Parameter associations or correlations were assessed using chi-squared (χ^2) tests, linear regression analysis for the effect of tumour histology or molecular subtype, or Kendall's τ_b.

Parameter	Histology	Molecular subtype	Grade
Vascularity Score	χ^2, *p*	χ^2, *p*	τ_b, [CI], *p*
Ipsilateral breast	5.26, 0.81	3.64, 0.73	-0.06, [-0.43 – 0.27], 0.81
Contralateral breast	8.01, 0.53	6.59, 0.36	-0.14, [-0.52 – 0.20], 0.43
Overall score	6.13, 0.73	4.70, 0.58	-0.04, [-0.42 – 0.28], 0.55
Significant breast vessels	R^2, *p*	R^2, *p*	τ_b, [CI], *p*
Ipsilateral breast	0.02, 0.89	0.05, 0.45	-0.04, [-0.37 – 0.32], 0.81
Contralateral breast	0.13, 0.32	0.04, 0.62	-0.12, [-0.55 – 0.17], 0.43
Total	0.06, 0.65	0.03, 0.60	-0.09, [-0.45 – 0.26], 0.55

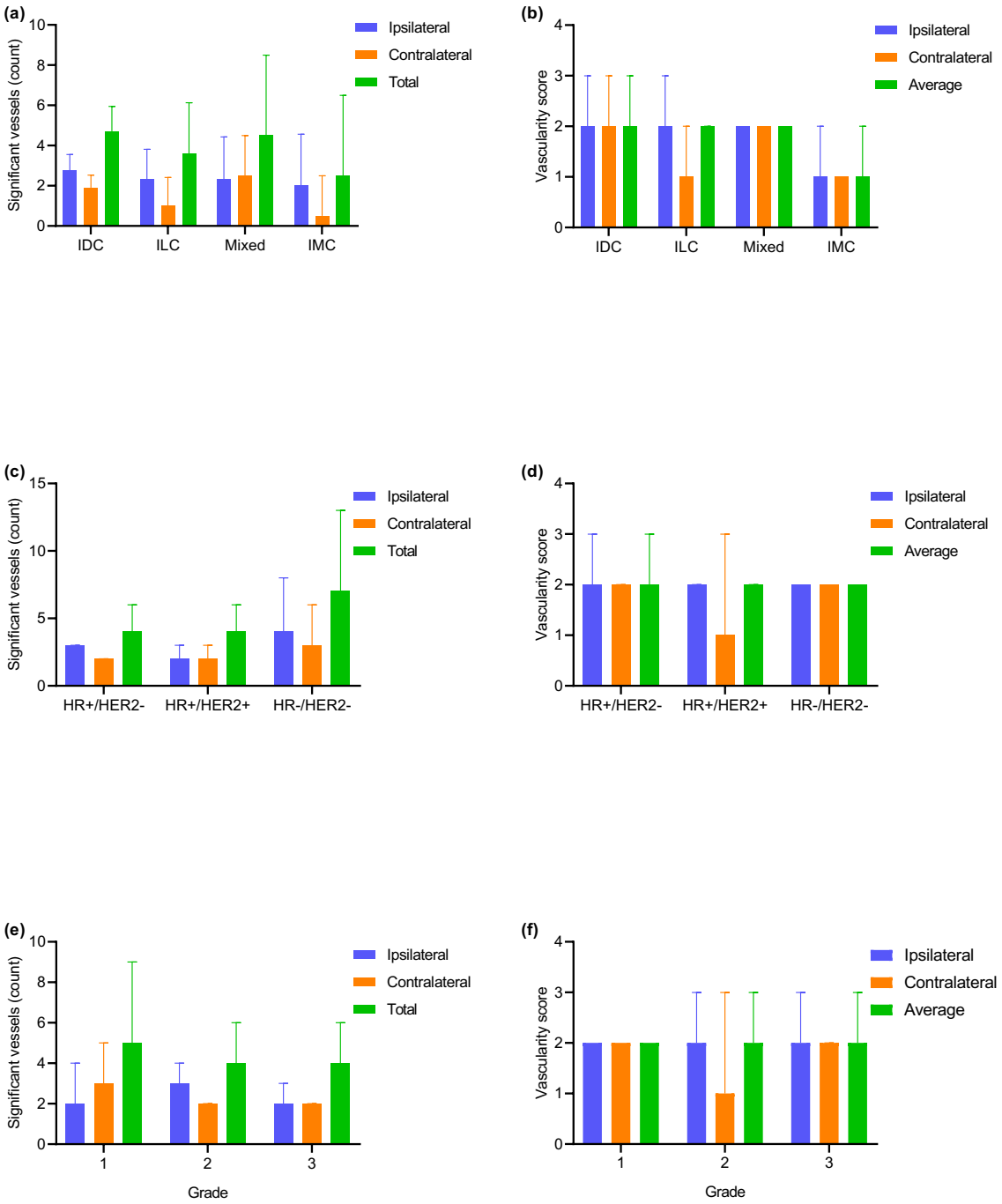

Figure 4.1: Number of significant vessels and whole-breast vascularity scores *vs* tumour histological subtype (a, b), molecular subtype (c, d) and grade (e, f) [*n*=29 patients]. Average numbers of significant breast vessels and 95% upper confidence intervals (CI) are presented for the ipsilateral and contralateral breast together with the total number of breast vessels observed in a patient. Median (upper range limit) vascularity scores are given for the whole breast (ipsilateral or contralateral) and for patients average scores.

Table 4.16: DCE-MRI, DWI and PET parameters according to the type of margins. Data are presented as median [range] or mean ± standard deviation (SD) as appropriate.

	Parameter	Margins: Irregular	Margins: Spiculated	*p*
A. DCE-MRI	Lesions (*n*=31)	16	15	
	K^{trans}	0.395 [0.129 – 1.978]	0.535 [0.099 – 1.285]	0.52[a]
	hs-K^{trans}	2.646 ± 0.449	2.760 ± 0.435	0.18[b]
	k_{ep}	0.254 [0.103 – 0.307]	0.286 [0.170 – 0.351]	0.03*[a]
	v_e	0.432 [0.213 – 0.838]	0.491 [0.259 – 0.949]	0.36[a]
	v_p	0.0 [0.213 – 0.838]	0.491 [0.259 – 0.949]	0.36[a]
B. DWI	Lesions (*n*=19)	10	9	
	ADC	0.949 [0.423 – 1.549]	1.079 [0.697 – 2.464]	0.55
	dp-ADC	0.758 [0.471 – 2.120]	0.842 [0.250 – 1.097]	0.35
C. PET	Lesions (*n*=32)	16	15	
	K_i	0.013 ± 0.534	0.028 ± 0.658	0.22[a]
	HF (%)	0.04 [0.00 – 2.58]	0.00 [0.0 – 4.74]	0.38[b]
	SUV_{mean}	1.19 ± 0.21	1.14 ± 0.25	0.86[a]
	SUV_{max}	1.64 ± 0.27	1.40 ± 0.45	0.96[a]
	T_{max}/M	1.11 ± 0.20	1.04 ± 0.31	0.42[a]
	T_{max}/P	0.88 ± 0.22	0.83 ± 0.23	0.35[a]

[a]Mann-Whitney *U* test
[b]Welch's *t* test
*p<0.05; **p<0.01

4.3.5 ^{18}F-FMISO-PET and MRI parameters *vs* descriptors of tumour morphology, enhancement and local or whole-breast vascularity

There was no significant difference between MRI and ^{18}F-FMISO parameters in cancers with irregular *vs* spiculated margins or tumours displaying different delayed enhancement curve patterns, with the exception of k_{ep}, which showed significant differences between cancers with irregular or spiculated margins, and v_e in lesions with type 2 and 3 kinetic curves (Tables 4.16.A and 4.17.A, respectively). As expected, cancers with kinetic curves type 2 and 3 were significantly associated with lower v_e values (Table 4.18). No correlation was observed between kinetic-curve type and other DCE-MRI pharmacokinetic parameters or PET hypoxia metrics (Table 4.18).

Axial images of two patients with 2 breast carcinomas of the same histological subtype (IDC) are presented in Figure 4.2. Linear regression analysis between DCE-MRI parameters and lesion AFV, adjusting for the effects of tumour LD or volume on AFV (see Section 4.3.4), resulted in significant positive associations between the number of adjacent feeding vessels, K^{trans} and v_e (Tables 4.19.A and 4.20.A; Figure 4.3), whereas no association was observed with other MRI metrics (Figure 4.3-4.4). Conversely, negative associations were found between AFV and hypoxic fraction or ^{18}F-FMISO K_i (Tables 4.19.C and 4.20.C; Figure 4.5), providing further evidence for a negative association between tumour vascularity and hypoxia. For K^{trans} and v_e there was an average increase of 4.3 – 6.7% and 1.8 – 2.4% per feeding vessel respectively when either LD or tumour volume were included as regressors in the model, with reductions of 4.0 – 5.8% and 2- 4% per feeding vessel in K_i and %HF respectively. Associations between AFV and other MRI or PET metrics were positive (Figures 4.3 – 4.5), but none of these relationships were statistically significant.

Except for hs-K^{trans}, k_{ep} and ADC, MRI parameters were significantly associated with the number of significant breast vessels in the ipsilateral breast, while no association was observed with the number of significant breast vessels in the contralateral breast (Table 4.21). Patient vascularity scores and the presence or number of enlarged vessels showed no or weak associations with MRI parameters (Tables 4.21 and 4.22 respectively). On the other hand, there were significant associations between whole-breast vascularity descriptors and K_i or %HF (Table 4.21.C). Interestingly, K_i and %HF were the only parameters which displayed significant negative associations with the number of significant breast vessels in the

contralateral breast (Table 4.21.C) or the number of enlarged vessels (Table 4.22.C). Finally, the presence of vascular asymmetry showed positive associations with v_e and v_p, and conversely a negative relationship with ^{18}F-FMISO K_i. No other statistically significant correlations were observed between breast vascularity descriptors and PET or MRI parameters of hypoxia and vascular function.

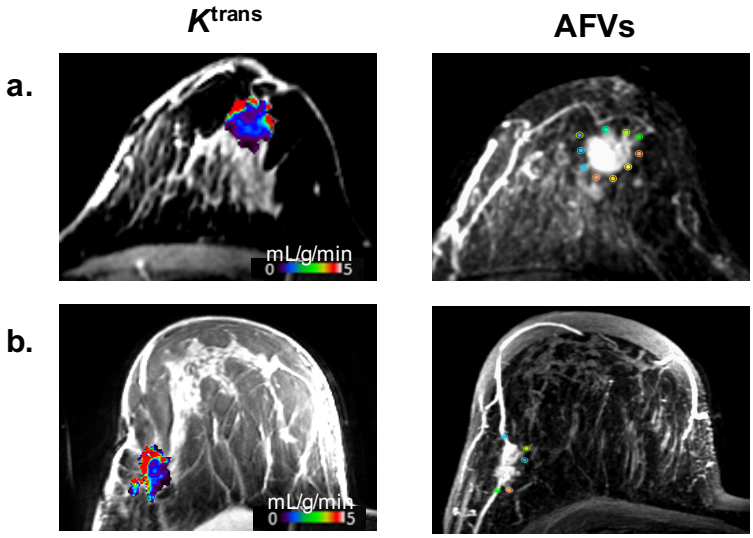

Figure 4.2. K^{trans} and adjacent feeding vessels (AFVs) of two invasive ductal carcinomas. The cancer in figure 4.2.a is bigger in size than the lesion in figure 4.2.b and therefore, it had more AFVs. Both cancers showed high K^{trans} in their periphery (area in red on K^{trans} maps) and lower K^{trans} in their centre (area in blue and purple on K^{trans} maps). Significant breast vessels can be observed on the subtracted axial DCE-MR images depicting AFVs.

Table 4.17: DCE-MRI, DWI and PET parameters according to delayed-phase enhancement characteristics. Data are presented as median [range] or mean ± standard deviation (SD) as appropriate.

	Parameter	Delayed-phase enhancement			p^a
		Persistent (Type 1)	Plateau (Type 2)	Washout (Type 3)	
A. DCE-MRI	Lesions (n=31)	2	15	14	
	K^{trans}	0.163 [0.099 – 0.227]	0.571 [0.129 – 1.285]	0.374 [0.144 – 1.978]	0.35[b]
	hs-K^{trans}	5.633 ± 7.188	6.488 ± 3.636	6.461 ± 3.031	0.83[c]
	k_{ep}	0.179 [0.170 – 0.187]	0.284 [0.192 – 0.351]	0.272 [0.103 – 0.307]	0.16[b]
	v_e	0.524 [0.411 – 0.637]	0.571 [0.259 – 0.949]	0.387 [0.213 – 0.648]	0.02*[b]
	v_p	0.021 [0.015 – 0.028]	0.128 [0.013 – 0.367]	0.063 [0.000 – 0.550]	0.15[b]
B. DWI	Lesions (n=19)	1	9	8	
	ADC ($\times 10^{-3}$)	1.021 [–]	1.079 [0.423 – 2.464]	0.895 [0.697 – 1.284]	0.55[b]
	dp-ADC ($\times 10^{-3}$)	0.819 [–]	0.842 [0.250 – 2.120]	0.780 [0.471 – 1.128]	0.02*[b]
C. PET	Lesions (n=32)	2	15	14	
	K_i ($\times 10^{-3}$)	0.367 [0.319 – 0.415]	0.084 [-0.621 – 0.001]	-0.056 [-0.736 – 0.002]	0.40[b]
	HF (%)	0.06 [0.00 – 0.13]	0.00 [0.0 – 4.74]	0.20 [0.0 – 3.07]	0.06[b]
	SUV_{mean}	1.11 ± 0.15	1.20 ± 0.26	1.12 ± 0.21	0.42[c]
	SUV_{max}	1.50 ± 0.16	1.64 ± 0.44	1.48 ± 0.28	0.24[d]
	T_{max}/M	1.03 ± 0.01	1.08 ± 0.30	1.08 ± 0.25	0.98[d]
	T_{max}/P	0.59 ± 0.29	0.84 ± 0.22	0.91 ± 0.21	0.39[d]

[a]Due to low number of cancers with persistent enhancement, p values are given for comparisons between type 2 and 3 kinetic curves.
[b]Mann-Whitney U test
[c]Student's t test
[d]Welch's t test
*p<0.05; **p<0.01

Table 4.18: Kendall's τ_b and 95% confidence intervals (CI) for the correlation between kinetic curve type and imaging parameters from DCE, DWI-MRI and PET.

	Parameter	τ_b, [CI]	*p*
A. DCE-MRI	Lesions (*n*=31)		
	K^{trans}	0.01, [-0.31 – 0.40]	0.97
	hs-K^{trans}	0.04, [-0.18 – 0.51]	0.79
	k_{ep}	-0.04, [-0.37 – 0.33]	0.77
	v_e	-0.34, [-0.67 – -0.08]	0.02*
	v_p	-0.07, [-0.36 – 0.35]	0.63
B. DWI	Lesions (*n*=19)		
	ADC ($\times 10^{-3}$)	-0.15, [-0.61 – 0.29]	0.46
	dp-ADC ($\times 10^{-3}$)	-0.1, [-0.58 – 0.34]	0.63
C. PET	Lesions (*n*=32)		
	K_i ($\times 10^{-3}$)	-0.20, [-0.43 – 0.28]	0.18
	HF (%)	0.29, [-0.19 – 0.50]	0.07
	SUV_{mean}	-0.07, [-0.44 – 0.28]	0.64
	SUV_{max}	-0.15, [-0.48 – 0.22]	0.32
	T_{max}/M	0.07, [-0.33 – 0.40]	0.63
	T_{max}/P	0.20, [-0.05 – 0.61]	0.18

*p<0.05; **p<0.01

Table 4.19: Fixed effects estimates (β) together with confidence intervals (CI) and *p* values for the association between MRI and PET parameters and the number of adjacent feeding vessels (AFV), the longest tumour diameter (LD) and the interaction between AFV and LD.

		AFV	**LD**	**AFV*LD**
		β, [CI], *p*	β, [CI], *p*	β, [CI], *p*
A. DCE-MRI	$ln(K^{trans})$	0.065, [0.002 – 0.129], 0.04*	0.011, [-0.010 – 0.033], 0.28	-0.001, [-2×10^{-3} – -7.26×10^{-5}], 0.04*
	hs-K^{trans}	0.044, [-0.021 – 0.110], 0.18	0.036, [0.014 – 0.058], 0.002**	-9.44×10^{-4}, [-2×10^{-3} – -2.42×10^{-4}], 0.11
	k_{ep}	-0.002, [-0.007 – 0.004], 0.55	-5.21×10^{-4}, [-0.007 – 0.004], 0.56	3.02×10^{-5}, [-6.67×10^{-4} – 1.27×10^{-4}], 0.53
	v_e	0.024, [0.008 – 0.039], 0.004**	0.001, [-0.004 – 0.006], 0.62	-3.50×10^{-4}, [-6.27×10^{-4} – -7.38×10^{-5}], 0.02*
	$ln(v_p)$	0.049, [-0.004 – 0.167], 0.06	0.017, [-0.011 – 0.045], 0.22	-0.001, [-3.00×10^{-3} – 3.60×10^{-5}], 0.06
B. DWI	ADC ($\times10^{-3}$)	0.006, [-0.058 – 0.070], 0.83	0.009, [-0.030 – 0.047], 0.63	-1.37×10^{-4}, [-1.00×10^{-3} – 7.69×10^{-4}], 0.75
	dp-ADC ($\times10^{-3}$)	-0.006, [-0.064 – 0.052], 0.82	0.008, [-0.027 – 0.042], 0.64	4.55×10^{-5}, [-7.73×10^{-4} – 8.64×10^{-4}], 0.91
C. PET	K_i ($\times10^{-3}$)	-0.058, [-0.106 – -0.103], 0.02*	-0.011, [-0.027 – 0.006], 0.19	0.001, [0.000 – 0.002], 0.04*
	HF (%)	-0.04, [-0.14 – -0.062], 0.04*	-0.004, [-0.037 – -0.030], 0.82	0.001, [-0.001 – 0.003], 0.23
	SUV_{mean}	0.008, [-0.011 – 0.028], 0.41	0.004, [-0.003 – 0.010], 0.24	-7.56×10^{-5}, [-4.18×10^{-4} – 2.67×10^{-4}], 0.65
	SUV_{max}	0.019, [-0.011 – 0.049], 0.22	0.007, [-0.004 – 0.017], 0.19	-2.82×10^{-4}, [-8.34×10^{-4} – 2.71×10^{-4}], 0.31
	T_{max}/M	0.011, [-0.010 – 0.032], 0.28	0.006, [-0.002 – 0.013], 0.13	-1.51×10^{-4}, [-5.33×10^{-4} – 2.30×10^{-4}], 0.42
	T_{max}/P	0.003, [-0.015 – 0.021], 0.72	0.005, [-0.001 – 0.011], 0.12	-4.91×10^{-5}, [-3.73×10^{-4} – 2.74×10^{-4}], 0.76

*p<0.05; **p<0.01; ***p<0.001

Table 4.20: Fixed effects estimates (β) together with confidence intervals (CI) and *p* values for the association between MRI and PET parameters and the number of adjacent feeding vessels (AFV), the longest tumour diameter (LD) and the interaction between AFV and LD.

		AFV β, [CI], *p*	**Volume** β, [CI], *p*	**AFV*Volume** β, [CI], *p*
A. DCE-MRI	$ln(K^{trans})$	0.043, [0.000 – 0.086], 0.04*	0.010, [-0.051 – 0.070], 0.74	-0.003, [-0.005 – -0.070], 0.04*
	hs-K^{trans}	0.033, [-0.018 – 0.084], 0.19	0.079, [0.007 – 0.150], 0.03*	-0.002, [-0.005 – 0.01], 0.17
	k_{ep}	-0.004, [-0.022 – 0.013], 0.62	-0.004, [-0.029 – 0.021], 0.74	0.03×10^{-2}, [-0.08×10^{-2} – -1.52×10^{-4}], 0.58
	v_e	0.018, [0.008 – 0.028], 0.001**	-0.002, [-0.016 – 0.012], 0.76	-8.2×10^{-4}, [-0.1×10^{-2} – -0.1×10^{-2}], 0.01*
	$ln(v_p)$	0.054, [-0.003 – 0.111], 0.06	0.016, [-0.066 – 0.097], 0.70	-0.3×10^{-2}, [-0.7×10^{-2} – -0.03×10^{-2}], 0.07
B. DWI	ADC ($\times10^{-3}$)	0.015, [-0.015 – 0.046], 0.30	-0.049, [-0.142 – 0.045], 0.29	0.05×10^{-2}, [-0.2×10^{-2} – 0.2×10^{-2}], 0.63
	dp-ADC ($\times10^{-3}$)	0.010, [-0.028 – 0.048], 0.59	-0.041, [-0.158 – 0.076], 0.46	0.06×10^{-2}, [-0.2×10^{-2} – 0.3×10^{-2}], 0.59
C. PET	K_i ($\times10^{-3}$)	-0.04, [-0.07 – -0.02], 0.04*	-0.03, [-0.08 – 0.02], 0.20	0.002, [0.00 – 0.004], 0.07
	HF (%)	-0.02, [-0.08 – 0.01], 0.20	0.03, [-0.07 – 0.12], 0.58	0.002, [-0.002 – 0.006], 0.36
	SUV_{mean}	0.007, [-0.006 – 0.020], 0.30	0.015, [-0.003 – 0.033], 0.10	-0.03×10^{-2}, [-0.1×10^{-2} – 0.05×10^{-2}], 0.51
	SUV_{max}	0.013, [-0.009 – 0.034], 0.23	0.022, [-0.008 – 0.052], 0.15	-0.07×10^{-2}, [-0.2×10^{-2} – 0.06×10^{-2}], 0.31
	T_{max}/M	0.008, [-0.005 – 0.022], 0.30	0.020, [0.001 – 0.039], 0.04*	-0.04×10^{-2}, [-0.1×10^{-2} – 0.04×10^{-2}], 0.33
	T_{max}/P	0.002, [-0.011 – 0.014], 0.77	0.015, [-0.002 – 0.033], 0.08	-0.01×10^{-2}, [-0.9×10^{-2} – 0.07×10^{-2}], 0.78

*p<0.05; **p<0.01; ***p<0.001

Table 4.21: Fixed effects estimates (β) together with confidence intervals (CI) and *p* values for the association between MRI and PET parameters and the of number of significant breast vessels in the ipsilateral and contralateral breast or the patient vascularity score.

		Significant breast vessels (number)		
	Parameter	**Ipsilateral breast** β, [CI], *p*	**Contralateral Breast**[a] *β*, [CI], *p*	**Patient vascularity score**[b] *β*, [CI], *p*
A. DCE-MRI	K^{trans}	0.125, [0.040 – 0.209], 0.005**	-0.050, [-0.263 – 0.162], 0.63[a]	0.246, [-0.093 – 0.583], 0.17[c]
	hs-K^{trans}	0.072, [-0.125 – 0.745], 0.46	0.083, [-0.196 – 0.362], 0.54	0.208, [-0.219 – 0.635], 0.35
	k_{ep}	-0.011, [-0.023 – 0.001], 0.08	-0.011, [-0.027 – 0.006], 0.21	-0.027, [-0.054 – 0.001], 0.05
	v_e	0.046, [0.005 – 0.088], 0.03*	-0.026, [-0.152 – 0.100], 0.68[a]	0.086, [-0.005 – 0.177], 0.08[c]
	v_p	0.034, [0.011 – 0.058], 0.006**	-0.054, [-0.356 – 0.249], 0.72[a]	0.052, [-0.002 – 0.106], 0.07[c]
B. DWI	ADC ($\times 10^{-3}$)	1.08, [0.99 – 1.18], 0.1[a]	0.003, [-0.137 – 0.143], 0.96[a]	0.114, [-0.061 – 0.288], 0.22[c]
	dp-ADC ($\times 10^{-3}$)	0.047, [-0.055 – 0.150], 0.34	-0.072, [-0.238 – 0.093], 0.29	0.082, [-0.164 – 0.328], 0.53[c]
C. PET	K_i ($\times 10^{-3}$)	-0.13, [-0.26 – -0.59], 0.04*	-0.201, [-0.363 – -0.391], 0.02*	-0.38, [-0.63 – -0.12], 0.005**
	HF (%)	-0.32, [-0.54 – -0.10], 0.006**	-0.33, [-0.65 – -0.003], 0.048*	-0.80, [-1.26 – -0.36], 0.001**
	SUV_{mean}	0.06, [0.01 – 0.11], 0.02*	-0.01, [-0.07 – 0.05], 0.73	0.06, [-0.05 – 0.18], 0.30
	SUV_{max}	0.07, [-0.01 – 0.15], 0.06	-0.02, [-0.12 – 0.09], 0.73	0.06, [-0.12 – 0.25], 0.50
	T_{max}/M	0.01, [-0.049 – 0.069], 0.73	-0.02, [-0.11 – -0.06], 0.56	-0.01, [-0.14 – 0.12], 0.86
	T_{max}/P	0.00, [-0.05 – 0.05], 0.87	-0.03, [-0.08 – -0.03], 0.35	-0.01, [-0.12 – 0.10], 0.88

[a]Two patients with bilateral cancers were excluded from associations of MRI and PET with the number of significant vessels in the contralateral breast.
[b]Fixed-effects estimates for the association between presence or absence of enlarged vessels and MRI or PET parameters were computed using mixed effects models with random intercepts for subjects.
[c]Where model residuals were not normally distributed as indicated by normality tests, dependent variables were transformed using the natural logarithm (*ln*).
$^{*}p<0.05$; $^{**}p<0.01$; $^{***}p<0.001$

Table 4.22: Fixed effects estimates (β) together with confidence intervals (CI) and *p* values for the association between the presence or number of enlarged vessels and vascular asymmetry.

		Enlarged Vessels		
	Parameter	**Presence**[a,b] β, [CI], *p*	**Number**[a] β, [CI], *p*	**Vascular asymmetry**[a,b] β, [CI], *p*
A. DCE-MRI	K^{trans}	0.109, [-0.454 – 0.673], 0.71[c]	0.056, [-0.284 – 0.396], 0.75[a]	0.248, [-0.292 – 0.788], 0.38
	hs-K^{trans}	0.557, [-0.454 – 0.673], 0.11	0.281, [-0.127 – 0.688], 0.19	0.407, [-0.370 – 1.183], 0.32
	k_{ep}	-0.030, [-0.072 – 0.011], 0.16	-0.030, [-0.054 – -0.006], 0.02*	-0.023, [-0.069 – 0.023], 0.33
	v_e	0.030, [-0.124 – 0.185], 0.71	-0.023, [-0.213 – 0.167], 0.88[c]	0.187, [0.031 – 0.344], 0.03*
	v_p	0.244, [-0.498 – 0.986], 0.53[c]	0.248, [-0.292 – 0.788], 0.38[c]	0.983, [0.314 – 1.651], 0.008** [c]
B. DWI	ADC ($\times 10^{-3}$)	0.017, [-0.306 – 0.340], 0.92[c]	-0.023, [-0.195 – 0.149], 0.80[c]	0.214, [-0.153 – 0.582], 0.27[c]
	dp-ADC ($\times 10^{-3}$)	-0.030, [-0.434 – 0.373], 0.89[c]	-0.089, [-0.301 – 0.122], 0.42[c]	0.154, [-0.193 – 0.501], 0.40[c]
C. PET	K_i ($\times 10^{-3}$)	-0.367, [-0.783 – 0.047], 0.09	-0.026, [-0.509 – -0.013], 0.048*	0.555, [-0.001 – -1.234], 0.02*
	HF	-0.207, [-1.137 – 0.723], 0.65	-0.156, [-0.709 – 0.397], 0.57	-0.837, [-1.751 – 0.078], 0.07
	SUV_{mean}	0.072, [-0.094 – 0.238], 0.40	0.017, [-0.085 – 0.119], 0.33	0.000, [-0.168 – 0.168], 0.99
	SUV_{max}	0.091, [-0.172 – 0.355], 0.50	0.027, [-0.134 – 0.188], 0.74	0.031, [-0.238 – 0.301], 0.82
	T_{max}/M	0.084, [-0.106 – 0.273], 0.38	0.043, [-0.070 – 0.156], 0.46	-0.011, [-0.783 – 0.047], 0.09
	T_{max}/P	0.025, [-0.136 – 0.186], 0.77	0.013, [-0.084 – 0.111], 0.79	-0.004, [-0.158 – 0.151], 0.96

[a]Fixed-effects estimates for the association between presence or absence of enlarged vessels and MRI or PET parameters were computed using mixed effects models. Random intercepts for subjects were included in the model.
[b]Two patients with bilateral cancers were excluded from associations between vascular asymmetry and MRI or PET parameters.
[c]Where model residuals were not normally distributed as indicated by normality tests, dependent variables were transformed using the natural logarithm (*ln*).

*p<0.05; **p<0.01; ***p<0.001

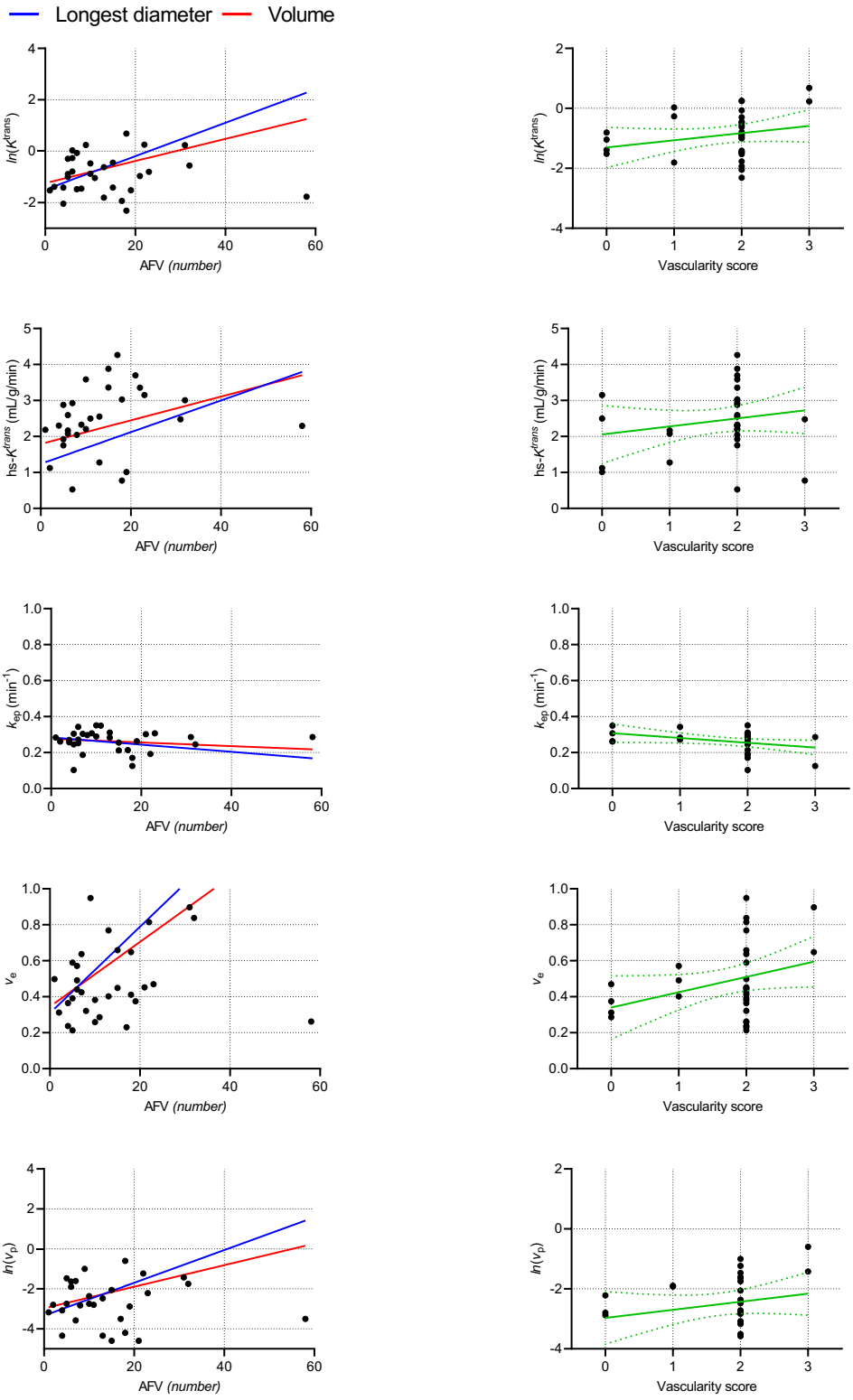

Figure 4.3. Scatter plots and regression lines of DCE-MRI parameters *vs* the number of adjacent feeding vessels (AFV) and patient vascularity scores. Regression lines of DCE-MRI metrics *vs* AFV indicate models adjusted for the tumour longest diameter (blue line) or volume (red line). Where normality tests indicated not normally distributed regression residuals, dependent variables (i.e. K^{trans} and v_p) were log-transformed.

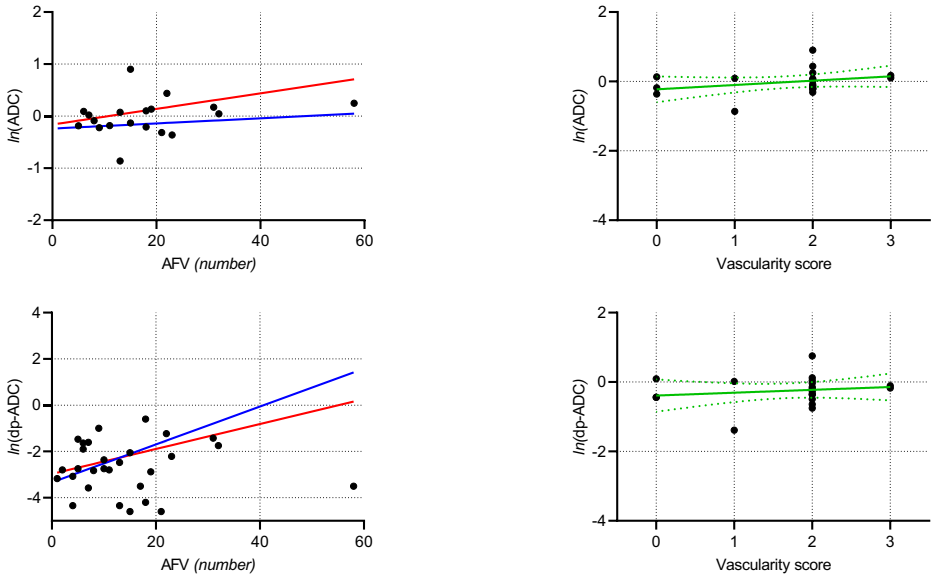

Figure 4.4. Scatter plots and regression lines of apparent diffusion coefficient in the whole lesion (ADC) and the darkest part of the tumour (dp-ADC) *vs* the number of adjacent feeding vessels (AFV) or patient vascularity scores. Regression lines of ADC and dp-ADC *vs* AFV indicate regression models adjusted for the tumour longest diameter (blue line) or volume (red line). ADC and dp-ADC were log-transformed prior to linear regression due to non-normal model residuals.

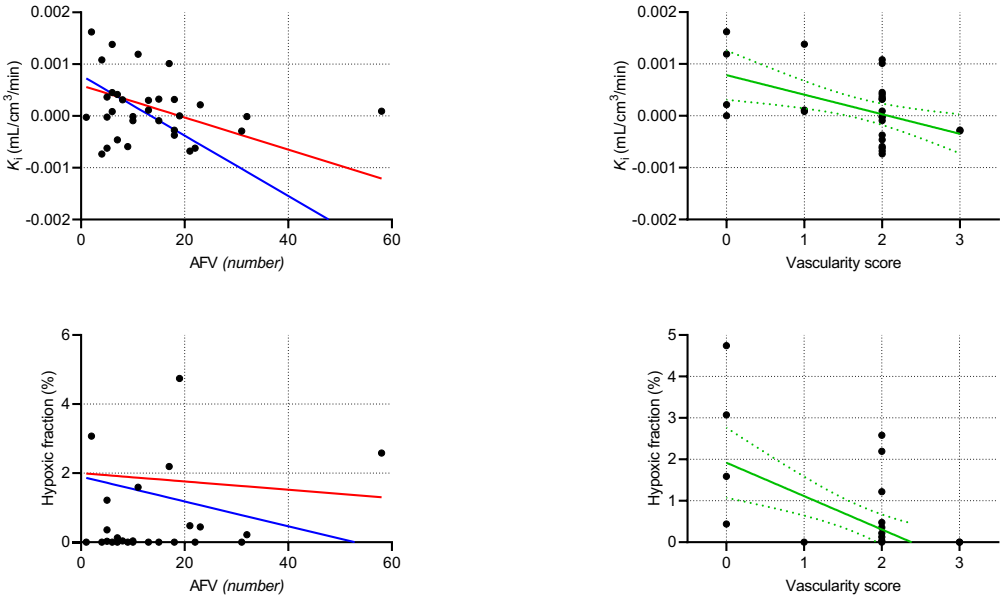

Figure 4.5. Scatter plots and regression lines of the ^{18}F-FMISO influx rate constant (K_i) and hypoxic fraction (%) *vs* the number of adjacent feeding vessels (AFV) or patient vascularity scores. Regression lines of K_i and hypoxic fraction *vs* AFV indicate regression models adjusted for the tumour longest diameter (blue line) or volume (red line).

4.4 Discussion

To the best of our knowledge, this was the first study in which ^{18}F-FMISO-PET quantitative parameters of tumour hypoxia were assessed together with vascular morphological and enhancement characteristics of breast cancers extracted from dynamic-contrast-enhanced magnetic resonance imaging (DCE-MRI) following the BI-RADS 5th edition lexicon. Despite not being included in the BI-RADS, we decided to add adjacent feeding vessels count (AFVs) to our analysis as it is an MRI feature which is closely related to the cancer vascular function and not studied in depth until now. Similarly, we correlated imaging parameters of tumour hypoxia and vascularity with vascular metrics of whole-breast vascularity which were obtained from DCE-MRI using Sardanelli *et al* method.

Increased vascularity in one breast is an MR imaging finding frequently associated with ipsilateral invasive cancer and early disease recurrence[2,23,24]. In this study, thirty-eight percent of the study participants showed increased vascularity in the ipsilateral breast in comparison to the other one. Seventy percent of cancer- bearing breasts depicted higher vascularity than "normal" or contralateral breasts. Enlarged breast vessels were noted in 52% of all patients. Patient vascularity scores were significantly associated with the presence and number of enlarged breast vessels; therefore, we could infer that the presence of enlarged breast vessels is an indicator of increased breast vascularity. Ipsilateral breast vascularity score and high number of significant breast vessels were associated with bigger cancers like the presence and number of enlarged breast vessels.

The median number of tumours AFV in these patients was 11 [1 – 58] vessels), whereas the mean number of significant breast blood vessels (vessels ≥ 3 cm in length and ≥ 2 mm in maximal diameter) was 4 ± 3 vessels. Local peri-tumoral vascularity, measured as tumour AFV, showed a non-significant positive correlation with whole-breast vascularity, measured as the number of breast vessels in the ipsilateral breast which means that high vascularity in the ipsilateral breast is associated to high peri-tumoral vascularity. Previous authors[25] have reported an increased sensitivity, specificity, accuracy and predictive value of the adjacent vessel sign (which refers to the presence of an adjacent feeding vessel but not to the total number of them) for breast cancer diagnosis in comparison with ipsilateral increased breast vascularity. However, no previous studies were found about the relationship between the number of tumour AFVs and ipsilateral increased breast vascularity. We observed that women

with vascular asymmetry between their breasts had a higher number of tumour AFV than women without asymmetry.

A previous study by Li *et al*[26] found that malignant breast lesions have 2 or more feeding vessels whereas, benign breast lesions have no or only one blood vessel. All cancers in our sample displayed more than two adjacent feeding vessels, which was in agreement with the results published by Li *et al*. Furthermore, in concordance with published literature[7], a statistically significant positive correlation was observed between tumour size (LD, ETV and ROI volumes) and the number of adjacent feeding vessels in the cancer. The higher prevalence of AFV with increasing cancer size could be explained by the higher degree of vascularisation in such lesions owing to increased metabolic demands[7,27]. In our study, there was no statistically significant difference in the median number of AFV between cancers with irregular and spiculated margins. Other authors[28] have reported that tumours with irregular or spiculated margins have significantly higher vascularity than tumours with smooth margins. We also observed that AFVs did not significantly vary between lesions displaying different delayed-phase curve enhancement patterns, though tumours with a higher number of feeding vessels tended to display a more aggressive kinetic-curve pattern.

No significant correlation was observed between the number of adjacent feeding vessels and tumour histology or molecular subtype. In general, there was a tendency for higher grade cancers to exhibit a higher number of AFV, however, associations between AFV and tumour grade were not statistically significant. Although this sample of cancers was likely small to evaluate differences in AFV in tumours of different histological/molecular subtype and grade, the results presented here are concordant with those of Dietzel *et al*[7], who did not observe a significant difference in the presence of the adjacent vessel sign between ductal and lobular carcinomas or a correlation with tumour grade. Histopathological features of the cancers did not show any association with whole-breast vascularity (presence and number of significant breast vessels, enlarged breast vessels or vascularity scores) in neither the ipsilateral nor the contralateral breast.

In this study, tumour histopathological prognostic factors (histology, molecular subtype or nuclear grade) did not significantly influence the tumour size (LD and ETV). However, HR+/HER- lesions were larger in size than HR+/HER2+ cancers, while also displaying a larger enhancing volume. It should be noted that HR+/HER- cancers constituted the majority in this

sample of tumours. High grade cancers also demonstrated larger size and ETV than low grade lesions. Stierer et al[29] found that high histologic grade, mitotic rate and high nuclear polymorphism were significant predictors for recurrence and survival in breast tumours less than 10mm.

Peripheral rim-enhancement was observed in all breast cancers examined. All time-signal intensity curves from these cancers demonstrated a rapid initial phase, which means rapid signal increase during the first 2 mins after contrast injection[30]. Almost half of the analysed breast cancers (48%) presented a kinetic curve with washout pattern (type 3), 45% of the cancers displayed a plateau pattern of the time-signal intensity curve (type 2 curve) and only 7% showed persistent signal intensity increase (type 1 kinetic curve). Relationships between tumour size metrics and delayed-phase kinetic curve patterns were not statistically significant, however breast cancers with type 3 kinetic curves tended to be larger than those displaying type 1 or type 2 curves. Aversely, there was a statistically significant difference in enhancing tumour volumes between cancers with irregular and spiculated margins. As previously stated in the literature[31,32], lesions with irregular or ill-defined margins should be considered malignant regardless of their size or enhancement pattern.

After comparing DCE-MRI quantitative parameters among lesions with different types of margins and kinetic curves, we observed that k_{ep} was the only DCE-MRI parameter which showed significant differences between cancers with irregular or spiculated margins, and v_e between lesions with type 2 and 3 kinetic curves. V_e was significantly lower in cancers showing a delayed washout pattern, as it has also been shown before[33]. Like in a previous study[33], whole-lesion K^{trans} did not differ significantly between cancers showing delayed plateau and washout curve patterns and either hotspot-$K^{trans.}$. To the best of my knowledge, previous researchers have not correlated hotspot K^{trans} with tumour signal intensity curve types. K_{ep} was slightly higher in breast cancers with a delayed plateau curve in comparison to cancers showing delayed washout. Conversely, Yi et al[33]. found significant higher values of k_{ep} in breast cancers with kinetic curve type 3. Breast cancers with a delayed plateau pattern showed higher median v_p than cancers exhibiting persistent signal increase and washout pattern, although these associations were not significant. With respect to DWI-MRI, ADC from the darkest part of the cancer showed a significant association with the type of tumour kinetic curve, opposite to whole lesion ADC. Breast cancers having delayed washout showed the lowest dp-ADC.

As far as we know, no studies have yet been published commenting about the relationship between ^{18}F-FMISO/PET imaging parameters of hypoxia and tumour signal-intensity curves. Overall, there were not significant differences of ^{18}F-FMISO parameters between cancers with irregular and spiculated margins or cancers with different patterns of kinetic curve. Median percentage of tumour hypoxic fractions, analysed on a voxel basis, were higher in breast cancers with a kinetic curve type 3 (or delayed washout) than in cancers with a kinetic curve type 2 and 1. The association between tumour hypoxic fractions and kinetic curve type came close to reaching statistical significance. ^{18}F-FMISO SUVs (mean and max) were higher in lesions with a kinetic curve type 2 than in lesions with different type of curves. The highest mean ^{18}F-FMISO tumour to blood ratio (T/B) was observed in breast cancers with delayed washout. Mean ^{18}F-FMISO T/B ratio did not change notably between breast cancers with a kinetic curve type 1 and a type 2 curve whereas, ^{18}F-FMISO tumour to muscle ratio (T/M) showed an in crescendo pattern between lesions with a kinetic curve type 1, 2 and 3; respectively.

From what we know of previous literature, there have not been studies reporting correlations between the number of tumour AFVs and DCE-MRI quantitative parameters in breast cancer. In this study, there were statistically significant associations between the number of tumour AFVs and whole-lesion K^{trans} and v_e. According to these results, we ought to expect to find higher perfusion and/or blood-vessel permeability in those breast cancers displaying more feeding vessels on DCE-MRI examinations. By contrast, there were no significant associations between tumour AFVs and other DCE or DWI-MRI parameters. The mixed effect statistical model revealed that the interaction between tumour size (LD and ROI volumes) and the number of AFVs could significantly influence on whole-lesion K^{trans} and $v_{e.}$. Quantitative parameters of the tumour vascular function (whole-lesion K^{trans}, v_e and v_p) were also significantly associated with metrics of the whole-breast vascularity in the ipsilateral breast.

This study for first time (because it has not been done before) correlated ^{18}F-FMISO-PET hypoxia parameters of breast cancers with the number of tumour adjacent feeding vessels. Significant negative associations were found between tumour AFV and ^{18}F-FMISO K_i and hypoxic fractions, providing evidence for an inverse association between peri-tumoral vascularity and hypoxia. Similarly, significant negative associations were observed between metrics of the whole-breast vascularity (number of significant breast vessels in the ipsilateral and contralateral breasts and vascularity score in the ipsilateral breast) and ^{18}F-FMISO

parameters of tumour hypoxia (K_i and hypoxic fractions). Therefore, it seems that the vascularity of the contralateral breast may influence on breast cancer hypoxic status as much as the vascularity of the ipsilateral breast. The explanation for this may be that in response to high tumour metabolic demands, the organism will supply more blood not only to the cancer bearing breast but also to the contralateral breast.

One of the main limitations of our study was the failure of the fat saturation (FAT-SAT) technique in one case's DCE-MRI which made the vascular characteristics of the patients' breasts and tumour unanalysable. Therefore, only 31 breast cancers were included for the quantitative and qualitative analysis of DCE-MRI whereas 32 breast cancers were analysed in ^{18}F-FMISO-PET/MRI. Additionally, a larger sample of patients could have provided stronger correlations between DCE-MRI tumour and breast vascular features and quantitative parameters of tumour hypoxia obtained from PET.

4.5 Conclusion

These results showed that the peri-tumoral vascularity is significantly related to the ipsilateral whole-breast vascularity. Since tumour AFVs presented a significant association with tumour size, the vascularity of the whole breast may indirectly influence the size of the malignant tumour. Tumour prognostic factors such as histology, molecular subtype and grade seem to not be related to the peri-tumoral (number of adjacent feeding vessels) or whole-breast vascularity, however, future studies with a bigger sample size may be needed to corroborate our results.

As expected, there was a significant association between the number of tumour AFVs, a qualitative marker of the tumour vascularity, and DCE-MRI quantitative parameters (whole-lesion K^{trans} and v_e) of the cancer vasculature. Similarly, whole-lesion K^{trans}, v_e and v_p showed significant correlations with metrics of the whole-breast vascularity. ^{18}F-FMISO parameters of tumour hypoxia, K_i and hypoxic fractions, showed significant negative associations with parameters of tumour and breast vascularity which confirms the negative relationship between tumour vascularity and hypoxia. K_{ep} significantly differentiated between lesions of irregular and spiculated margins and v_e between lesions with type 2 and 3 kinetic curves, like DWI-MRI dp-ADC. PET quantitative parameters of tumour hypoxia did not vary significantly between cancers with different margins or kinetic curve patterns.

References

1. Kuhl, C. K. *et al.* Dynamic Breast MR Imaging: Are Signal Intensity Time Course Data Useful for Differential Diagnosis of Enhancing Lesions? *Radiology* **211**, 101–110 (1999).
2. Sardanelli, F., Iozzelli, A., Fausto, A., Carriero, A. & Kirchin, M. A. Gadobenate dimeglumine-enhanced MR imaging breast vascular maps: Association between invasive cancer and ipsilateral increased vascularity. *Radiology* (2005). doi:10.1148/radiol.2353040733
3. Rao, A. A., Feneis, J., Lalonde, C. & Ojeda-Fournier, H. A pictorial review of changes in the BI-RADS fifth edition. *Radiographics* (2016). doi:10.1148/rg.2016150178
4. Choi, E. J., Choi, H., Choi, S. A. & Youk, J. H. Dynamic contrast-enhanced breast magnetic resonance imaging for the prediction of early and late recurrences in breast cancer. *Medicine (Baltimore).* **95**, e5330 (2016).
5. Siewert, C. *et al.* Is there a correlation in breast carcinomas between tumor size and number of tumor vessels detected by gadolinium-enhanced magnetic resonance mammography? *Magn. Reson. Mater. Physics, Biol. Med.* (1997). doi:10.1007/BF02592262
6. Fischer, D. R. *et al.* The adjacent vessel on dynamic contrast-enhanced breast MRI. *AJR. Am. J. Roentgenol.* (2006). doi:10.2214/AJR.05.0377
7. Dietzel, M. *et al.* The adjacent vessel sign on breast MRI: New data and a subgroup analysis for 1,084 histologically verified cases. *Korean J. Radiol.* (2010). doi:10.3348/kjr.2010.11.2.178
8. Han, M., Kim, T. H., Kang, D. K., Kim, K. S. & Yim, H. Prognostic role of MRI enhancement features in patients with breast cancer: Value of adjacent vessel sign and increased ipsilateral whole-breast vascularity. *Am. J. Roentgenol.* (2012). doi:10.2214/AJR.11.7895
9. Mahfouz, A. E. *et al.* Gadolinium-enhanced MR angiography of the breast: Is breast cancer associated with ipsilateral higher vascularity? *Eur. Radiol.* (2001). doi:10.1007/s003300000668
10. Carriero, A., Di Credico, A., Mansour, M. & Bonomo, L. Maximum intensity projection analysis in magnetic resonance of the breast. in *Journal of Experimental and Clinical Cancer Research* (2002).
11. Seifalian, A. M., Chahupka, K. & Parbhoo, S. P. Laser doppler perfusion imaging - a

new technique for measuring breast skin blood flow. *Int. J. Microcirc. Exp.* (1995). doi:10.1159/000178963

12. Kang, D. K., Eun, J. K., Ho, S. K., Joo, S. S. & Yong, S. J. Correlation of whole-breast vascularity with ipsilateral breast cancers using contrast-enhanced MDCT. *Am. J. Roentgenol.* (2008). doi:10.2214/AJR.07.2784
13. Wilson, C. B. J. H., Lammertsma, A. A., McKenzie, C. G., Sikora, K. & Jones, T. Measurements of Blood Flow and Exchanging Water Space in Breast Tumors Using Positron Emission Tomography: A Rapid and Noninvasive Dynamic Method. *Cancer Res.* (1992).
14. Sardanelli, F., Fausto, A., Menicagli, L. & Esseridou, A. Breast vascular mapping obtained with contrast-enhanced MR imaging: Implications for cancer diagnosis, treatment, and risk stratification. *Eur. Radiol. Suppl.* (2007). doi:10.1007/s10406-007-0228-3
15. Nishino, M., Jagannathan, J. P., Ramaiya, N. H. & Van Den Abbeele, A. D. Revised RECIST guideline version 1.1: What oncologists want to know and what radiologists need to know. *American Journal of Roentgenology* (2010). doi:10.2214/AJR.09.4110
16. Baek, J. E., Kim, S. H. & Lee, A. W. Background parenchymal enhancement in breast MRIs of breast cancer patients: Impact on tumor size estimation. *Eur. J. Radiol.* (2014). doi:10.1016/j.ejrad.2014.05.007
17. Sardanelli, F. Vessel Analysis on Contrast-Enhanced MRI of the Breast: Global or Local Vascularity? *Am. J. Roentgenol.* **195**, 1246–1249 (2010).
18. Belton, M. *et al.* Hypoxia and tissue destruction in pulmonary TB. *Thorax* (2016). doi:10.1136/thoraxjnl-2015-207402
19. Hylton, N. M. Vascularity assessment of breast lesions with gadolinium-enhanced MR imaging. *Magn. Reson. Imaging Clin. N. Am.* **9**, 321—32, vi (2001).
20. Kuhl, C. K. Current status of breast MR imaging: Part 2. Clinical applications. *Radiology* (2007). doi:10.1148/radiol.2443051661
21. Avendano, D. *et al.* Limited role of DWI with apparent diffusion coefficient mapping in breast lesions presenting as non-mass enhancement on dynamic contrast-enhanced MRI. *Breast Cancer Res.* (2019). doi:10.1186/s13058-019-1208-y
22. Bedair, R. *et al.* Effect of Radiofrequency Transmit Field Correction on Quantitative Dynamic Contrast-enhanced MR Imaging of the Breast at 3.0 T. *Radiology* **279**, 368–377 (2016).
23. Choi, E. J., Choi, H. M., Choi, S. A. & Youk, J. H. Dynamic contrast-enhanced breast

magnetic resonance imaging for the prediction of early and late recurrences in breast cancer. *Med. (United States)* (2016). doi:10.1097/MD.0000000000005330

24. Wright, H. *et al.* Increased ipsilateral whole breast vascularity as measured by contrast-enhanced magnetic resonance imaging in patients with breast cancer. in *American Journal of Surgery* (2005). doi:10.1016/j.amjsurg.2005.06.015
25. Kul, S. *et al.* Contrast-enhanced MR angiography of the breast: Evaluation of ipsilateral increased vascularity and adjacent vessel sign in the characterization of breast lesions. *Am. J. Roentgenol.* (2010). doi:10.2214/AJR.10.4368
26. Li, L. *et al.* Parameters of dynamic contrast-enhanced mri as imaging markers for angiogenesis and proliferation in human breast cancer. *Med. Sci. Monit.* (2015). doi:10.12659/MSM.892534
27. Bevilacqua, P. *et al.* Prognostic value of intratumoral microvessel density, a measure of tumor angiogenesis, in node-negative breast carcinoma - results of a multiparametric study. *Breast Cancer Res. Treat.* (1995). doi:10.1007/BF00666041
28. Fernández-Guinea, O. *et al.* Relationship between morphological features and kinetic patterns of enhancement of the dynamic breast magnetic resonance imaging and clinico-pathological and biological factors in invasive breast cancer. *BMC Cancer* (2010). doi:10.1186/1471-2407-10-8
29. Stierer, M. *et al.* Long term analysis of factors influencing the outcome in carcinoma of the breast smaller than one centimeter. *Surg. Gynecol. Obstet.* (1992).
30. Mayrhofer, R. M., Ng, H. P., Putti, T. C. & Kuchel, P. W. Magnetic Resonance in the Detection of Breast Cancers of Different Histological Types. *Magn. Reson. Insights* (2013). doi:10.4137/mri.s10640
31. Helbich, T. H. Contrast-enhanced magnetic resonance imaging of the breast. *Eur. J. Radiol.* (2000). doi:10.1016/S0720-048X(00)00200-X
32. Kelkar, P. S. *et al.* Solitary breast metastasis as the first sign of a squamous cell carcinoma of the cervix: Imaging findings. *Eur. J. Radiol.* (1997). doi:10.1016/S0720-048X(96)01080-7
33. Yi, B. *et al.* Is there any correlation between model-based perfusion parameters and model-free parameters of time-signal intensity curve on dynamic contrast enhanced MRI in breast cancer patients? *Eur. Radiol.* (2014). doi:10.1007/s00330-014-3100-6

Chapter 5. Correlations between immunohistochemistry and ^{18}F-FMISO-PET/MRI parameters of hypoxia and vascular function in breast cancer

5.1 Background

The direct measurement of oxygen pressure in tumours using polarographic oxygen electrodes is considered the gold standard method for detecting tumour hypoxia[1]. However, this method is invasive and often fails to detect the whole regions of hypoxia due to its limited sampling capability and the known heterogeneity of tumours[2]. Furthermore, oxygen probes can fail to discriminate between viable hypoxic tissue and areas of necrosis, therefore not always providing accurate information about tumour oxygenation.

Hypoxia can also be measured in tissue specimens by assessing protein expression with immunohistochemistry (IHC) using either endogenous or exogenous markers[3]. Exogeneous markers typically involve nitroimidazole compounds, such as pimonidazole and EF-5[2], which are biochemically reducible and accumulate in cells under hypoxic conditions. On the other hand, endogenous markers represent genes or proteins that are specifically upregulated in hypoxia. One of the most extensively studied endogenous hypoxia marker is hypoxia-inducible factor-1 alpha (HIF-1α), which regulates genes involved in angiogenesis, cell metabolism and apoptosis[4]. Expression levels of HIF-1α as measured by IHC are typically higher in more aggressive breast cancers since HIF-1α increases with tumour pathologic stage[5]. Furthermore, its expression has been related to increased proliferation and expression of oestrogen receptors (ER) and vascular endothelial growth factor (VEGF)[6].

Other endogenous markers, including membrane-bound hypoxia-related proteins have also been used for measuring hypoxia in tumours[7]. Those more relevant to breast cancer are carbonic anhydrase-IX (CAIX), glucose transporter 1 (GLUT 1), C-X-C chemokine receptor type-4 (CXCR4)[8] and insulin-like growth factor-1 receptor (IGF1R)[9,10]. Previous studies have shown different expression rates for these proteins on the surface of breast cancer cells, with a rate of 35% for CAIX[7].

Studies comparing ^{18}F-FMISO-PET with hypoxia endogenous markers show controversial results. In squamous cell carcinoma, Sato et al[11] showed a correlation between ^{18}F-FMISO PET

uptake and HIF-1α expression. In head and neck cancer, Norikane at al[12] reported a weak correlation between ^{18}F-FMISO hypoxic tumour volumes and HIF-1α obtained on immunohistochemical examinations. In clinical glioma studies[12,13], the correlation between ^{18}F-FMISO uptake and expression of HIF-1α was not demonstrated. This lack of correlation in gliomas may be due to the fact that in addition to hypoxia, many non-hypoxic stimuli such as cytokines and growth factors, can also activate HIF-1α[14]. Another explanation is that the up-regulation of HIF-1α is dependent on the duration and degree of hypoxia in the tumour[12].

Imaging methods, such as Positron Emission Tomography (PET) and MRI can provide a non-invasive and three-dimensional assessment of the pathophysiological properties of cancers, in principle permitting a more direct evaluation of intra-tumoral hypoxia and vascularity. PET is the preferred method for the evaluation of tumour hypoxia[15] and ^{18}F-FMISO is one of the most extensively used PET radiotracers and was the first one to be used in the clinical practice to assess tumour hypoxia. Given the inconsistencies in results of comparisons between ^{18}F-FMISO/PET, polarographic measurements and endogenous biomarkers in different types of solid tumours, we decided to establish comparisons between ^{18}F-FMISO/PET parameters and endogenous biomarkers in breast cancer. Furthermore, we aimed to establish comparisons between DCE-MRI vascular parameters and IHC markers of tumour vascularity.

Like imaging parameters of hypoxia, vascular parameters obtained from Dynamic Contrast Enhanced (DCE) MRI have also been compared to immunohistochemical biomarkers of neo-angiogenesis, such as micro-vessel density and vascular endothelial growth factor (VEGF)[16,17] to further understand the pathophysiological basis for dynamic contrast enhancement in breast cancer[18,19,20,21]. CD31, located in tumour endothelial cells, is one of the best known endogenous biomarkers for examining tumour micro-vessel density and for quantifying tumour blood vessels[22]. Its immunohistochemical expression as well as that of CD105, which is also expressed in endothelial cells of tumour capillaries[23], is a prognostic indicator of long-term outcome in breast cancer patients[23,24]. CD31 immunostaining seems to be more accurate than CD105 immunostaining[24].

Previous chapters studied the relationship between ^{18}F-FMISO-PET/MR parameters of hypoxia and vascularity in breast tumours. The purpose of this study was to determine if functional imaging parameters extracted from combined ^{18}F-FMISO-PET/MRI and DCE-MRI correlate with endogenous immunohistochemical markers of hypoxia and vascularity in

breast malignant lesions in order to assess the ability of tumour imaging markers to adequately identify hypoxia in breast cancer. Likewise, I was interested in correlating IHC markers of hypoxia and vascularity with each other. Other pathological features of the tumour such as percentage of tumour cells and stromal tumour infiltrating lymphocytes (TILs) were also analysed in this chapter due to their clinical relevance. Tumour-infiltrating lymphocytes are regarded as significant prognostic markers in patients with breast cancer[25] and they have been previously related to tumour angiogenesis, as measured by micro vessel density[26]. Information on the percentage of tumour cells is considered essential for a correct interpretation of the results from molecular testing by pathologists[27] and, previous authors[28] have reported an increase of tumour growth factors which leads to increased tumour cell proliferation under hypoxic conditions.

5.2 Methods

5.2.1 Patients

This study was approved by a National Research Ethics Committee (14/EE/0145) and the Administration of Radioactive Substances Advisory Committee (ARSAC), UK. Patients aged >18 years old with biopsy-confirmed primary breast cancer and a tumour diameter >10 mm on mammography and/or ultrasound were eligible for the study. The inclusion and exclusion criteria are provided in Chapter 3, Section 3.4. For correlations with immunohistochemistry, only patients undergoing primary surgery as part of their clinical management were included in this analysis.

5.2.2 PET/MRI acquisition

^{18}F-FMISO-PET-MR examinations were performed on a SIGNA PET-MR scanner (GE Healthcare, Waukesha, WI). Patients underwent a 60-min simultaneous PET/MR scan of the breasts 120 min after injection of a target activity of 300 MBq of ^{18}F-FMISO. The MRI protocol included a 2-point Dixon sequence for PET attenuation correction, T_1 and T_2-weighted images, DWI and a DCE series. MR sequence information is given in Chapter 3, Table 3.1. A detailed description of the PET/MR acquisition protocol is presented in Chapter 3, Section 3.4.2.

5.2.3 Image analysis

5.2.3.1 Qualitative image analysis

Three radiologists reviewed the MR images and identified malignant lesions in each patient in consensus, using information from the post-contrast T_1-weighted and subtraction images as previously described in Chapter 3, Section 3.4.3. For each cancer observed on PET/MR examinations, the following tumour characteristics were evaluated: location, size (longest diameter and tumour volume), morphology, and enhancement kinetics.

Lesion morphology and enhancement kinetics: Morphology and kinetic curve assessment used descriptors from the Fifth Edition of the ACR BI-RADS Atlas[29] as explained in Chapter 4, Section 4.2.3.1.

Tumour region of interest (ROI) delineation: Tumour regions were manually delineated in OsiriX, version 8.0.2 (Pixmeo SARL, Switzerland) on the peak-enhancing phase of the DCE-MRI series (phase 19) on all consecutive axial images encompassing the enhancing mass and including multifocal/multicentric disease. Bilateral breast cancers were treated as individual lesions[30]. The readers were blinded to the pathological findings at the time of image evaluation.

Tumour adjacent feeding vessel count: MIPs of subtraction images were used for counting adjacent feeding vessels (AFV) in tumours[31]. Either all vessels leading to the enhancing tumour mass or in contact with the edges of the lesion on the DCE-MR images were considered as AFV[32]. In cases of multifocal or multicentric breast cancers, the aggregate AFV count was calculated.

5.2.3.2 Quantitative image analysis

Quantitative analysis of DCE-MRI and PET series was performed using the methodology detailed in Chapter 3, Section 3.4.3. A brief description is provided below.

DCE-MRI: Pharmacokinetic analysis of DCE-MRI data was performed in MIStar, version 3.2.63 (Apollo Medical Imaging, Melbourne, Australia) using the extended Tofts' model to calculate the: volume transfer constant, K^{trans}, efflux rate constant, k_{ep}, extravascular-extracellular volume fraction v_e, and plasma volume fraction, v_p. Modelling utilised a

population-based arterial input function based on the modified Fritz-Hansen model. In addition to pharmacokinetic analysis, the enhancing tumour volume (ETV) was calculated for each patient using the signal enhancement ratio method[33] (Chapter 4, Section 4.2.3.2).

DWI: Calculation of apparent diffusion coefficient (ADC) maps from DWI data was performed in OsiriX, using *b*-values of 0 and 900 s/mm^2 (Chapter 3, Section 3.4.3). Mean ADC values for the whole lesion and for the darkest part of the tumour (dp-ADC) were calculated. dp-ADC measurements used a 5-mm circular region in the visually darkest area of the tumour[34,35] (Chapter 3, Section 3.4.3).

PET: The last six of the registered frames of the ^{18}F-FMISO dynamic series were averaged, registered to the peak-enhancing phase of the DCE series and employed for the determination of ^{18}F-FMISO uptake as standardised uptake values normalised by body weight (SUV_{bw}), tumour-to-plasma (T_{max}/P) and tumour-to-muscle (T_{max}/M) ratios in the ROIs defined on the DCE-MRI. The influx rate of ^{18}F-FMISO into the trapped (hypoxic) tissue compartment (K_i) was determined as a more specific measure of tumour hypoxia by using Patlak-plot analysis. Hypoxic fractions (%HF) in tumour regions were calculated as the percentage of voxels with values >2×standard deviations (SD) of the mean K_i in normoxic muscle on PET images. PET image analysis was performed in Analyze 12.0 (AnalyzeDirect Inc., Overland Park, KS). K_i maps were generated using in-house software implemented in Matlab R2016b (Mathworks Inc., Natick, MA).

5.2.4 Histology

Histopathological information including type, grade, oestrogen receptors (ER), progesterone receptors (PR) and human epidermal growth factor receptor 2 (HER2) were obtained from surgical tumour specimens. Tumours were graded using the Elston-Ellis scoring system[36]. Cancers with positive ER or PR expression were classified as hormone-receptor (HR) positive. Hormone and HER2 expressions were measured by IHC.

5.2.5 Immunohistochemistry

Following surgical excision, sections of formalin-fixed and paraffin-embedded (FFPE) tumour samples were cut at 3 μm and baked for 1 hour at 60°C before deparaffinization and rehydration on a Leica ST5020 (Leica Biosystems) as standard. All sections were subsequently loaded onto a BOND III instrument (Leica Biosystems) and pre-treated using epitope retrieval solution 1

(Cat. No. AR9961, Leica Biosystems) at 100°C for 20 minutes. Immunohistochemical staining was performed on sections containing sufficient tumour tissue using a polymer refine detection system (Cat No. DS9800, Leica Biosystems) with diaminobenzidine (DAB) enhancer (Cat No. AR9432, Leica Biosystems). Endogenous peroxidase was blocked with a 3% hydrogen peroxide solution for 5 minutes and sections were counterstained with haematoxylin and eosin.

Table 5.1 Characteristics of the antibodies used for the IHC analysis.

Target	Cat. No.	Host/Clonality	Type	Incubation time (min)	Dilution/ Concentration	Retrieval time (min)	Retrieval agent
CD31	Dako, M0823	mouse/ moAB	Primary	15	1:50/4.1 µg/ml	20	Sodium citrate
HIF-1α	Abcam, ab51608	rabbit/ moAB	Primary	15	1:100/23.36 µg/ml	20	Sodium citrate
CAIX	BioScience Slovakia, AB1001	mouse/ moAB	Primary	15	1:1000/ 1 µg/ml	20	Sodium citrate

Cat. No.: Catalogue number

Samples were stained with CD31, HIF-1α and CAIX using previously optimised conditions (see Table 5.1 for specific details). Staining for haematoxylin and eosin (H&E) was performed at a concentration of 0.1%. Following immunohistochemistry, slides were removed from the BOND III instrument, rehydrated and cleared on the Leica ST5020, and finally mounted on a Leica CV5030 (Leica Biosystems).

All stained tumour sections were visually evaluated by an expert breast histopathologist blinded to the clinicopathological and PET/MR imaging variables. The distribution of immunostaining was classified as either homogeneous or heterogeneous: uniform staining throughout the tumour tissue was considered homogeneous staining, whereas accentuated staining in either the central area or the periphery of the lesion was considered heterogeneous. For HIF-1α and CAIX immunohistochemistry, staining intensity assessment was based on a 4-point scale from 0 to 3, representing no, mild, moderate and marked immunostaining, respectively. The extent of staining was recorded as a percentage of the target tumour sample

that had positive expression of HIF-1α or CAIX. CD31-stained slides were digitalised at microscopic resolution and the following histopathological parameters were obtained using in-house software: the total number of micro-vessels, the median vessel diameter (μm), and micro-vessel density (MVD; number of vessels per mm^2). Additionally, tumour cell and stromal TIL percentages[37] were derived from all available H&E-stained slides. For tumours where more than one consecutive IHC sections were available, median parameter values were calculated and used in statistical analyses.

5.2.6 Statistical analysis

Statistical analysis was performed in IBM SPSS Statistics for MacOS, v25.0 (IBM Corp., Armonk, NY) or Matlab 2016b. Continuous data were checked for normality using the Anderson-Darling test. Correlations between continuous variables were assessed using Pearson (r) or Spearman (ρ) correlation, whereas Kendall's τ_b was used to measure correlations between ordinal or ordinal and continuous variables. Associations between nominal variables were assessed using chi-squared (χ^2) tests. Linear regression analysis was utilised for assessing the relationship between continuous imaging parameters. *t* tests were used for comparison between means of two groups, and ANOVA when more than two groups were compared. Where data were not normally distributed, or normality could not be assessed, Mann-Whitney *U* and Mood's median or Kruskal-Wallis *H* tests were employed for comparisons between two or more groups respectively. p-values <0.05 were considered statistically significant, unless otherwise indicated.

5.3 Results

The patient population for this study consisted of a group of 22 women with 24 breast cancers, who underwent primary surgery as part of their treatment plan. Clinical characteristics of the patient population are given in Table 5.2. Due to insufficient diagnostic tumour material for histopathological analysis, H&E, CD31, CAIX and HIF-1α immunohistochemistry was performed on a total of 23 cancers. However, only 22 cancers had CAIX and CD31 data available and 21 cancers had HIF-1 alpha data. Stromal TIL and tumour cell percentages were derived from 23 cancers. PET-MRI information was obtained from the 23 breast cancers with IHC information available. However, DCE-MRI quantitative parameters were only extracted from 21 breast cancers (one patient presented inadequate acquisition of the DCE-MRI series and another DCE-MRI examination was excluded due to poor quality of images) and ADC calculations were done on 12 patients (and 12 breast lesions) with a successful DWI-MRI scan.

The majority of the lesions (14/23; 61%) were invasive ductal carcinomas (IDC) with nuclear grade 2 or 3 (20/23; 87%). All tumours were HR-positive, with 18/23 (78%) cancers being negative for HER2. Tumour characteristics are presented in Table 5.3.

Table 5.2 Clinical characteristics for the patient population undergoing primary surgery (*n*=22 patients). Data are presented as mean ± standard deviation (SD) or number (%).

Characteristic	Metric
Age at diagnosis (years)[a]	59 ± 12
Menopausal status[b]	
Pre-menopausal	5 (23)
Post-menopausal	17 (77)
Disease presentation[b]	
Unilateral	20 (91)
Bilateral	2 (9)
Weight (kg)[a]	76 ± 15
BMI (kg/m^2)[a]	27.5 ± 5.2

[a]Data presented as mean ± standard deviation (SD).
[b]Data presented as number (%) patients.

With respect to the morphological features of the breast cancers evaluated (Table 5.4), the median tumour longest diameter on MRI was 24mm with a range of 10-117mm. Except for one cancer (1/23; 4%) which depicted an oval shape, all tumours showed an irregular shape (22/23). All malignant masses presented non-circumscribed margins, rim enhancement and fast initial phase enhancement. Almost half of the tumours (10/21) showed a plateau pattern[1] in the delayed phase, 43% (9/21) washout and 10% (2/21) illustrated persistent enhancement (Table 5.4). The mean number of AFV was 13 ± 9 vessels, while the median ETV was 2.26 [0.29 – 22.02] cm^3.

[1] Kinetic curve assessment was not performed in 2/23 lesions due to inadequate DCE-MRI acquisition (1 lesion) and poor kinetic curve fitting (1 lesion).

Table 5.3 Characteristics of tumours for which immunohistochemistry (IHC) information was available (*n*=23 lesions). TNM information was available for *n*=23 lesions.

Characteristic	***n* (%)**
Lesion laterality	
Left	11 (48)
Right	12 (52)
Lesion size (mm)[a]	22 [10 – 63]
Histological sub-type	
Ductal (IDC)	14 (61)
Lobular (ILC)	5 (22)
Mixed[b]	2 (9)
Mucinous (IMC)	2 (9)
Histological grade	
1	3 (13)
2	11 (48)
3	9 (39)
Molecular subtype	
HR+/HER2-	18 (78)
HR+/HER2+	5 (22)
Carcinoma *in situ*	
Absence	4 (17)
Presence	19 (83)
Tumour (T) status	
1	12 (52)
2	8 (35)
3	3 (13)
Nodal (N) status	
0	13 (57)
1	7 (30)
2	3 (13)
Metastatic (M) status	
0	23 (100)

[a]Pathological tumour size. Data are presented as median [range].

[b]Invasive carcinomas for which histology indicated the presence of both lobular and ductal components.

HR: hormone receptor; HER2: Human epidermal growth factor receptor 2.

Table 5.4 Morphological[a] and enhancement[b] characteristics of tumours for which immunohistochemistry (IHC) information was available. Data are presented as median [range], mean ± standard deviation (SD) or number (%) as appropriate.

Characteristic	Metric
Longest diameter (LD) on MRI (mm)[a,c]	24 [10 - 117]
Adjacent feeding vessels (AFV; number)[a,b,d]	13 ± 9
Volume (cm^3)[a,c]	2.38 [0.29 – 27.74]
Enhancing tumour volume (ETV; cm^3)[b,c]	2.26 [0.29 – 22.02]
Shape[a]	
Oval	1 (4)
Irregular	22 (96)
Margins[a,e]	
Non-circumscribed	
Irregular	12 (48)
Spiculated	11 (52)
Internal enhancement characteristics[a,e] (*n*=21)	
Rim enhancement	21 (100)
Signal intensity (S/I) curve description[b,e] (*n*=21)	
Initial phase	
Fast	21 (100)
Delayed phase	
Persistent (Type 1)	2 (10)
Plateau (Type 2)	10 (48)
Washout (Type 3)	9 (43)

[a]Evaluation of morphological features was performed in the 23 cancers for which IHC data was available.
[b]Internal enhancement, AFVs, ETV and signal intensity curve descriptors were evaluated in 21 of the 23 cancers for which IHC data was available.
[c]Data presented as median [range].
[d]Data presented as mean ± SD.
[e]Data presented as number (%).

5.3.1 CD31, HIF-1α and CAIX immunohistochemistry

A summary of expression values for the IHC markers used in this study is shown in Table 5.5. Representative examples of two cancers stained with HIF-1α, CAIX and CD31 are given in Figure 5.1.

In the 22 lesions stained with CD31, the median number of blood vessels was 15643 [2364 – 49074]. The mean micro vessel density (MVD) was 50.3 ± 21.9 vessels/mm^2, while the median vessel diameter was 10.10 ± 0.75 μm. The correlation between MVD and total micro vessels number (ρ=0.45; p=0.03) or diameter of micro-vessels (r=0.66; p<0.001) was statistically significant, while no correlation was observed between the number and diameter of tumour micro vessels (ρ=0.18; p=0.41).

Six out of 22 tumours (27%) stained positive for CAIX (intensity score ≥1), with all 6 lesions exhibiting heterogeneous immunostaining of either moderate (n=2 tumours) or marked (n=4 tumours) intensity. The percentage staining in CAIX-positive tumours ranged from 1 to 20% and correlated significantly with CAIX intensity scores (τ_b=0.90; p=<0.001). Among cancers positive for CAIX, 3/6 tumours (50%) were IDC with the remaining being two mucinous carcinomas (IMC) and a lobular cancer. Negative HER2 expression was found in 4/6 (67%) CAIX-positive tumours.

Positive staining for HIF-1α (intensity score ≥1) was found in 17/21 (80%) of the lesions[2], being characterised as mild (13/21 cancers; 62%) or moderate (4/21 cancers; 19%). Homogeneous staining was observed in 6/17 (35%) tumours. Of the 11 cancers with a heterogenous staining distribution, 3 (27%) presented accentuated staining in the periphery, while 8 (73%) showed central staining. There was a strong correlation between HIF-1α intensity scores and staining percentages (τ_b=0.74; p=<0.001), which varied between 2 and 20% in HIF-1α-positive tumours. Ductal cancers constituted approximately two-thirds of the lesions staining positively for HIF-1α (11/17; 65%), 3/17 (18%) were invasive lobular carcinomas (ILC), 2/17 (12%) were IMC and another one (5%) was a mixed cancer with lobular and ductal components. Negative HER2 expression was found in 12/17 (71%) tumours positive for HIF-1α.

[2] HIF-1α immunohistochemistry was performed in n=21 lesions.

Table 5.5 Summary of immunohistochemistry (IHC) results for HIF-1α, CAIX, CD31 and haematoxylin and eosin (H&E). Data are presented as number (%), median [range], mean ± standard deviation (SD) as appropriate.

Characteristic	Metric
HIF-1α[a]	
Intensity score[b]	
0	4 (19)
1	13 (62)
2	4 (19)
3	0 (0)
% Staining[c]	5 [0 – 20]
CAIX[d]	
Intensity score[b]	
0	16 (73)
1	0 (0)
2	2 (9)
3	4 (18)
% Staining[c]	0 [0 – 20]
CD31[d]	
Microvessel count (number)[c]	15643 [2364 – 49074]
Microvessel density (MVD; vessels/mm^2)[e]	50.3 ± 21.9
Microvessel diameter (μm)[e]	10.10 ± 0.75
Stromal tumour infiltrating lymphocytes (TILs; %)[c,f]	10 [0 - 70]
Tumour cells (%)[e,f]	63.0 ± 22.9

[a]HIF-1α immunohistochemistry was performed in *n*=21 lesions.
[b] Data presented as number (%).
[c]Data presented as median [range].
[d]CAIX and CD31 immunohistochemistry was performed in *n*=22 lesions.
[e]Data presented as mean ± SD.
[f]H&E immunohistochemistry was performed in *n*=23 lesions.

There was a weak level of agreement between HIF-1α and CAIX staining intensity scores (Cohen's κ = 0.1, % agreement = 23%, p=0.08) and staining percentages (ρ=0.22; p=0.33). Correlations between CD31 parameters and HIF-1α immunostaining percentages were positive and statistically significant for micro vessel density (ρ=0.47; p=0.03), but not for tumour micro vessel count (ρ=0.10; p=0.66) or micro vessel calibre (ρ=0.23; p=0.31). On the other hand, CAIX staining percentage correlated negatively with CD31 parameters, however none of these results were significant (micro vessel count: ρ=-0.08; p=0.74; MVD: ρ=-0.28; p=0.21; micro

vessel diameter: ρ=-0.31; p=0.16). Correlations between CD31 immunohistochemistry results and HIF-1α or CAIX staining intensity followed similar patterns, though also none of these were found to be significant (HIF-1α: micro vessel count: τ_b=0; p=1; MVD: τ_b=0.20; p=0.26; micro vessel diameter: τ_b=-0.01; p=0.94 | CAIX: micro vessel count: τ_b =-0.05; p=0.77; MVD: τ_b=-0.23; p=0.19; micro vessel diameter: τ_b=-0.27; p=0.13).

The percentage of stromal TILs showed non-significant negative correlations with HIF-1α, CAIX and CD31 parameters, with the exception of total micro vessel count which showed a significant negative correlation with percentage of TILs (ρ=-0.491; p=0.02). Percentage of tumour cells showed positive correlations with CAIX and HIF-1α parameters, and also with CD31 micro vessel density (correlations with HIF-1α intensity and percentages were statistically significant; ρ=0.645; p=0.004 and ρ=0.681; p=0.002, respectively). Non-significant negative correlations were seen between percentage of tumour cells and CD31-derived total count of vessels and micro vessel calibre.

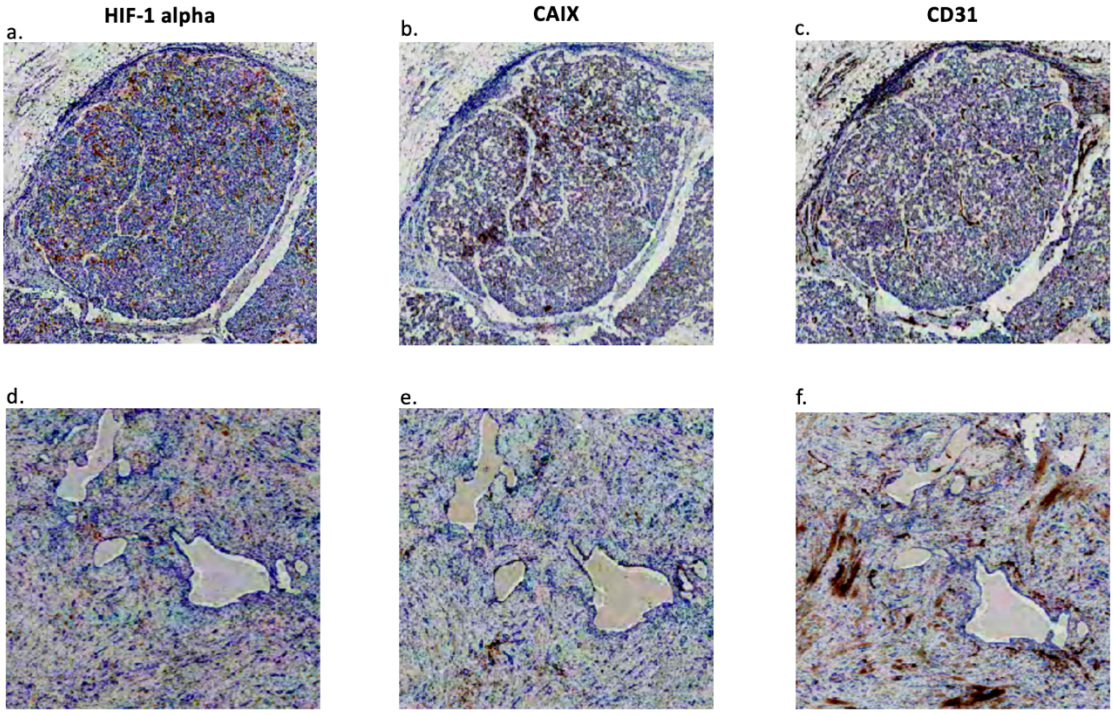

Figure 5.1. Pathological microarrays of two grade 2, HR+/HER2- breast cancers. (*Top row*) Invasive mucinous carcinoma (IMC); (*bottom row*) invasive ductal carcinoma (IDC). In both cancers there is presence of ductal carcinoma *in situ* (DCIS). Immunostaining for HIF-1α, CAIX and CD31 can be seen in brown colour. In (**a**) and (**b**) there is moderate-marked immunostaining for both HIF-1α and CAIX. The staining pattern is diffuse for HIF-1α and more focal for CAIX, whereas in (**c**) poor vascularity can be interpreted from the mild CD31 staining. The opposite occurs in the IDC lesion where there is mild HIF-1α (**d**) and CAIX (**e**) staining but marked CD31 staining (**f**).

Table 5.6 Associations between clinical variables and parameters from the expression of immunohistochemistry (IHC) markers. Correlations were computed using Kendall's τ_b, Pearson (r) or Spearman (ρ) correlation co-efficient. Associations between markers intensity scores and lesion laterality were performed using chi-squared (χ^2) tests. Asterisks denote statistically significant correlations/associations.

Parameter	Age	Weight	BMI	Menopausal status	Laterality
Intensity score	τ_b, p	τ_b, p	τ_b, p	χ^2, p	χ^2, p
HIF-1α	-0.05, 0.80	0.25, 0.19	0.19, 0.34	2.2, 0.34	2.0, 0.36
CAIX	0.09, 0.63	-0.01, 0.97	0.02, 0.93	2.9, 0.24	1.8, 0.40
% Staining	ρ, p	ρ, p	ρ, p	p	p
HIF-1α	-0.22, 0.36	0.29, 0.22	0.06, 0.81	0.29[a]	0.27[a]
CAIX	0.04, 0.86	-0.08, 0.74	-0.05, 0.82	0.63[a]	0.31[a]
CD31	ρ, p	ρ, p	ρ, p	p	p
Microvessel count	-0.30, 0.20	0.16, 0.51	0.20, 0.41	0.59[a]	0.11[a]
	r, p	r, p	ρ, p	p	p
MVD	-0.21, 0.37	0.13, 0.60	-0.07, 0.77	0.58[b]	0.73[b]
Microvessel diameter	0.02, 0.92	-0.11, 0.96	-0.05, 0.85	0.51[b]	0.69[b]
	ρ, p	ρ, p	ρ, p	p	p
Stromal TILs (%)	0.02, 0.94	-0.54, 0.009**	-0.61, 0.002**	0.21[a]	0.49[a]
	r, p	r, p	ρ, p	p	p
Tumour cells (%)	-0.30, 0.17	0.26, 0.25	-0.01, 0.96	0.10[b]	0.90[b]

[a]Mann-Whitney U test
[b]Student's t test.
*p<0.05; **p<0.01
BMI: body mass index (kg/mm^2); TILs: tumour infiltrating lymphocytes.

5.3.2 Immunohistochemistry markers *vs* clinicopathological variables

There was no statistically significant association between HIF-1α or CAIX expression parameters with clinical variables, such as patient age at diagnosis, weight, BMI, menopausal status or lesion laterality (Table 5.6). Similarly, no significant correlations were observed between these clinical parameters and the percentage of tumour cells or micro-vessel count, density, and diameter from CD31 immunostaining (Table 5.6). However, the percentage of stromal TILs presented a significant negative correlation with patient weight and BMI, indicating a potential interaction effect between these two variables in this sample of cancers (Table 5.6).

Tables 5.7 – 5.10 present IHC results with respect to standard clinicopathological variables. HIF-1α and CAIX staining intensity showed no statistically significant associations with tumour pathological size, histology, grade, the presence of *in situ* carcinoma, HER2 and nodal status (Table 5.7). CAIX staining intensity and percentages showed statistically significant negative correlations with tumour T status (Table 5.7 and Table 5.8) which was measured on the pathological slide containing the tumour's largest dimension. Similarly, tumour total vessel count obtained from CD31 immunostaining demonstrated statistically significant correlations with T status and tumour pathological size (Table 5.8). CAIX staining percentage and CD31-derived tumour total vessel count were the only IHC parameters that were significantly associated with tumour histology (Tables 5.9) with a higher percentage of CAIX-positive cells observed in IMC in comparison to other histological categories. Invasive lobular cancers exhibited a higher vessel count than other histological types examined, despite of not being bigger in size than other cancers. (Table 5.9). It should be noted that the majority of tumours in this sample were ductal carcinomas, which may have limited the evaluation of the effect of tumour histology on CAIX, HIF-1α and CD31 immuno expression. CD31 tumour vessel diameter showed a significant association with tumour HER-2 status. The diameter of tumour micro vessels was lower in HER2-positive cancers than in HER2-negative ones (Table 5.10). No significant associations were observed between IHC parameters and the presence of *in situ* carcinoma (Table 5.10).

Table 5.7 Associations between standard clinicopathological variables and staining intensity scores for HIF-1α and CAIX. Asterisks denote statistically significant correlations/associations.

Parameter	Staining intensity score	
	HIF-1α	CAIX
Pathological size (τ_b, p)[a]	-0.03, 0.86	0.03, 0.85
Histology (χ^2, p) [b]	2.22, 0.90	7.71, 0.26
Grade (τ_b, p) [a]	-0.08, 0.70	-0.04, 0.84
HER2 status (χ^2, p) [b]	1.60, 0.45	2.43, 0.30
Carcinoma *in situ* (χ^2, p) [b]	3.54, 0.17	0.57, 0.75
T stage (τ_b, p) [a]	-0.16, 0.47	-0.49, 0.02*
N stage (τ_b, p) [a]	-0.26, 0.23	-0.19, 0.37

[a]Kendall's τ_b.
[b] Chi-squared (χ^2) test.
*p<0.05; **p<0.01
HER2: Human epidermal growth factor receptor 2

Table 5.8 Spearman (ρ) and Kendall (τ_b) correlation coefficients between continuous parameters from immunohistochemistry (IHC) with respect to tumour pathological size, nuclear grade, T and N status.

Parameter	Pathological size	Grade	T stage	N stage
	ρ, p	τ_b, p	τ_b, p	τ_b, p
% Staining – HIF-1α	-0.02, 0.93	-0.10, 0.66	-0.12, 0.60	-0.12, 0.61
% Staining – CAIX	0.10, 0.65	-0.07, 0.76	-0.52, 0.02*	-0.19, 0.40
CD31 – Vessel count	0.58, 0.005**	0.16, 0.48	0.61, 0.004**	0.06, 0.78
CD31 – MVD	0.11, 0.62	0.13, 0.58	0.17, 0.47	0.03, 0.90
CD31 – Vessel diameter	-0.13, 0.59	0.02, 0.92	0.05, 0.83	0.06, 0.81
Stromal TILs (%)	-0.27, 0.21	-0.08, 0.71	-0.42, 0.05	0.17, 0.46
Tumour cells (%)	0.02, 0.93	-0.07, 0.77	-0.29, 0.19	-0.29, 0.19

*p<0.05; **p<0.01
MVD: Micro-vessel density (vessels/mm^2); TILs: tumour infiltrating lymphocytes.

Table 5.9 Continuous parameters from immunohistochemistry (IHC) with respect to tumour histology. Data are presented as median [range].

Parameter	IDC	ILC	IMC	Mixed	*p*
Lesions (*n*=21)	*14*	*4*	*2*	*1*	
% Staining – HIF-1α	5 [0 – 20]	2 [0 – 20]	5 [5 – 5]	2 [2 – 2]	0.88[a]
Lesions (*n*=22)	*14*	*4*	*2*	*2*	
% Staining – CAIX	0 [0 – 10]	0 [0 – 5]	15 [10 – 20]	0 [0 – 0]	0.04*[b]
CD31 – Vessel count	15375 [2364 – 38201]	20088 [13471 – 49074]	17658 [15439 – 19878]	11827 [10567 – 13087]	0.046*[c]
CD31 – MVD	51.72 [11.81 – 94.66]	40.31 [30.61 – 91.71]	41.22 [40.64 – 41.81]	40.84 [33.19 – 48.49]	0.91[a]
CD31 – Vessel diameter	10.31 [8.66 – 11.87]	9.44 [8.91 – 10.27]	9.96 [9.78 – 10.13]	10.14 [9.72 – 10.57]	0.37[a]
Lesions (*n*=23)	*15*	*4*	*2*	*2*	
Stromal TILs (%)	10 [0 – 50]	5 [0 – 10]	40 [2 – 70]	20 [20 – 20]	0.79[d]
Tumour cells (%)	70 [25 – 90]	80 [25 – 95]	73 [50 – 95]	48 [35 – 60]	0.61[a]

[a]Mood's median test.
[b]Multinomial logistic regression of tumour histology *vs* % staining for CAIX adjusted for an interaction between T stage and % staining for CAIX. The *p* value from the unadjusted model was *p*=0.01. Inclusion of an interaction term was based on results given in Table 5.8.
[c]Multinomial logistic regression of tumour histology *vs* CD31 micro-vessel count adjusted for the interaction between vessel count and T stage (*p*=0.04). Adjustment for an interaction between pathological size and micro-vessel count yielded *p*=0.47. The *p* value from the unadjusted model was *p*=0.35. Inclusion of an interaction term was based on results given in Table 5.8.
[d]Multinomial logistic regression of tumour histology *vs* % stromal tumour infiltrating lymphocytes (TILs) adjusted for the interaction between BMI and % staining for CAIX. Adjustment for an interaction between weight and % staining for CAIX yielded *p*=0.31. The *p* value from the unadjusted model was *p*=0.11. Inclusion of an interaction term was based on results given in Table 5.8.
IDC: invasive ductal carcinoma; ILC: invasive lobular carcinoma; IMC: invasive mucinous carcinoma; Mixed: invasive carcinoma with ductal and lobular components; MVD: Micro-vessel density (micro vessels/mm^2); TILs: tumour infiltrating lymphocytes.

Table 5.10 Continuous parameters from immunohistochemistry (IHC) with respect to tumour HER2 status and the presence of carcinoma *in situ*. Data are presented as median [range] or mean ± standard deviation (SD).

	HER2 status			Carcinoma *in situ*		
Parameter	**Negative**	**Positive**	***p***	**Absent**	**Present**	***p***
Lesions (*n*=21)	*16*	*5*		*4*	*17*	
% Staining – HIF-1α	5 [0 – 20]	2 [1 – 5]	0.35[a]	1 [0 – 5]	5 [0 – 20]	0.14[a]
Lesions (*n*=22)	*17*	*5*		*4*	*18*	
% Staining – CAIX	0 [0 – 20]	0 [0 – 10]	0.80[b]	0 [0 – 10]	0 [0 – 20]	0.84[e]
CD31 – Vessel count	16604 [2364 – 49074]	13471 [3469 – 19440]	0.12[c]	17391 [9403 – 28525]	15643 [2364 – 49074]	0.34[f]
CD31 – MVD	54.6 ± 21.9	35.6 ± 16.1	0.09[d]	38.0 ± 24.8	44.2 ± 11.8	0.47[d]
CD31 – Vessel diameter	10.31 ± 0.68	9.40 ± 0.54	0.01*[d]	10.14 ± 0.47	10.09 ± 0.81	0.90[d]
Lesions (*n*=23)	*18*	*5*		*4*	*19*	
Stromal TILs (%)	10 [0 – 70]	5 [0 – 30]	0.62[a]	8 [2 – 30]	10 [0 – 70]	0.71[a]
Tumour cells (%)	63 ± 22	62 ± 29	0.91[d]	45 [30 – 50]	75 [25 – 95]	0.06[a]

[a]Mann-Whitney *U* test.
[b]Binomial logistic regression of HER2 status *vs* % staining for CAIX adjusted for an interaction between T stage and % staining for CAIX. The *p* value from the unadjusted model was *p*=0.73. Inclusion of an interaction term was based on results given in Table 5.8.
[c]Binomial logistic regression of HER2 status *vs* CD31 micro-vessel count adjusted for the interaction between vessel count and T stage. Adjustment for an interaction between pathological size and micro-vessel count yielded *p*=0.83. The *p* value from the unadjusted model was *p*=0.35. Inclusion of an interaction term was based on results given in Table 5.8.
[d]Student's *t* test.
[e]Binomial logistic regression of carcinoma *in-situ* status *vs* % staining for CAIX adjusted for an interaction between T stage and % staining for CAIX. The *p* value from the unadjusted model was *p*=0.73. Inclusion of an interaction term was based on results given in Table 5.8.
[f]Binomial logistic regression of carcinoma *in-situ* status *vs* CD31 micro-vessel count adjusted for the interaction between vessel count and T stage. The *p* value from the unadjusted model was *p*=0.74. Inclusion of an interaction term was based on results given in Table 5.8.
HER2: human epidermal growth factor 2; MVD: micro-vessel density (micro vessels/mm2); TILs: tumour infiltrating lymphocyte

5.3.3 Associations between immunohistochemistry markers and radiological descriptors

Table 5.11 presents associations of IHC parameters with morphological or enhancement descriptors from DCE-MRI. The number of tumour micro vessels and HIF-1α staining intensity were the only IHC parameters exhibiting significant correlations with morphology or enhancement descriptors (Table 5.11). Moderate-strong positive correlations were observed between CD31 micro vessel count and tumour longest diameter on MRI (LD), volume, number of AFV and ETV (Table 5.11). Additionally, cancers with spiculated margins tended to display significantly lower HIF-1α intensity scores than those with irregular boundaries (0.73 ± 0.45 *vs* 1.33 ± 0.71, respectively). The intensity and percentage of HIF-1$^{\alpha}$ immunostaining showed positive correlations with tumour kinetic-curve type, and these results almost reached statistical significance. CAIX intensity and percentage also showed positive corelations with the type of tumour curve. The highest median of CAIX staining intensity scores and percentages were observed in cancers with a type 3 kinetic curve (2 [0-3] and 1 [0-10], respectively). Similarly, the highest median HIF-1 alpha intensity and percentages (1 [0-2] and 2 [0-20], respectively) were observed in cancers with kinetic curve type 3. ER positive cancers with a kinetic curve type 3 also presented the highest mean (20245.7 ± 2634.7) of total tumour vessels and the highest median (56.379 [11.809-91.707]) of tumour micro-vessels density. On the other hand, the cancers with a kinetic curve type 2 presented the highest mean (3.092 ± 2.561) of micro-vessels calibre. Negative correlations, which were close to statistical significance, were obtained between the percentage of expression of stromal TILs and tumour volume or ETV (Table 5.11).

Given the significant association between the number of AFV and the tumour longest diameter or volume reported in Chapter 4 (see Section 4.3.4), relationships between IHC parameters and AFV were also explored using regression analysis adjusted for an interaction effect between tumour size and the number of feeding vessels. In the pre-surgical sample of cancers considered in this chapter, there was a significant positive correlation between the number of AFV and the tumour longest diameter (ρ=0.50, p=0.01), whereas the correlation between AFV and tumour volume was close to statistical significance (ρ=0.39, p=0.07). Linear or ordinal regression analysis between continuous or ordinal IHC variables, respectively, with AFV adjusted for an interaction between AFV and either tumour LD or volume, did not alter the significance of the associations presented in Table 5.11, except for % HIF-1α staining, which exhibited a negative association with AFV when an interaction effect of the tumour longest diameter was included in the model (slope estimate: -0.01, R^2=0.42, p=0.003).

Table 5.11 Associations between immunohistochemistry (IHC) parameters and tumour morphological or enhancement characteristics. Correlation coefficients (CC) and *p* values were computed to describe relationships between continuous IHC and radiological parameters, whereas chi-squared ($\chi 2$) tests were used to test the association between nominal and ordinal variables. Associations between continuous IHC parameters and margin type were evaluated using independent two-sample tests as appropriate.

Parameter	LD CC, *p*	Volume CC, *p*	Margins *p*	AFV CC, *p*	ETV CC, *p*	Delayed enhancement type CC, *p*
HIF-1α – Intensity score[a]	0.06[a], 0.77	0.01[a], 0.94	0.045*[c]	-0.08[a], 0.68	0.03[a], 0.87	0.42[a], 0.05
HIF-1α – % Staining[b]	0.01[b], 0.69	0.00[b], 0.99	0.25[d]	-0.27[b], 0.25	0.06[b], 0.81	0.36[a], 0.09
CAIX – Intensity score[a]	-0.03[a], 0.90	-0.18[a], 0.32	0.99[e]	0.03[a], 0.88	-0.14[a], 0.47	0.31[a], 0.15
CAIX – % Staining[b]	-0.09[b], 0.69	-0.28[b], 0.22	0.97[d]	-0.07[b], 0.76	-0.23[b], 0.33	0.34[a], 0.11
CD31 – Vessel count	0.70[b], <.001***	0.68[b], 0.001**	0.35[d]	0.47[b], 0.03*	0.67[b], 0.002**	0.03[a], 0.89
CD31 – MVD	0.13[b], 0.59	0.07[b], 0.75	0.30[e]	0.27[g], 0.23	0.13[b], 0.60	0.01[a], 0.94
CD31 – Vessel diameter	-0.10[b], 0.67	-0.19[b], 0.40	0.90[f]	0.03[g], 0.90	-0.12[b], 0.60	-0.11[a], 0.56
Stromal TILs (%)	-0.35[b], 0.11	-0.37[b], 0.09	0.31[d]	-0.34[b], 0.12	-0.42[b], 0.06	0.17[a], 0.40
Tumour cells (%)	-0.10[b], 0.69	-0.03[b], 0.89	0.99[f]	-0.13[b], 0.56	-0.02[b], 0.92	0.23[a], 0.23

[a]Kendall's τ_b.
[b]Spearman's ρ
[c]Chi-squared (χ^2) test
[d]Mann-Whitney *U* test
[e]Welch's *t* test
[f]Student's *t* test
[g]Pearson's *r*
*p<0.05; **p<0.01; ***p<0.001
LD: tumour longest diameter on MRI (mm); Volume: tumour volume (cm^3); AFV: adjacent feeding vessels; ETV: enhancing tumour volume (cm^3); MVD: micro vessel density (vessels/mm^2); TILs: tumour infiltrating lymphocytes.

Table 5.12 Kendall's τ_b and p values for the correlation between HIF-1α and CAIX intensity scores and ^{18}F-FMISO-PET/MRI parameters. Asterisks denote statistically significant correlations.

	Staining intensity scores	
	HIF-1α	**CAIX**
Parameter	τ_b, p	τ_b, p
DCE-MRI		
K^{trans}	0.13, 0.51	0.17, 0.37
hs-K^{trans}	-0.09, 0.62	-0.02, 0.93
k_{ep}	0.01, 0.97	-0.11, 0.57
v_e	-0.08, 0.68	-0.09, 0.63
v_p	0.09, 0.62	0.12, 0.52
DWI		
ADC	0.00, 1.00	0.30. 0.25
dp-ADC	-0.14, 0.58	0.31, 0.26
PET		
K_i	-0.15, 0.41	0.36, 0.046*
%HF	-0.03, 0.88	0.24, 0.25
SUV_{max}	-0.02, 0.93	-0.03, 0.87
SUV_{mean}	-0.02, 0.94	-0.03, 0.88
T_{max}/M	0.06, 0.77	-0.09, 0.63
T_{max}/P	0.19, 0.32	0.11, 0.57

$^{*}p<0.05$; $^{**}p<0.01$

K^{trans}: contrast influx rate (mL/g/min); k_{ep}: contrast efflux rate (min^{-1}); v_e: fractional volume of extravascular-extracellular space; v_p: plasma fractional volume; ADC: apparent diffusion coefficient (mm^2/s); dp-ADC: ADC (mm^2/s) in the darkest part of the tumour; K_i: ^{18}F-FMISO influx rate ($mL/cm^3/min$); %HF: percentage hypoxic fraction; SUV: standardised uptake value (g/mL); T_{max}/M: tumour-to-muscle ratio; T_{max}/P: tumour-to-plasma ratio.

5.3.4 Correlations between immunohistochemistry biomarkers and PET/MRI parameters

Table 5.12 presents correlations between HIF-1α and CAIX staining intensity *vs* MRI and PET parameters. ^{18}F-FMISO-PET/MRI revealed hypoxic fractions higher than 0% in 8 out of 23 cancers. Results from the linear regression of ^{18}F-FMISO-PET/MRI metrics vs continuous IHC parameters are shown in Tables 5.13, 5.14 and 5.15. Scatter plots illustrating the relationships between K^{trans} and ^{18}F-FMISO K_i *vs* HIF-1α, CAIX or CD31 immunohistochemistry are illustrated in Figures 5.2 and 5.3. Plots indicating relationships between IHC and DCE-MRI pharmacokinetic parameters, DWI ADC *vs* HIF-1α and CAIX staining percentages or CD31 immunohistochemistry are shown in Figures 5.4 and Figures 5.5 – 5.6 respectively.

No associations were observed between DCE-MRI pharmacokinetic parameters and HIF-1α or CAIX immunohistochemistry (Tables 5.12 and 5.13; Figures 5.2 and 5.4). Similarly, ^{18}F-FMISO PET parameters were not significantly associated with HIF-1α or CAIX immunohistochemistry results (Tables 5.12 and 5.13), except for K_i which showed a significant positive association with both the intensity and percentage of CAIX immunostaining (Tables 5.12 and 5.13, respectively; Figures 5.2). Additionally, a statistically significant positive association was found between ADC values in the darkest part of the tumour (dp-ADC) and CAIX percentages (Table 5.13; Figure 5.4).

Table 5.13 Fixed effects estimates (β) together with confidence intervals (CI) and *p* values from linear regression of MRI and PET parameters *vs* HIF-1α or CAIX staining percentage. Associations between the percentage of hypoxic fraction (%HF) and HIF-1α or CAIX staining percentages were calculated using Kendall's τ_b. Asterisks denote statistically significant *p* values.

	% Staining	
	HIF-1α	**CAIX**
Parameter	β, [CI], *p*	β, [CI], *p*
DCE-MRI		
K^{trans}	0.245, [-4.178 – 4.666], 0.90	0.062, [-4.640 – 4.764], 0.98
hs-K^{trans}	3.289, [-3.792 – 10.369], 0.34	-4.192, [-11.649 – 3.265], 0.25
k_{ep}	0.177, [-0.355 – 0.710], 0.49	-0.102, [-0.673 – 0.469], 0.71
v_e	-0.707, [-2.554 – 1.140], 0.43	-0.751, [-2.725 – 1.224], 0.44
v_p	0.055, [-1.149 – 1.260], 0.92	0.010, [-1.273 – 1.293], 0.99
DWI		
ADC ($\times10^{-3}$)	4.702, [-13.176 – 22.581] 0.57	6.432, [-1.278 – 14.142], 0.09
dp-ADC ($\times10^{-3}$)	4.857, [-10.333 – 20.047] 0.49	6.867, [1.022 – 12.711], 0.03*
PET		
K_i ($\times10^{-3}$)	-0.003, [-0.009 – 0.002], 0.21	0.009, [0.002 – 0.014], <.001***
%HF[a]	-0.06, 0.75	0.30, 0.14
SUV_{max}	-1.26, [-4.46 – 1.93], 0.42	-1.86, [-5.10 – 1.39], 0.25
SUV_{mean}	-0.74, [-2.76 – 1.25], 0.44	-0.80, [-2.87 – 1.27], 0.43
T_{max}/M	-0.38, [-2.65 – 1.90], 0.73	0.67, [-3.08 – 1.73], 0.56
T_{max}/P	0.92, [-0.86 – 2.70], 0.29	0.26, [-1.66 – 2.18], 0.78

[a]Kendall's τ_b.
$^{*}p<0.05$; $^{**}p<0.01$; $^{***}p<0.001$
K^{trans}: contrast influx rate (mL/g/min); k_{ep}: contrast efflux rate (min^{-1}); v_e: fractional volume of extravascular-extracellular space; v_p: plasma fractional volume; ADC: apparent diffusion coefficient (mm^2/s); dp-ADC: ADC (mm^2/s) in the darkest part of the tumour; K_i: ^{18}F-FMISO influx rate ($mL/cm^3/min$); %HF: percentage hypoxic fraction; SUV: standardised uptake value (g/mL); T_{max}/M: tumour-to-muscle ratio; T_{max}/P: tumour-to-plasma ratio.

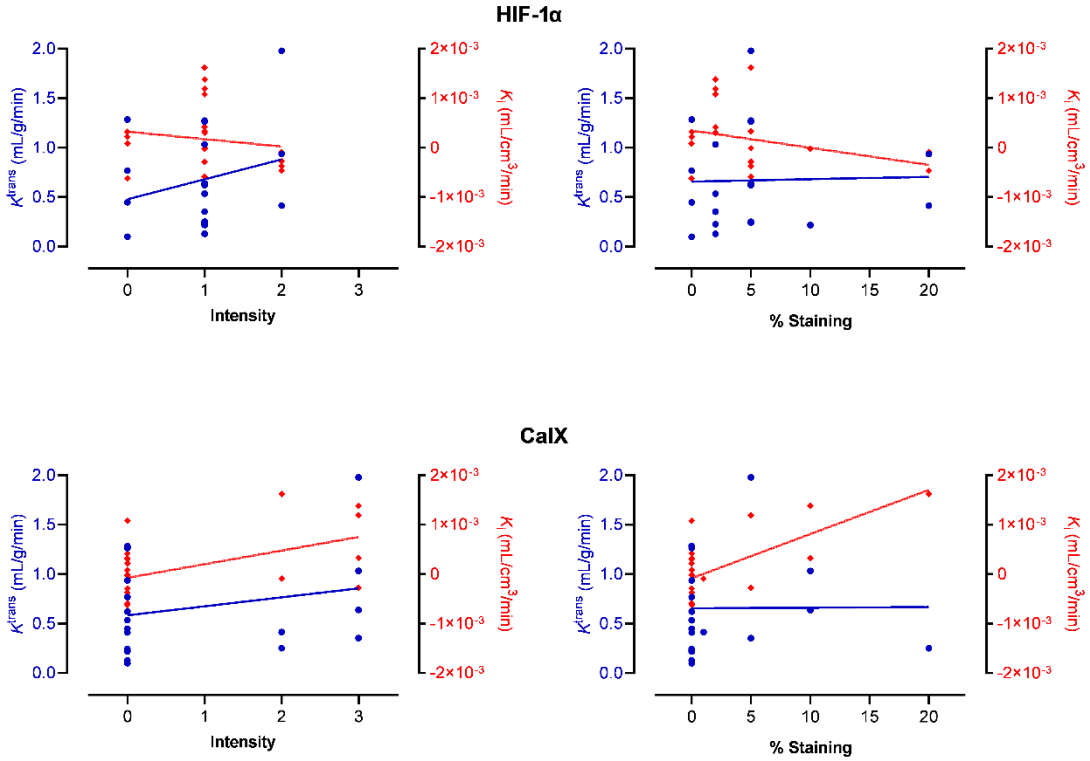

Figure 5.2: Scatter plots and regression lines of the contrast influx rate K^{trans} (mL/g/min) from DCE-MRI and the ^{18}F-FMISO influx rate K_i (mL/cm^3/min) *vs* HIF-1α or CAIX staining intensity (*left column*) and percentage (*right column*).

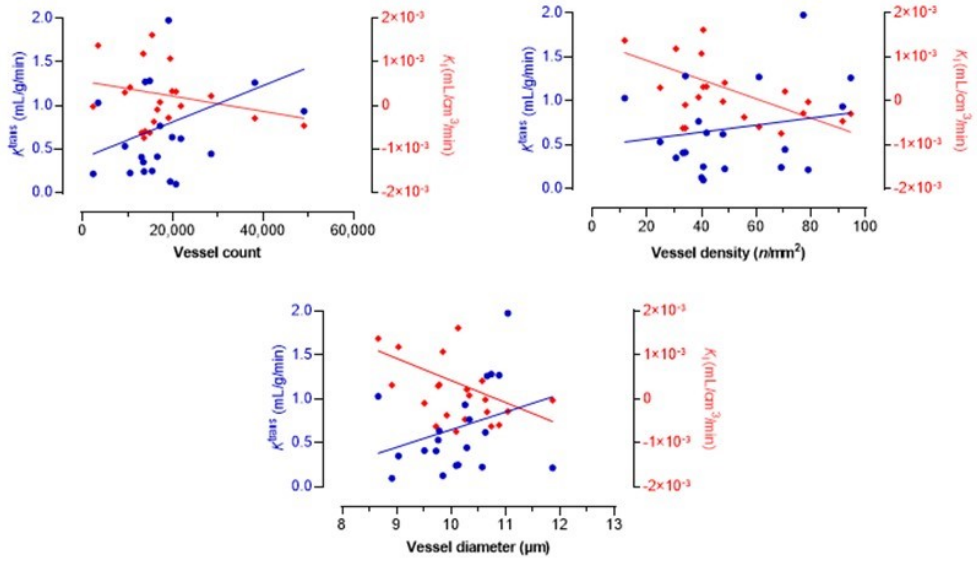

Figure 5.3: Scatter plots and regression lines of the contrast influx rate K^{trans} (mL/g/min) from DCE-MRI and the ^{18}F-FMISO influx rate K_i (mL/cm^3/min) *vs* the CD31 parameters of tumour micro vessel count, micro vessel density (MVD; number of micro vessels/mm^2) in the top row, and vessel diameter (μm).

Table 5.14 Fixed effects estimates (β) together with confidence intervals (CI) and *p* values from linear regression of MRI and PET parameters *vs* HIF-1α or CAIX staining percentage. Associations between the percentage hypoxic fraction (%HF) and HIF-1α or CAIX percent staining were calculated using Kendall's τ_b. Asterisks denote statistically significant *p* values.

Parameter	CD31 Microvessel count β, [CI], p	CD31 MVD β, [CI], p	CD31 Microvessel diameter β, [CI], p
DCE-MRI			
K^{trans}	1.12×10^{-5}, [$-1.10 – 3.34$] $\times10^{-5}$, 0.30	0.006, [-0.04 – 0.017], 0.21	0.208, [-0.09 – 0.51], 0.17
hs-K^{trans}	2.17×10^{-5}, [$-1.44 – 5.79$] $\times10^{-5}$, 0.22	-8.354×10^{-4}, [-0.001 – 0.001], 0.74	-0.310, [-0.812 – 0.193], 0.21
k_{ep}	6.73×10^{-7}, [$-2.01 – 3.44$] $\times10^{-6}$, 0.62	-0.102, [-0.673 – 0.469], 0.71	-0.006, [-0.045 – 0.032], 0.73
v_e	7.82×10^{-7}, [$-9.00 – 1.06$] $\times10^{-5}$, 0.87	0.002, [-0.003 – 0.006], 0.46	0.104, [-0.022 – 0.230], 0.10
v_p	2.78×10^{-6}, [$-3.32 – 8.87$] $\times10^{-6}$, 0.35	0.002, [-0.001– 0.005], 0.11	0.073, [-0.006 – 0.152], 0.07
DWI			
ADC	4.702, [-13.176 – 22.581] 0.57	-0.004, [-0.018 – 0.011], 0.60	-0.017, [-0.502 – 0.468], 0.94
dp-ADC	4.857, [-10.333 – 20.047] 0.49	-0.003, [-0.016 – 0.009], 0.60	-0.063, [-0.476 – 0.350], 0.74
PET			
K_i	-1.75×10^{-8}, [$-4.78 – 1.28$] $\times10^{-8}$, 0.24	-1.56×10^{-5}, [-2.83×10^{-5} – -2.86×10^{-6}], 0.02*	-4.34×10^{-4}, [-8.19×10^{-4} – -4.84×10^{-6}], 0.03*
%HF[a]	-0.13, 0.47	-0.21, 0.24	-0.22, 0.21
SUV_{max}	1.19×10^{-5}, [$-3.88 – 2.77$] $\times10^{-5}$, 0.13	-2.78×10^{-4}, [-0.008 – 0.008], 0.94	-0.022, [-0.251 – 0.206], 0.84
SUV_{mean}	4.83×10^{-6}, [$-5.42 – 1.51$] $\times10^{-5}$, 0.34	-2.29×10^{-4}, [-0.005 – 0.005], 0.92	-0.010, [-0.133 – 0.152], 0.88
T_{max}/M	6.60×10^{-6}, [$-5.09 – 1.83$] $\times10^{-5}$, 0.25	-1.16×10^{-4}, [-0.006 – 0.006], 0.97	0.069, [-0.207 – 0.119], 0.58
T_{max}/P	4.30×10^{-5}, [$-5.10 – 1.37$] $\times10^{-5}$, 0.35	0.001, [-0.003 – 0.006], 0.57	0.62, [-0.065 – 0.189], 0.32

[a]Kendall's τ_b.

$^{*}p<0.05$; $^{**}p<0.01$; $^{***}p<0.001$

K^{trans}: contrast influx rate (mL/g/min); k_{ep}: contrast efflux rate (min^{-1}); v_e: fractional volume of extravascular-extracellular space; v_p: plasma fractional volume; ADC: apparent diffusion coefficient (mm^2/s); dp-ADC: ADC (mm^2/s) in the darkest part of the tumour; K_i: ^{18}F-FMISO influx rate ($mL/cm^3/min$); %HF: percentage hypoxic fraction; SUV: standardised uptake value (g/mL); T_{max}/M: tumour-to-muscle ratio; T_{max}/P: tumour-to-plasma ratio.

Table 5.15 Fixed effects estimates (β) together with confidence intervals (CI) and *p* values from linear regression of MRI and PET parameters *vs* the percent expression of stromal tumour infiltrating lymphocytes (%TILs) and tumour cells. Kendall's τ_b. Asterisks denote statistically significant *p* values.

Parameter	% TILs CC, *p*	% Tumour Cells CC, *p*
DCE-MRI		
K^{trans}	-0.610, [-1.918 – 0.699], 0.98	-0.166, [-1.167 – 0.834], 0.73
hs-K^{trans}	-1.617, [-3.996 – 0.763], 0.17	-0.445, [-2.305 – 1.416], 0.62
k_{ep}	-0.064, [-0.218 – 0.090], 0.39	0.025, [-0.091 – 0.142], 0.45
v_e	-0.319, [-0.931 – 0.292], 0.29	-0.334, [-0.777 – 0.110], 0.13
v_p	-0.159, [-0.517 – 0.199], 0.36	-0.009, [-0.283 – 0.265], 0.94
DWI		
ADC ($\times10^{-3}$)	1.486, [-3.243 – 3.380], 0.96	-1.101, [-2.674 – 0.472], 0.15
dp-ADC ($\times10^{-3}$)	-0.072, [-2.907 – 2.763], 0.96	-0.641, [-2.073 – 0.791], 0.34
PET		
K_i ($\times10^{-3}$)	0.001, [-0.001 – 0.003], 0.38	3.1×10^{-4}, [-0.001 – 0.002], 0.65
%HF[a]	0.19, 0.28	0.20, 0.25
SUV_{max}	-0.92, [-1.76 – -0.08], 0.03*	-0.16, [-0.88 – 0.56], 0.65
SUV_{mean}	-0.47, [-1.03 – 0.08], 0.09	-0.21, [-0.66 – 0.23], 0.33
T_{max}/M	-0.09, [-1.10 – 0.21], 0.17	0.02, [-0.51 – 0.54], 0.95
T_{max}/P	-0.09, [-0.58 – 0.40], 0.71	0.22, [-0.14 – 0.58], 0.22

[a]Kendall's τ_b.
$^{*}p<0.05$; $^{**}p<0.01$; $^{***}p<0.001$
K^{trans}: contrast influx rate (mL/g/min); k_{ep}: contrast efflux rate (min^{-1}); v_e: fractional volume of extravascular-extracellular space; v_p: plasma fractional volume; ADC: apparent diffusion coefficient (mm^2/s); dp-ADC: ADC (mm^2/s) in the darkest part of the tumour; K_i: ^{18}F-FMISO influx rate ($mL/cm^3/min$); %HF: percentage hypoxic fraction; SUV: standardised uptake value (g/mL); T_{max}/M: tumour-to-muscle ratio; T_{max}/P: tumour-to-plasma ratio.

The associations between DCE-MRI parameters and the percentage expression of stromal TILs or tumour cells were negative and not statistically significant (Table 5.15). ^{18}F-FMISO K_i and %HF showed positive relationships with these IHC parameters, which were not statistically significant (Table 5.15). On the other hand, ^{18}F-FMISO parameters were negatively associated with percentages of TIL expression, with SUV_{max} being the only parameter exhibiting a statistically significant *p* value (Table 5.15). Mean whole lesion ADC showed a positive relationship with TILs (%) and a negative relationship with the percentage of tumour cells which were not statistically significant (Table 5.15). ADC from the darkest part of the tumour showed non-significant negative correlations with percentages of TILs and tumour cells.

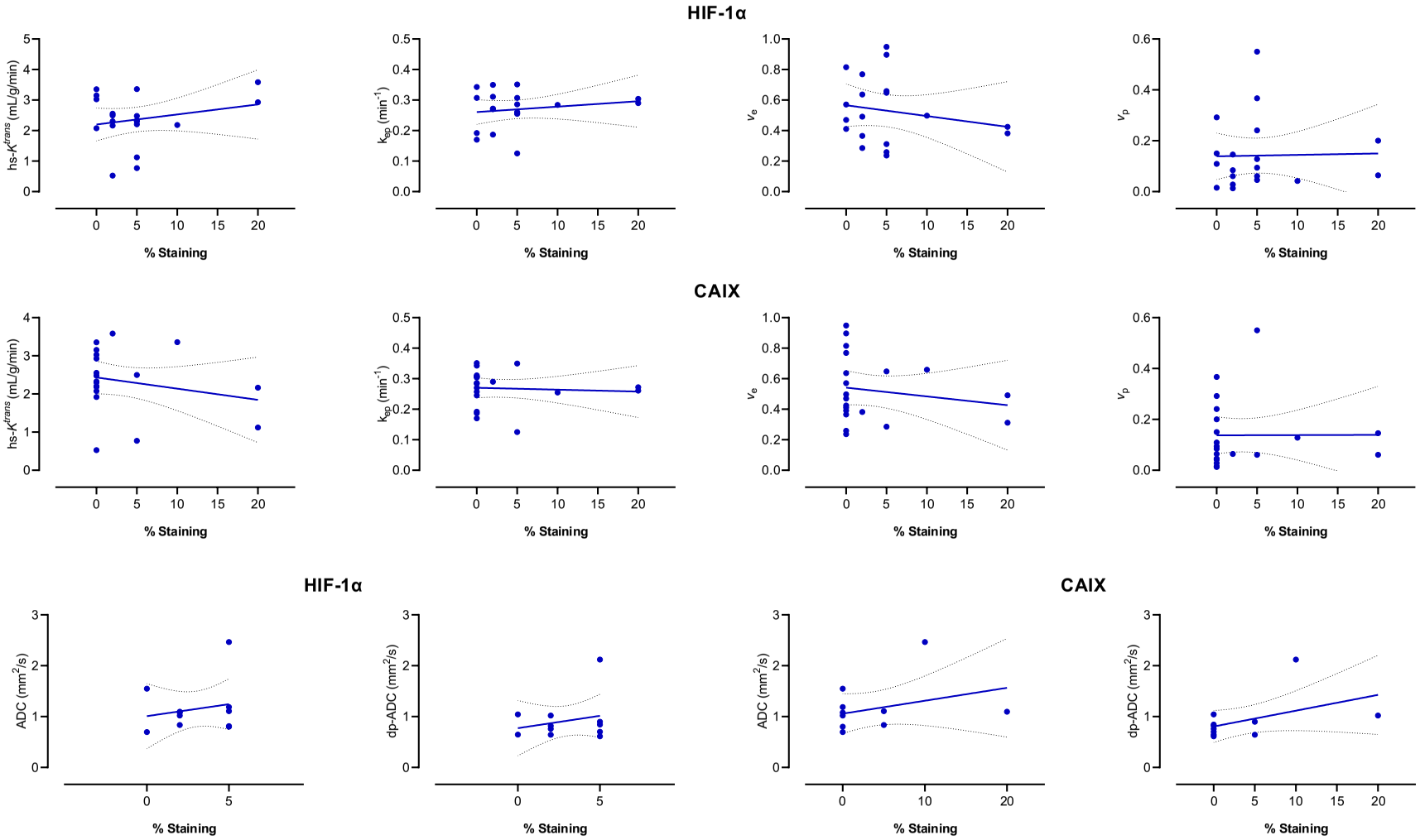

Figure 5.4 Scatter plots and regression lines of the DCE-MRI parameters: hotspot contrast influx rate, hs-K^{trans} (mL/g/min); contrast efflux rate, k_{ep} (min^{-1}), volume of the extravascular-extracellular space, v_e, and plasma fraction, v_p *vs* HIF-1α (*top row*) or CAIX (*middle row*) staining percentage. (*Bottom row*) Mean apparent diffusion coefficient (ADC; mm^2/s) in the whole tumour lesion and ADC of the darkest part of the tumour (dp-ADC) vs HIF-1α or CAIX staining percentage.

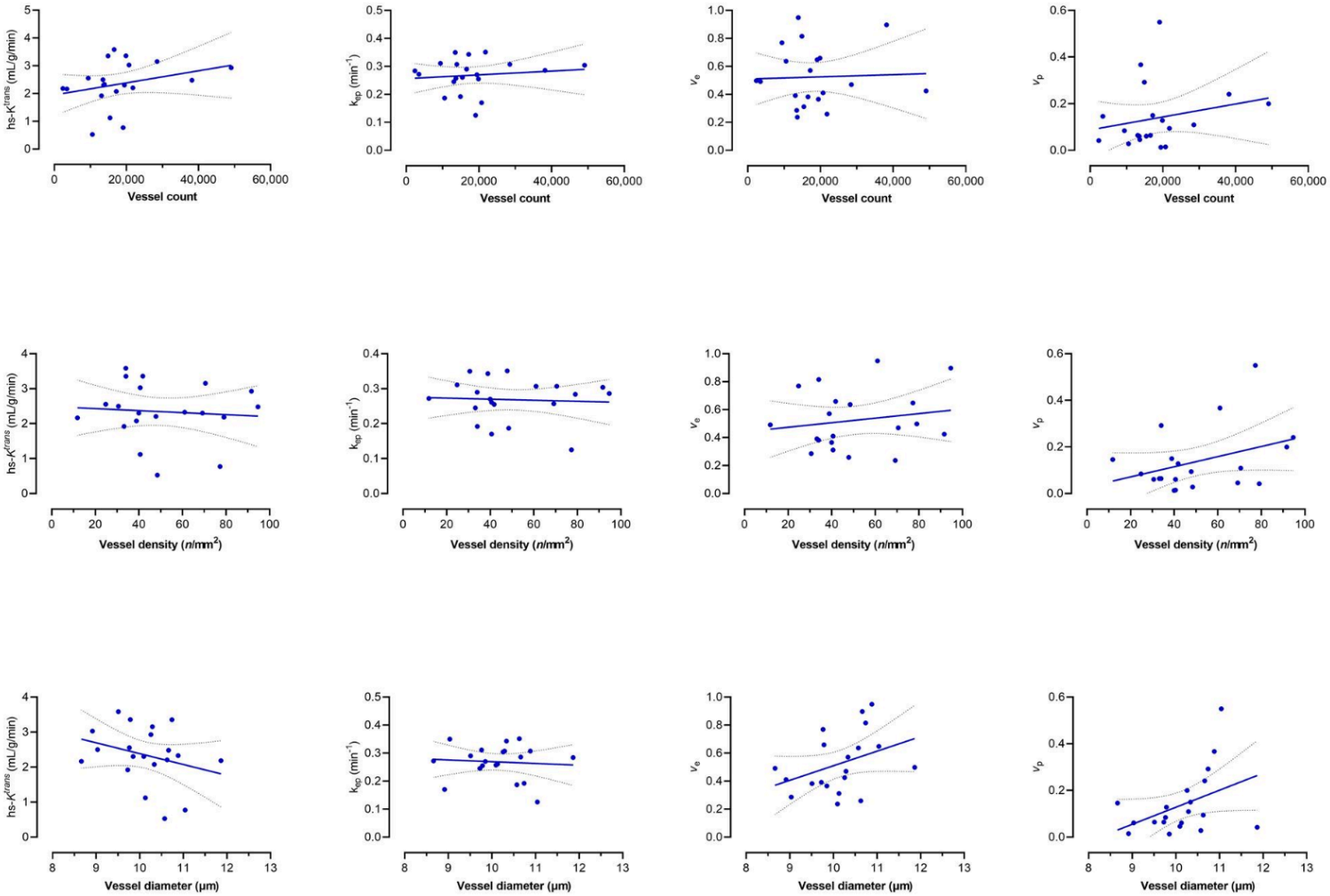

Figure 5.5 Scatter plots and regression lines with 95% confidence intervals for the following DCE-MRI parameters: hotspot contrast influx rate, hs-K^{trans} (mL/g/min); contrast efflux rate, k_{ep} (min^{-1}), volume of the extravascular-extracellular space, v_e, and plasma fraction, v_p *vs* CD31 micro vessel counts (*top row*), micro vessel density (MVD; *middle row*) and vessel diameter (*bottom row*)

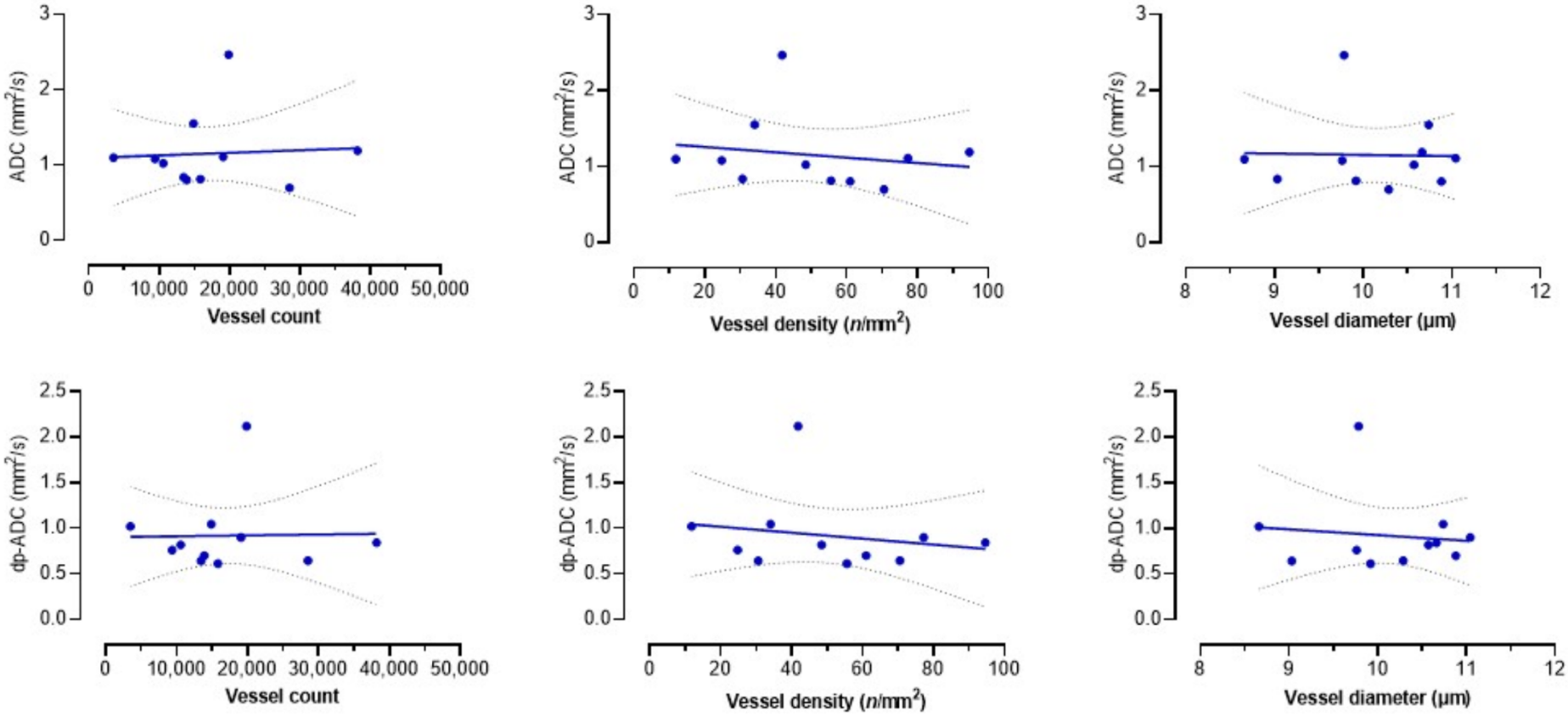

Figure 5.6 Scatter plots and regression lines with 95% confidence intervals for (*top row*) mean whole lesion apparerent diffusion coefficient (ADC; mm^2/s) and (*bottom row*) the darkest part of the tumour ADC (dp-ADC) *vs* CD31 micro vessel counts (*left column*), micro vessel density (MVD; *middle column*) and micro vessel diameter (*right column*).

5.4 Discussion

The aim of our study was to determine if functional imaging parameters extracted from hybrid PET-MRI and DCE-MRI correlate with endogenous immunohistochemical markers of hypoxia and vascularity in ER+ breast cancers. Therefore, we correlated IHC biomarkers with ^{18}F-FMISO-PET/MRI parameters from ER+ breast cancers. Immunohistochemistry analysis of CAIX, HIF-1α and CD31 was performed in tumour slides containing the highest proportion of tumour tissue.

The median tumour size after surgical excision was 22mm, ranging between 10 and 63mm, whereas the median MRI tumour longest axis was 24mm with a range of 10-117mm. As it is widely known, ER+ breast masses are smaller in comparison to ER- breast cancers[16]. We found a statistically significant positive correlation between tumour pathological size and tumour longest axis from MRI (r=0.746, p=0.000).

Even though the histological groups of cancers were unbalanced, CAIX expression was higher in IMC than in other cancers of different histological type. Ductal invasive carcinomas and mucinous carcinomas showed more HIF-1α expression (0-20%) than lobular and mixed cancers, those with ductal and lobular components (0-2%). HIF-1α staining intensity did not vary between histological groups. On the other hand, lobular carcinomas presented higher median of total tumour vessels, determined by immunohistochemical staining using anti-CD31 monoclonal antibody in the paraffin blocks, than other histological types of cancers. Vessel density seemed to be lower in IMC whereas vessel calibre was lower in mixed carcinomas in comparison with other histological categories.

Percentage of tumour cells was similar among the different histological types of cancers; however, mixed carcinomas and the IMC depicted higher percentage of TILs than ductal and lobular tumours. As previous authors have found[38], we observed varying levels of TILs in ductal carcinomas (0-50%).

Regarding tumour nuclear grade, CAIX expression and staining intensity remained modest in low- and high-grade cancers, similar to HIF-1α staining intensity. Surprisingly in this study, HIF-1α expression was higher in low grade cancers (grade 1) than in cancers of grade 2 and 3. Our results differ from those of Campbell et al[39] who stated that HIF-1α activation was associated with higher tumour grade and pathological stage. The explanation given was that

grade 1 tumours had higher ascorbate levels than grade 2 and 3 tumours and higher ascorbate levels were associated with lower HIF-1α activity. Grade 3 cancers presented higher mean of total tumour vessels and greater vessel density and calibre than grade 1 and 2 cancers. Like us, Sener et al[40] did not observe a significant association between micro-vessel density and other prognostic factors such as histological type or nuclear grade in breast carcinomas. Percentage of tumour cells and stromal TILs were higher in low grade cancers than in high grade cancers.

Some researchers have reported a positive correlation between carbonic anhydrase IX expression and ER negativity in breast cancer[41]. In line with this, only 6/22 (27%) of the breast cancers in our sample were positive for CAIX staining (all cancers were ER+). On the other hand, some authors are of the opinion that CAIX expression under hypoxic conditions might be cancer type dependant[42]. Perhaps, another explanation why few cancers in our sample stained positive for CAIX could be that ^{18}F-FMISO PET-MRI only detected a hypoxic status in 8 out of 23 breast cancers and perhaps, there was relatively little hypoxia present in our sample of cancers. CAIX staining intensity and percentages were significantly correlated to cancer size (when divided into categories) and CAIX percentages were also significantly associated with breast cancer histology in keeping with findings of other authors[41,43] but we did not observe any significant correlation of CAIX expression with tumour grade or presence of *in situ* carcinoma.

It is widely recognised that HIF-1α is activated under the presence of hypoxia in cancer[44]. However, in ER positive breast cancers the activation of HIF-1α may not be related to tumour hypoxia. Previous studies have found that HIF-1α can be regulated by oestrogen receptor (ER) alpha under normoxia and hypoxia[45]. Similarly, different studies have also stated that HIF-1 alpha can be regulated by 17-beta oestradiol (E2) in the absence of hypoxia because HIF-1α possesses an oestrogen response element[46,47]. It has also been described that in all biological tissues including malignant tumours, HIF-1α can activate oestrogen receptors (ER) alpha and beta in the absence of ligand (hormone) and inversely, unoccupied ER beta can inhibit HIF-1α[48]. In the present study, 81% (17/21) ER+ breast cancers stained positive for HIF-1α. Since only 8 out of 23 cancers showed hypoxia in ^{18}F-FMISO PET/MRI, it was assumed that HIF-1 alpha activation in these cancers was due to the influence of either oestrogen receptors or the hormone itself. It could be inferred that the reason why 19% of the cancers stained negative for HIF-1α was the presence of unoccupied ER beta inhibiting HIF-1α. Future studies comparing

HIF-1α expression in both ER positive and ER negative breast cancers may be needed to specify the relationship between HIF-1α and oestrogen receptors.

HIF-1α staining intensity or percentages did not show significant correlations with tumour pathological size, histology, grade, presence of *in situ* carcinoma and tumour nodal or T status. HIF-1α (%) showed a significant positive correlation with tumour micro-vessels density calculated from quantitative analysis of CD31 immunostaining. Other authors have also found an association between increased levels of HIF-1α and breast cancer micro-vessel formation; furthermore, it has been proved that HIF-1α can upregulate VEGF which is a major lymphangiogenic and angiogenic factor[49,50,51].

The total number of tumour micro vessels calculated from CD31 staining was significantly associated with tumour pathological size and T status. Similarly, the number of tumour micro vessels significantly varied between histological types of breast cancer, being higher in ILC. Previous studies have confirmed that neo-angiogenesis enables tumour growth and leads to vascular hyperpermeability[52,53]. In concordance with this, the total count of tumour vessels had statistically significant positive correlations with tumour size metrics (MRI tumour longest diameter, ROI volume and ETV) and with tumour AFVs in our study, meaning that larger cancers seem to have more blood vessels. Likewise, the total number of tumour vessels was significantly correlated to the density and calibre of tumour vessels. Tumour micro-vessel density and calibre showed a poor positive correlation between each other. The diameter of tumour micro-vessels was significantly associated with tumour's HER-2 status and in this study HER-2 negative cancers presented bigger diameters of tumour micro vessels than HER-2 positive cancers.

Tumour neo-angiogenesis influences on the tumour metastatic potential. High intra-tumoral micro-vascular density produced by an overexpression of VEGF via HIF-1α is related to greater incidence of lymph node metastasis[51,54,55]. However, we were unable to show significant correlations between lymph node status of the cancers (nodal status from the TNM classification) and CD31 parameters, total count of tumour blood vessels, tumour micro-vessels density and calibre. This may be due to the low numbers of patients in our study with relatively low numbers of lymph node involvement.

In the present study, we could not demonstrate any significant association between the hypoxic endogenous markers, HIF-1α and CAIX in ER+ breast cancers. In head and neck cancers no association between HIF-1α and CAIX expression has been found either[56]. Equally, Arno Kuijper et al. did not find any association between HIF-1α and CAIX in phyllodes tumours of the breast[57].

We observed a non-significant positive correlation between the percentage of stromal TILs and the percentage of tumour cells. Perhaps, increased cell tumour proliferation in ER+ breast cancers is related to an increase of immune cells in the tumour stroma as the immune system tries to attack the cancer. Our results may be in concordant with those of Kurozumi et al[25] who stated that high expression of TILs in ER positive breast tumours was a poor prognosis marker.

This study shows a significant positive association between HIF-1α expression and the percentage of tumour cells. Previous authors have reported an increase of tumour growth factors under hypoxic conditions related to HIF-1α activation, which leads to tumour cell proliferation[28]. Likewise, it has been described that the activation of HIF-1α stimulates tumour growth by VEGF expression[58]. We also found a negative correlation between HIF-1α expression and TILs (%), although this was not statistically significant. Our results are similar to those of Doedens et al., who reported a suppression of tumour-infiltrating T cells by HIF-1α expression in macrophages of a murine model of breast cancer[59]. Similarly, Duechler et al[60] observed that the level of HIFs correlated with hormone receptor status and the expression of several immunosuppressive molecules in breast cancer.

We reported a non-significant positive correlation between CAIX expression and percentage of tumour cells, meaning that high CAIX levels in the tumour may be related to increased proliferation of tumour cells like it has been proved before[61,62]. These results are also in concordance with the results of Güttler et al[63], who observed a reduction in the number of tumour cells after inhibiting CAIX with CA9 siRNA. Likewise, we found a non-significant positive correlation between CAIX (i) and percentage of TILs and a negative correlation between CAIX (%) and TILs. To our knowledge, there is no literature reporting the association of CAIX with tumour infiltrating lymphocytes in breast tumours.

Our results showed negative correlations between CD31 parameters (total number of tumour vessels and tumour-vessel calibre) and percentage of tumour cells. These results support the theory that breast cancers with increased cell proliferation rate outgrow their vascular supply and consequently, they possess few blood vessels. On the other hand, in colorectal carcinoma, a positive correlation has been found between tumour vascularity and tumour cell proliferation[64].

With respect to percentage of TILs, there was a statistically significant negative correlation between the total number of tumour vessels (which is closely related to tumour angiogenesis) and percentage of TILs. We also observed negative correlations between other CD31 derived vascular parameters (tumour micro-vessel density and calibre) and TILs (%). Our results support previous statements about how the tumour vasculature constitutes a barrier for T-cells and how endothelial cells lining the vessels can suppress T cell activity[65].

The number of tumour adjacent feeding vessels demonstrated negative correlations with endogenous hypoxic biomarkers and positive correlations with CD31 derived vascular parameters. The only statistically significant positive correlation was observed with the total number of tumour micro vessels. It would be logical to find positive correlations between AFVs and CD31 derived total count of tumour vessels, micro-vessels density and calibre since all of them are indicators of the tumour vascularity, although AFVs are a macroscopic vascular metric and CD31 parameters are measured microscopically.

Almost half of the tumours (10/21) showed a delayed plateau pattern, 43% washout and only 10% developed persistent enhancement. It is known that ER positive cancers depict less malignant DCE-MRI kinetics than ER- breast cancers[16]. The highest median CAIX expression (immune-staining and percentage) was observed in cancers with a type 3 kinetic curve. Similarly, the highest median HIF-1α intensity scores and percentage were observed in cancers with kinetic curve type 3. ER positive cancers with a kinetic curve type 3 also presented the highest mean of total tumour vessels and the highest median of tumour micro-vessels density. On the other hand, the cancers with a kinetic curve type 2 presented the highest mean of micro-vessels calibre. Breast cancers with kinetic curve type 3, which represents higher aggressive potential[66], showed the highest percentages of stromal TILs and higher percentages of tumour cells than breast cancers with curves type 1 or 2. This is the first study assessing the relationship between IHC endogenous biomarkers and DCE-MRI tumour kinetics in breast cancer.

Our results showed a significant positive correlation between ^{18}F-FMISO K_i mean (an imaging marker of hypoxia) and CAIX expression (staining and percentage) and a non-significant positive correlation between tumour hypoxic fractions and CAIX, meaning that CAIX could be an indicator of hypoxia in ER+ breast cancers. Some previous authors believe that CAIX is unreliable for assessing tumour hypoxia[42], however, others believe that CAIX is a good indicator of hypoxia in breast cancer due to its significant association with necrosis[43] which we could not demonstrate because only 2 out of 23 cancers in this sample presented areas of necrosis. Further studies with bigger sample size and necrotic tumours are needed in order to show the exact potential and role of CAIX as an immunohistochemical hypoxic marker in ER+ breast cancers. There were non-significant positive correlations between CAIX expression and DCE-MRI K^{trans} and v_p. Negative non-significant correlations were found between CAIX expression and DCE-MRI K^{ep} and v_e. Newbold et al[67] did not find correlations between DCE-MRI or perfusion CT parameters and CAIX staining in head and neck cancers.

In our study, HIF-1α (intensity and percentage) showed negative correlations with ^{18}F-FMISO derived K_i and with tumour hypoxic fractions, although they were not significant. A previous study reported as well a poor correlation between ^{18}F-FMISO uptake and HIF-1α expression in ER+ breast cancers[68]. As previously explained, the presence of HIF-1α in our study does not appear to indicate hypoxia in our ER+ breast cancer cohort.

We observed a non-statistically significant positive correlation between K^{trans} and HIF-1α (%). In ovarian cancer, negative correlations have been found between K^{trans} and HIF-1α[69]. However, in human head and neck squamous cell carcinomas positive correlations have been reported between K^{trans} and HIF-1α expression[70] whereas in prostate cancer no correlations were found between HIF-1α and DCE-MRI parameters[71]. In this study, we also observed a positive correlation between K^{ep} and HIF-1α IHC results. By contrast, Lindgren et al[69]. found a negative correlation between K^{ep} and HIF-1α while studying DCE-MRI perfusion parameters in ovarian cancer. V_e was negatively correlated to HIF-1α staining and percentage (p=>0.05). We observed positive correlations between v_p and HIF-1 alpha intensity and percentage (p= >0.05). No previous results were found in relation to the association between v_e and v_p with hypoxic endogenous biomarkers.

In summary, we can conclude that results of correlations between DCE-MRI quantitative parameters and IHC tumour hypoxic markers are controversial among different types of

cancers and therefore, at present time no relationship has been clearly identified between imaging vascular parameters and IHC hypoxic markers of malignant tumours, including breast cancer. In particular, we believe that the presence of HIF-1α in ER positive breast cancers may not indicate hypoxia and perhaps, for this reason HIF-1α was weakly correlated to DCE-MRI parameters.

Most of CD31 derived vasculature parameters demonstrated positive associations with DCE-MRI quantitative parameters, with the exception of hotspot K^{trans} and k^{ep} which showed negative correlations with tumour micro vessel density and calibre. CD31 derived vascular features were inversely correlated to ^{18}F-FMISO PET tumour K_i. The negative correlations between tumour K_i, tumour micro vessel density and calibre were statistically significant. Previous correlations performed in different types of cancer between hypoxia PET parameters and tumour endogenous vascular markers have been inconsistent: Studies on gliomas[72] have reported weak correlations between ^{18}F-FMISO-PET parameters and VEGF, another vascular endogenous biomarker. However, another study on non-small cell lung cancer showed a significant positive correlation between ^{18}F-FETNIM uptake (^{18}F-Fluoroerythronitroimidazole, another hypoxia radiotracer) and VEGF[73].

This study showed positive non-significant correlations between tumour cells (%) and ^{18}F-FMISO-PET/MRI derived K_i and hypoxic fractions (%). This results are in concordance with the fact that tumour hypoxia has been closely related to rapid cell growth and proliferation[74]. Evans et al[75] observed that proliferating cells (Ki-67-positive cells) could be found in regions of high EF5 binding (EF5 is a hypoxic exogenous marker) in many human glioblastoma tissue sections. On the other hand, some immunohistochemical (IHC) studies have reported an inverse spatial relationship between hypoxic and proliferating cells[76,77].

Concerning the relationship between ^{18}F-FMISO-PET imaging parameters and TILs (%); Siegers et al[78] reported an increased infiltration of immune Gamma delta T cells in areas of hypoxia in a small cohort of breast cancers. In line with their results, we observed positive correlations between TILs (%) and ^{18}F-FMISO-PET derived K_i and hypoxic fractions (p= >0.05).

There was a statistically significant negative correlation between ^{18}F-FMISO SUV max and TILs (%). Likewise, ^{8}F-FMISO SUV mean and tumour ratios were inversely correlated to TILs

(%), although these correlations were not statistically significant. These results support previous findings that confirm the existence of immunosuppression in breast cancer[59,60]. An explanation for how breast tumour cells restrict lymphocytic infiltration leading to immunosuppression may be that pathways which promote cell proliferation and malignant transformation are tightly associated with increased rates of glycolysis and thus secretion of lactic acid within the breast tumour microenvironment and lactic acid inhibits T-cell activation[79]

There were negative and non-significant correlations between TILs (%) and all DCE-MRI parameters. Contrast-enhanced MRI quantitative parameters are indicators of the tumour vascularity and their negative correlation with the percentage of TILs may be associated with the finding of Siegers et al[78] about increased TILs in hypoxic areas, from which we may interpret that poorly vascularised areas (hypoxic regions) will have a high percentage of TILs and by opposite, highly vascularised areas might present low number of TILs. To our knowledge, this is the first study which shows correlations between DCE-MR quantitative imaging parameters and TILs in ER positive cancers.

DCE-MRI parameters (excepting K^{ep}) showed non-significant negative correlations with percentage of tumour cells. The proportion of tumour cells depends on the tumour growth rate. Results of previous studies about the relationship between DCE-MRI quantitative parameters and tumour proliferation markers such as Ki67 have been inconsistent. Some authors have found no association between DCE-MRI vascular parameters and Ki67[80,81]. Other authors have reported an association between quantitative parameters of DCE-MRI and Ki67 expression in breast tumours[17,82]. Jong et al[83] found that k^{trans} was associated with the Ki67 status of patients with ER+ breast cancers.

Finally, correlations with ADC were obtained from 12 patients (12 breast cancers) who had successful DWI and for whom IHC data was available. There was a significant positive association between CAIX staining percentage and ADC obtained from the darkest part of the tumour. This is an interesting result, and we recommend repeating this work in a larger dataset of ER positive and negative tumours.

The main limitation of our study was the small sample size. Other limitations were that our tumour sample contained only ER positive tumours and the fact that these cancers were

relatively small. Few large cancers now go straight to surgery making this type of investigation correlating imaging biomarkers with pathology difficult.

5.5 Conclusion

All ER+ cancers stained positive for CD31, whereas 17 were positive for HIF-1 alpha and 6 for CAIX. A significant positive correlation was found between the imaging parameter of hypoxia, k_i and CAIX expression measured by IHC. HIF-1α may be an unreliable marker of hypoxia in ER positive breast cancer. Likewise, significant negative correlations were shown between tumour k_i and CD31-derived tumour micro vessel density and calibre. These results from correlations between imaging and IHC markers of tumour vascularity and hypoxia demonstrated that hypoxia measurements from ^{18}F-FMISO-PET/MRI are reliable and support the hypothesis of perfusion-driven hypoxia in breast cancer.

References

1. Wood, K. A., Wong, W. L. & Saunders, M. I. [64Cu]diacetyl-bis(N4-methyl-thiosemicarbazone) - a radiotracer for tumor hypoxia. *Nuclear Medicine and Biology* (2008). doi:10.1016/j.nucmedbio.2008.02.002
2. Xu, Z., Li, X. F., Zou, H., Sun, X. & Shen, B. 18F-Fluoromisonidazole in tumor hypoxia imaging. *Oncotarget* (2017). doi:10.18632/oncotarget.21662
3. Ljungkvist, A. S. E., Bussink, J., Kaanders, J. H. A. M. & Van Der Kogel, A. J. Dynamics of tumor hypoxia measured with bioreductive hypoxic cell markers. *Radiation Research* (2007). doi:10.1667/RR0719.1
4. Le, Q. T. & Courter, D. Clinical biomarkers for hypoxia targeting. *Cancer and Metastasis Reviews* (2008). doi:10.1007/s10555-008-9144-9
5. Liu, Z. ji, Semenza, G. L. & Zhang, H. feng. Hypoxia-inducible factor 1 and breast cancer metastasis. *Journal of Zhejiang University: Science B* (2015). doi:10.1631/jzus.B1400221
6. Bos, R. *et al*. Levels of Hypoxia-Inducible Factor-1 During Breast Carcinogenesis. *JNCI J. Natl. Cancer Inst.* **93**, 309–314 (2001).
7. Adams, A. *et al*. The potential of hypoxia markers as target for breast molecular imaging - a systematic review and meta-analysis of human marker expression. *BMC Cancer* (2013). doi:10.1186/1471-2407-13-538
8. Cronin, P. A., Wang, J. H. & Redmond, H. P. Hypoxia increases the metastatic ability of breast cancer cells via upregulation of CXCR4. *BMC Cancer* (2010). doi:10.1186/1471-2407-10-225
9. Vaupel, P., Thews, O. & Hoeckel, M. Treatment resistance of solid tumors: Role of hypoxia and anemia. *Medical Oncology* (2001). doi:10.1385/MO:18:4:243
10. Riedemann, J. & Macaulay, V. M. IGF1R signalling and its inhibition. in *Endocrine-Related Cancer* (2006). doi:10.1677/erc.1.01280
11. Sato, J. *et al*. 18F-fluoromisonidazole PET uptake is correlated with hypoxia-inducible factor-1a expression in oral squamous cell carcinoma. *J. Nucl. Med.* (2013). doi:10.2967/jnumed.112.114355
12. Norikane, T. *et al*. Correlation of 18F-fluoromisonidazole PET findings with HIF-1α and p53 expressions in head and neck cancer: Comparison with 18F-FDG PET. *Nucl. Med. Commun.* (2014). doi:10.1097/MNM.0000000000000010

13. Cher, L. M. *et al*. Correlation of hypoxic cell fraction and angiogenesis with glucose metabolic rate in gliomas using 18F-fluoromisonidazole, 18F-FDG PET, and immunohistochemical studies. *J. Nucl. Med*. (2006).
14. Déry, M. A. C., Michaud, M. D. & Richard, D. E. Hypoxia-inducible factor 1: Regulation by hypoxic and non-hypoxic activators. *International Journal of Biochemistry and Cell Biology* (2005). doi:10.1016/j.biocel.2004.08.012
15. Fleming, I. N. *et al*. Imaging tumour hypoxia with positron emission tomography. *British Journal of Cancer* **112**, 238–250 (2015).
16. Chen, J. H., Baek, H. M., Nalcioglu, O. & Su, M. Y. Estrogen receptor and breast MR imaging features: A correlation study. *J. Magn. Reson. Imaging* (2008). doi:10.1002/jmri.21330
17. Kim, J. Y. *et al*. Enhancement parameters on dynamic contrast enhanced breast MRI: Do they correlate with prognostic factors and subtypes of breast cancers? *Magn. Reson. Imaging* (2015). doi:10.1016/j.mri.2014.08.034
18. Hulka, C. A. *et al*. Benign and malignant breast lesions: Differentiation with echo-planar MR imaging. *Radiology* (1995). doi:10.1148/radiology.197.1.7568850
19. Hulka, C. A. *et al*. Dynamic echo-planar imaging of the breast: Experience in diagnosing breast carcinoma and correlation with tumor angiogenesis. *Radiology* (1997). doi:10.1148/radiology.205.3.9393545
20. Buckley, D. L., Drew, P. J., Mussurakis, S., Monson, J. R. T. & Horsman, A. Microvessel density in invasive breast cancer assessed by dynamic Gd-DTPA enhanced MRI. *J. Magn. Reson. Imaging* (1997). doi:10.1002/jmri.1880070302
21. Stomper, P. C. *et al*. Angiogenesis and dynamic MR imaging gadolinium enhancement of malignant and benign breast lesions. *Breast Cancer Res. Treat*. (1997). doi:10.1023/A:1005897227030
22. Charpin, C. *et al*. Tumor neoangiogenesis by CD31 and CD105 expression evaluation in breast carcinoma tissue microarrays. *Clin. Cancer Res*. (2004). doi:10.1158/1078-0432.CCR-04-0021
23. Dales, J. P. *et al*. CD105 expression is a marker of high metastatic risk and poor outcome in breast carcinomas: Correlations between immunohistochemical analysis and long-term follow-up in a series of 929 patients. *Am. J. Clin. Pathol*. (2003). doi:10.1309/1KF54L6RB625556W
24. Dales, J. P. *et al*. Long-Term Prognostic Significance of Neoangiogenesis in Breast

Carcinomas: Comparison of Tie-2/Tek, CD105, and CD31 Immunocytochemical Expression. *Hum. Pathol.* (2004). doi:10.1016/j.humpath.2003.10.008

25. Kurozumi, S. *et al.* Prognostic significance of tumour-infiltrating lymphocytes for oestrogen receptor-negative breast cancer without lymph node metastasis. *Oncol. Lett.* **17**, 2647–2656 (2019).
26. Eerola, A. K., Soini, Y. & Pääkkö, P. Tumour infiltrating lymphocytes in relation to tumour angiogenesis, apoptosis and prognosis in patients with large cell lung carcinoma. *Lung Cancer* (1999). doi:10.1016/S0169-5002(99)00072-0
27. Smits, A. J. J. *et al.* The estimation of tumor cell percentage for molecular testing by pathologists is not accurate. *Mod. Pathol.* (2014). doi:10.1038/modpathol.2013.134
28. Franovic, A. *et al.* Translational up-regulation of the EGFR by tumor hypoxia provides a nonmutational explanation for its overexpression in human cancer. *Proc. Natl. Acad. Sci. U. S. A.* (2007). doi:10.1073/pnas.0702387104
29. Rao, A. A., Feneis, J., Lalonde, C. & Ojeda-Fournier, H. A pictorial review of changes in the BI-RADS fifth edition. *Radiographics* (2016). doi:10.1148/rg.2016150178
30. Belton, M. *et al.* Hypoxia and tissue destruction in pulmonary TB. *Thorax* (2016). doi:10.1136/thoraxjnl-2015-207402
31. Baek, J. E., Kim, S. H. & Lee, A. W. Background parenchymal enhancement in breast MRIs of breast cancer patients: Impact on tumor size estimation. *Eur. J. Radiol.* (2014). doi:10.1016/j.ejrad.2014.05.007
32. Sardanelli, F. Vessel Analysis on Contrast-Enhanced MRI of the Breast: Global or Local Vascularity? *Am. J. Roentgenol.* **195**, 1246–1249 (2010).
33. Hylton, N. M. Vascularity assessment of breast lesions with gadolinium-enhanced MR imaging. *Magn. Reson. Imaging Clin. N. Am.* **9**, 321—32, vi (2001).
34. Kuhl, C. K. Current status of breast MR imaging: Part 2. Clinical applications. *Radiology* (2007). doi:10.1148/radiol.2443051661
35. Avendano, D. *et al.* Limited role of DWI with apparent diffusion coefficient mapping in breast lesions presenting as non-mass enhancement on dynamic contrast-enhanced MRI. *Breast Cancer Res.* (2019). doi:10.1186/s13058-019-1208-y
36. Bedair, R. *et al.* Effect of Radiofrequency Transmit Field Correction on Quantitative Dynamic Contrast-enhanced MR Imaging of the Breast at 3.0 T. *Radiology* **279**, 368–377 (2016).
37. Adams, S. *et al.* Prognostic value of tumor-infiltrating lymphocytes in triple-negative

breast cancers from two phase III randomized adjuvant breast cancer trials: ECOG 2197 and ECOG 1199. *J. Clin. Oncol.* **32**, 2959–2966 (2014).

38. Dieci, M. V. *et al.* Update on tumor-infiltrating lymphocytes (TILs) in breast cancer, including recommendations to assess TILs in residual disease after neoadjuvant therapy and in carcinoma in situ: A report of the International Immuno-Oncology Biomarker Working Group on Bre. *Seminars in Cancer Biology* (2018). doi:10.1016/j.semcancer.2017.10.003
39. Campbell, E. J. *et al.* Activation of the hypoxia pathway in breast cancer tissue and patient survival are inversely associated with tumor ascorbate levels. *BMC Cancer* (2019). doi:10.1186/s12885-019-5503-x
40. Şener, E., Şipal, S. & Gündoğdu, C. Comparison of microvessel density with prognostic factors in invasive ductal carcinomas of the breast. *Turk Patoloji Derg.* (2016). doi:10.5146/tjpath.2016.01366
41. Tan, E. Y. *et al.* The key hypoxia regulated gene CAIX is upregulated in basal-like breast tumours and is associated with resistance to chemotherapy. *Br. J. Cancer* (2009). doi:10.1038/sj.bjc.6604844
42. Li, J., Zhang, G., Wang, X. & Li, X. F. Is carbonic anhydrase IX a validated target for molecular imaging of cancer and hypoxia? *Future Oncology* (2015). doi:10.2217/fon.15.11
43. Chia, S. K. *et al.* Prognostic significance of a novel hypoxia-regulated marker, carbonic anhydrase IX, in invasive breast carcinoma. *J. Clin. Oncol.* (2001). doi:10.1200/JCO.2001.19.16.3660
44. Ziello, J. E., Jovin, I. S. & Huang, Y. Hypoxia-Inducible Factor (HIF)-1 regulatory pathway and its potential for therapeutic intervention in malignancy and ischemia. *Yale J. Biol. Med.* **80**, 51–60 (2007).
45. Yang, J. *et al.* Estrogen receptor-α directly regulates the hypoxiainducible factor 1 pathway associated with antiestrogen response in breast cancer. *Proc. Natl. Acad. Sci. U. S. A.* (2015). doi:10.1073/pnas.1422015112
46. Fuady, J. H. *et al.* Estrogen-dependent downregulation of hypoxia-inducible factor (HIF)-2β in invasive breast cancer cells. *Oncotarget* (2016). doi:10.18632/oncotarget.8866
47. Yang, J. *et al.* Estrogen receptor-α directly regulates the hypoxia-inducible factor 1 pathway associated with antiestrogen response in breast cancer. *Proc. Natl. Acad. Sci.*

U. S. A. **112**, 15172–7 (2015).

48. Lim, W. *et al*. Hypoxia-inducible factor 1α activates and is inhibited by unoccupied estrogen receptor β. *FEBS Lett*. (2009). doi:10.1016/j.febslet.2009.03.028
49. Bos, R. *et al*. Levels of hypoxia-inducible factor-1α during breast carcinogenesis. *J. Natl. Cancer Inst*. (2001). doi:10.1093/jnci/93.4.309
50. Nalwoga, H., Ahmed, L., Arnes, J. B., Wabinga, H. & Akslen, L. A. Strong expression of hypoxia-inducible factor-1α (HIF-1α) is associated with Axl expression and features of aggressive tumors in African breast cancer. *PLoS One* (2016). doi:10.1371/journal.pone.0146823
51. Ni, X. *et al*. Hypoxia-induced factor-1 alpha upregulates vascular endothelial growth factor C to promote lymphangiogenesis and angiogenesis in breast cancer patients. *J. Biomed. Res*. (2013). doi:10.7555/JBR.27.20130021
52. Connolly, D. T. Vascular permeability factor: A unique regulator of blood vessel function. *J. Cell. Biochem*. (1991). doi:10.1002/jcb.240470306
53. Hoeben, A. *et al*. Vascular endothelial growth factor and angiogenesis. *Pharmacological Reviews* (2004). doi:10.1124/pr.56.4.3
54. Weidner, N. Current pathologic methods for measuring intratumoral microvessel density within breast carcinoma and other solid tumors. *Breast Cancer Res. Treat*. (1995). doi:10.1007/BF00666038
55. Jaeger, T. M. *et al*. Tumor Angiogenesis Correlates with Lymph Node Metastases in Invasive Bladder Cancer. *J. Urol*. (1995). doi:10.1016/S0022-5347(01)67230-6
56. Kappler, M. *et al*. Immunohistochemical detection of HIF-1α and CAIX in advanced head-and-neck cancer: Prognostic role and correlation with tumor markers and tumor oxygenation parameters. *Strahlentherapie und Onkol*. (2008). doi:10.1007/s00066-008-1813-7
57. Kuijper, A., van der Groep, P., van der Wall, E. & van Diest, P. J. Expression of hypoxia-inducible factor 1 alpha and its downstream targets in fibroepithelial tumors of the breast. *Breast Cancer Res*. (2005). doi:10.1186/bcr1296
58. Tang, N. *et al*. Loss of HIF-1α in endothelial cells disrupts a hypoxia-driven VEGF autocrine loop necessary for tumorigenesis. *Cancer Cell* (2004). doi:10.1016/j.ccr.2004.09.026
59. Doedens, A. L. *et al*. Macrophage expression of hypoxia-inducible factor-1α suppresses T-cell function and promotes tumor progression. *Cancer Res*. (2010). doi:10.1158/0008-

5472.CAN-10-1439

60. Duechler, M. *et al*. The heterogeneous immune microenvironment in breast cancer is affected by hypoxia-related genes. *Immunobiology* (2014). doi:10.1016/j.imbio.2013.09.003

61. Chiche, J. *et al*. Hypoxia-inducible carbonic anhydrase IX and XII promote tumor cell growth by counteracting acidosis through the regulation of the intracellular pH. *Cancer Res*. (2009). doi:10.1158/0008-5472.CAN-08-2470

62. Chen, Z. *et al*. Differential expression and function of CAIX and CAXII in breast cancer: A comparison between tumorgraft models and cells. *PLoS One* (2018). doi:10.1371/journal.pone.0199476

63. Güttler, A. *et al*. Cellular and radiobiological effects of carbonic anhydrase IX in human breast cancer cells. *Oncol. Rep*. (2019). doi:10.3892/or.2019.7001

64. Vermeulen, P. B. *et al*. Microvessel density, endothelial cell proliferation and tumour cell proliferation in human colorectal adenocarcinomas. *Ann. Oncol*. (1995). doi:10.1093/oxfordjournals.annonc.a059043

65. Lanitis, E., Irving, M. & Coukos, G. Targeting the tumor vasculature to enhance T cell activity. *Current Opinion in Immunology* (2015). doi:10.1016/j.coi.2015.01.011

66. Bluemke, D. A. *et al*. Magnetic resonance imaging of the breast prior to biopsy. *J. Am. Med. Assoc*. (2004). doi:10.1001/jama.292.22.2735

67. Newbold, K. *et al*. An Exploratory Study Into the Role of Dynamic Contrast-Enhanced Magnetic Resonance Imaging or Perfusion Computed Tomography for Detection of Intratumoral Hypoxia in Head-and-Neck Cancer. *Int. J. Radiat. Oncol. Biol. Phys*. (2009). doi:10.1016/j.ijrobp.2008.07.039

68. Cheng, J. *et al*. 18F-fluoromisonidazole PET/CT: A potential tool for predicting primary endocrine therapy resistance in breast cancer. *J. Nucl. Med*. (2013). doi:10.2967/jnumed.112.111963

69. Lindgren, A. *et al*. Dynamic contrast-enhanced perfusion parameters in ovarian cancer: Good accuracy in identifying high HIF-1α expression. *PLoS One* (2019). doi:10.1371/journal.pone.0221340

70. Meyer, H. J., Leifels, L., Hamerla, G., Höhn, A. K. & Surov, A. Associations between Histogram Analysis Parameters Derived from DCE-MRI and Histopathological Features including Expression of EGFR, p16, VEGF, Hif1-alpha, and p53 in HNSCC. *Contrast Media Mol. Imaging* (2019). doi:10.1155/2019/5081909

71. Borren, A. *et al*. Expression of hypoxia-inducible factor-1α and -2α in whole-mount prostate histology: Relation with dynamic contrast-enhanced MRI and Gleason score. *Oncol. Rep*. (2013). doi:10.3892/or.2013.2392

72. Kawai, N. *et al*. Correlation between 18 F-fluoromisonidazole PET and expression of HIF-1α and VEGF in newly diagnosed and recurrent malignant gliomas. *Eur. J. Nucl. Med. Mol. Imaging* (2014). doi:10.1007/s00259-014-2776-9

73. Hu, M. *et al*. Hypoxia imaging with 18F-fluoroerythronitroimidazole integrated PET/CT and immunohistochemical studies in non-small cell lung cancer. *Clin. Nucl. Med*. (2013). doi:10.1097/RLU.0b013e318279fd3d

74. Rofstad, E. K., Galappathi, K., Mathiesen, B. & Ruud, E. B. M. Fluctuating and diffusion-limited hypoxia in hypoxia-induced metastasis. *Clin. Cancer Res*. (2007). doi:10.1158/1078-0432.CCR-06-1967

75. Evans, S. M. *et al*. The relationship among hypoxia, proliferation, and outcome in patients with de nouo glioblastoma: A pilot study. *Transl. Oncol*. (2010). doi:10.1593/tlo.09265

76. Hoskin, P. J., Sibtain, A., Daley, F. M., Saunders, M. I. & Wilson, G. D. The immunohistochemical assessment of hypoxia, vascularity and proliferation in bladder carcinoma. *Radiother. Oncol*. (2004). doi:10.1016/j.radonc.2004.03.017

77. Wijffels, K. I. E. M. *et al*. Tumour cell proliferation under hypoxic conditions in human head and neck squamous cell carcinomas. *Oral Oncol*. (2008). doi:10.1016/j.oraloncology.2007.04.004

78. Siegers, G. M., Dutta, I., Lai, R. & Postovit, L. M. Functional plasticity of Gamma delta T cells and breast tumor targets in hypoxia. *Front. Immunol*. (2018). doi:10.3389/fimmu.2018.01367

79. Fischer, K. *et al*. Inhibitory effect of tumor cell-derived lactic acid on human T cells. *Blood* (2007). doi:10.1182/blood-2006-07-035972

80. Koo, H. R. *et al*. Correlation of perfusion parameters on dynamic contrast-enhanced MRI with prognostic factors and subtypes of breast cancers. *J. Magn. Reson. Imaging* (2012). doi:10.1002/jmri.23635

81. Li, L. *et al*. Parameters of dynamic contrast-enhanced mri as imaging markers for angiogenesis and proliferation in human breast cancer. *Med. Sci. Monit*. (2015). doi:10.12659/MSM.892534

82. Ma, W. *et al*. Breast cancer Ki67 expression prediction by DCE-MRI radiomics features.

Clin. Radiol. (2018). doi:10.1016/j.crad.2018.05.027

83. Shin, J. K. & Kim, J. Y. Dynamic contrast-enhanced and diffusion-weighted MRI of estrogen receptor-positive invasive breast cancers: Associations between quantitative MR parameters and Ki-67 proliferation status. *J. Magn. Reson. Imaging* (2017). doi:10.1002/jmri.25348

Chapter 6. Correlations between breast cancer imaging vascular biomarkers and tumour response to neoadjuvant chemotherapy

Hypoxia is a well-known factor contributing to chemotherapy resistance in breast cancer. In previous chapters, the relationship between hypoxia, vascular function and immunohistochemistry markers of hypoxia and vascularity were investigated in a cohort of patients with treatment-naïve breast cancer, with the results supporting the hypothesis of perfusion-driven hypoxia in breast tumours. Given that vascular parameters from DCE-MRI may serve as surrogate markers of hypoxia in breast tumours prior to therapy, this chapter aims to investigate changes in qualitative and quantitative parameters of tumour vascular function in patients undergoing neo-adjuvant chemotherapy. The relationship between DCE-MRI qualitative and quantitative parameters with pathological response will also be investigated.

6.1 Background

Early-stage breast cancer patients are typically treated surgically to extract the tumour and with post-operative therapies, such as chemotherapy and/or radiotherapy, to kill remaining malignant cells. Primary systemic treatment or neoadjuvant chemotherapy (NAC), has become the standard initial treatment for patients who present with late stage disease or locally advanced breast cancer (LABC)[1,2]. One main advantage of NAC is the reduction of the size of the primary tumour, which allows breast surgery to be undertaken in patients considered inoperable prior to treatment. It also increases the probability that breast-conserving surgery can be performed in a minority of patients[3,4]. Patients with no evidence of residual macroscopic disease (pathological complete response) after NAC have an increased disease-free survival (DFS) and overall survival (OS) rate[5,6,7]. For this reason, pathological complete response (pCR) has been adopted as the primary end point for neoadjuvant chemotherapy trials but unfortunately, it has been shown that tumour pathological complete response only occurs in a subgroup of patients (3-34%)[8,9,10,11].

The monitoring of response to NAC is usually undertaken by clinical examination and mammography however, both have been shown to be inaccurate[12]. Clinical examination can overestimate the degree of residual disease due to the presence of fibrosis induced by chemotherapy[13,12,14], while the accuracy of mammography is affected by chemotherapy-

induced fibrosis and breast tissue density[12,14,15]. MRI is superior to physical examination and other imaging techniques like mammography and ultrasound in assessing tumour response after NAC because it can differentiate fibrosis from tumour[12,14,15] and its accuracy is not affected by the presence of dense breast tissue[16]. MRI has demonstrated high accuracy in predicting pathological complete remission[17,18]. As changes in tumour size tend to occur after physiological changes in the tumour[19,20], DCE-MRI can also enable the evaluation of physiological changes during treatment, which can help identify early treatment failures and allowing prompt implementation of second-line therapy[2].

Neoadjuvant chemotherapy agents typically act by targeting cells with a high proliferation rate, which is a hallmark of cancer cells[21]. Given that physiological alterations in tumour perfusion and vascular permeability during treatment will manifest earlier than gross changes in tumour size, DCE-MRI pharmacokinetic modelling has the potential to monitor response to treatment by tracking the kinetics of contrast through the lesion of interest[22]. It is generally accepted that NAC will induce changes in enhancement patterns of the tumour from wash-out to a less aggressive pattern of plateau or persistent enhancement[20]. Previous studies have reported a statistically significant reduction of up to a third in both the contrast influx (K^{trans}) and efflux (k_{ep}) rates in breast cancer patients receiving NAC, whereas an increase in v_e of nearly a third has been shown in patients not responding to treatment[23]. Although a change in K^{trans} greater than 40% has often been considered as a threshold for definitive response[24], discrepancies have been observed in the results reported by different studies. Some reports have shown little or no decrease in K^{trans}, k_{ep} or other pharmacokinetic parameters after NAC[2,25,26], while others have indicated that an early change in tumour size is a better response predictor than pharmacokinetic parameters from DCE-MRI during the early course of NAC[26,27]. Analysis of K^{trans} hotspots prior to or early during treatment has provided superior results than mean lesion K^{trans} in differentiating between responders and non-responders[28].

Despite variable results in treatment response prediction, previous literature[29,30] indicates the suitability of DCE-MRI in monitoring changes in vascular function and, in a surrogate manner, tumour oxygenation during treatment. K^{trans} has been shown to be indicative of naturally occurring or treatment-induced hypoxia in several types of cancer when hypoxia was caused by low blood perfusion[31,32,33]. Given that cancer therapy will induce some vascular damage to the tumour and taking into account the potential coupling of hypoxia and hypoperfusion in breast cancer as illustrated in previous chapters of this thesis, it can be hypothesised that

parameters of tumour vascular functionality derived from DCE-MRI can provide valuable information on both the vascular and hypoxic status of tumours. Assessment of the tumour altered vascularity with DCE-MRI may also provide additional information about the chemosensitivity of cancers and better understanding of mechanisms of resistance, as several common chemotherapeutic regimens used in breast cancer, which include combinations of 5-fluouracil[34,35], carboplatin[34,35] and taxanes[30,34] have demonstrated limited efficacy in hypoxic conditions[36].

The aim of this chapter was to investigate changes in DCE-MRI quantitative and qualitative parameters of tumour vascular function and vascularity in patients with primary breast cancer undergoing NAC. Pharmacokinetic parameters from DCE-MRI and tumour morphological features, including tumour diameter and volume, were assessed before, during and after NAC, and changes in these parameters were calculated and correlated with pathological response. Furthermore, changes in morphological metrics of local vascularity were evaluated by assessing the number of adjacent feeding vessels (AFV) [37,38,39] during NAC in order to assess the ability of a qualitative marker of vascularity to predict pathological response.

6.2 Materials and methods

6.2.1 Patient population

This research was approved by a National Research Ethics Committee (13/LO/0411) and informed consent was obtained from all study participants. Imaging data from 82 patients, recruited between October 2014 and October 2017, were collected for a prospective analysis. Women with pathologically confirmed breast cancer undergoing NAC prior to surgery, and a lesion ≥10 mm in size on mammography and/or ultrasound were considered eligible for the study. Patients unable to provide informed consent, who were medically unstable or with known contraindications to MRI were excluded from this study. Additional exclusion criteria included: previous surgery or radiotherapy for cancer, including chemotherapy or hormonal therapy for breast cancer; previous surgery in the ipsilateral breast for benign disease prior to diagnosis; history of serious breast trauma or undergoing MRI for the assessment of the integrity of breast implants.

6.2.2 Neo-adjuvant chemotherapy (NAC) treatment protocol

According to the NAC protocol followed in our institution, patients received chemotherapy once every 21 days (the duration of each cycle) for up to a total of 6 or 7 cycles. For patients with HER2-negative cancers on core biopsy, the chemotherapy regimen typically involved the administration of reverse sequences of a **t**axane (docetaxel; T) for 3 or 4 cycles and a combination of anthracyclines (**f**luorouracil and/or **e**pirubicin) and **c**yclophosphamide (FEC) for 3 cycles. Patients with HER2-positive tumours received either anthracycline-taxane based treatment in combination with a HER2-targetted agent, such as trastuzumab (Herceptin, Genetech Inc., CA) with or without the addition of pertuzumab (Perjeta, Genetech Inc., CA) for 3 or 4 cycles, or a combination of docetaxel and trastuzumab (with or without pertuzumab) for the entire duration of treatment. To offset cardiotoxicity risks associated with the co-administration of trastuzumab and anthracycline-based treatment, trastuzumab was not given during FEC. Patients were assessed clinically before and after each cycle of chemotherapy and continued to a total of 6 or 7 cycles provided there was no evidence of disease progression or complete response. Details regarding the NAC treatment sequences administered to patients in this study are provided in Table 6.1.

Table 6.1 Neoadjuvant chemotherapy (NAC) regimens given to patients.

NAC regimen	Number of Cycles	Description
Taxane (T) + Anthracyclines (A)	6 or 7	T (3 or 4 cycles) - A (3 cycles)
Anthracyclines (A) + Taxane (T) + Herceptin (H) and/or Pertuzumab (P)	6 or 7	A (3 cycles) / T + H (3 cycles) *or* T + H (3 cycles) / A (3 cycles) *or* A (3 cycles) / T + H + P (3 or 4 cycles) *or* T + H + P (3 or 4 cycles) / A (3 cycles)
Taxane (T) + Herceptin (H)	4 or 6	T + H (2 cycles) / T (4 cycles)
		T + H (4 – 6 cycles)
Taxane + Other[a] (O)	4 or 7	T (3 cycles) / O (4 Cycles) T + O (4 cycles)

[a]Chemotherapy involving co-administration of a Taxane and cyclophosphamide or carboplatin.

6.2.3 Imaging protocol

Patient imaging was undertaken at four time-points: (*i*) prior to the initiation of NAC (baseline); (*ii*) after the first cycle of chemotherapy (PC#1); (*iii*) midway through treatment (after 3 or 4 cycles of chemotherapy) and (*iv*) at the end of NAC, before surgery. All examinations were performed on a 3T MRI scanner (MR750, GE Healthcare), using an 8-channel breast coil with the subjects lying in the prone position. The imaging protocol

included T_1 and T_2-weighted images, T_1 and B_1 mapping sequences, and a DCE series involving five pre-contrast phases and 48 phases following the administration of Gadovist (Bayer Healthcare) as described in Chapter 3 (Section 3.4.2.2). MRI sequence parameters are given in Chapter 3, Table 3.1.

6.2.4 Image analysis

6.2.4.1 Qualitative analysis

Two radiologists (with three and >20 years of experience in breast MRI, respectively) reviewed the images and identified lesions in consensus, using information from T_1, T_2-weighted and DCE-MR images. In patients with multi-focal or multicentric disease, the largest measurable lesion, i.e. the largest focus that could be accurately measured in at least one dimension with a minimum size of 10 mm[40], was regarded as the index lesion. Synchronous unilateral or bilateral cancers were regarded as independent lesions[37]. Morphological and enhancement features of the cancers such as shape, margins and internal enhancement characteristics were reported for all imaging examinations according to the 5th edition of the ACR BI-RADS lexicon[41]. Both readers were blinded to the histopathological outcome of the lesions.

6.2.4.2 Tumour vascularity assessment

Tumour vascularity was assessed by counting the number of feeding vessels adjacent to the tumour. The number of adjacent feeding vessels (AFV), defined as blood vessels either contacting the edge of the lesion or penetrating it, were counted using methodology previously described in Chapter 4 (Section 4.2.3.1).

6.2.4.3 Region-of-interest (ROI) delineation and size assessment

Tumour regions of interest (ROIs) were manually delineated in OsiriX, version 8.0.2 (Pixmeo SARL, Switzerland) on the peak-enhancing DCE-MR image (post-contrast T1WI 19 of the DCE-MRI), and included all consecutive axial sections encompassing the enhancing tumour mass. Subtracted images were used to display a clear tumour margin so as not to exceed tumour boundaries. In cases of multifocality or multicentricity on the MRI, ROIs were drawn for the largest enhancing tumour focus, excluding possible *in situ* carcinoma observed as non-mass suspicious enhancement around the enhancing tumour mass. Areas of low enhancement within

the tumour, which could be indicative of necrosis, and tumour blood vessels adjacent to the mass were not included in the ROIs. To maximise consistency in region delineation, ROIs for sequential imaging examinations for a patient were drawn with the baseline MRI exam displayed on the screen.

Tumour size was estimated according to the criteria outlined in RECIST 1.1 by evaluating changes in the longest diameter of the enhancing lesion regardless of orientation[40]. In cases of tumour fragmentation during treatment, the longest diameter of each fragment was aggregated to calculate the size of the index lesion. In addition, total tumour volume was calculated by summing the volume of tumour areas across all slices encompassing the cancer and multiplying by the slice thickness (i.e. 1.4 mm).

6.2.4.4 Quantitative analysis

Pharmacokinetic analysis of the DCE-MRI series was performed in MIStar, version 3.2.63 (Apollo Medical Imaging, Melbourne, Australia) using the extended Tofts' model to calculate the contrast influx rate constant, K^{trans}; the contrast efflux rate constant, k_{ep}, and the volume of extravascular-extracellular space, v_e. Prior to pharmacokinetic modelling, corrections for the effect of transmission-field inhomogeneity on DCE-MR images were performed as previously described (Chapter 3, Section 3.4.2.2). K^{trans} in the most vascularised area of the tumour (hotspot K^{trans}) were calculated by averaging pixel values within a 3×3-pixel region placed around the area exhibiting the highest K^{trans} value on the K^{trans} parametric maps[28].

6.2.5 Histology

Histopathological information including histological subtype, grade, and the expression of oestrogen receptors (ER), progesterone receptors (PR) and human epidermal growth factor receptor 2 (HER2) were obtained from pathology reports. Tumours were graded according to the Elston-Ellis scoring system[42]. For the purposes of analysis, tumour histological types were classified as follows[43]: breast cancers of no special type (NST), including invasive ductal and medullary carcinomas; invasive lobular carcinomas (ILC); mixed carcinomas involving two or more histological components, and breast cancers of special type including mucinous, apocrine, micropapillary or tubular carcinomas. Cancers with positive ER or PR expression were classified as hormone-receptor (HR) positive. Lesion molecular subtypes were categorised as follows: HR-positive/HER2-negative, HR-positive/HER2-positive (triple-

positive), HR-negative/HER2-positive (HER2-enriched) and HR-negative/HER2-negative (triple negative).

6.2.6 Tumour pathological response

The assessment of pathological tumour response to neoadjuvant chemotherapy was performed by pathologists with >15 years of experience in breast cancer according to the criteria proposed by Pinder *et al* [44]:

1. *Pathological complete response* (pCR) involving either no residual invasive cancer or only including residual *in-situ* carcinoma.
2. *Pathological partial response* to therapy (pPR), involving either:
    i. minimal residual disease or near total response with < 10% of tumour remaining
    ii. evidence of response to therapy with 10 – 50% of tumour remaining, or
    iii. evidence of tumour cellularity of >50% when compared with the previous core biopsy sample, with presence of some features of response to therapy (e.g. fibrosis).
3. *No evidence of response* to therapy when no changes were observed in tumour cellularity in comparison with pre-treatment core-biopsies.

In this study, breast cancers only showed either partial or complete pathological response to NAC. Patients whose cancers showed pathological partial response to chemotherapy were classified as partial responders, whereas those with lesions that showed complete pathological response to chemotherapy were classified as complete responders.

6.2.7 Statistical analysis

Data is presented as *n* (%), mean ± SD or median [range] as appropriate. Statistical analysis was performed in IBM SPSS Statistics for MacOS, v25.0 (IBM Corp., Armonk, NY) or R v3.5.2 (The R Foundation for Statistical Computing 2018). Continuous data were checked for normality using the Anderson-Darling test. Correlations between continuous variables were assessed via Pearson (*r*) or Spearman correlation (ρ), whereas associations between categorical variables were assessed using χ^2 or Fisher's exact tests and Cramer's *V*. Comparison between means of two independent groups were performed using *t*-tests, and ANOVA when more than two groups were compared. Where data was not normally distributed, or normality could not be assessed, Mann-Whitney *U* and Kruskal-Wallis *H* or Mood's median tests were employed for comparisons between two or more groups, respectively *p*-values <0.05 were considered

statistically significant, except for cases in which *p*-values were adjusted using the Holm-Bonferroni method.

Linear mixed effects (LME) models with random intercepts and slopes for subjects were used to assess changes in DCE-MRI parameter during chemotherapy and *p* values from post-hoc analyses were adjusted for multiple comparisons using the Holm-Bonferroni method. Where the ensuing residuals for the mixed effects models were not normally distributed as indicated by normality tests and Q-Q plots, dependent variables (i.e. quantitative DCE-MRI parameters) were transformed using the natural logarithm to yield more normally distributed residuals. The percentage rate of change in DCE-MRI metrics during NAC was calculated using $100\times (e^{\beta} - 1)$, where β refers to the regression coefficient for chemotherapy cycle as estimated by the mixed models. Factors affecting DCE-MRI parameter changes during NAC were identified through univariate analyses and included into the models if *p*-values were ≤ 0.1.

Binomial logistic regression was used to evaluate the probability of complete pathological response based on quantitative DCE-MRI parameters at baseline, post-cycle 1 and changes between these time points. Prior to logistic regression, case-wise deletion was applied to observations with missing data. In combination models involving quantitative DCE-MRI metrics and tumour prognostic factors (i.e. histological subtype, molecular subtype, grade, presence of *in situ* carcinoma), variables were selected for inclusion into the logistic regression based on univariate analysis using a cut-off for significance of $p=0.1$ for main effects and $p=0.25$ for interactions. Receiver-operating characteristic (ROC) curve analysis and the area under the curve (AUC) was used to assess the ability of DCE-MRI metrics in predicting pathological response. The AUC, sensitivity and specificity for each parameter or parameter combination were estimated using the De Long method, while the optimal cut-off point (i.e. the point on the ROC curve, which is furthest from the line of no discrimination and minimises the overall rate of misclassification) was selected according to the Youden index. *p* values were adjusted for multiple comparisons using the Holm-Bonferroni method.

6.3 Results

6.3.1 Clinical characteristics of the patient population

Eighty-two women with 86 breast cancers were analysed. The median age of the patients was 53 [28 – 75] years, with the vast majority 95% (78/82) presenting only one tumour. Of the breast lesions examined, 83% (71/86) were invasive carcinomas of no special type (NST), 11% (10/86) were cancers of special type and lobular carcinomas (ILC), while 5% were mixed invasive carcinomas (2 invasive carcinomas with NST and ILC components; 1 NST and mucinous carcinoma; 2 NST cancers with apocrine or micropapillary features, respectively). Our sample consisted of intermediate and high-grade tumours (grade 2 or 3), with 59/86 (69%) lesions being grade 3 NST carcinomas (nuclear grade *vs* tumour histology: Cramer's V=0.34, p=0.02). Two-thirds of the tumours examined (57/86) were positive for hormone receptors, with 31% (27/86) also being positive for HER2. Approximately a quarter of the lesions (21/86; 24%) were characterised as triple-negative, while HER2-enriched tumours constituted 9% (8/86) of the sample examined. Furthermore, two-thirds of the grade 3 tumours examined were classified as either triple-positive or triple-negative (39/59; 66%), while 56% (15/27) of the grade 2 cancers were HR+/HER2- (nuclear grade *vs* molecular subtype: Cramer's V=0.32, p=0.04). Clinical information about the patient population at the time of diagnosis is given in Table 6.2. Tumour histological characteristics are presented in Table 6.3.

Table 6.2 Clinicopathological characteristics for the patient population. (*n*=82 patients and *n*=86 breast cancers).

Characteristic	***n* (%)**
Age at diagnosis (years)[a]	53 [28 – 75][a]
Disease presentation (*n*=82)	
Unilateral (single tumour)	78 (95)
Unilateral (two tumours)	3 (4)
Bilateral	1 (1)
Tumour location (*n*=86)	
Right breast	43 (50)
Left breast	43 (50)
Neoadjuvant chemotherapy regimen (*n*=86)	
Taxane + anthracyclines	50 (58)
Taxane + trastuzumab (with anthracyclines)	33 (38)
Taxane + trastuzumab (without anthracyclines)	2 (2)
Taxane + others[b]	1 (1)

[a]Data presented as median [range].

[b]Chemotherapy involving co-administration of a taxane and cyclophosphamide or carboplatin.

Table 6.3 Tumour histological characteristics (*n*=86 lesions).

Characteristic	***n* (%)**
Histological sub-type	
No specific type (NST)	71 (83)
Lobular (ILC)	3 (3)
Mixed[a]	5 (6)
Special type	7 (8)
Histological Grade	
1	0 (0)
2	27 (31)
3	59 (69)
Molecular subtype	
HR+/HER2-	30 (35)
HR+/HER2+	27 (31)
HR-/HER2+	8 (9)
HR-/HER2-	21 (24)
Presence of *in situ* carcinoma after surgery	
Absent	36 (42)
DCIS	29 (34)
LCIS	1 (1)
Mixed[b]	1 (1)
No information	19 (22)
Pathological size after surgery (mm)	16 [0 – 152][b]

[a]Invasive or *in situ* carcinoma for which histology indicated the presence of two or more histological components.
[b]Data presented as median [range].
HR: hormone receptor; HER2: Human epidermal growth factor receptor 2; DCIS: ductal carcinoma *in situ*; LCIS: lobular carcinoma *in situ*.

6.3.2 Clinical characteristics and pathological response

Overall, 58% (50/86) of the cancers were treated with an anthracycline and taxane-based NAC regimen, and 40% (35/86) with a HER2-targeted agent in combination with taxanes with or without anthracyclines (Table 6.2). The clinico-histological characteristics of the breast tumours examined according to their therapeutic response are presented in Table 6.4. The majority of cancers (59/86; 69%) had pathological partial response (pPR) to NAC, while 31% (27/86) of the lesions showed pathological complete response (pCR). There were no cancers with no evidence of response to chemotherapy or disease progression and no significant association was observed between histological subtype or grade and pathological response (Table 6.4). However, it should be noted that most lesions examined were grade 3 (59/86; 69%)

and NST carcinomas (71/86; 83%). A statistically significant association was observed between molecular subtype and response (Cramer's $V = 0.44$, $p<0.001$; Table 6.4), with triple-negative cancers more likely to have a pCR (12/21; 57%) and HR-positive tumours to have a pPR (46/57; 81%). No statistically significant association was observed between the presence of *in situ* carcinoma on post-surgical pathological specimens and pathological response (Table 6.4).

Table 6.4 Tumour histological characteristics according to therapeutic response (*n*=86 lesions).

Characteristic	**Pathological response**		***p***
	pCR ***n***	**pPR** ***n***	
Lesions	27	59	
Histological sub-type			
NST	23	48	0.12[b]
ILC	0	3	
Mixed	0	5	
Special type	4	3	
Grade			
2	5	22	0.13[a]
3	22	37	
Molecular subtype			
HR+/HER2-	2	28	<0.001[b]
HR+/HER2+	9	18	
HR-/HER2+	4	4	
HR-/HER2-	12	9	
In situ carcinoma (*n*=67 lesions)			
Absent	13	23	0.43[a]
Present	8	23	
Neoadjuvant chemotherapy regimen			
Taxane + anthracyclines	14	36	0.82[b]
Taxane + trastuzumab (w/-w/o Anthracyclines)	12	23	
Taxane + others	1	0	
Neoadjuvant chemotherapy schedule			
Taxane first	14	30	0.78[b]
Taxane second	9	23	
Taxane throughout	4	6	

[a]Fisher's exact test
[b]χ^2 test with continuity correction

pCR: pathological complete response; pPR: pathological partial response.

As described previously, all patients received taxane-based therapy with or without anthracyclines (Table 6.2). The type of NAC and the sequence of taxane administration (i.e. taxane use during the first or second phase of NAC, or for the entire duration of treatment) was not associated with therapeutic response (Table 6.4).

Following surgery, 6/82 (7%) patients in our cohort died from cancer-related causes within 3 years from diagnosis. Of the remaining 76 women, 4 (5%) developed local cancer recurrence or distal metastases within 3 years from initial diagnosis (records accessed in December 2019).

6.3.2 MRI scans

Of the recruited patients, 45% (37/82) underwent MRI examinations at baseline, mid-treatment and end-of-treatment, while a third of the patients (27/82) completed the baseline and all follow-up MRI scans. Post-cycle 1 MRI data were available from 36/82 (44%) women. In total, 257 MRI examinations were available for analysis. Morphological data, enhancement characteristics and local vascularity features were extracted from 256 MRI examinations, with 1 scan excluded from visual assessment (no contrast in the heart and blood vessels was seen). Pharmacokinetic analysis of DCE-MRI series included data from 244 scans and consisted of 77 baseline, 33 post-cycle 1, 72 mid-treatment and 62 end-of-treatment MRI scans. A total of 13 examinations were excluded from pharmacokinetic analysis due to inadequate MRI acquisition or DCE-MRI post-processing (errors in fat saturation or the acquisition of B_1 and T_1 mapping sequences and faulty correction of magnetic field inhomogeneity) and poor visualisation of contrast in the heart and blood vessels following injection. Eight patients showed complete radiological response on their MRI follow-ups and, pharmacokinetic estimates or morphology measurements could not be derived from 8 scans owing to the absence of a malignant lesion in the images (Figure 6.1). The median time between baseline and mid-treatment or mid-treatment and end-of-treatment MRI scans was 42 [34 – 49] days, and the median time from the first DCE-MRI scan to the first cycle of NAC was 5 [2 – 10] days.

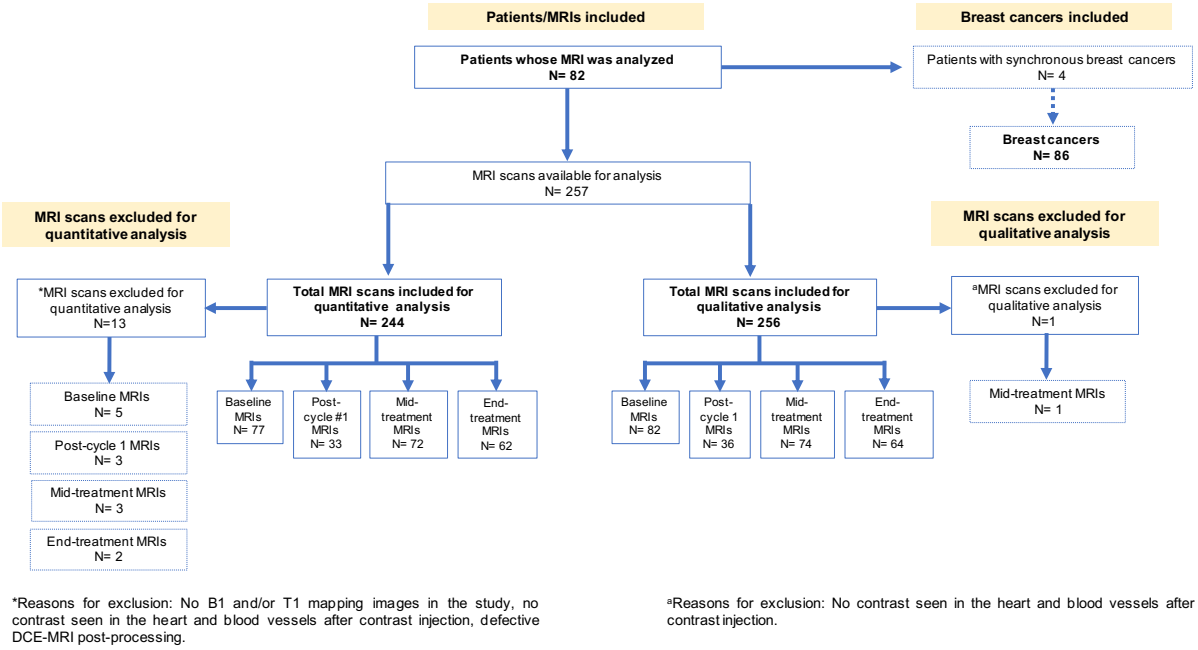

Figure 6.1 Flow chart of DCE-MRI scans included in the analysis.

6.3.3 Tumour morphological and enhancement characteristics at baseline and associations with pathological response

Tumour morphology and enhancement characteristics at baseline and according to tumour pathological response are summarised in Tables 6.5 and 6.6 respectively. The median tumour longest diameter on MRI at baseline was 30 [11 – 70] mm (Table 6.5), with no significant difference between lesions with pCR and pPR (Table 6.6). Similarly, no significant difference in tumour volume or the number of AFV was found between tumours in the two response groups (Table 6.6). However, a statistically significant association was observed between pathological response and the longest tumour diameter at baseline when cancers were classified as being ≤20 mm or >20 mm in the longest diameter (Cramer's $V = 0.26$, p=0.03; Table 6.6). Masses featuring an irregular shape and non-circumscribed margins were prevalent among the breast cancers evaluated (Table 6.5), while 76% (65/86) of the lesions showed rim enhancement. Shape and margin descriptors at baseline were not extracted for 3/86 (3%) cancers, as these presented with non-mass like enhancement on the pre-treatment MRI. No association was observed between pathological response and AFV, morphological or enhancement characteristics at baseline (Table 6.6).

Table 6.5 Tumour morphological and enhancement characteristics at baseline (*n*=86 lesions).

Characteristic	***n* (%)**
Lesion longest diameter on MRI (mm)	30 [11 – 70][a]
≤ 20 mm	17 (20)
> 20 mm	69 (80)
ROI volume (cm^3)	4.6 [0.5 – 106.6][a]
Shape	
Oval	10 (12)
Round	2 (2)
Irregular	71 (83)
Not evaluated[b]	3 (3)
Margins	
Circumscribed	2 (2)
Non-circumscribed	81 (94)
Irregular	34 (40)
Spiculated	47 (55)
Not evaluated[b]	3 (3)
Internal enhancement	
Heterogeneous	21 (24)
Rim enhancement	65 (76)
Adjacent feeding vessels (AFV; number)	36 [9 -112][a]

[a]Data presented as median [range].
[b]Morphological descriptors were not evaluated for lesions showing non-mass-like enhancement on the MRI.

Table 6.6 Tumour morphology and enhancement characteristics at baseline according to therapeutic response (*n*=86 lesions).

Characteristic	Pathological Response		*p*
	pCR	pPR	
	n	*n*	
Lesions	27	59	
Longest diameter on MRI (mm)	28 [14 – 70]	32 [11 - 69]	
≤ 20 mm (*n*=17)	6	11	0.26[a,b]
> 20 mm (*n*=69)	21	48	0.03*[c]
Volume (cm^3)	3.7 [1.0 – 30.7]	5.0 [0.5 – 106.6]	0.21[a,b]
Shape (*n*=83 lesions[e])			0.30[d]
Oval	5	5	
Round	0	2	
Irregular	22	49	
Margins (*n*=83 lesions[e])			0.12[d]
Circumscribed	2	0	
Irregular	11	23	
Spiculated	14	33	
Internal enhancement			0.19[c]
Heterogeneous	4	17	
Rim enhancement	23	42	
Adjacent feeding vessels (AFV; number)	31 [9 – 82]	42 [12 – 112]	0.27[a,b]

[a]Data presented as median [range].
[b]Mann-Whitney *U* test
[c]Fisher's exact test
[d]χ^2 test with continuity correction
[e]Morphological descriptors not evaluated for lesions appearing as non-mass like on the MRI.
*p<0.05; **p<0.01; ***p<0.001
pCR: pathological complete response; pPR: pathological partial response.

6.3.4 Changes in DCE-MRI parameters during NAC

There was no statistically significant difference in DCE-MRI metrics between patients who received their mid-treatment scan after 3 or 4 cycles of chemotherapy (Table 6.7). Similarly, no difference was observed in hs-K^{trans}, AFV, the longest lesion diameter and volume in patients who underwent a total of either 6 or 7 cycles of NAC (Table 6.7). However, significant differences in K^{trans}, k_{ep} and v_e were observed between 6 or 7 cycles of NAC, indicating that end-of-treatment DCE-MRI metrics could not be pooled in a single time point for subsequent

statistical comparisons. Consequently, the NAC cycle at which each patient received an MRI examination was explicitly specified in mixed effects analyses evaluating changes in DCE-MRI metrics during treatment.

Associations between DCE-MRI pharmacokinetic parameters, patient age at diagnosis and the longest tumour diameter or volume were evaluated using LME models with covariates for age, chemotherapy cycle and tumour LD or volume. The mixed models included terms for the interaction between chemotherapy cycle and LD or volume, and random effects for subject intercepts and slopes. Normality tests and Q-Q plots indicated that model residuals were not normally distributed for all the DCE-MRI parameters examined, hence these parameters were transformed using the natural logarithm before being inserted into the model (see Section 6.2.7).

Table 6.7 Median and range of DCE-MRI parameters at the mid and end-of-treatment timepoints. Statistical comparisons were performed using the Mann-Whitney *U* test.

	Mid-treatment			**End-of-treatment**		
Parameter	3 cycles	4 cycles	*p*	6 cycles	7 cycles	*p*
Lesions (*n*)	62	8		45	8	
K^{trans}	0.18 [0.01 – 2.10]	0.20 [0.04 – 0.64]	0.89	0.11 [0.00 – 3.71]	0.26 [0.11 – 1.16]	0.01*
hs-K^{trans}	1.61 [0.03 – 4.99]	1.69 [0.08 – 5.00]	0.63	0.57 [0.01 – 4.86]	1.7 [0.25 – 4.98]	0.11
k_{ep}	0.34 [0 – 1.96]	0.33 [0.11 – 1.85]	0.84	0.21 [0 – 1.86]	0.39 [0.15 – 1.10]	0.02*
v_e	0.42 [0.01 – 0.99]	0.44 [0.14 – 0.80]	0.95	0.35 [0.00 – 0.99]	0.56 [0.34 – 0.87]	0.01*
Lesions (*n*)	62	7		43	11	
AFV	12 [1 – 38]	12 [2 – 29]	0.99	10 [4 - 39]	9 [3 - 17]	0.80
Lesions (*n*)	64	8		46	12	
LD	24 [9 – 62]	34.5 [20 – 54]	0.07	19.5 [1 – 32]	21 [12 – 48]	0.16
Volume	1.35 [0.05 – 27.4]	1.60 [0.03 – 6.5]	0.75	0.72 [0.01 – 4.38]	0.71 [0.01 – 3.67]	0.73

$^{*}p<0.05$; $^{**}p<0.01$; $^{***}p<0.001$

K^{trans}: contrast influx transfer rate (mL/g/min); k_{ep}: contrast efflux transfer rate (min^{-1}); v_e: fractional volume of extravascular-extracellular space; AFV: adjacent feeding vessels (number); LD: tumour longest diameter on MRI (mm); volume: cm^3

Tables 6.8 and 6.9 present fixed effects estimates from LME models exploring the associations between log-transformed parameters from DCE-MRI and the longest lesion diameter or volume, respectively. Analyses revealed no statistically significant association between patient age at diagnosis and DCE-MRI metrics, except for the number of AFVs which displayed a significant increase of ~1% per year of age. Similarly, hs-K^{trans} and AFV exhibited positive associations with tumour LD and volume during NAC (Tables 6.8 and 6.9 respectively), indicating a tendency for larger tumours to display a higher number of feeding vessels and higher hs-K^{trans} values. More specifically, hs-K^{trans} showed an increase of 1.6% per mm of tumour diameter and 1.5% per cm^3 of tumour volume, while the number of AFV increased by 2.8% per mm and 1.1% per cm^3. Cancers with smaller volumes at baseline tended to exhibit a larger percentage reduction in hs-K^{trans} during NAC than lesions with bigger volumes (Figure 6.2b.), whereas the rate of decrease in AFV during chemotherapy was higher for lesions displaying a larger tumour diameter (Figure 6.2c.). No statistically significant associations were observed between the other DCE-MRI pharmacokinetic parameters and the longest lesion diameter or tumour volume (Tables 6.8 and 6.9 respectively).

Table 6.8 Fixed-effects estimates (β) together with 95% confidence intervals (CI) and *p*-values for the association between DCE-MRI parameters and chemotherapy cycle, patient age at diagnosis, the tumour longest diameter (LD) on MRI and the interaction effect between the tumour longest diameter and chemotherapy cycle.

Parameter	**Cycle** β, [CI], *p*	**Age** β, [CI], *p*	**LD** β, [CI], *p*	**LD*Cycle** β, [CI], *p*
$ln(K^{trans})$	-0.127, [-0.252 – -0.002], 0.047*	0.007, [-0.006 – 0.021], 0.28	0.007, [-0.006 – 0.019], 0.29	-0.001, [-0.006 – 0.003], 0.51
ln(hs-K^{trans})	-0.219, [-0.361 – -0.077], 0.003**	0.007, [-0.007 – 0.021], 0.35	0.016, [0.002 – 0.029], 0.02*	0.002, [-0.004 – 0.007], 0.57
$ln(k_{ep})$	-0.144, [-0.236 – -0.052], 0.002**	0.009, [0.000 – 0.018], 0.05	0.002, [-0.006 – 0.010], 0.63	-0.001, [-0.005 – 0.002], 0.49
$ln(v_e)$	-0.013, [-0.084 – 0.058], 0.71	0.004, [-0.004 – 0.013], 0.30	0.000, [-0.007 – 0.007], 0.99	0.000, [-0.002 – 0.003], 0.74
ln(AFV)	-0.122, [0.194 – -0.051], 0.001***	0.010, [0.002 – 0.018], 0.02*	0.028, [0.020 – 0.036], <.001***	-0.003, [-0.006 – 0.000], 0.03*
LD	-0.009, [-0.105 – -0.07], <.001***	0.001, [-0.006 – 0.008], 0.82	-	-
Volume	-0.355, [-0.396 – 0.314], <.001***	0.015, [-0.006 – 0.036], 0.17	-	-

*p<0.05; **p<0.01; ***p<0.001

Table 6.9 Fixed-effects estimates (β) together with 95% confidence intervals (CI) and *p*-values for the association between DCE-MRI parameters and chemotherapy cycle, patient age at diagnosis, whole tumour volume and the interaction effect between tumour volume and chemotherapy cycle.

Parameter	**Cycle** β, [CI], *p*	**Age** β, [CI], *p*	**Volume** β, [CI], *p*	**Volume*Cycle** β, [CI], *p*
$ln(K^{trans})$	-0.203, [-0.273 – -0.133], <.001***	0.008, [-0.005 – 0.022], 0.24	0.003, [-0.010 – 0.015], 0.68	-0.010, [-0.023 – 0.003], 0.13
ln(hs-K^{trans})	-0.137, [-0.216 – -0.059], <.001***	0.005, [-0.009 – 0.019], 0.48	0.015, [0.001 – 0.029], 0.04*	0.020, [0.004 – 0.036], 0.02*
$ln(k_{ep})$	-0.202, [-0.253 – -0.151], <.001***	0.009, [0.000 – 0.019], 0.045*	0.004, [-0.004 – 0.013], 0.32	-0.010, [-0.021 – 0.000], 0.05
$ln(v_e)$	-0.028, [-0.067 – 0.0.12], 0.17	0.005, [-0.003 – 0.014], 0.20	-0.005, [-0.012 – 0.003], 0.23	-0.005, [-0.013 – 0.002], 0.14
AFV	0.222, [-0.261 – -0.199], <.001***	0.011, [0.000 – 0.021], 0.04*	0.011, [0.002 – 0.020], 0.02*	0.002, [-0.007 – -0.011], 0.66

*p<0.05; **p<0.01; ***p<0.001

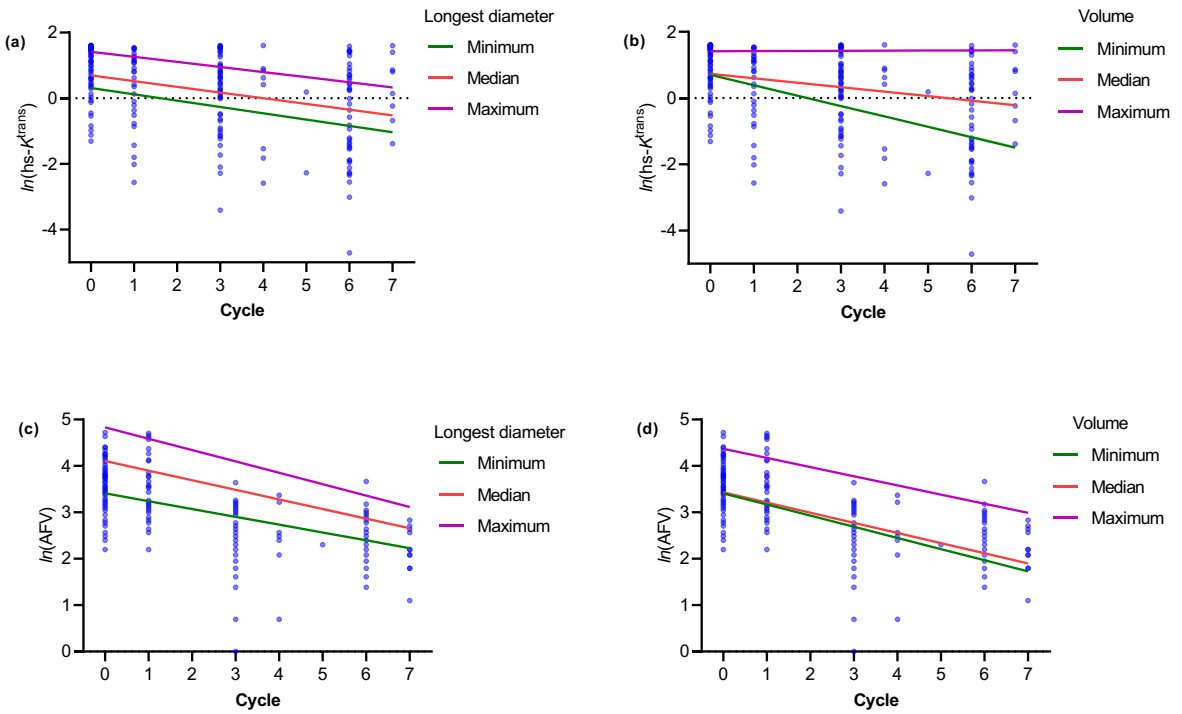

Figure 6.2 (a, b) Scatter plots of log-transformed values of hotspot K^{trans} (hs-K^{trans}; mL/g/cm^3) and **(c, d)** the number of adjacent feeding vessels (AFV) *vs* chemotherapy cycle (*n*=86 lesions). Regression lines indicate the relationship between hs-K^{trans} or AFV and chemotherapy cycle at the minimum, median, and maximum values of the tumour longest diameter and volume.

Changes in log-transformed DCE-MRI parameters as a function of chemotherapy cycle were assessed using LME models which included chemotherapy cycle as a fixed effect together with random intercepts and slopes for subjects. Estimates for the fixed-effects proportion of the model together with 95% confidence intervals (CI) and *p*-values are presented in Table 6.10.

With the exception of v_e, there was a statistically significant decrease in DCE-MRI parameters during the course of NAC (Table 6.10; Figure 6.3 and 6.4). The largest decrease per treatment cycle was observed for tumour volume (-30.5%) followed by AFV (-21.9%) and hs-K^{trans} (-19.9%) (Table 6.10). These relationships were upheld when considering NST carcinomas alone, which constituted the majority in the sample of cancers examined (Table 6.11).

Table 6.10 Fixed effect estimates (β) with 95% confidence intervals (CI) and *p*-values for the associations between chemotherapy cycle and log-transformed parameters from DCE-MRI. Percentage (%) changes in DCE-MRI parameters were calculated according to $100\times(e^{\beta} - 1)$, where β denotes the slope estimate for each parameter as derived from LME models.

	Cycle		**%Change per cycle**
Parameter	β, [CI], *p*	**Parameter**	%, [CI]
ln(K^{trans})	-0.173, [-0.229 – -0.117], <.001*	K^{trans}	-15.9, [-20.5 – -11.0]
ln(hs-K^{trans})	-0.222, [-0.282 – -0.163], <.001*	hs-K^{trans}	-19.9, [-24.6 – -15.0]
ln(k_{ep})	-0.174, [-0.192 – -0.126], <.001*	k_{ep}	-16.0, [-19.0 – -12.7]
ln(v_e)	0.016, [-0.035 – 0.027], <0.80	v_e	1.6, [-3.4 – 2.7]
ln(AFV)	-0.244, [-0.272 – -0.216], <.001*	AFV	-21.6, [-23.8 – -19.4]
ln(LD)	-0.090, [-0.114 – -0.067], <.001*	LD	-8.6, [-10.7 – -6.5]
ln(Volume)	-0.363, [-0.414 – -0.312], <.001*	Volume	-30.5, [-33.9 – -26.8]

$^{*}p<0.05$; $^{**}p<0.01$; $^{***}p<0.001$

Table 6.11 Fixed effect estimates (β) with 95% confidence intervals (CI) and *p*-values for the associations between chemotherapy cycle and log-transformed parameters from DCE-MRI for carcinomas of no special type (NST). Percentage (%) changes in DCE-MRI parameters were calculated according to $100\times(e^{\beta} - 1)$, where β denotes the slope estimate for each parameter as derived from LME models.

	Cycle		**%Change per cycle**
Parameter	β, [CI], *p*	**Parameter**	%, [CI]
ln(K^{trans})	-0.179, [-0.241 – -0.117], <.001*	K^{trans}	-16.4, [-21.4 – -11.0]
ln(hs-K^{trans})	-0.229, [-0.298 – -0.161], <.001*	hs-K^{trans}	-20.5, [-25.8 – -14.9]
ln(k_{ep})	-0.175, [-0.218 – -0.132], <.001*	k_{ep}	-16.1, [-19.6 – -12.4]
ln(v_e)	-0.005, [-0.044 – 0.033], <0.78	v_e	-0.5, [-4.3 – 3.4]
ln(AFV)	-0.242, [-0.272 – -0.211], <.001*	AFV	-21.5, [-23.8 – -19.0]
ln(LD)	-0.080, [-0.101 – -0.059], <.001*	LD	-7.7, [-9.6 – -5.7]
ln(Volume)	-0.362, [-0.417 – -0.306], <.001*	Volume	-30.4, [-34.1 – -26.4]

$^{*}p<0.05$; $^{**}p<0.01$; $^{***}p<0.001$

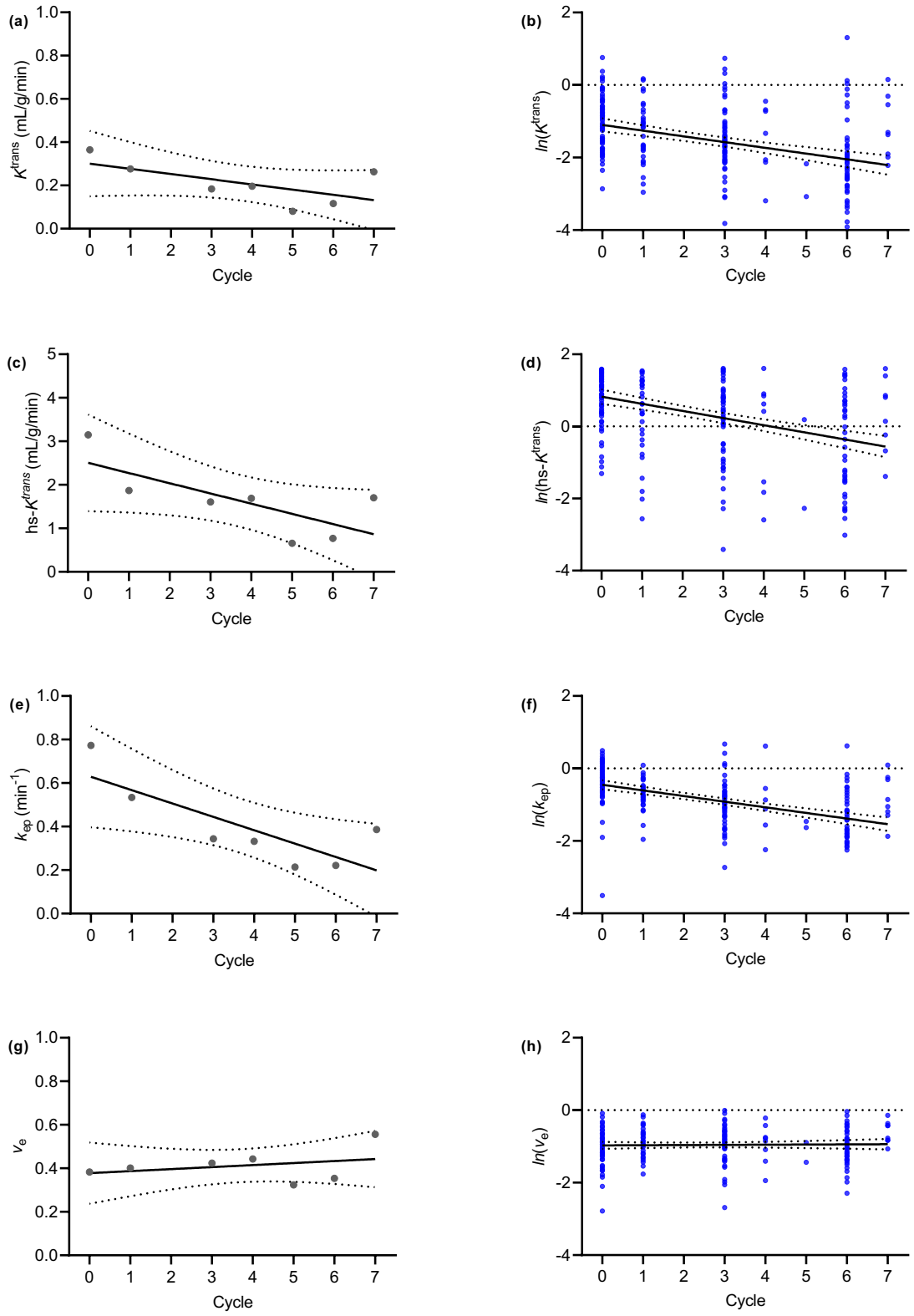

Figure 6.3 (*Left to right*) Scatter plots and regression line of median (column 1) and log-transformed (column 2) DCE-MRI pharmacokinetic parameters *vs* chemotherapy cycle (*n*=86 lesions).

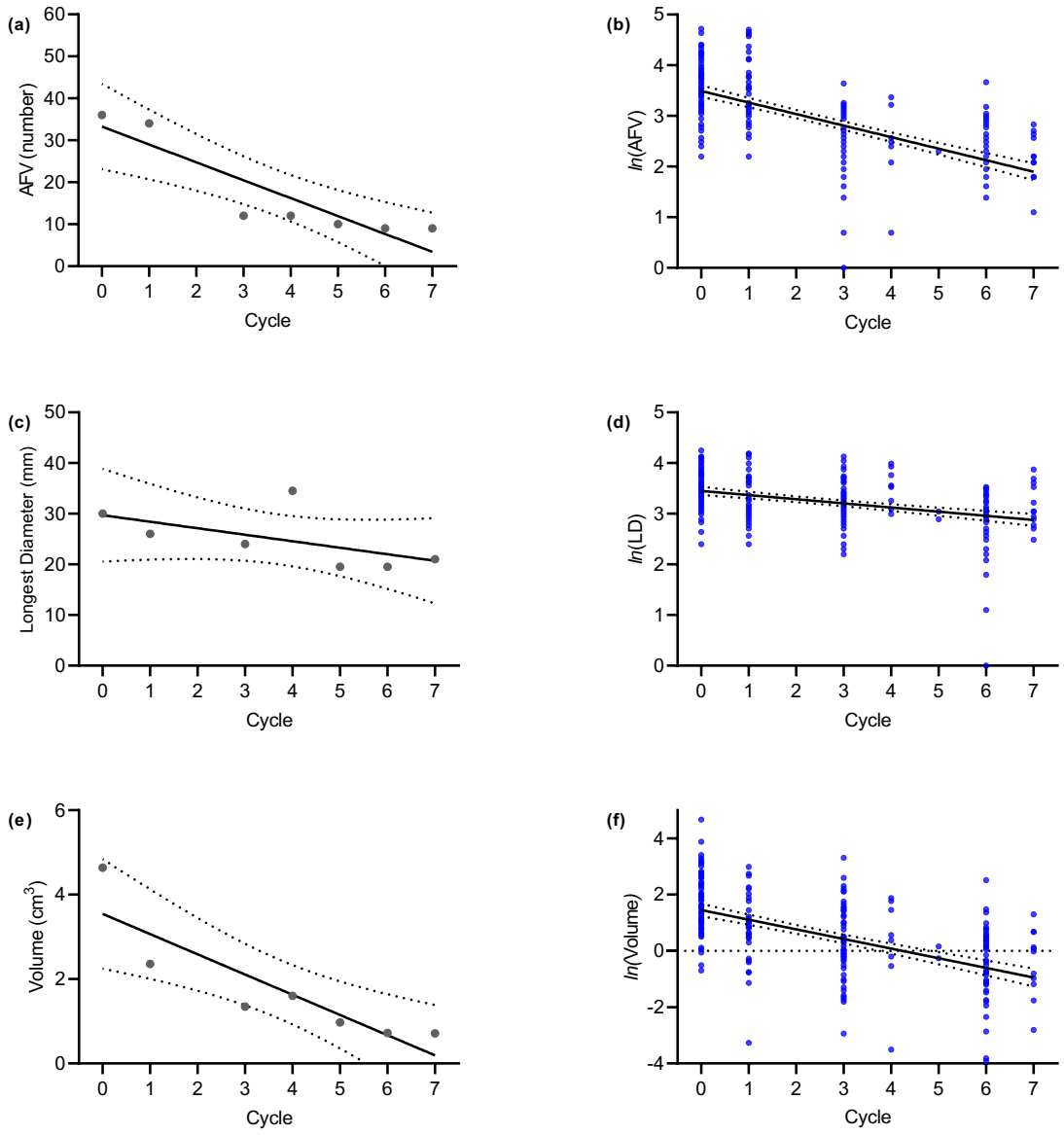

Figure 6.4 (*Left to right*) Scatter plots and regression line of median (column 1) and log-transformed (column 2) values of the number of adjacent feeding vessels (AFV), the tumour longest diameter (LD) and volume *vs* chemotherapy cycle (*n*=86 lesions).

6.3.4.1 Effect of tumour prognostic factors on DCE-MRI parameters during NAC

Table 6.12 presents *p* values for the association between log-transformed DCE-MRI parameters during NAC and tumour histology (A), molecular subtype (B), grade (C) and the presence of *in situ* carcinoma (D) on post-surgical tumour specimens.

Table 6.12 Statistical significance (*p*-values) of fixed effects for the association between log-transformed DCE-MRI parameters and (A) tumour histological subtype, (B) nuclear grade, (C) molecular subtype and (D) presence of *in situ* carcinoma.

A. Histological subtype			
Parameter	**Cycle**	**Histological subtype**	**Histological subtype*Cycle**
ln(K^{trans})	0.02*	0.45	0.43
ln(hs-K^{trans})	0.005**	0.51	0.81
ln(k_{ep})	<.001***	0.85	0.57
ln(v_e)	0.91	0.49	0.72
ln(AFV)	<.001***	0.23	0.38
ln(LD)	<.001***	0.005**	0.002**
ln(Volume)	<.001***	0.04*	0.047*

B. Nuclear grade			
Parameter	**Cycle**	**Grade**	**Grade*Cycle**
ln(K^{trans})	<.001***	0.30	0.86
ln(hs-K^{trans})	<.001***	0.46	0.93
ln(k_{ep})	<.001***	0.33	0.35
ln(v_e)	0.64	0.048*	0.54
ln(AFV)	<.001***	0.57	0.01*
ln(LD)	<.001***	0.46	0.94
ln(Volume)	<.001***	0.55	0.17

C. Molecular subtype			
Parameter	**Cycle**	**Molecular subtype**	**Molecular subtype*Cycle**
ln(K^{trans})	<.001***	0.20	0.76
ln(hs-K^{trans})	<.001***	0.89	0.72
ln(k_{ep})	<.001***	0.65	0.93
ln(v_e)	0.98	0.25	0.29
ln(AFV)	<.001***	0.01*	0.73
ln(LD)	<.001***	0.22	0.95
ln(Volume)	<.001***	0.14	0.63

D. Presence of *in situ* carcinoma			
Parameter	**Cycle**	***In situ* carcinoma**	***In situ*Cycle**
ln(K^{trans})	<.001***	0.55	0.59
ln(hs-K^{trans})	<.001***	0.02*	0.50
ln(k_{ep})	<.001***	0. 24	0.36
ln(v_e)	0.40	0.63	0.26
ln(AFV)	<.001***	0.48	0.41
ln(LD)	<.001***	0.03*	1.00
ln(Volume)	<.001***	0.04*	0.73

*p<0.05; **p<0.01; ***p<0.001

The relationships between log-transformed DCE-MRI metrics and tumour histology as a function of chemotherapy cycle together with mean effects plots and percentage changes during treatment according to histological subtype are shown in Figures 6.5 and 6.6. The percentage rate of change in DCE-MRI parameter values during NAC according to histological subtype is provided in Table 6.13. There was no statistically significant association between tumour histology and log-transformed values of DCE-MRI pharmacokinetic parameters or the number of AFV during NAC. Furthermore, no significant differences in average parameter values between histological subtypes were observed (Figures 6.5 (c), (g), (k) and (o)). However, the effects for both histological subtype and the interaction between histological subtype and chemotherapy cycle were significant on the tumour longest diameter and volume (Table 6.12.A). On average, mixed and NST carcinomas tended to be larger in size (either in terms of the longest tumour diameter or volume) than special-type or lobular tumours (Figures 6.6 (g) and (k)). Furthermore, special-type cancers displayed the largest percentage decrease in tumour size metrics per chemotherapy cycle (Table 6.13; Figure 6.6), while all histological subtypes displayed statistically significant rates of reduction in the number of AFV during treatment (Table 6.13; Figure 6.6 (d)). Significant decreases in K^{trans} and k_{ep} were also observed for NST and mixed cancers (Figure 6.5 (d) and (l)). It should be noted however that NST carcinomas were the majority in this sample (Table 6.3), which limited exploration of the effect of tumour histology on DCE-MRI metrics during the course NAC.

The number of AFV was the only parameter displaying a significant association with nuclear grade (Table 6.12.B). Although grade 2 cancers displayed higher v_e values than grade 3 tumours ($ln(v_e)$ [95% CI] – grade 2 *vs* grade 3: -0.87 [-10.4 – -0.70] *vs* -1.03 [-1.15 – -0.91], p=0.12[1]; Figure 6.7), the effect of tumour grade on v_e only trended towards statistical significance (Table 6.12.B). On the other hand, grade 3 tumours showed a larger percentage decrease in the number of AFV (Table 6.14.A) and a lower average number of AFV than grade 2 cancers (*ln*(AFV) [95% CI] – grade 2 *vs* grade 3: 3.07 [2.86 – 3.28] *vs* 2.81 [2.67 – 2.94], p=0.04[2]; Figure 6.8 (c)). Analogous relationships between tumour grade and the DCE-MRI parameters were observed when considering the portion of NST cancers in this sample (Tables 6.14.A and 6.15.A; Figures 6.9 and 6.10). However, the statistical significance of the association between

[1] Untransformed mean estimates of v_e with 95% confidence intervals [CI] in grade 2 *vs* grade 3 tumours were 0.419 [0.353 – 0.496] *vs* 0.357 [0.317 – 0.402], respectively.
[2] Untransformed mean estimates of AFV with 95% confidence intervals [CI] in grade 2 *vs* grade 3 tumours were 22 [17 – 27] *vs* 17 [14 – 19] vessels, respectively.

ln(v_e) and nuclear grade was not maintained for NST carcinomas, while associations between *ln*(AFV) and grade were trending towards significance (Table 6.15.A).

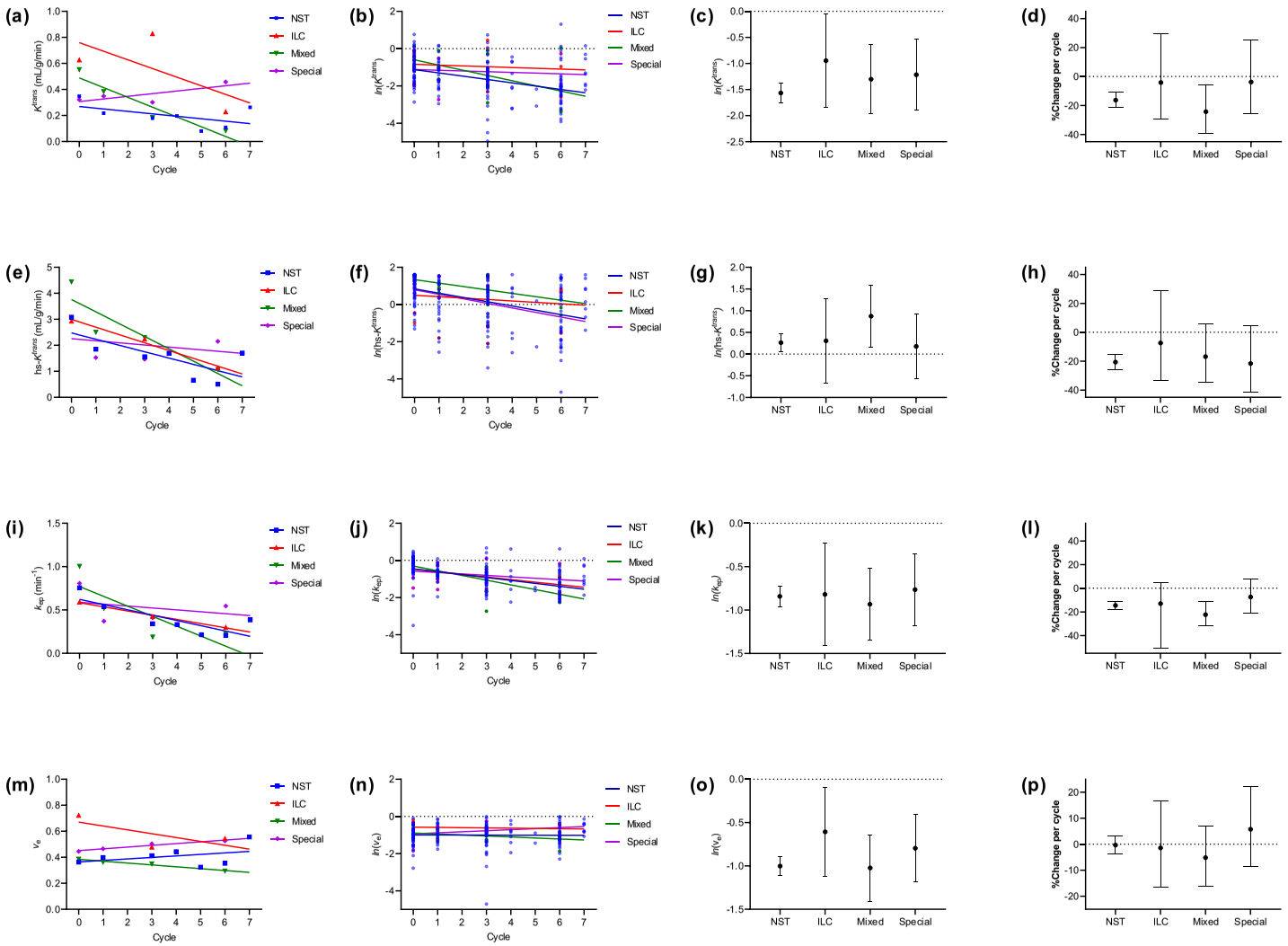

Figure 6.5 (*Left to right*) Scatter plots and regression lines of median (column 1) and log-transformed (column 2) DCE-MRI pharmacokinetic parameters *vs* chemotherapy cycle for the tumour histological subtypes examined (n=86 lesions). Mean-effects plots and percentage (%) changes in parameter values per chemotherapy cycle according to tumour histological subtypes are given in columns 3 and 4, respectively. Error bars denote 95% confidence intervals. NST: carcinoma of no specific type; ILC: invasive lobular carcinoma; Mixed: carcinomas with presence of two histological components; Special: special-type carcinomas.

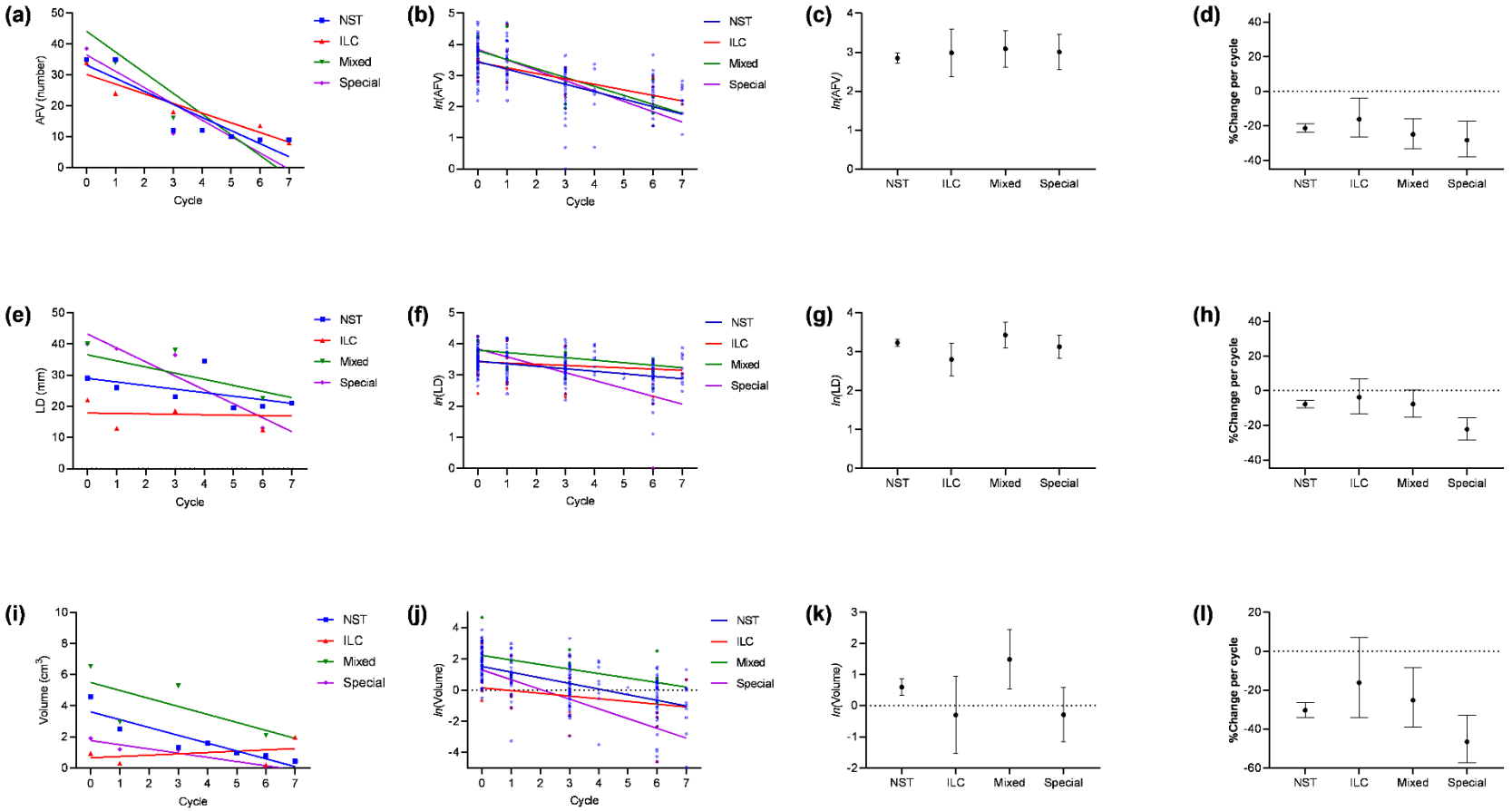

Figure 6.6 (*Left to right*) Scatter plots and regression lines of median (column 1) and log-transformed (column 2) values of the number of feeding vessels (AFV), the tumour longest diameter (LD) and volumes *vs* chemotherapy cycle for the histological subtypes of cancer examined (n=86 lesions). Mean-effects plots and percentage (%) changes of parameter values per chemotherapy cycle according to tumour histological subtype are given in columns 3 and 4, respectively. Error bars denote 95% confidence intervals. NST: carcinoma of no specific type; ILC: invasive lobular carcinoma; Mixed: carcinomas with presence of two histological components; Special: special-type carcinomas.

Table 6.13 Percentage (%) change in DCE-MRI parameter values per chemotherapy cycle together with 95% confidence intervals (CI) and *p* values for the tumour histological subtypes considered in this study. Percentage changes were calculated according to $100\times(e^{\beta} - 1)$, where β denotes the slope estimate for each parameter and histological subtype as derived from LME models.

	Histological subtype			
	NST	**ILC**	**Mixed**	**Special type**
Parameter	%, [CI], *p*	%, [CI], *p*	%, [CI], *p*	%, [CI], *p*
K^{trans}	-16.3, [-21.3 – -10.9], <.001***	-4.2, [-29.1 – 29.4], 0.78	-24.3, [-39.3 – -5.6], 0.01*	-3.8, [-25.9 – 24.9], 0.77
hs-K^{trans}	-20.6, [-25.8 – -15.0], <.001***	-7.4, [-33.6 – 29.0], 0.65	-16.8, [-34.6 – 5.8], 0.13	-21.7, [-41.4 – 4.7], 0.10
k_{ep}	-14.5, [-17.6 - -11.4], <.001***	-13.0, [-27.7 – 4.8], 0.14	-22.4, [-31.9 – -11.5], <.001***	-7.4, [-11.5 – 8.2], 0.33
v_e	-0.3, [-3.7 – 3.3], 0.86	-1.4, [-16.6 – 16.6], 0.87	-5.2, [-16.1 – 7.1], 0.39	5.8, [-8.5 – 22.3], 0.44
AFV	-21.4, [-23.8 – -18.9], <.001***	-16.2, [-26.7 – -4.2], 0.01*	-25.0, [-33.2 – -15.9], <.001***	-28.3, [-37.9 – -17.3], <.001***
LD	-7.8, [-10.0 – -5.5], <.001***	-3.8, [-13.4 – 6.8], 0.46	-7.8, [-15.4 – 0.5], 0.06	-22.4, [-28.6 – -18.3], <.001***
Volume	-30.4, [-34.2 – -26.4], <.001***	-16.1, [-34.2 – 6.9], 0.15	-25.2, [-39.0 – -8.3], 0.006**	-46.5, [-57.3 – 33.0], <.001***

*p<0.05; **p<0.01; ***p<0.001

Table 6.14 Percentage (%) change in DCE-MRI parameter values per chemotherapy cycle together with 95% confidence intervals (CI) and *p* values for tumour nuclear grades. Percentage changes were calculated according to $100\times(e^{\beta} - 1)$, where β denotes the slope estimate for each parameter and histological subtype as derived from LME models.

	A. All histological subtypes		**B. NST carcinomas**	
	Nuclear grade		**Nuclear grade**	
	2	**3**	**2**	**3**
Parameter	%, [CI], *p*	%, [CI], *p*	%, [CI], *p*	%, [CI], *p*
K^{trans}	-17.6, [-23.4 – -11.1], <.001***	-13.4, [-18.1 – -8.5], <.001***	-18.9, [-27.9 – -8.9], <.001***	-15.3, [-21.6 – -8.6], <.001***
hs-K^{trans}	-20.1, [-26.7 – -12.8],	-18.1, [-23.1 – -12.6],	-22.4, [-31.7 – -11.7], <.001***	-19.8, [-26.4 – -12.7], <.001***
k_{ep}	-14.4, [-19.1 – -9.43],	-15.0, [-18.4 – -11.3],	-13.8, [-19.5 – -7.9], 0.001**	-14.8, [-18.5 – -10.8], <.001***
v_e	-2.1, [-6.0 – 2.0], 0.50	1.4, [-1.7 – 4.5], 0.90	-2.0, [-6.8 – -3.2], 0.54	1.9, [-1.5 – 5.3], 0.97
AFV	-17.7, [-21.3 – -13.9], <.001***	-23.3, [-25.7 – -20.9], <.001***	-17.6, [-22.2 – -12.8], <.001***	-23.0, [-25.7 – -20.2], <.001***
LD	-8.5, [-11.1 – -5.7], <.001***	-8.3, [-10.2 – -6.4], <.001***	-6.3, [-9.8 – -2.6], 0.002**	-8.2, [-10.5 – -5.9], <.001***
Volume	-27.0, [-31.9 – -21.7], <.001***	-31.3, [-34.7 – -27.8], <.001***	-26.0, [-33.4 – -17.7], <.001***	-32.0, [-27.3 – -36.4], <.001***

*p<0.05; **p<0.01; ***p<0.001

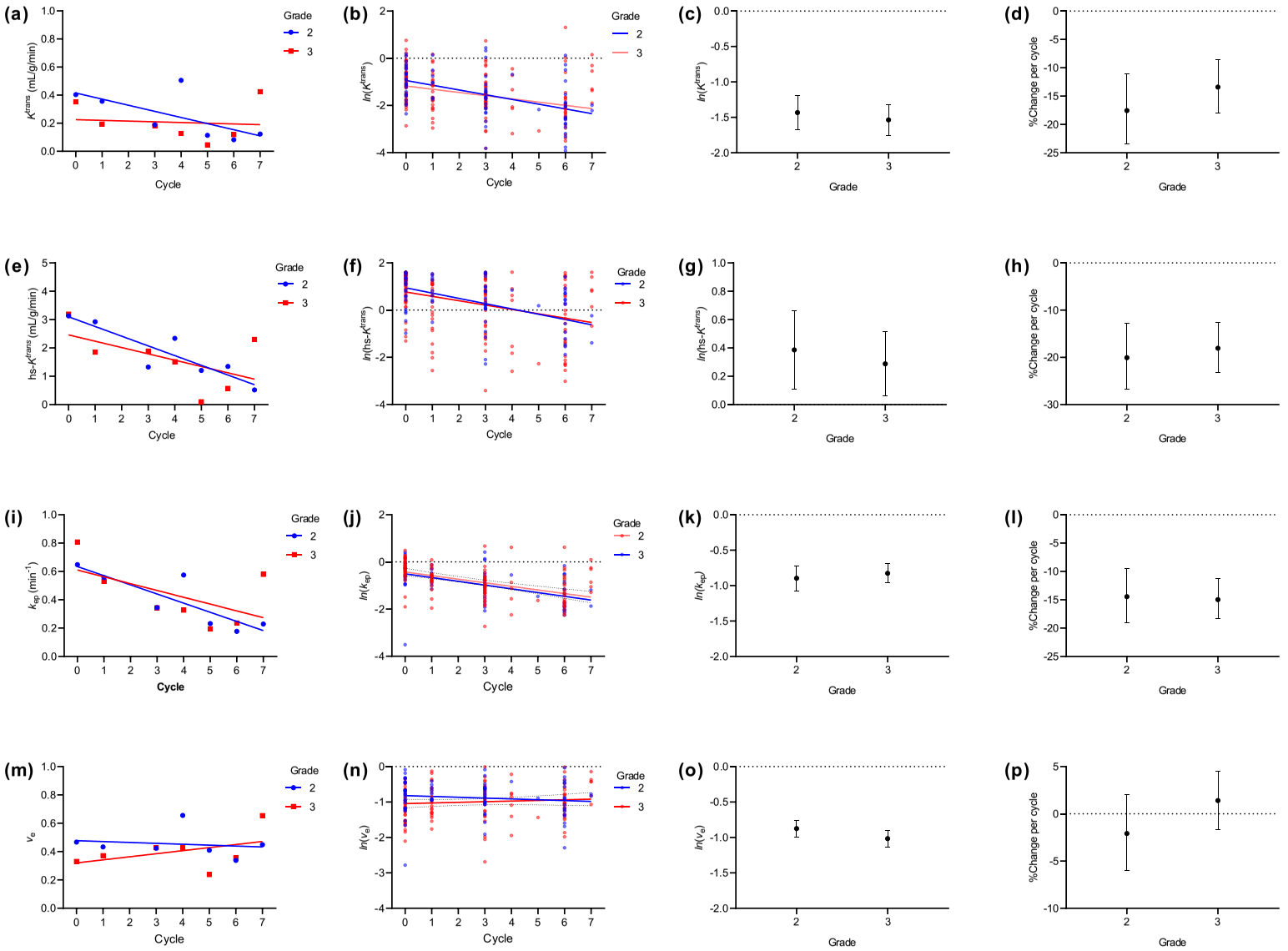

Figure 6.7 (*Left to right*) Scatter plots and regression lines of median (column 1) and log-transformed (column 2) DCE-MRI pharmacokinetic parameters *vs* chemotherapy cycle for tumour nuclear grades (n=86 lesions). Mean-effects plots and percentage (%) changes in parameter values per chemotherapy cycle according to nuclear grade are given in columns 3 and 4, respectively. Error bars denote 95% confidence intervals.

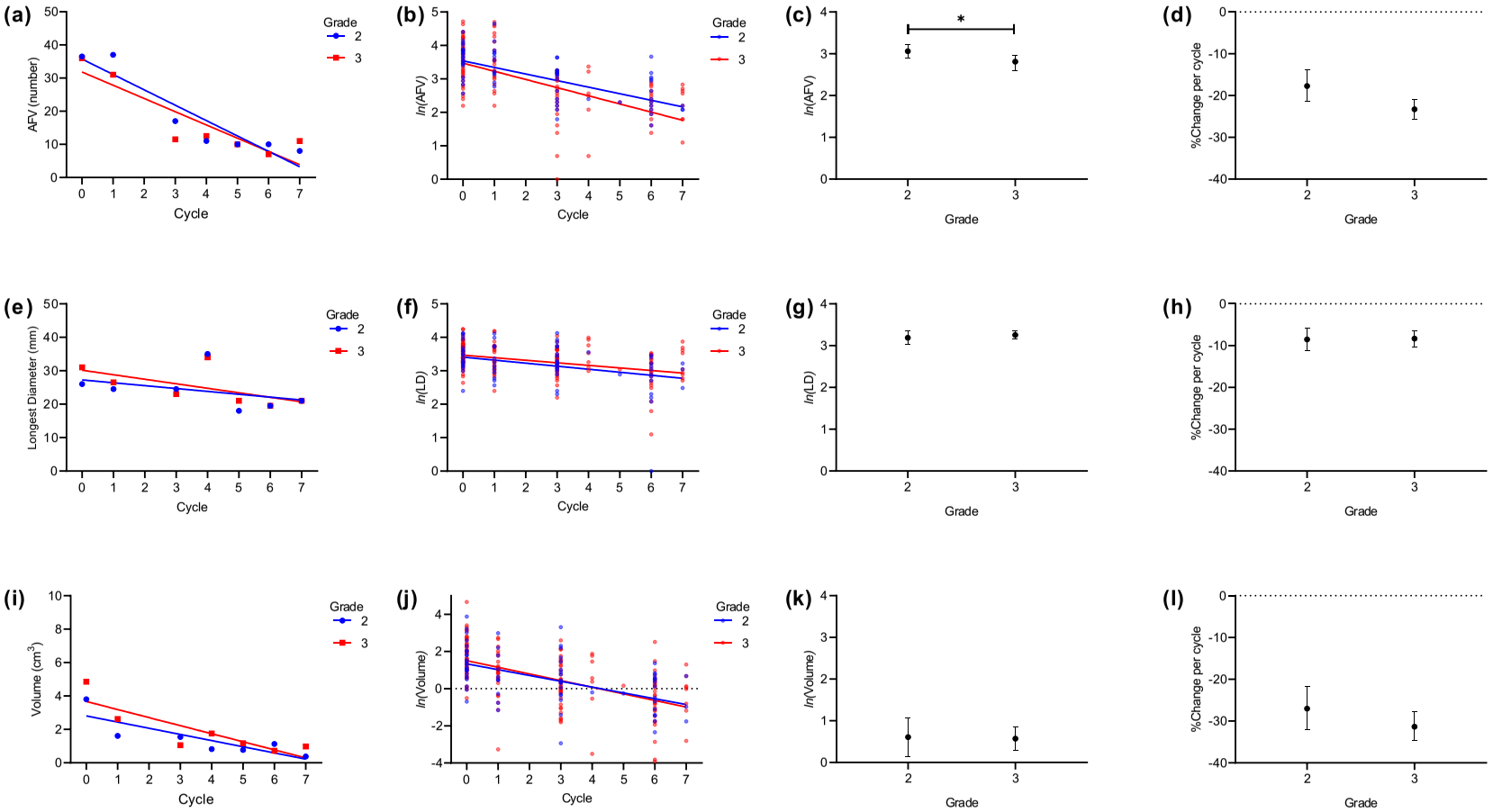

Figure 6.8 (*Left toright*) Scatter plots and regression lines of median (column 1) and log-transformed (column 2) values of the number of feeding vessels (AFV), the tumour longest diameter (LD) and volume *vs* chemotherapy cycle for tumour nuclear grades (n=86 lesions). Mean-effects plots and percentage (%) changes in parameter values per chemotherapy cycle according to nuclear grade are given in columns 3 and 4, respectively. Error bars denote 95% confidence intervals.

With the exception of *ln*(AFV), associations between molecular subtype and log-transformed DCE-MRI parameters were not statistically significant for either the entire sample of tumours (Table 6.12.C) or when considering NST cancers alone (Table 6.15.B). In general, mean pharmacokinetic parameter estimates were higher for HER2-enriched than other molecular sub-types (Figures 6.11 and 6.13), while triple-positive cancers displayed larger volumes (Figures 6.12 (k) and 6.14 (k)) and consequently a higher number of feeding vessels than triple-negative lesions (*ln*(AFV) [95% CI] – HR+/HER2+ *vs* HR-/HER2-: 3.10 [2.91 – 3.20] *vs* 2.57 [2.35 – 2.79], p=0.004[3]; Figures 6.12 (c) and 6.14 (c)). Additionally, HR-positive and triple-negative cancers showed significant reductions in all DCE-metrics aside from v_e (Table 6.16), and similar relationships were observed for the group of NST cancers in this sample (Table 6.17).

Finally, the presence of *in situ* carcinoma in post-surgical tumour specimens was not significantly associated with K^{trans}, k_{ep}, v_e or the number of AFV during NAC, although there was a tendency for cancers with an *in-situ* component to display a larger percentage reduction per NAC cycle and higher values in these parameters than cancers without *in situ* carcinoma (Table 6.12.D; Figures 6.15 and 6.16). hs-K^{trans} was the only parameter exhibiting statistically significant differences between cancers with and without an *in-situ* component either for entire sample of lesions (*ln*(hs-K^{trans}) – absence *vs* presence: 0.09 [-0.17 – 0.34] *vs* 0.46 [0.19 – 0.73], p=0.04[4]) or the sub-group of NST cancers (*ln*(hs-K^{trans}) – absence *vs* presence: -0.04 [-0.30 – 0.23] *vs* 0.44 [0.16 – 0.73], p=0.02[5]; also see Tables 6.12.D and 6.15.C; Figures 6.15 and 6.17).

As expected, the presence of *in situ* carcinoma had a statistically significant effect on tumour size metrics when the entire sample of lesions was taken into consideration (Table 6.12.D), as tumours without an *in-situ* component were smaller in both the longest axis and volume than these in which *in situ* carcinoma was present (Figures 6.16 and 6.18).

[3] Untransformed mean estimates of AFV with 95% confidence intervals [CI] in HR+/HER+ *vs* HR-/HER- tumours were 22 [18 – 27] *vs* 13 [10 – 16] vessels, respectively.
[4] Untransformed mean estimates of hs-K^{trans} with 95% confidence intervals [CI] in cancers with absence *vs* presence of carcinoma *in situ* were 1.091 [0.846 – 1.408] *vs* 1.586 [1.212 – 2.075] mL/g/min, respectively.
[5] Untransformed mean estimates of hs-K^{trans} with 95% confidence intervals [CI] in NST cancers with absence *vs* presence of carcinoma *in situ* were 0.96 [0.742 – 1.254] *vs* 1.556 [1.172 – 2.065] mL/g/min, respectively.

Table 6.15 Statistical significance (*p*-values) of fixed effects for the association between log-transformed DCE-MRI parameters and (A) nuclear grade, (C) molecular subtype and (D) presence of *in situ* carcinoma in carcinomas of no specific type (NST).

		A. Nuclear grade	
Parameter	**Cycle**	**Grade**	**Grade*Cycle**
ln(K^{trans})	<.001***	0.34	0.53
ln(hs-K^{trans})	<.001***	0.26	0.68
ln(k_{ep})	<.001***	0.12	0.29
ln(v_e)	0.62	0.20	0.59
ln(AFV)	<.001***	0.37	0.05
ln(LD)	<.001***	0.78	0.38
ln(Volume)	<.001***	0.49	0.18

		B. Molecular subtype	
Parameter	**Cycle**	**Molecular subtype**	**Molecular subtype*Cycle**
ln(K^{trans})	<.001***	0.40	0.63
ln(hs-K^{trans})	<.001***	0.97	0.62
ln(k_{ep})	<.001***	0.65	0.97
ln(v_e)	0.83	0.58	0.40
ln(AFV)	<.001***	0.04*	0.63
ln(LD)	<.001***	0.48	0.81
ln(Volume)	<.001***	0.32	0.27

		C. Presence of *in situ* carcinoma	
Parameter	**Cycle**	***In situ* carcinoma**	***In situ**Cycle**
ln(K^{trans})	<.001***	0.35	0.61
ln(hs-K^{trans})	<.001***	0.008**	0.53
ln(k_{ep})	<.001***	0.17	0.34
ln(v_e)	0.33	0.46	0.21
ln(AFV)	<.001***	0.79	0.30
ln(LD)	<.001***	0.18	0.36
ln(Volume)	<.001***	0.06	0.60

*p<0.05; **p<0.01; ***p<0.001

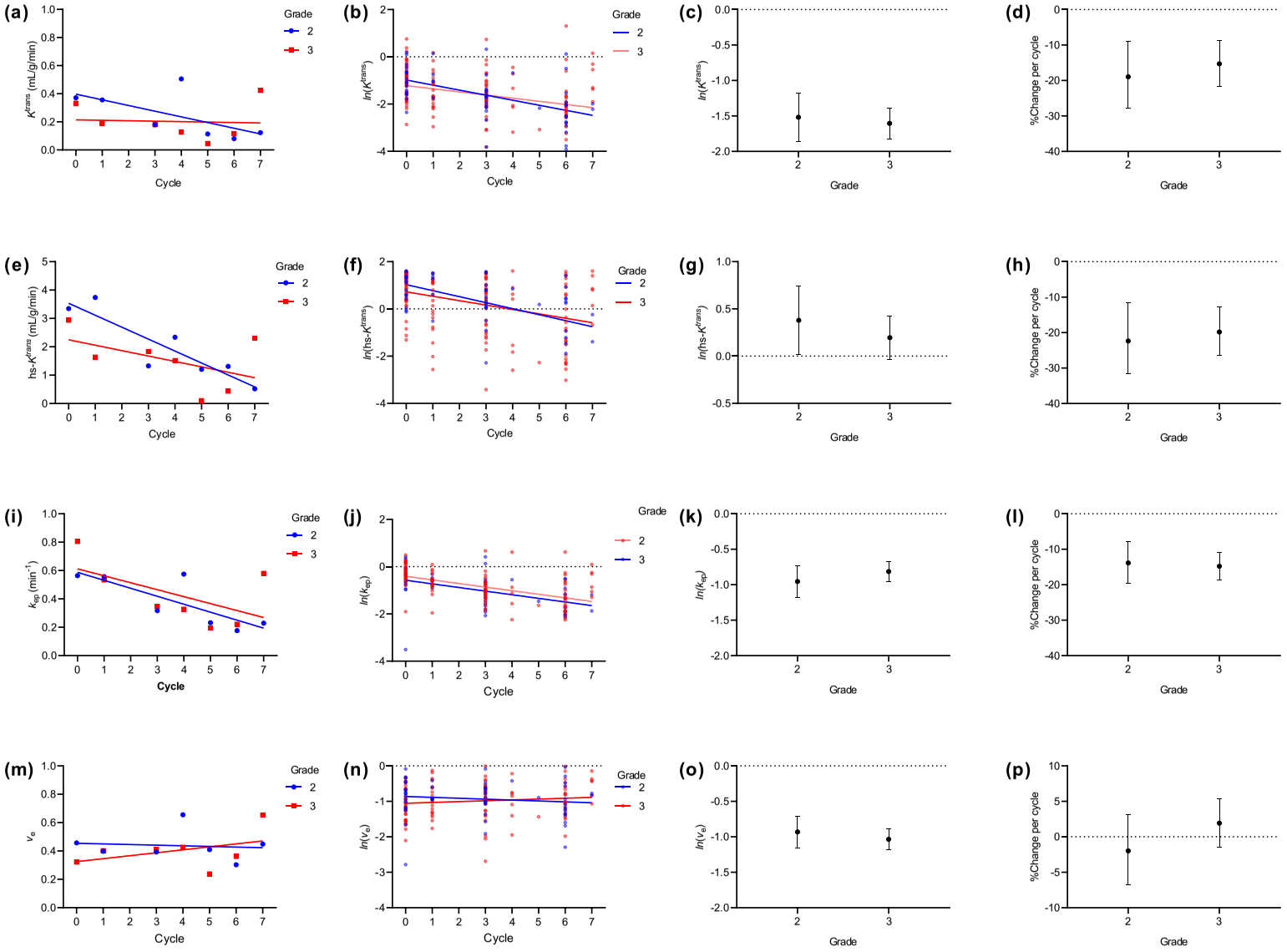

Figure 6.9 (*Left to right*) Scatter plots and regression lines of median (column 1) and log-transformed (column 2) DCE-MRI pharmacokinetic parameters *vs* chemotherapy cycle for nuclear grades in tumours of no specific type (NST; *n*=71 lesions). Mean-effects plots and percentage (%) changes in parameter values per chemotherapy cycle according to nuclear grade are given in columns 3 and 4, respectively. Error bars denote 95% confidence intervals.

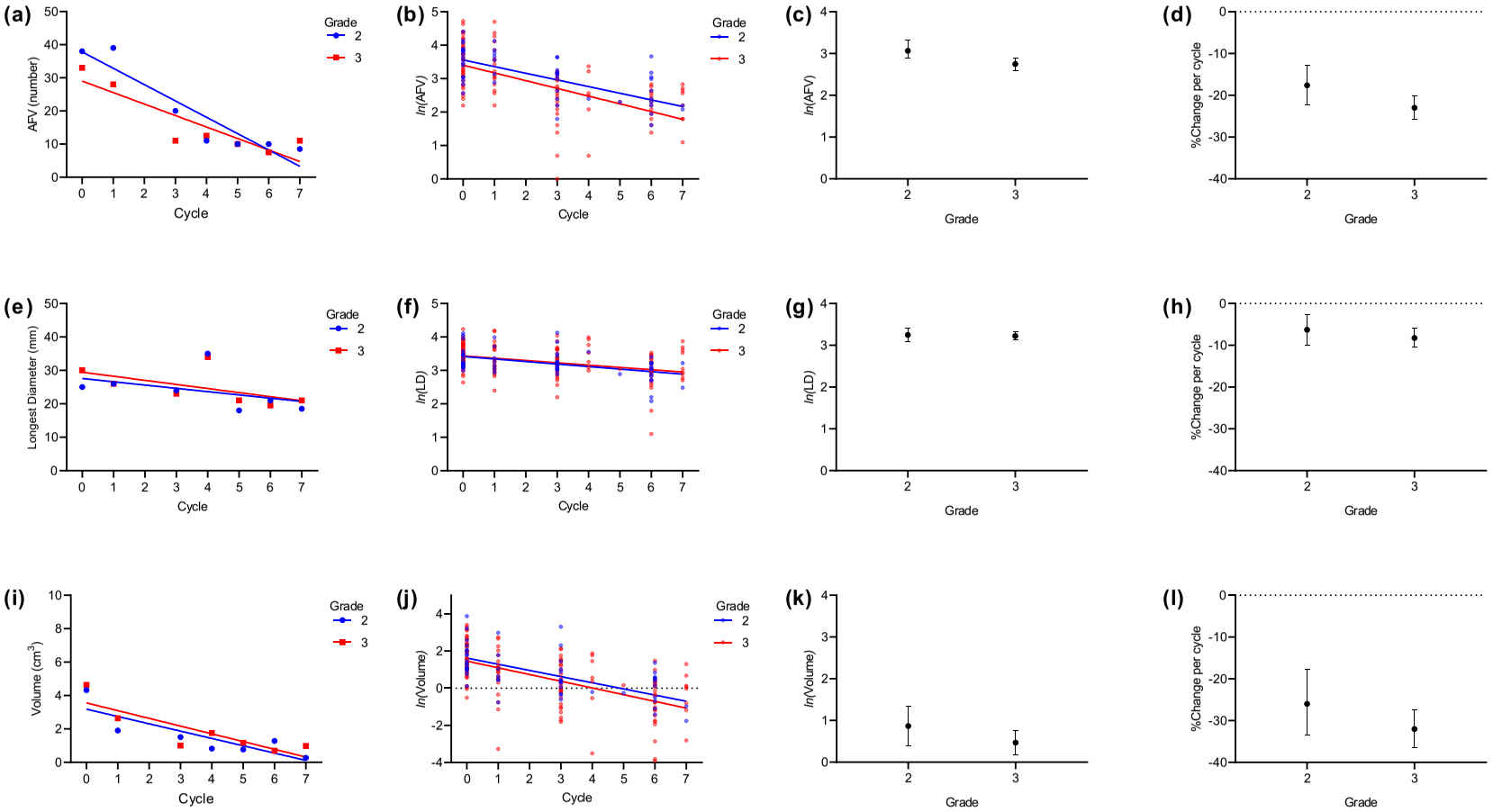

Figure 6.10 (*Left to right*) Scatter plots and regression lines of median (column 1) and log-transformed (column 2) values of the number of feeding vessels (AFV), the tumour longest diameter (LD) and volume *vs* chemotherapy cycle for nuclear grades in cancers of no specific type (NST; *n*=71 lesions). Mean-effects plots and percentage (%) changes in parameter values per chemotherapy cycle according to nuclear grade are given in columns 3 and 4, respectively. Error bars denote 95% confidence intervals.

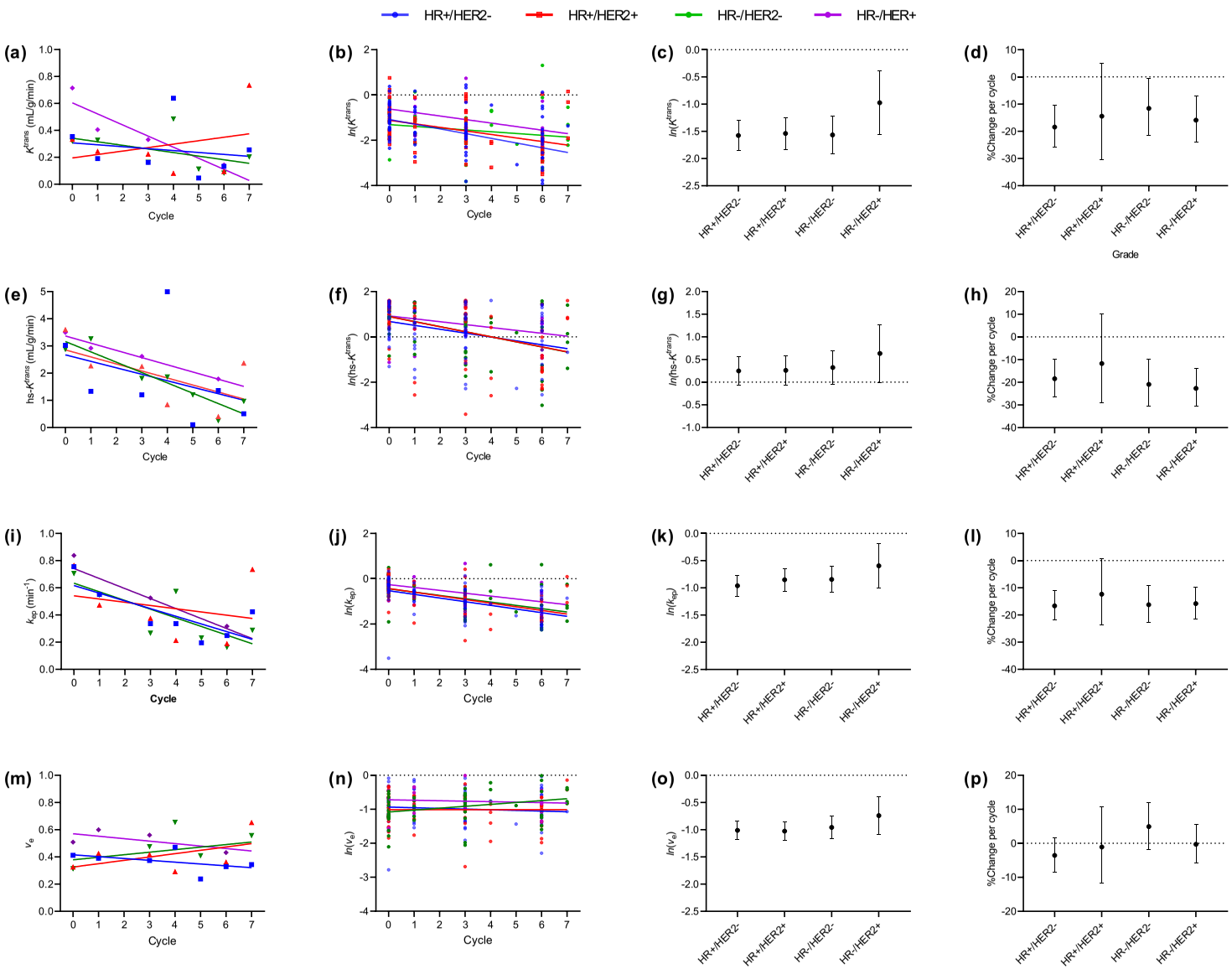

Figure 6.11 (*Left to right*) Scatter plots and regression lines of median (column 1) and log-transformed (column 2) DCE-MRI pharmacokinetic parameters *vs* chemotherapy cycle for tumour molecular subtypes (n=86 lesions). Mean-effects plots and percentage (%) changes in parameter values per chemotherapy cycle according to molecular subtype are given in columns 3 and 4, respectively. Error bars denote 95% confidence intervals. HR: hormone receptor; HER2: human epidermal growth factor 2.

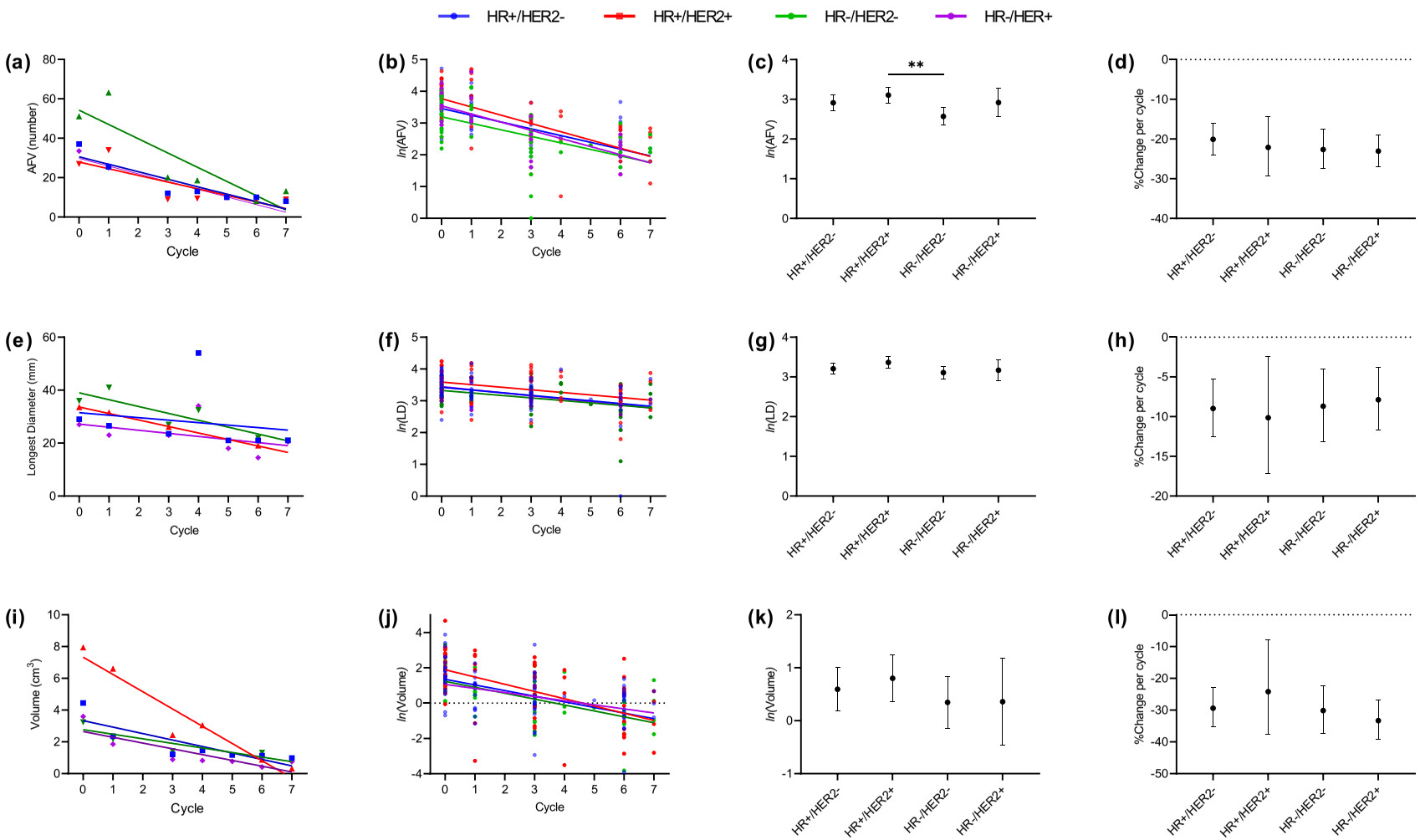

Figure 6.12 (*Left to right*) Scatter plots and regression lines of median (column 1) and log-transformed (column 2) values of the number of feeding vessels (AFV), the tumour longest diameter (LD) and volume *vs* chemotherapy cycle for tumour molecular subtypes (n=86 lesions). Mean-effects plots and percentage (%) changes in parameter values per chemotherapy cycle according to molecular subtype are given in columns 3 and 4, respectively. Error bars denote 95% confidence intervals. HR: hormone receptor; HER2: human epidermal growth factor 2.

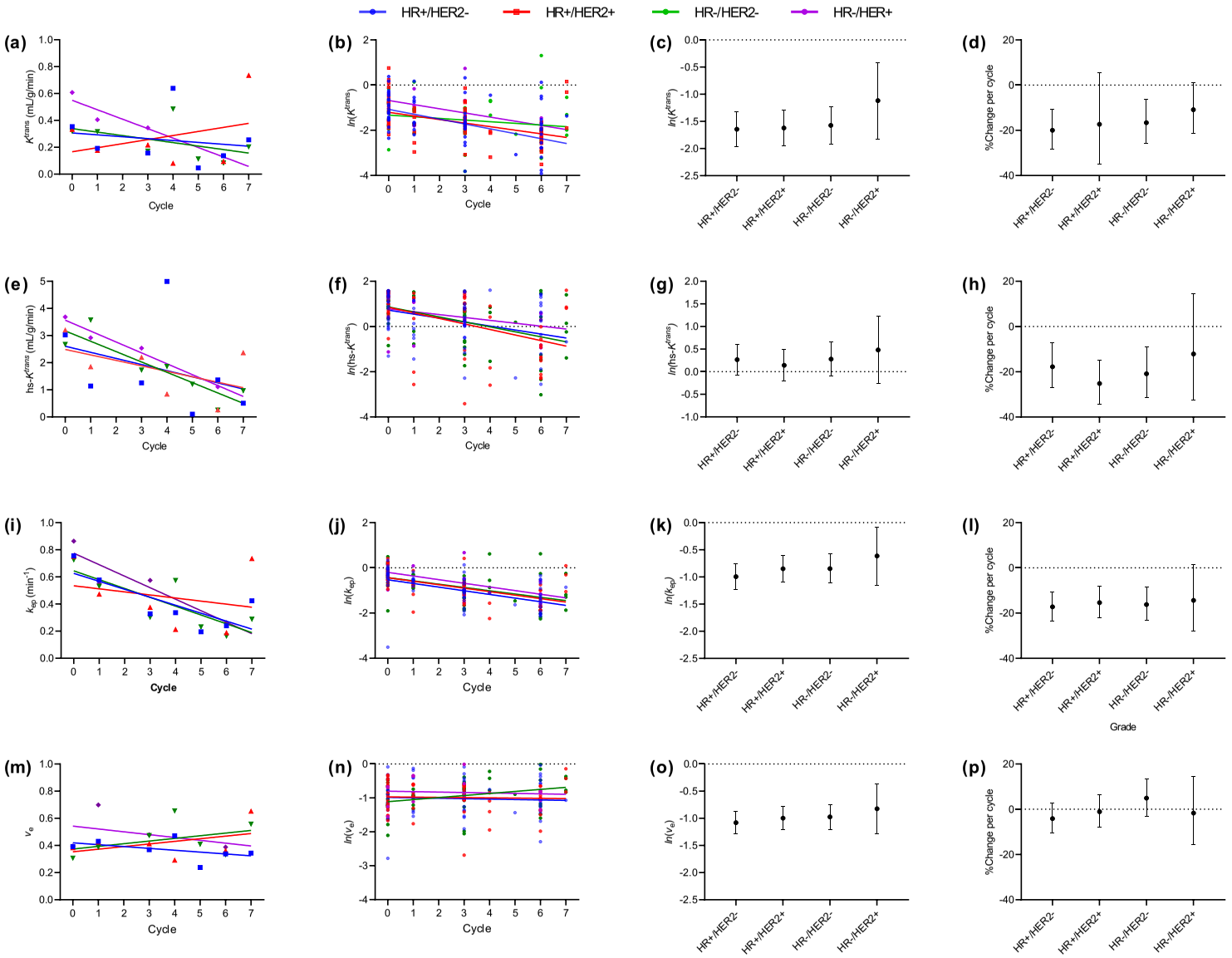

Figure 6.13 (*Left to right*) Scatter plots and regression lines of median (column 1) and log-transformed (column 2) DCE-MRI pharmacokinetic parameters *vs* chemotherapy cycle for molecular subtypes in cancers of no specific type (NST; *n*=71 lesions). Mean-effects plots and percentage (%) changes in parameter values per chemotherapy cycle according to molecular subtype are given in columns 3 and 4, respectively. Error bars denote 95% confidence intervals. HR: hormone receptor; HER2: human epidermal growth factor 2.

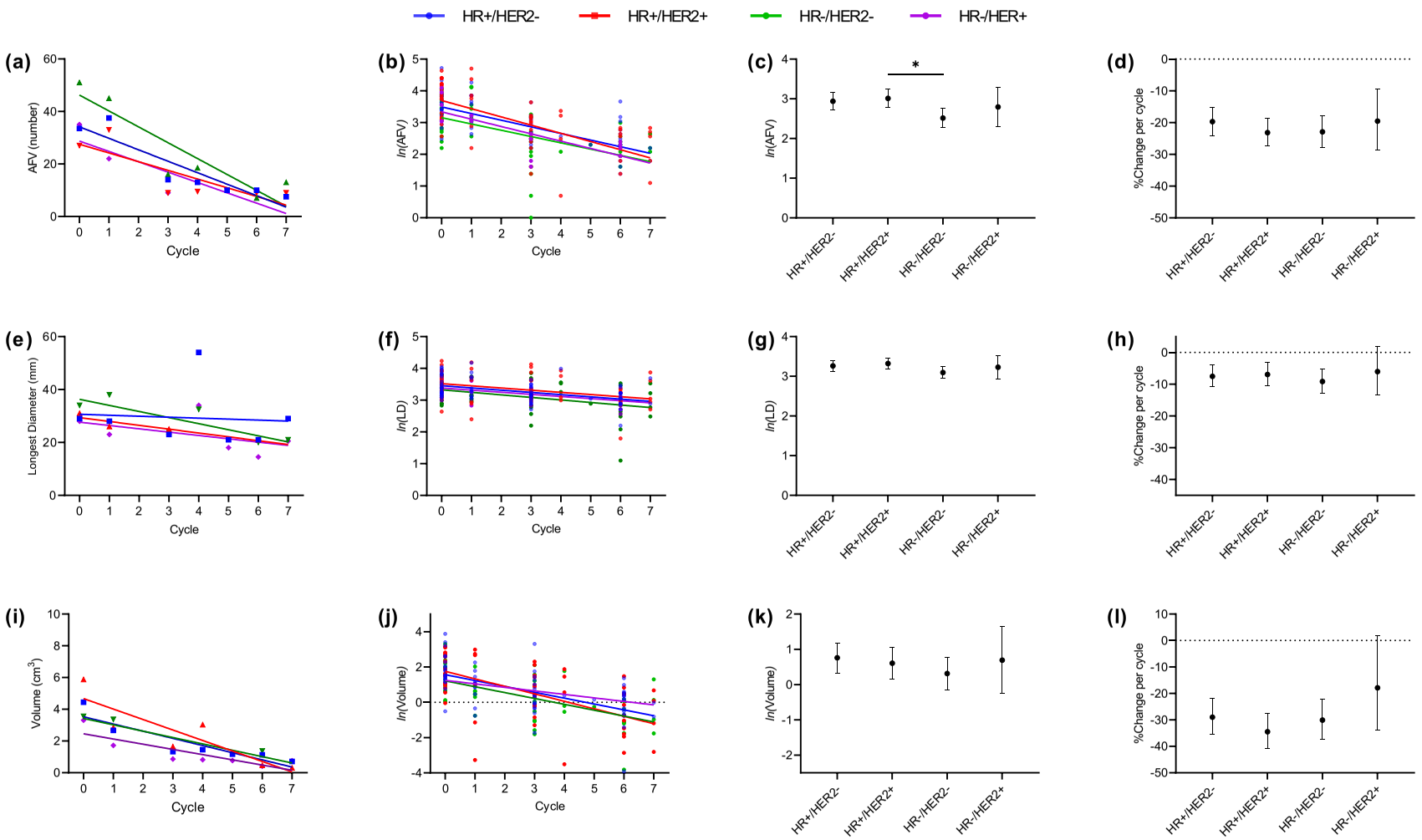

Figure 6.14 (*Left to right*) Scatter plots and regression lines of median (column 1) and log-transformed (column 2) values of the number of feeding vessels (AFV), the tumour longest diameter (LD) and volume *vs* chemotherapy cycle for molecular subtypes in cancers of no specific type (NST; *n*=71 lesions). Mean-effects plots and percentage (%) changes in parameter values per chemotherapy cycle according to molecular subtype are given in columns 3 and 4, respectively. Error bars denote 95% confidence intervals. HR: hormone receptor; HER2: human epidermal growth factor 2.

Table 6.16 Percentage (%) change in DCE-MRI parameter values per chemotherapy cycle together with 95% confidence intervals (CI) and *p* values for the tumour molecular subtypes considered in this study. Percentage changes were calculated according to $100\times(e^{\beta}-1)$, where β denotes the slope estimate for each parameter and molecular subtype as derived from LME models.

	Molecular subtype			
	HR+/HER2-	**HR+/HER2+**	**HR-/HER2-**	**HR-/HER2+**
Parameter	%, [CI], *p*	%, [CI], *p*	%, [CI], *p*	%, [CI], *p*
K^{trans}	-18.5, [-25.8 – -10.3], <.001***	-15.9, [-24.0– -6.9], 0.001**	-11.6, [-21.5 – -0.4], 0.04*	-14.4, [-30.4 – 5.1], 0.13
hs-K^{trans}	-18.5, [-26.4 – -9.7], <.001***	-22.7, [-30.6 – -13.7], <.001***	-20.9, [-30.5 – -10.0], <.001***	-11.8, [-29.2 – 9.9], 0.26
k_{ep}	-16.6, [-21.9 – -11.0], <.001***	-12.4, [-23.7 – 0.8], <.001***	-16.2, [-22.8 – -9.2], <.001***	-15.8, [-21.4 – 9.8], 0.06
v_e	-3.5, [-8.5 – 1.7], 0.18	-1.1, [-11.8 – 10.7], 0.91	4.9, [-1.8 – 12.1], 0.16	-0.3, [-5.7 – 5.4], 0.84
AFV	-20.1, [-24.0 – -16.0], <.001***	-22.1, [-29.3 – -14.3], <.001***	-22.7, [-27.5 – -17.6], <.001***	-23.1, [-27.0 – -18.9], <.001***
LD	-9.0, [-12.5 – -5.3], <.001***	-10.2, [-17.1 – -2.5], <.001***	-8.7, [-13.2 – -4.0], <.001***	-7.9, [-11.7 – -3.8], 0.01*
Volume	-29.4, [-35.3 – -22.9], <.001***	-24.2, [-37.6 – -8.0], <.001***	-30.2, [-37.3 – -22.3], <.001***	-33.3, [-39.3 – -26.8], 0.006**

*p<0.05; **p<0.01; ***p<0.001

Table 6.17 Percentage (%) change in DCE-MRI parameter values per chemotherapy cycle together with 95% confidence intervals (CI) and *p* values for molecular subtypes in carcinomas of no specific type (NST). Percentage changes were calculated according to $100\times(e^{\beta}-1)$, where β denotes the slope estimate for each parameter and molecular subtype as derived from LME models.

	Molecular subtype			
	HR+/HER2-	**HR+/HER2+**	**HR-/HER2-**	**HR-/HER2+**
Parameter	%, [CI], *p*	%, [CI], *p*	%, [CI], *p*	%, [CI], *p*
K^{trans}	-20.0, [-28.2 – -10.8], <.001***	-16.6, [-25.8– -6.3], 0.003**	-10.9, [-21.3 – 1.1], 0.07	-17.3, [-35.1 – 5.3], 0.12
hs-K^{trans}	-17.8, [-27.0 – -7.3], <.001***	-25.2, [-34.2 – -14.8], <.001***	-20.9, [-31.2 – -9.0], <.001***	-12.1, [-32.6 – 14.6], 0.33
k_{ep}	-17.2, [-23.4 – -10.6], <.001***	-15.4, [-22.0 – -8.1], <.001***	-15.4, [-23.3 – -8.4], <.001***	-14.4, [-27.8 – 1.5], 0.07
v_e	-4.1, [-10.5 – 2.8], 0.23	-1.1, [-8.0 – 6.4], 0.77	4.9, [-3.0 – 13.4], 0.23	-1.7, [-5.7 – 14.6], 0.82
AFV	-19.7, [-24.0 – -15.1], <.001***	-23.1, [-27.4 – -18.7], <.001***	-22.9, [-27.7 – -17.7], <.001***	-19.5, [-28.5 – -9.3], <.001***
LD	-7.5, [-10.8 – -4.0], <.001***	-6.9, [-13.4 – -3.3], <.001***	-9.1, [-10.5 – -5.3], <.001***	-6.0, [-13.4 – 2.0], 0.13
Volume	-30.0, [-35.5 – -21.7], <.001***	-34.5, [-40.8 – -27.5], <.001***	-30.2, [-37.2 – -22.2], <.001***	-17.9, [-33.8 – 2.0], 0.07

*p<0.05; **p<0.01; ***p<0.001

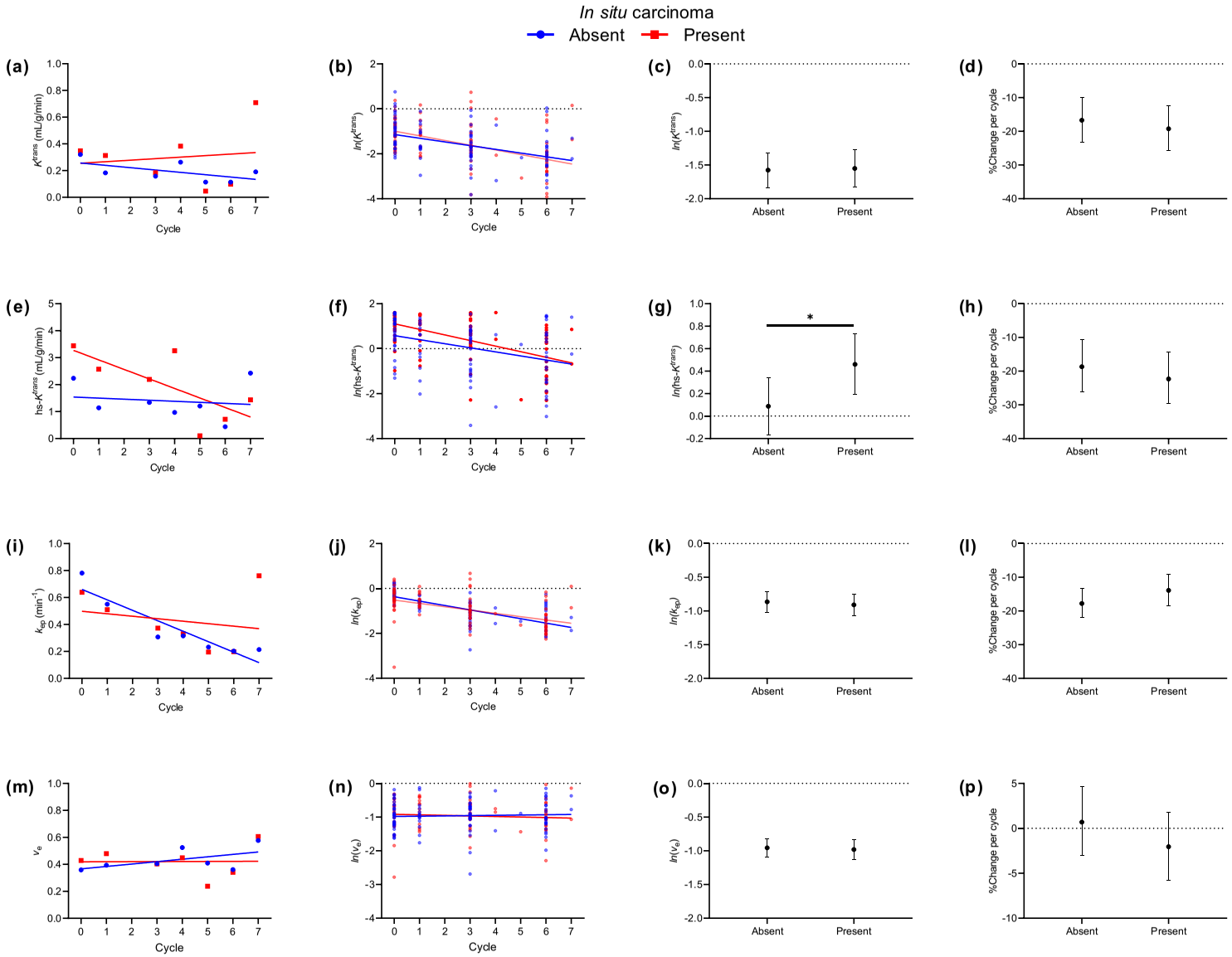

Figure 6.15 (*Left to right*) Scatter plots and regression lines of median (column 1) and log-transformed (column 2) DCE-MRI pharmacokinetic parameters *vs* chemotherapy cycle for tumours in which *in situ* carcinoma was either present or absent (n=67 lesions). Mean-effects plots and percentage (%) changes in parameter values per chemotherapy cycle according to the presence of *in situ* carcinoma are given in columns 3 and 4, respectively. Error bars denote 95% confidence intervals.

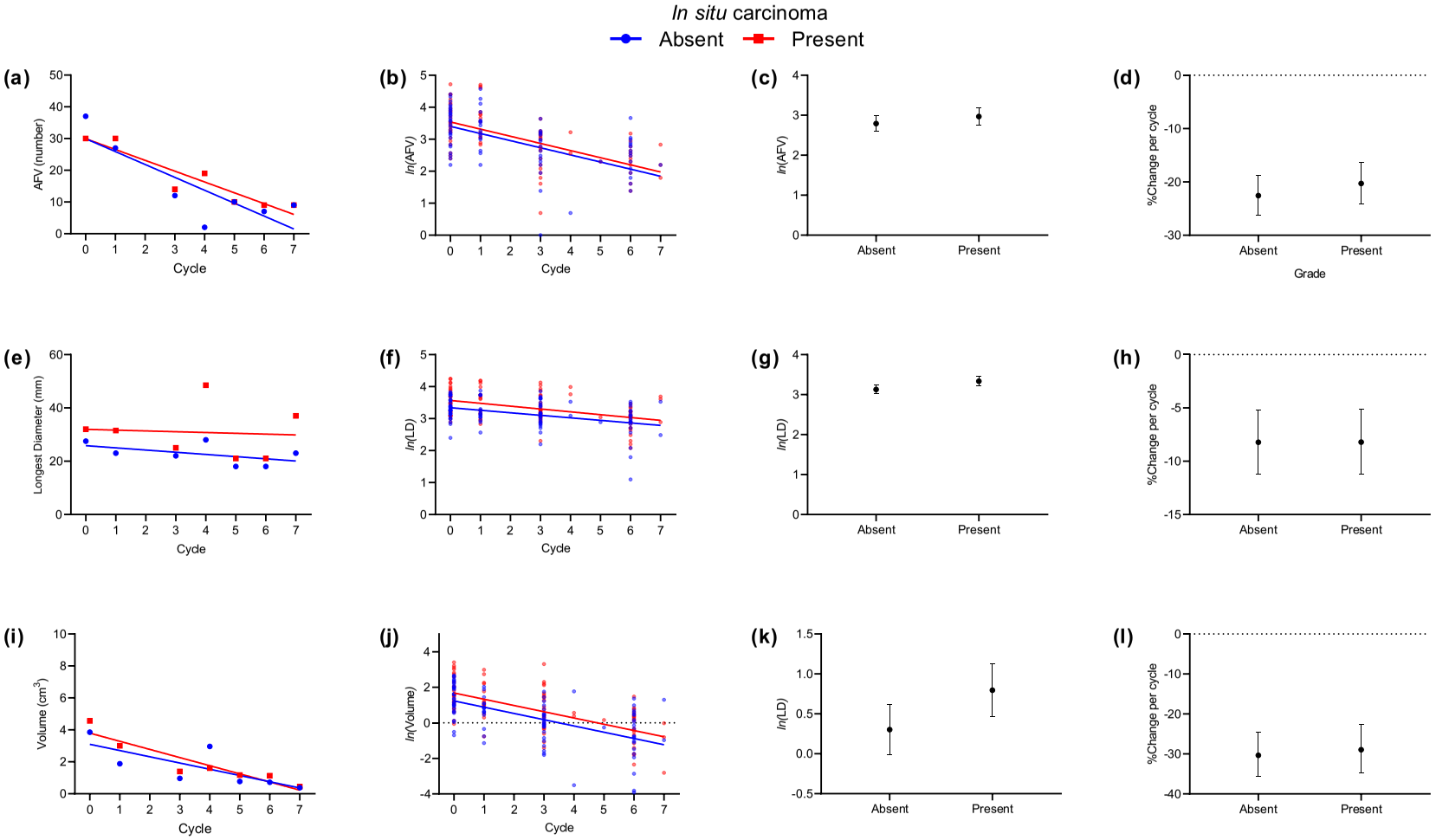

Figure 6.16 (*Left to right*) Scatter plots and regression lines of median (column 1) and log-transformed (column 2) values of the number of feeding vessels (AFV), the tumour longest diameter (LD) and volume *vs* chemotherapy in tumours in which *in situ* carcinoma was either present or absent (n=67 lesions). Mean-effects plots and percentage (%) changes in parameter values per chemotherapy cycle according to the presence of *in situ* carcinoma are given in columns 3 and 4, respectively. Error bars denote 95% confidence intervals.

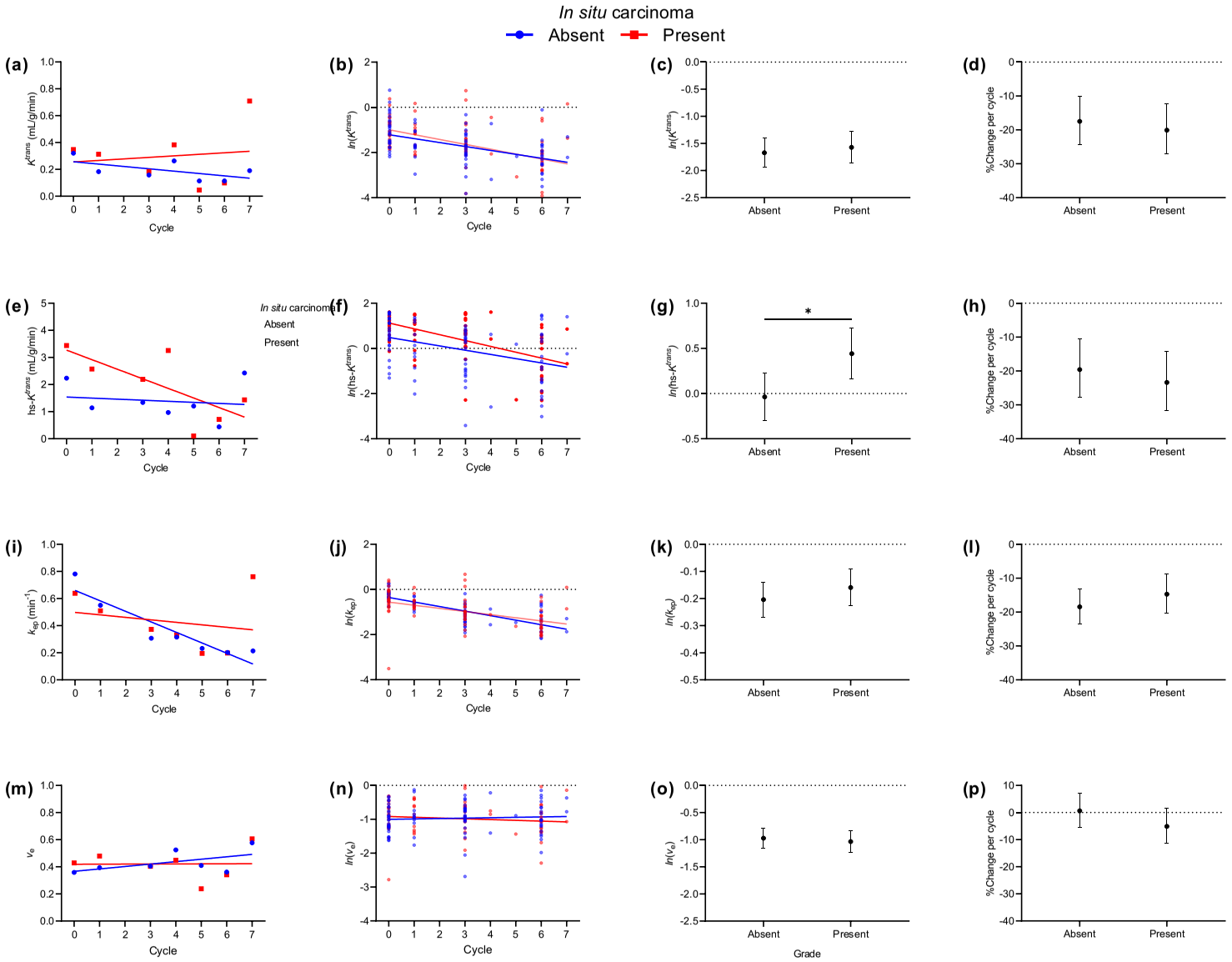

Figure 6.17 (*Left to right*) Scatter plots and regression lines of median (column 1) and log-transformed (column 2) DCE-MRI pharmacokinetic parameters *vs* chemotherapy cycle for tumours of no specific type (NST) in which *in situ* carcinoma was either present or absent (*n*=57 lesions). Mean-effects plots and percentage (%) changes in parameter values per chemotherapy cycle according to the presence of *in situ* carcinoma are given in columns 3 and 4, respectively. Error bars denote 95% confidence intervals.

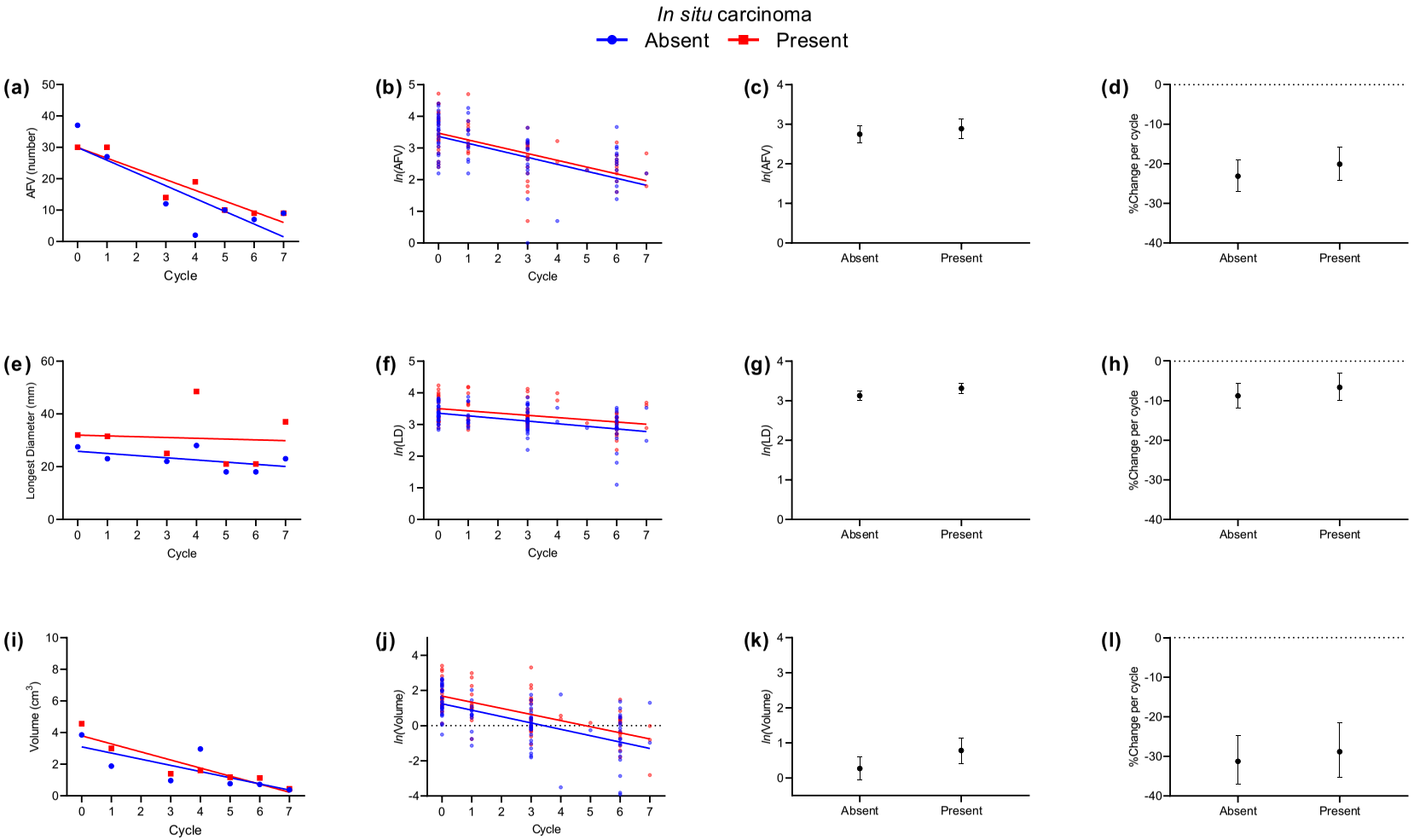

Figure 6.18 (*Left to right*) Scatter plots and regression lines of median (column 1) and log-transformed (column 2) values of the number of feeding vessels (AFV), the tumour longest diameter (LD) and volume *vs* chemotherapy in cancers of no specific type (NST) in which *in situ* carcinoma was either present or absent (n=57 lesions). Mean-effects plots and percentage (%) changes in parameter values per chemotherapy cycle according to the presence of *in situ* carcinoma are given in columns 3 and 4, respectively. Error bars denote 95% confidence intervals.

Table 6.18 Percentage (%) change in DCE-MRI parameter values per chemotherapy cycle together with 95% confidence intervals (CI) and *p* values for the absence or presence of *in situ* carcinoma in tumours. Percentage changes were calculated according to $100\times(e^{\beta} - 1)$, where β denotes the slope estimate for each parameter according as derived from LME models.

	A. All histological subtypes		**B. NST carcinomas**	
	***In situ* carcinoma**		***In situ* carcinoma**	
	Absence	**Presence**	**Absence**	**Presence**
Parameter	%, [CI], *p*	%, [CI], *p*	%, [CI], *p*	%, [CI], *p*
K^{trans}	-16.7, [-23.0 – -9.9], <.001***	-19.3, [-25.6 – -12.4], <.001***	-17.5, [-24.4 – -10.0], <.001***	-20.1, [-27.1 – -12.4], <.001***
hs-K^{trans}	-18.7, [-26.1 – -10.6], <.001***	-22.4, [-29.5 – -14.4], <.001***	-19.6, [-27.8 – -10.5], <.001***	-23.4, [-31.5 – -14.2], <.001***
k_{ep}	-18.0, [-22.7 – -13.2], <.001***	-15.0, [-19.8 – -9.8], <.001***	-18.5, [-23.5 – -13.1], 0.001**	-14.7, [-20.3 – -8.8], <.001***
v_e	0.5, [-4.4 – 5.7] 0.84	-3.6, [-8.5 – 1.6], 0.17	0.7, [-5.4 – 7.1], 0.83	-5.1, [-11.2 – 1.5], 0.12
AFV	-22.5, [-26.2 – -18.7], <.001***	-20.3, [-24.1 – -16.3], <.001***	-23.1, [-27.0 – -19.0], <.001***	-20.1, [-24.3 – -15.6], <.001***
LD	-8.2, [-11.1 – -5.2], <.001***	-8.2, [-11.2 – -5.1], <.001***	-8.8, [-11.8 – -5.6], <.001***	-6.6, [-10.0 – -3.1], <.001***
Volume	-30.4, [-35.7 – -24.6], <.001***	-29.0, [-34.8 – -22.6], <.001***	-31.3, [-37.1 – -24.8], <.001***	-28.8, [-35.4 – -21.], <.001***

*p<0.05; **p<0.01; ***p<0.001

Table 6.19 Statistical significance (*p*-values) of fixed effects for the association between log-transformed DCE-MRI parameters and (A) neoadjuvant chemotherapy (NAC) regimens or (B) the sequence of taxane administration.

		A. NAC regimen	
Parameter	**Cycle**	**Regimen**	**Regimen*Cycle**
$ln(K^{trans})$	0.06	0.06	0.70
ln(hs-K^{trans})	0.06	0.43	0.40
$ln(k_{ep})$	0.002**	0.31	0.82
$ln(v_e)$	0.81	0.43	0.56
ln(AFV)	<.001***	0.48	0.59
ln(LD)	0.002**	0.55	0.65
ln(Volume)	<.001***	0.43	0.97

		B. Sequence of taxane administration	
Parameter	**Cycle**	**Sequence**	**Sequence*Cycle**
$ln(K^{trans})$	0.003**	0.03*	0.97
ln(hs-K^{trans})	0.001**	0.07	0.71
$ln(k_{ep})$	<.001***	0.27	0.83
$ln(v_e)$	0.86	0.27	0.84
ln(AFV)	<.001***	0.13	0.60
ln(LD)	<.001***	0.14	0.47
ln(Volume)	<.001***	0.08	0.51

$^{*}p<0.05$; $^{**}p<0.01$; $^{***}p<0.001$

6.3.4.2 Effect of treatment regimens DCE-MRI parameters during NAC

There were no statistically significant differences in DCE-MRI parameters during NAC between patients on different types of chemotherapy (taxane and anthracycline-based treatment with/without a HER2-targeted agent, or combinations of taxanes with other drugs; Tables 6.19.A; Figure 6.19). On average, women receiving a combination of taxanes and HER2-targetted treatment tended to display higher values in DCE-MRI pharmacokinetic parameter estimates than women on other types of NAC, but these differences were not significant (Figures 6.19). Furthermore, patients receiving taxane and anthracycline-based therapy with or without the addition of HER2-targeted agent exhibited a tendency for a larger percentage reduction in imaging parameters than patients receiving a combination of a taxane and other drugs (Figures 6.19 and 6.20), apart from v_e which showed no change during treatment for all NAC regimens (Figures 6.19 (p)).

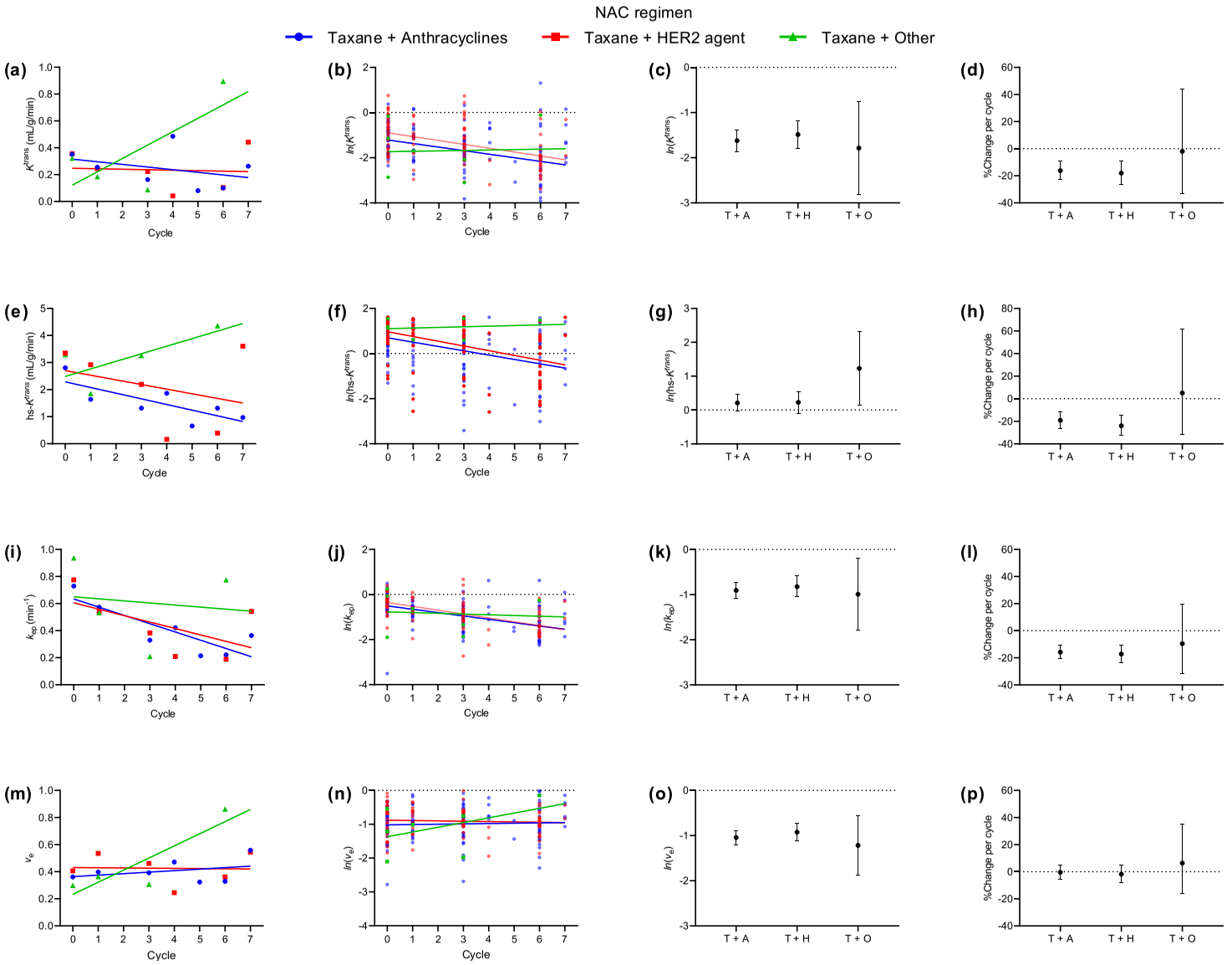

Figure 6.19 (*Left to right*) Scatter plots and regression lines of median (column 1) and log-transformed (column 2) DCE-MRI pharmacokinetic parameters *vs* chemotherapy cycle in patients receiving taxanes and anthracyclines (with or without the addition of HER2-targetted agent) or taxanes in combination with other drugs (n=86 lesions). Mean-effects plots and percentage (%) changes in parameter values per chemotherapy cycle according to chemotherapy regimen are given in columns 3 and 4, respectively. Error bars denote 95% confidence intervals.

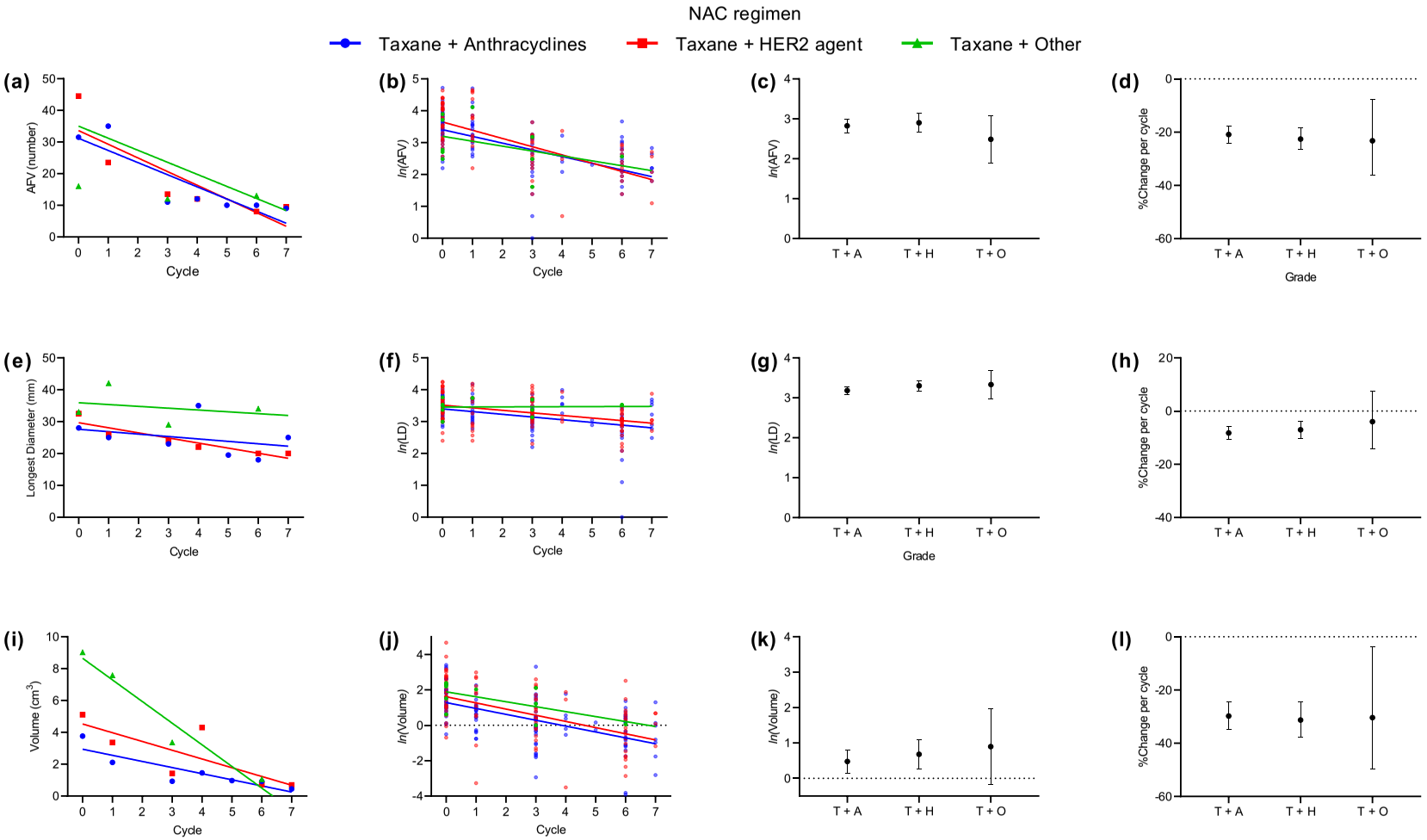

Figure 6.20 (*Left to right*) Scatter plots and regression lines of median (column 1) and log-transformed (column 2) values of the number of feeding vessels (AFV), the tumour longest diameter (LD) and volume *vs* chemotherapy cycle in patients receiving taxanes and anthracyclines (with or without the addition of HER2-targetted agent) or taxanes in combination with other drugs (*n*=86 lesions). Mean-effects plots and percentage (%) changes in parameter values per chemotherapy cycle according to chemotherapy regimen are given in columns 3 and 4, respectively. Error bars denote 95% confidence intervals.

Table 6.20 Percentage (%) change per chemotherapy cycle in DCE-MRI parameter values together with 95% confidence intervals (CI) and *p* values for (A) neoadjuvant chemotherapy (NAC) regimens or (B) sequences of taxane administration. Percentage changes were calculated according to $100\times(e^{\beta} - 1)$, where β denotes the slope estimate for each parameter and NAC regimen as derived from LME models.

	A. NAC regimen		
Parameter	**Taxane + anthracyclines** %, [CI], *p*	**Taxane + anthracyclines + HER2 agent** %, [CI], *p*	**Taxane + other** %, [CI], *p*
ln(K^{trans})	-16.5, [-22.6 – -9.9], <.001***	-15.9, [-23.2 – -8.0], <.001***	-1.9, [-32.6 – 42.7], 0.92
ln(hs-K^{trans})	-20.0, [-26.3 – -13.2], <.001***	-20.7, [-28.0 – -12.6], <.001***	5.3, [-30.1 – 58.7], 0.80
ln(k_{ep})	-16.0, [-20.3 – -11.6], <.001***	-16.4, [-21.3 – -11.0], <.001***	-8.9, [-30.0 – 18.5], 0.48
ln(v_e)	-0.3, [-4.5 – 4.1], 0.88	-1.2, [-6.0 – 4.0], 0.65	7.3, [-13.0 – 32.3], 0.51
ln(AFV)	-21.0 [-24.1 – -17.9], <.001***	-22.7, [-26.1 – -19.1], <.001***	-22.3, [-35.2 – -6.8], 0.007**
ln(LD)	-9.3, [-12.2 – -6.4], <.001***	-8.0, [-11.3 – -4.5], <.001***	-4.2, [-16.1 – 9.4], 0.52
ln(Volume)	-30.9, [-35.5 – -25.8], <.001***	-29.9, [-35.5 – -23.8], <.001***	-31.1, [-50.0 – -5.0], 0.02*

	B. Sequence of taxane administration		
Parameter	**First phase** %, [CI], *p*	**Second phase** %, [CI], *p*	**Throughout** %, [CI], *p*
ln(K^{trans})	-15.2, [-21.5 – 8.5], <.001***	-16.5, [-24.0 – 8.2], <.001***	-16.6, [-35.7 – 8.3], 0.17
ln(hs-K^{trans})	-21.2, [-27.3 – -14.5], <.001***	-18.3, [-26.0 – 9.7], <.001***	-12.9, [-34.5 – 16.0], 0.34
ln(k_{ep})	-15.2, [-29.5 – 2.3], <.001***	-17.3, [-22.4 – 11.8], <.001***	-15.0, [-29.5 – 2.3], 0.09
ln(v_e)	0.6, [-3.6 – 5.0], 0.78	-2.4, [-7.5 – 2.9], 0.36	3.9, [-10.2 – 20.2], 0.61
ln(AFV)	-21.4, [-24.4 – 18.2], <.001***	-21.5, [-25.2 – 17.7], <.001***	-26.1, [-34.2 – -17.0], <.001***
ln(LD)	-9.8, [-12.6 – 7.0], <.001***	-7.2, [-10.7 – -3.5], <.001***	-7.1, [-15.0 – 1.5], 0.10
ln(Volume)	-32.2, [-36.7 – -27.3], <.001***	-27.6, [-33.6 – -21.1], <.001***	-30.6, [-45.2 – 12.4], 0.002**

*p<0.05; **p<0.01; ***p<0.001

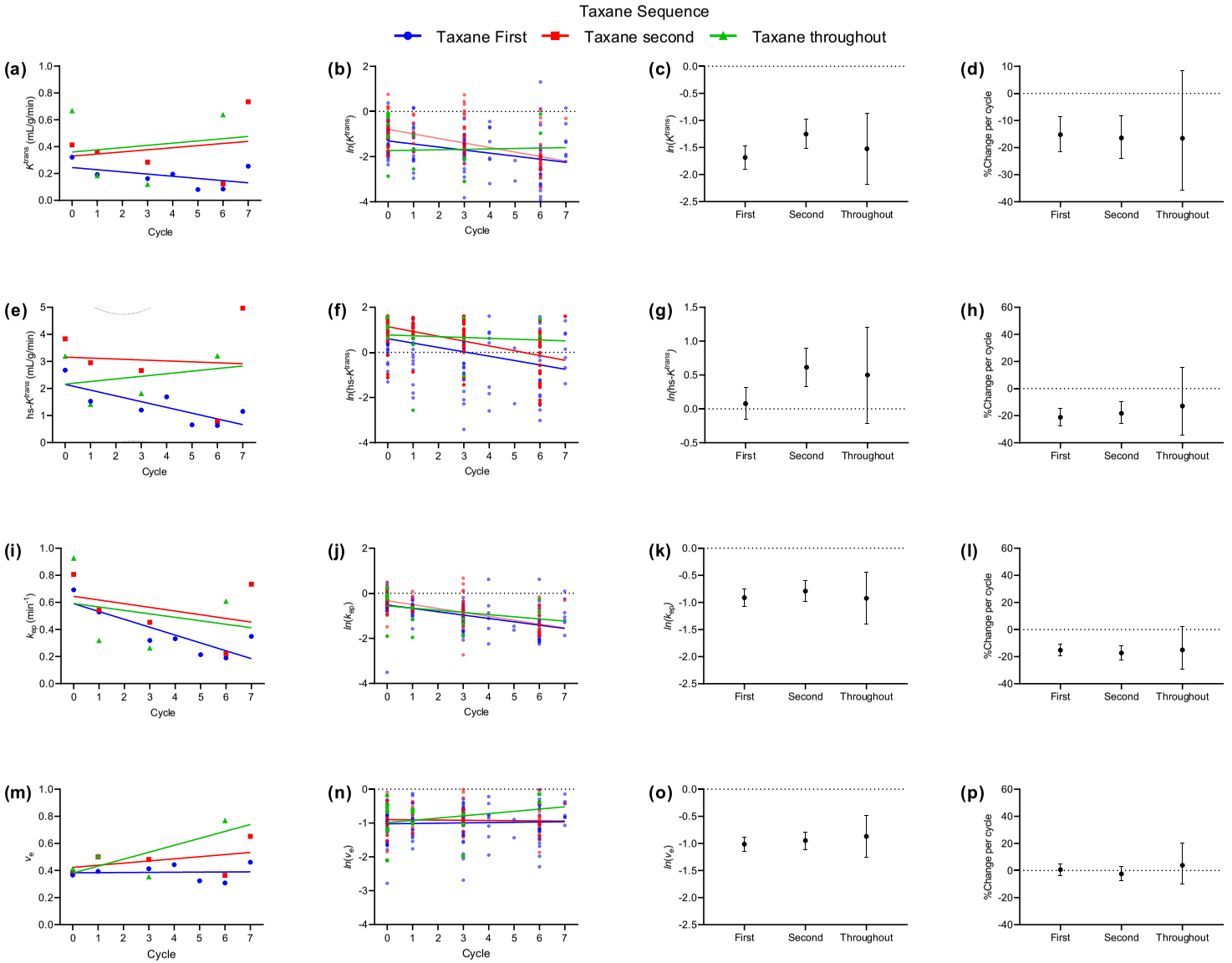

Figure 6.21 (*Left to right*) Scatter plots and regression lines of median (column 1) and log-transformed (column 2) DCE-MRI pharmacokinetic parameters *vs* chemotherapy cycle in patients receiving taxanes in reverse sequences or throughout treatment (n=86 lesions). Mean-effects plots and percentage (%) changes in parameter values per chemotherapy cycle according to taxane sequence are given in columns 3 and 4, respectively. Error bars denote 95% confidence intervals.

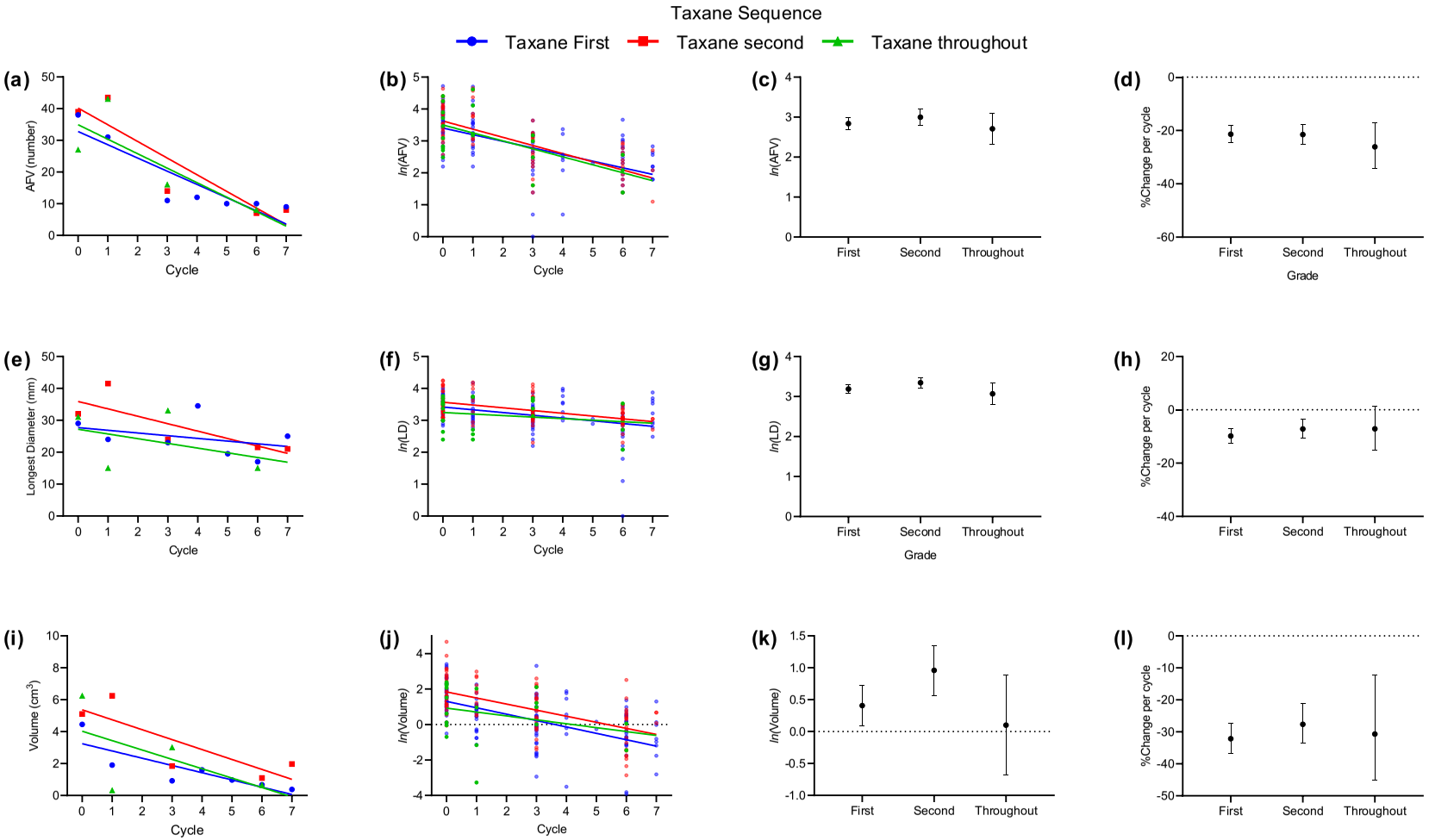

Figure 6.22 (*Left to right*) Scatter plots and regression lines of median (column 1) and log-transformed (column 2) values of the number of feeding vessels (AFV), the tumour longest diameter (LD) and volume *vs* chemotherapy cycle in patients receiving taxanes in reverse sequences or throughout treatment (n=86 lesions). Mean-effects plots and percentage (%) changes in parameter values per chemotherapy cycle according to taxane sequence are given in columns 3 and 4, respectively. Error bars denote 95% confidence intervals.

In a similar manner, the sequence of taxane administration during chemotherapy, i.e. taxane given during the first or last 3 or 4 cycles of NAC, or throughout treatment (see Table 6.1), did not influence any of the imaging metrics (Table 6.19.B). Patients receiving reverse sequences of taxanes showed similar rates of decrease in DCE-MRI parameter estimates, both of which were higher on average than for women on taxanes for the entire duration of treatment (Table 6.20.B; Figures 6.21 (d), (h), (l) and (p)). Furthermore, women starting on anthracyclines exhibited higher pharmacokinetic parameter values and numbers of AFV than women receiving taxanes during the first phase of NAC or throughout treatment (Figure 6.22 (c)). However, differences in parameter reduction rates or values between these chemotherapy sequences were not statistically significant. Among DCE-MRI pharmacokinetic estimates, only K^{trans} allowed differentiation between regimens involving reverse taxanes administration sequences, but the statistical significance of this comparison was not upheld after Holm-Bonferroni adjustment of *p*-values (Table 6.20.B; Figure 6.21 (c)). There was no statistically significant difference in the tumour longest diameter or volume between patients on different taxanes sequences (Figures 6.22 (g) and (k), respectively), with size metrics also displaying similar reduction rates during NAC (Table 6.20.B; Figures 6.22 (h) and (l) for the tumour longest diameter and volume respectively).

6.3.5 DCE-MRI parameters during NAC and pathological response

DCE-MRI images and pharmacokinetic maps during NAC of two representative lesions showing partial and complete pathological response are given in Figures 6.23 and 6.24, respectively. Associations between DCE-MRI metrics and pathological response were assessed using LME models with fixed effects for chemotherapy cycle and pathological response as well as terms for the interaction between pathological response and chemotherapy cycle and pathological response and molecular subtype (see Section 6.3.2). Random effects included intercepts and slopes for subjects. The fixed-effects estimates for the association between log-transformed DCE-MRI metrics and model regressors, together with confidence intervals and *p*-values are given in Tables 6.21 and 6.22 for the whole sample of cancers and NST carcinomas, respectively. Figures 6.25 – 6.28 plot the median untransformed and log-transformed DCE-metrics *vs* chemotherapy cycle according to response category, together with mean-effect estimates and percentage changes in each parameter per treatment cycle.

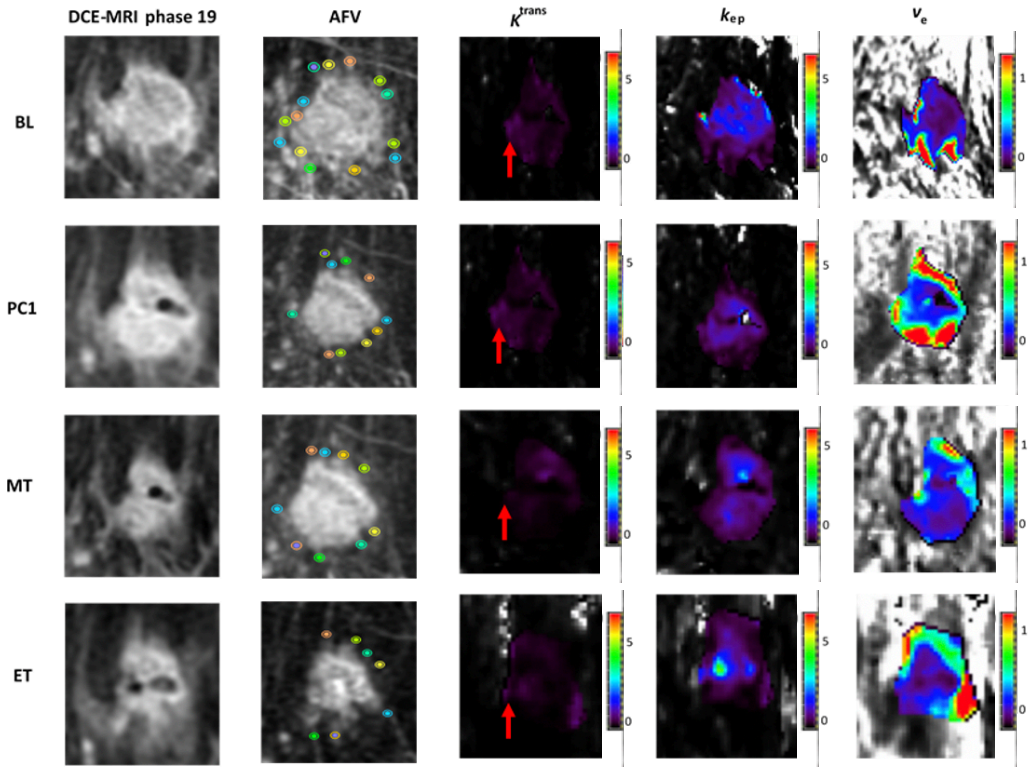

Figure 6.23 62-year-old female patient presenting with a HR-/HER2+, grade 3 breast carcinoma of no specific type (NST). Red arrows on K^{trans} maps indicate the area of the tumour that depicted the highest K^{trans} at baseline (in this area K^{trans} decreased during the course of NAC). The patient showed pathological partial response (pPR) after surgery and radiological stable disease after neoadjuvant chemotherapy (NAC). Patient treatment involved the administration of taxanes and Herceptin for 3 cycles, followed by anthracyclines for another 3 cycles (6 cycles of treatment in total). The cancer is shown at four time points during NAC: baseline (BL), post cycle 1 (PC1), mid-treatment (MT) and at the end of treatment (ET). *Left to right*: DCE-MR image at peak enhancement (phase 19); maximum intensity projection (MIP) image depicting the tumour adjacent feeding vessels (AFV); K^{trans}, k_{ep} and v_e maps of the lesion.

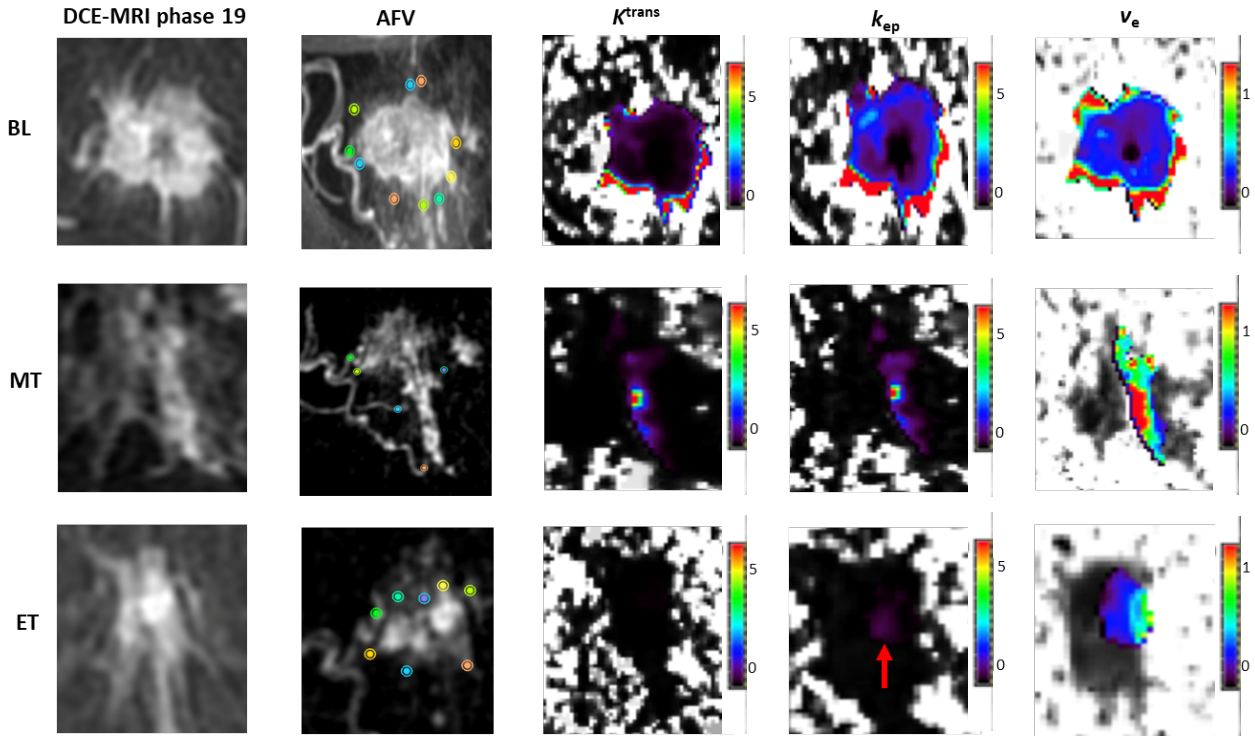

Figure 6.24 60-year-old female patient presenting with a triple-negative, grade 2 carcinoma of no specific type (NST). The patient showed pathological complete response (pCR) after surgery and radiological partial response after neoadjuvant chemotherapy (NAC). The patient received taxane and anthracycline-based treatment for 6 cycles in total. The cancer is shown at three time points during NAC: baseline (BL), mid-treatment (MT) and at the end of treatment (ET). The red arrow on the K_{ep} map at the end of treatment points out a small lesion observed in purple. *Left to right*: DCE-MR image at peak enhancement (phase 19); maximum intensity projection (MIP) image depicting the tumour adjacent feeding vessels (AFV); K^{trans}, k_{ep} and v_e maps of the lesion.

Table 6.21 Fixed-effects estimates (β) together with 95% confidence intervals (CI) and *p*-values for the association between DCE-MRI parameters and pathological response and the interaction effect between pathological response and chemotherapy cycle.

Parameter	Cycle β, [CI], *p*	Response β, [CI], *p*	Response*Cycle β, [CI], *p*
$ln(K^{trans})$	-0.181, [-0.246 – -0.116], <.001***	0.118, [-0.233 – 0.469], 0.51	0.028, [-0.103 – 0.158], 0.68
$ln(\text{hs-}K^{trans})$	-0.258, [-0.327 – -0.189], 0.003**	0.026, [-0.365 – 0.418], 0.89	0.136, [-0.001 – 0.274], 0.06
$ln(k_{ep})$	-0.188, [-0.232 – -0.143], <.001***	0.111, [-0.349 – 0.127], 0.36	0.052, [-0.037– 0.142], 0.25
$ln(v_e)$	0.002, [-0.035 – 0.038], 0.09	0.062, [-0.152 – 0.276], 0.57	-0.025, [-0.097 – 0.048], 0.51
*l*n(AFV)	-0.259, [-0.291 – -0.227], <.001***	0.222, [-0.042 – 0.486], 0.10	0.058, [-0.007 – 0.122], 0.09
LD	-0.100, [-0.125 – -0.074], <.001***	0.063, [-0.113 – 0.239], 0.46	0.039, [-0.013 – 0.091], 0.14
Volume	-0.379, [-0.437 – 0.321], <.001***	0.413, [-0.046 – 0.872], 0.08	0.069, [-0.047 – 0.185], 0.25

$^{*}p<0.05$; $^{**}p<0.01$; $^{***}p<0.001$

Table 6.22 Fixed-effects estimates (β) together with 95% confidence intervals (CI) and *p*-values for the association between DCE-MRI parameters and pathological response and the interaction effect between pathological response and chemotherapy cycle in carcinomas of no specific type (NST).

Parameter	Cycle β, [CI], *p*	Response β, [CI], *p*	Response*Cycle β, [CI], *p*
$ln(K^{trans})$	-0.188, [-0.259 – -0.118], <.001***	0.144, [-0.245 – 0.532], 0.47	0.035, [-0.106 – 0.176], 0.63
$ln(\text{hs-}K^{trans})$	-0.264, [-0.341 – -0.187], <.001***	0.102, [-0.340 – 0.545], 0.65	0.120, [-0.013 – 0.294], 0.08
$ln(k_{ep})$	-0.195, [-0.244 – -0.146], <.001***	-0.173, [-0.433 – 0.087], 0.20	0.081, [-0.017– 0.180], 0.11
$ln(v_e)$	0.000, [-0.043 – 0.044], 0.98	0.066, [-0.175 – 0.308], 0.59	-0.030, [-0.118 – 0.058], 0.51
*l*n(AFV)	-0.256, [-0.291 – -0.221], <.001***	0.266, [-0.022 – 0.554], 0.08	0.061, [-0.009 – 0.131], 0.09
LD	-0. 088, [-0.110 – -0.065], <.001***	0.109, [-0.067 – 0.284], 0.23	0.037, [-0.008 – 0.082], 0.11
Volume	-0.372, [-0.433 – -0.311], <.001***	0.485, [0.027 – 0.943], 0.04*	0.054, [-0.068 – 0.176], 0.39

$^{*}p<0.05$; $^{**}p<0.01$; $^{***}p<0.001$

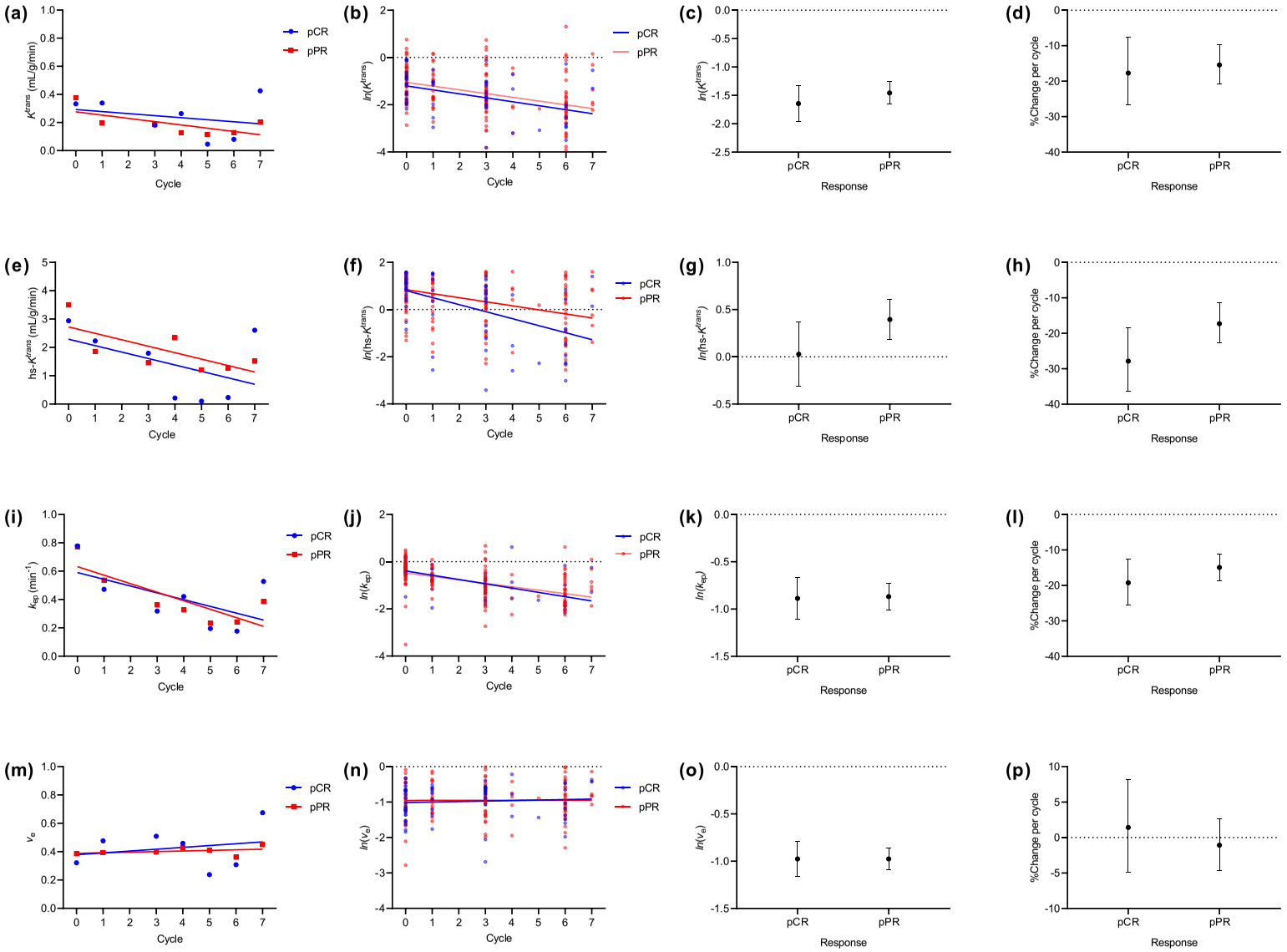

Figure 6.25 (*Left to right*) Scatter plots and regression lines of median (column 1) and log-transformed (column 2) DCE-MRI pharmacokinetic parameters *vs* chemotherapy cycle per pathological response category (n=86 lesions). Mean-effects plots and percentage (%) changes in parameter values per chemotherapy cycle according to pathological response are given in columns 3 and 4, respectively. Error bars denote 95% confidence intervals. pPR: pathological partial response; pCR: pathological complete response.

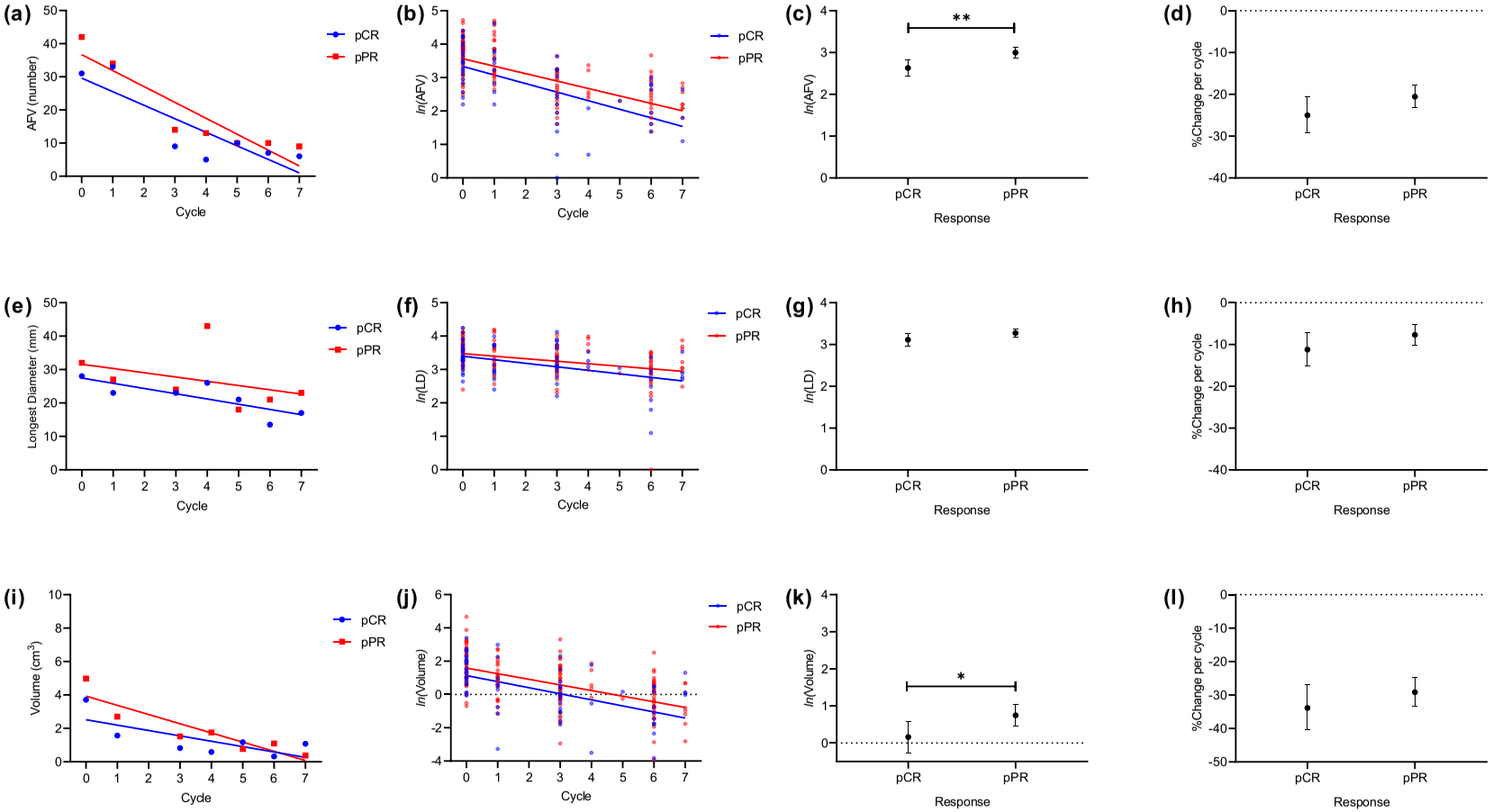

Figure 6.26 (*Left to right*) Scatter plots and regression lines of median (column 1) and log-transformed (column 2) values of the number of feeding vessels (AFV), the tumour longest diameter (LD) and volume *vs* chemotherapy cycle per pathological response category (*n*=86 lesions). Mean-effects plots and percentage (%) changes in parameter values per chemotherapy cycle according to pathological response are given in columns 3 and 4, respectively. Error bars denote 95% confidence intervals. pPR: pathological partial response; pCR: pathological complete response.

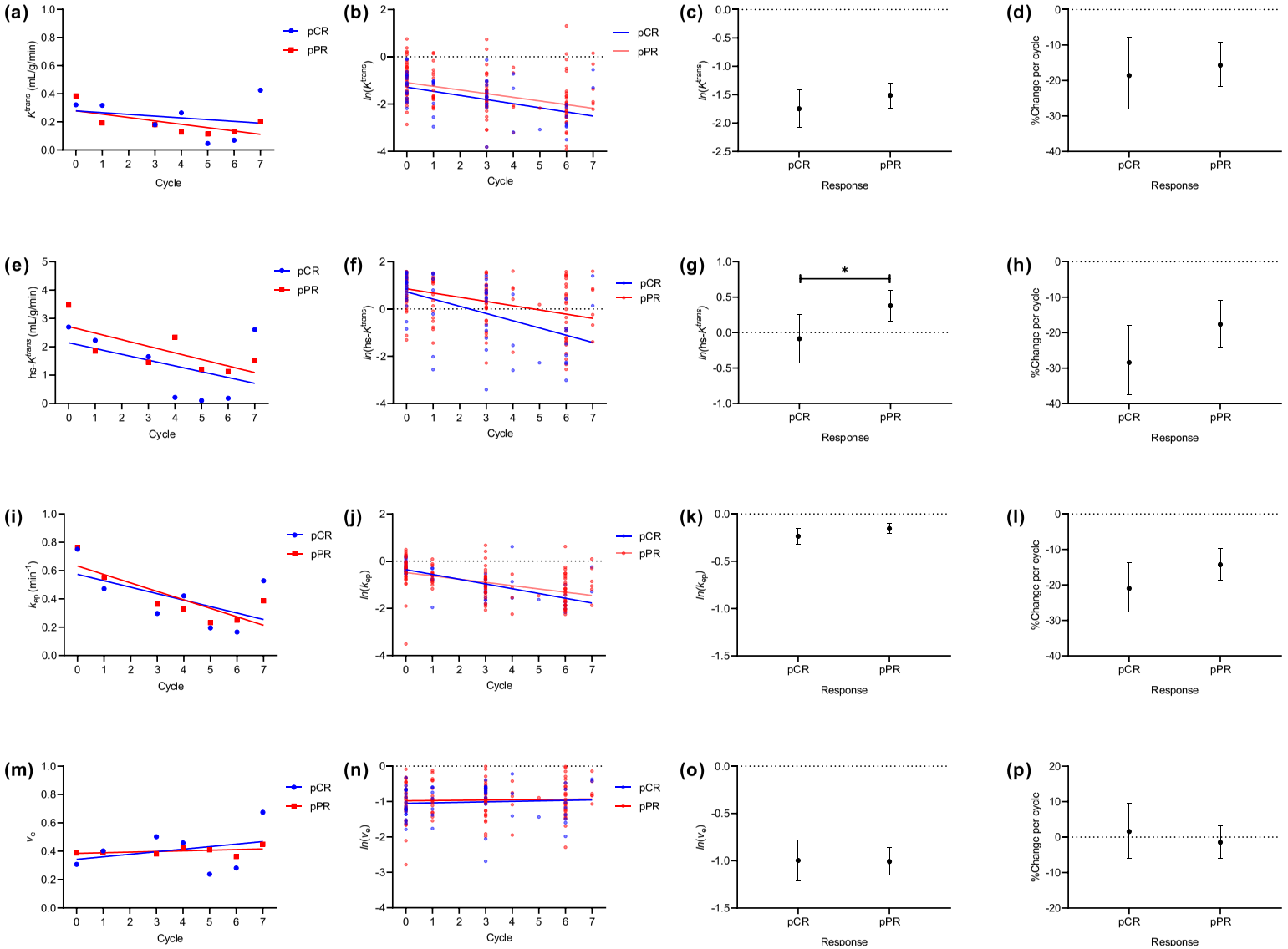

Figure 6.27 (*Left to right*) Scatter plots and regression lines of median (column 1) and log-transformed (column 2) DCE-MRI pharmacokinetic parameters *vs* chemotherapy cycle per pathological response category in carcinomas of no specific type (NST; *n*=71 lesions). Mean-effects plots and percentage (%) changes in parameter values per chemotherapy cycle according to pathological response are given in columns 3 and 4, respectively. Error bars denote 95% confidence intervals. pPR: pathological partial response; pCR: pathological complete response.

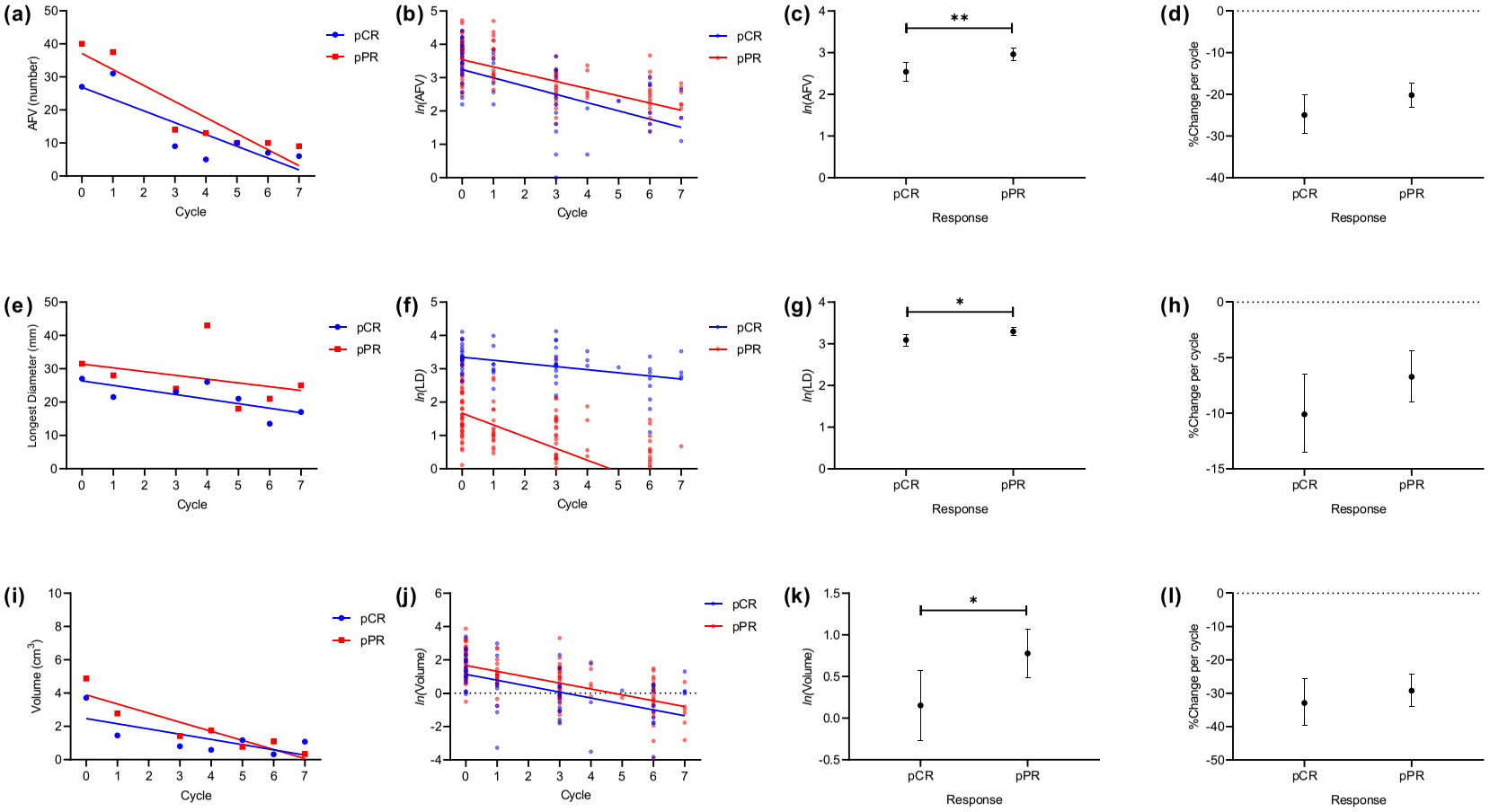

Figure 6.28 (*Left to right*) Scatter plots and regression lines of median (column 1) and log-transformed (column 2) values of the number of feeding vessels (AFV), the tumour longest diameter (LD) and volume *vs* chemotherapy cycle per pathological response category in carcinomas of no specific type (NST; *n*=71 lesions). Mean-effects plots and percentage (%) changes in parameter values per chemotherapy cycle according to pathological response are given in columns 3 and 4, respectively. Error bars denote 95% confidence intervals. pPR: pathological partial response; pCR: pathological complete response.

Table 6.23 Percentage (%) change in DCE-MRI parameter values per chemotherapy cycle together with 95% confidence intervals (CI) and *p* values according to pathological response category. Percentage changes were calculated according to $100\times(e^{\beta} - 1)$, where β denotes the slope estimate for each parameter and response category as derived from LME models.

	A. All histological subtypes		**B. NST carcinomas**	
	Pathological response		**Pathological response**	
	Complete	**Partial**	**Complete**	**Partial**
Parameter	%, [CI], *p*	%, [CI], *p*	%, [CI], *p*	%, [CI], *p*
K^{trans}	-17.7, [-26.7 – -7.6], <.001***	-19.3, [-20.8 – -9.6], <.001***	-18.6, [-28.0 – -7.9], 0.001***	-15.7, [-21.8 – -9.2], <.001***
hs-K^{trans}	-27.8, [-3621 – -18.4], <.001***	-17.3, [-22.8 – -11.4], <.001***	-28.4, [-37.5 – -18.0], <.001***	-17.6, [-24.0 – -10.8], <.001***
k_{ep}	-19.3, [-25.5 – -12.5], <.001***	-14.9, [-18.6 – -11.0], <.001***	-21.0, [-27.6 – -1381], <.001***	-14.3, [-18.5 – -9.8], <.001***
v_e	1.4, [-4.9 – 8.2], 0.66	-1.1, [-4.7 – 2.6], 0.56	0.7, [-5.4 – 7.1], 0.83	-5.1, [-11.2 – 1.5], 0.12
AFV	-25.0, [-29.2 – -20.5], <.001***	-20.5, [-23.2 – -17.9], <.001***	-24.9, [-29.5 – -20.1], <.001***	-20.2, [-23.0 – -17.2], <.001***
LD	-11.2, [-15.1 – -7.1], <.001***	-7.7, [-10.1 – -5.2], <.001***	-10.1, [-13.5 – -6.5], <.001***	-6.8, [-9.0 – -4.4], <.001***
Volume	-33.9, [-40.2 – -26.8], <.001***	-29.2, [-33.4 – -24.1], <.001***	-32.9, [-39.6 – -25.5], <.001***	-29.2, [-33.9 – -24.2.], <.001***

$^{*}p<0.05$; $^{**}p<0.01$; $^{***}p<0.001$

All DCE-MRI parameters examined showed a significant decrease during chemotherapy regardless of response category, with the exception of v_e which showed no significant change throughout treatment for both response groups (Tables 6.23.A and 6.23.B for all lesions and the group of NST cancers, respectively). Breast tumours in the pCR group displayed a larger percentage decrease per chemotherapy cycle in all parameter values than these in the pPR group, with hs-K^{trans}, tumour volume and AFV showing the largest reduction rates among the parameters examined in both the entire sample of tumours or NST cancers alone (Table 6.23.A and 6.23.B, respectively). Though no significant difference between response groups was observed for the pharmacokinetic estimates examined, there was an overall tendency for mean parameter values to be higher in tumours showing pPR than those displaying pCR (Figures 6.25 and 6.27 for the whole lesion sample and NST cancers, respectively).

On the other hand, statistically significant differences between pathological response groups were found in the tumour volume (*ln*(Volume) [95% CI] – pCR *vs* pPR: 0.160 [-0.271 – 0.591] *vs* 0.746 [0.464 – 1.032], p=0.03[6]) and number of AFV (*ln*(AFV) [95% CI] – pCR *vs* pPR: 2.632 [2.428 – 2.835] *vs* 2.997 [2.863 – 3.131], p=0.004[7]), which were upheld when considering NST cancers alone (pCR *vs* pPR - *ln*(Volume) [95% CI]: 0.153 [-0.267 – 0.572] *vs* 0.777 [0.490 – 1.064], p=0.02[8]; *ln*(AFV) [95% CI]: 2.542 [2.314 – 2.769] *vs* 2.963 [2.809 – 3.118], p=0.003[9]). In NST cancers, hs-K^{trans} and the tumour longest diameter also showed significant differences between pathological response categories (pCR *vs* pPR - *ln*(hs-K^{trans}) [95% CI]: -0.086 [-0.431 – 0.259] *vs* 0.379 [0.156 – 0.602], p=0.03[10]; *ln*(LD) [95% CI]: 3.091 [2.952 – 3.230] *vs* 3.294 [3.199 – 3.388], p=0.02[11]).

[6] Untransformed mean estimates of tumour volume with 95% confidence intervals [CI] in cancers with pCR *vs* pPR were 1.2 [0.8 – 1.8] *vs* 2.1 [1.6 – 2.8] cm^3, respectively.
[7] Untransformed mean estimates of AFV with 95% confidence intervals [CI] in cancers with pCR *vs* pPR were 14 [11 – 17] *vs* 20 [18 – 23] vessels, respectively.
[8] Untransformed mean estimates of tumour volume with 95% confidence intervals [CI] in NST cancers with pCR *vs* pPR were 1.2 [0.8 – 1.8] *vs* 2.2 [1.6 – 2.9] cm^3, respectively.
[9] Untransformed mean estimates of AFV with 95% confidence intervals [CI] in NST cancers with pCR *vs* pPR were 13 [10 – 16] *vs* 19 [17 – 23] vessels, respectively.
[10] Untransformed mean estimates of hs-K^{trans} with 95% confidence intervals [CI] in NST cancers with pCR *vs* pPR were 0.918 [0.650 – 1.296] *vs* 1.418 [1.169 – 1.826] cm^3, respectively.
[11] Untransformed mean estimates of the longest tumour diameter (LD) with 95% confidence intervals [CI] in NST cancers with pCR *vs* pPR were 22 [19 – 25] *vs* 27 [25 – 30] mm, respectively.

6.3.6 Evaluation of pre-treatment and early changes in DCE-MRI parameters for the prediction of pathological response

Table 6.24 summarises DCE-MRI parameters at baseline and after one cycle of NAC according to response category. Absolute and percentage changes between baseline and after one cycle of chemotherapy are given in Table 6.25.

There were no significant differences in DCE-MRI parameters between lesions exhibiting pCR and pPR at either baseline or after one cycle of treatment (Table 6.24). Similarly, no significant absolute or percentage differences were observed between responding cancers and those partially responding to treatment (Table 6.25). Interestingly, tumours having pPR showed larger percentage changes between these two time points than cancers with pCR (Table 6.25.B), however it should be noted that from the 37 cancers included in the evaluation of differences between metrics at post-cycle 1 and baseline, 25 (68%) exhibited pPR.

Single parameters from DCE-MRI at baseline and post cycle 1 (Table 6.26) showed low predictive ability for pCR based on ROC analysis for either the whole sample of tumours or the group of NST cancers (AUC: <0.70; p=0.05-0.83). Except for k_{ep}, the probability of pathological complete response declined with increasing values in parameter values (Figure 6.29), indicating that cancers with lower values in DCE-MRI metrics at baseline or after one cycle of treatment were more likely to achieve pCR. However, and as also indicated by the results of the ROC analysis, no single DCE-MRI parameter achieved a probability of >50% in predicting response. Overall, the best predictive ability was observed for the tumour longest diameter and volume at post cycle 1, with a sensitivity of >70% and a specificity of >62% at optimal cut-off values (Table 6.26B). Similarly, absolute and percentage differences in DCE-MRI parameter values between baseline and after one cycle of treatment showed little ability in predicting pathological response (Table 6.27), with mean tumour K^{trans} performing marginally better than other metrics.

Logistic regression models involving single DCE-MRI parameters and tumour prognostic factors selected from univariate analyses (i.e., histological subtype, molecular subtype and grade) improved associations with pathological response (Table 6.28). In general, inclusion of both clinicopathologic factors and DCE-MRI metrics into regression models resulted in moderate-to-good ability for predicting pathological response, with AUC >0.75 for all

quantitative parameters examined. Compared to models including only the factors of histological and molecular subtype as well as grade in the regression, the introduction of single DCE-MRI metrics at baseline and after one cycle of NAC resulted in an increase in specificity of up to 22% (Table 6.29), with similar increases observed when entering changes between baseline and post-cycle 1 in DCE parameters into the model (Table 6.30). Overall, combination models including tumour volume, the longest diameter or AFV after 1 cycle of chemotherapy performed better resulting in a sensitivity and specificity of >80%.

Table 6.24 Tumour DCE-MRI parameters at (A) baseline and (B) after one cycle of chemotherapy according to therapeutic response category. Data are presented as median [range] or mean ± standard deviation as appropriate.

A. Baseline			
Parameter	**pCR**	**pPR**	***p***
Lesions (*n*)	25	55	
K^{trans}	0.333 [0.113 – 0.937]	0.376 [0.057 – 2.133]	0.38[a]
hs-K^{trans}	2.940 [0.270 – 4.988]	3.498 [0.077 – 4.850]	0.31[a]
k_{ep}	0.803 ± 0.227	0.782 ± 0.324	0.38[b]
v_e	0.321 [0.158 – 0.723]	0.386 [0.062– 0.917]	0.25[a]
Lesions (*n*)	27	56	
AFV	31 [9 – 82]	42 [12 – 112]	0.27[a]
Lesions (*n*)	27	59	
LD	28 [11 – 70]	32 [11 – 66]	0.26[a]
Volume	4.64 [0.50 – 106.57]	2.36 [0.04 – 19.79]	0.21[a]
B. Post Cycle 1			
Parameter	**pCR**	**pPR**	***p***
Lesions (*n*)	10	23	
K^{trans}	0.339 [0.052 – 0.601]	0.195 [0.065 – 1.190]	0.68[a]
hs-K^{trans}	2.426 ± 1.909	2.021 ± 1.265	0.57[b]
k_{ep}	0.472 [0.141 – 0.889]	0.537 [0.208 – 1.092]	0.75[c]
v_e	0.476 [0.172 – 0.600]	0.394 [0.214– 0.880]	1.00[a]
Lesions (*n*)	11	25	
AFV	33 [9 – 101]	34 [14 – 110]	0.42[a]
Lesions (*n*)	12	25	
LD	23 [11 – 54]	27 [13 – 66]	0.24[a]
Volume	5.99 [0.04 – 19.79]	3.87 [0.31 – 15.45]	0.07[a]

[a]Mann-Whitney *U* test
[b]Welch's *t* test
pCR: pathological complete response; pPR: pathological partial response; K^{trans}: contrast influx transfer rate (mL/g/min); k_{ep}: contrast efflux transfer rate (min^{-1}); v_e: fractional volume of extravascular-extracellular space; AFV: adjacent feeding vessels (number); LD: tumour longest diameter on MRI (mm); volume: cm^3

Table 6.25 Absolute (A) and percentage changes (B) in DCE-MRI parameters between post-cycle 1 and baseline according to therapeutic response category. Data are presented as median [range] or mean ± standard deviation as appropriate.

A. Absolute change			
Parameter	**pCR**	**pPR**	***p***
Lesions (*n*)	10	23	
K^{trans}	-0.016 [-0.527 – 0.188]	-0.136 [-0.671 – 0.607]	0.42[a]
hs-K^{trans}	-0.201 ± 1.489	-1.011 ± 1.422	0.20[b]
k_{ep}	-0.313 ± 0.409	-0.258 ± 0.246	0.66[b]
v_e	0.056 ± 0.100	0.014 ± 0.138	0.46[b]
Lesions (*n*)	11	25	
AFV	-4 ± 26	-5 ± 26	0.90[b]
Lesions (*n*)	12	25	
LD	-4 [-10 – 6]	-2 [-21 – 17]	0.37[a]
Volume	-1.38 [-20.4 – 6.5]	-1.56 [-20.2 – 0.8]	0.21[a]
B. Percentage (%) change			
Parameter	**pCR**	**pPR**	***p***
Lesions (*n*)	10	23	
K^{trans}	-10.3 [-76.6 – 45.5]	-24.3 [-79.8 – 112.4]	0.87[a]
hs-K^{trans}	-24.2 [-96.0 – 98.7]	-28.2 [-93.3 – 140.2]	0.98[a]
k_{ep}	-33.2 ± 33.9	-28.0 ± 23.0	0.57[b]
v_e	16.6 [-21.5 – 88.7]	7.5 [-37.5 – 114.3]	0.56[a]
Lesions (*n*)	11	25	
AFV	5.7 [-84.2 – 131.6]	1.1 [-63.6 – 147.4]	0.87[a]
Lesions (*n*)	12	25	
LD	-14.8 [-34.5 – 16.7]	-6.7 [-56.8 – 70.8]	0.17[a]
Volume	-67.6 [-89.1 – 49.3]	-49.4 [-90.3 – 16.1]	0.18[a]

[a]Mann-Whitney *U* test
[b]Student's *t* test
pCR: pathological complete response; pPR: pathological partial response; K^{trans}: contrast influx transfer rate (mL/g/min); k_{ep}: contrast efflux transfer rate (min^{-1}); v_e: fractional volume of extravascular-extracellular space; AFV: adjacent feeding vessels (number); LD: tumour longest diameter on MRI (mm); volume: cm^3.

Table 6.26 Odds ratios (OR) and area under the curve (AUC) with *p* values and confidence intervals [CI] for the DCE-MRI parameters at baseline (A) and after 1 cycle of treatment (B) as predictors of pathological response. The sensitivity (%) and specificity (%) of each parameter at optimal cut-off thresholds are also given.

	A. Baseline				
	Odds ratio (OR) OR, [CI], *p*	**Cut-off[a]**	**Sensitivity** %, [CI]	**Specificity** %, [CI]	**AUC** AUC, [CI], *p*
K^{trans}	0.40, [0.08 – 1.97], 0.26	0.536	36.4, [23.8 – 50.4]	84.0, [63.9 – 95.5]	0.582, [0.442 – 0.724], 0.25
hs-K^{trans}	0.87, [0.62 – 1.21], 0.41	3.688	49.1, [35.4 – 62.9]	76.0, [54.9 – 90.6]	0.557, [0.421 – 0.694], 0.41
k_{ep}	1.27, [0.26 – 6.32], 0.77	1.288	9.1, [3.0 – 20.0]	100, [86.3 – 100.0]	0.479, [0.338 – 0.610], 0.77
v_e	0.21, [0.01 – 3.55], 0.28	0.299	74.5, [61.0 – 85.3]	44.0, [24.4 – 65.1]	0.576, [0.440 – 0.711], 0.27
AFV	0.99, [0.97 – 1.01], 0.23	34	62.5, [48.5 – 75.1]	63.0, [42.4 – 80.6]	0.580, [0.450 – 0.711], 0.23
LD	0.98, [0.95 – 1.02], 0.37	21	94.9, [85.9 – 98.9]	22.2, [8.6 – 42.3]	0.558, [0.433 – 0.683], 0.36
Volume	0.96, [0.90 – 1.03], 0.27	3.03	78.0, [65.3 – 87.7]	44.4, [25.5 – 64.7]	0.584, [0.441 – 0.727], 0.25

	B. Post cycle 1				
	Odds ratio (OR) OR, [CI], *p*	**Cut-off[a]**	**Sensitivity** %	**Specificity** %	**AUC** AUC, [CI], *p*
K^{trans}	0.28, [0.01 – 6.99], 0.44	0.384	36.0, [18.0 – 57.5]	88.9, [51.8 – 99.7]	0.596, [0.359 – 0.832], 0.43
hs-K^{trans}	1.22, [0.71 – 2.09], 0.47	0.165	100.0, [86.3–100.0]	22.2, [2.8 – 60.0]	0.430, [0.238 – 0.622], 0.47
k_{ep}	0.51, [0.01 – 27.5], 0.74	0.482	68.0, [46.5 – 85.1]	55.6, [21.2 – 86.3]	0.533, [0.329 – 0.738], 0.75
v_e	0.31, [0.00 – 31.1], 0.62	0.662	24.0, [9.4 – 45.1]	100.0, [66.4–100.0]	0.556, [0.332 – 0.800], 0.63
AFV	0.99, [0.96 – 1.02], 0.46	47	40.7, [22.4 – 61.2]	90.0, [55.5 – 99.7]	0.578, [0.373 – 0.784], 0.45
LD	0.97, [0.92 – 1.03], 0.32	24	70.4, [49.8 – 86.2]	63.6, [30.8 – 89.1]	0.600, [0.405 – 0.795], 0.31
Volume	0.98, [0.83 – 1.16], 0.82	1.91	70.4, [49.8 – 86.2]	72.7, [39.0 – 94.0]	0.520, [0.340 – 0.699], 0.83

[a]Cut-off thresholds were determined using the Youden index.
pCR: pathological complete response; pPR: pathological partial response; K^{trans}: contrast influx transfer rate (mL/g/min); k_{ep}: contrast efflux transfer rate (min^{-1}); v_e: fractional volume of extravascular-extracellular space; AFV: adjacent feeding vessels (number); LD: tumour longest diameter on MRI (mm); volume: cm^3

Table 6.27 Odds ratios (OR) and area under the curve (AUC) with *p* values and confidence intervals [CI] for absolute (A) and percentage (%) changes in DCE-MRI parameters as predictors of pathological response. The sensitivity (%) and specificity (%) of each parameter at optimal cut-off thresholds are also given. Absolute changes were calculated as: $Parameter_{PC1} - Parameter_{Baseline}$. Percentage (%) changes were calculated as: $100\times(Parameter_{PC1} - Parameter_{Baseline})/Parameter_{Baseline}$.

A. Absolute changes

Parameter	Odds ratio (OR) OR, [CI], *p*	Cut-off	Sensitivity %	Specificity %	AUC AUC, [CI], *p*
K^{trans}	1.72, [0.038 – 77.98], 0.78	-0.100	58.3, [36.6 – 77.9]	71.4, [29.0 – 96.3]	0.607, [0.332 – 0.881], 0.44
hs-K^{trans}	1.49, [0.80 – 2.76], 0.20	-0.223	50.0, [29.1 – 70.9]	71.4, [29.0 – 96.3]	0.523, [0.239 – 0.808], 0.87
k_{ep}	0.51, [0.03 – 9.28], 0.51	-0.223	50.0, [29.1 – 70.9]	71.4, [29.0 – 96.3]	0.523, [0.239 – 0.808], 0.87
v_e	1.41, [0.15 – 12.8], 0.44	-0.053	33.0, [15.6 – 55.3]	100.0, [62.2 –100]	0.595, [0.375 – 0.815], 0.40
AFV	0.99, [0.97 – 1.02], 0.80	-10	44.4, [25.5 – 64.7]	70.0, [34.8 – 93.3]	0.522, [0.299 – 0.745], 0.85
LD	0.98, [0.89 – 1.08], 0.68	-14	11.5, [2.4 – 30.2]	100.0, [71.5–100.0]	0.411, [0.194 – 0.628], 0.42
Volume	1.00, [0.87 – 1.15], 0.98	-1.56	53.8, [33.4 – 73.4]	60.0, [26.2 – 87.8]	0.484, [0.254 – 0.714], 0.90

B. Percentage (%) changes

Parameter	Odds ratio (OR) OR, [CI], *p*	Cut-off %	Sensitivity %	Specificity %	AUC AUC, [CI], *p*
K^{trans}	0.97, [0.18 – 8.02], 0.97	-11.2	75.0, [53.3 – 90.2]	57.1, [18.4 – 90.1]	0.524, [0.218– 0.830], 0.88
hs-K^{trans}	1.04, [0.26 – 4.27], 0.95	-33.3	45.8, [82.4–100.0]	71.4, [3.7 – 71.0]	0.489, [0.164 – 0.752], 0.95
k_{ep}	0.44, [0.15 – 12.62], 0.63	-33.3	45.8, [25.6 – 67.2]	71.4, [29.0– 96.3]	0.464, [0.176 – 0.752], 0.81
v_e	2.09, [0.20 – 21.94], 0.54	-3.9	41.7, [22.1 – 63.4]	85.7, [42.1 – 99.6]	0.577, [0.354 – 0.801], 0.50
AFV	1.16, [0.32 – 4.27], 0.82	-41.1	88.5, [69.8 – 97.6]	30.0, [6.7 – 65.2]	0.519, [0.281 – 0.757], 0.87
LD	0.21, [0.01 – 7.24], 0.39	-45.1	11.5, [2.4 – 30.2]	100.0, [71.5–100.0]	0.357, [0.144 – 0.569], 0.19
Volume	0.44, [0.04 – 5.25], 0.51	-16.1	100, [86.8–100.0]	10.0, [0.3 – 44.5]	0.350, [0.120 – 0.580], 0.20

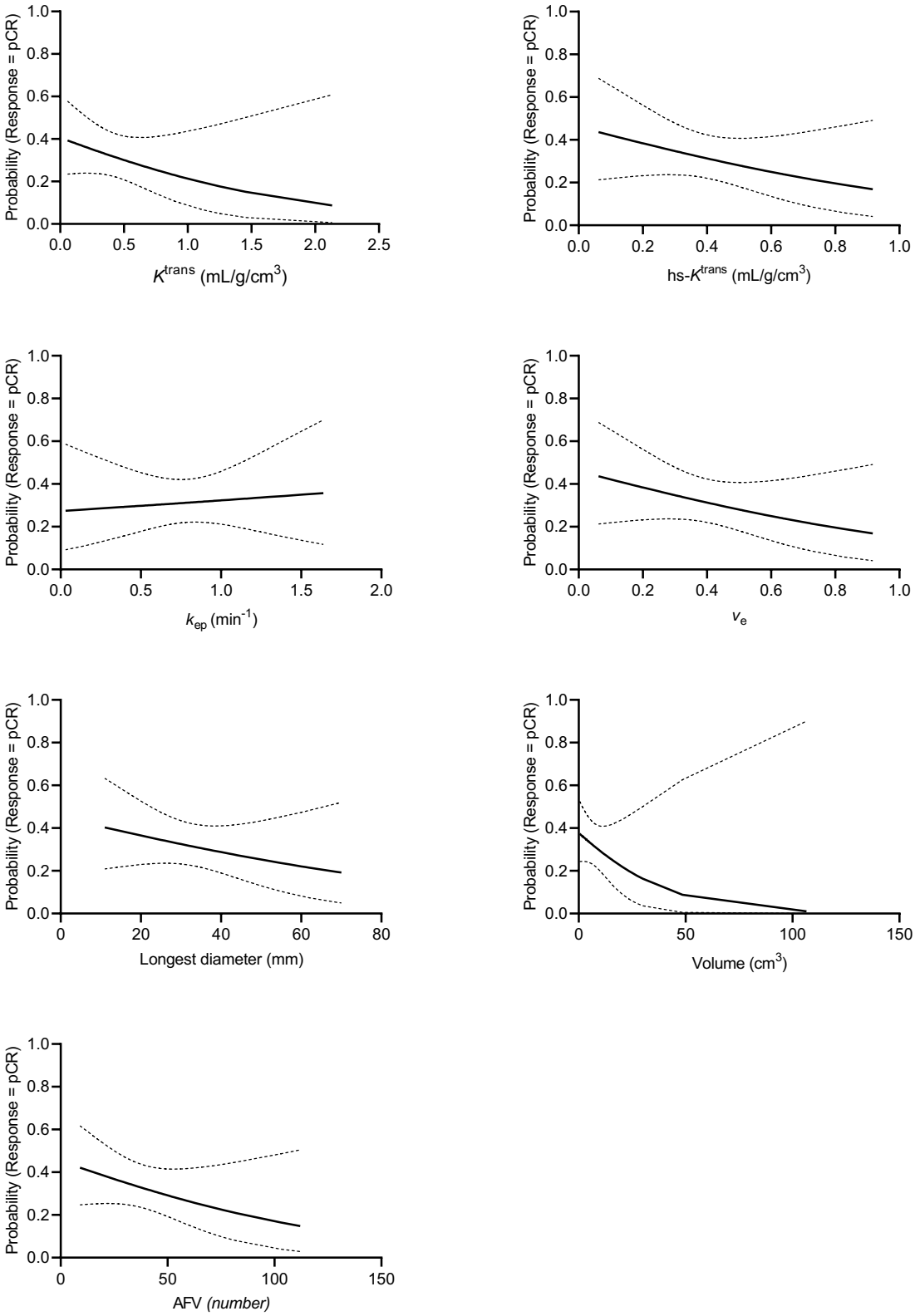

Figure 6.29 Probability of complete pathological response (pCR) *vs* DCE-MRI pharmacokinetic parameters at baseline.

Table 6.28 Univariate analyses of tumour prognostic factors and chemotherapy regimens as predictors of pathological response. The statistical significance (p) and area under the curve (AUC) of each parameter in predicting pathological response were calculated using binomial logistic regression. Main and interaction effects with $p \leq 0.01$ and $p \leq 0.25$ were selected for inclusion into multiple logistic regression models involving quantitative DCE-MRI parameters. *p*-values were adjusted using the Holm-Bonferroni method.

Parameter	Statistical significance *p*	AUC AUC, [CI], *p*
Histological subtype	0.1	0.606, [0.474 – 0.738], 0.009
Molecular sub-type	<0.001***	0.758, [0.640 – 0.875], <.001
Grade	0.1	0.594, [0.461 – 0.726], 0.04
In situ carcinoma	0.63	0.560, [0.409 – 0.711], 0.17
NAC regimen	0.81	0.765, [0.650 – 0.882], 0.45
NAC regimen*Molecular subtype	0.79	
Taxane sequence	0.81	0.540, [0.397 – 0.662], 0.31

Table 6.29 Area under the curve (AUC), sensitivity (%) and specificity (%) of the DCE-MRI parameters at baseline (A) and after one cycle of chemotherapy (B), derived from multiple logistic regression models including the histological subtype, molecular subtype and grade as factors.

	A. Baseline		
Parameter	Sensitivity %	Specificity %	AUC AUC, [CI], *p*
K^{trans}	88.0, [67.8 – 82.7]	65.5, [62.8 – 69.5]	0.835, [0.730 – 0.941], <.001
hs-K^{trans}	76.0, [69.9 – 82.5]	80.0, [77.7 – 82.5]	0.846, [0.744 – 0.949], <.001
k_{ep}	76.0, [44.0 – 92.0]	76.4, [52.7 – 86.3]	0.829, [0.722 – 0.936], <.001
v_e	72.0, [40.0 – 88.0]	80.0, [58.2 – 92.7]	0.836, [0.731 – 0.942], <.001
AFV	70.4, [40.7 – 85.2]	82.1, [58.8 – 92.9]	0.835, [0.733 – 0.937], <.001
LD	77.8, [48.1 – 88.9]	79.7, [39.0 – 89.8]	0.845, [0.747 – 0.795], <.001
Volume	88.9, [66.7 – 85.2]	69.5, [15.3 – 83.1]	0.846, [0.340 – 0.699], <.001
pFactors[a]	*88.9, [69.2 – 100.0]*	*59.3, [40.0 – 73.2]*	*0.817, [0.712 – 0.923],* <.001

	B. Post cycle 1		
	Sensitivity %	Specificity %	AUC AUC, [CI], *p*
K^{trans}	88.9, [11.1 – 100.0]	76.0, [24.0 – 88.0]	0.778, [0.347– 0.887], 0.01
hs-K^{trans}	88.9, [44.4 – 100.0]	64.0, [16.0 – 80.0]	0.769, [0.571 – 0.967], 0.01
k_{ep}	88.9, [33.3 – 100.0]	68.0, [24.0 – 80.1]	0.769, [0.571 – 0.967], 0.01
v_e	88.9, [33.3 – 100.0]	60.0, [20.0 – 80.0]	0.760, [0.559 – 0.961], 0.01
AFV	80.0, [20.0 – 100.0]	92.6, [37.0 – 100.0]	0.874, [0.725 – 1.000], <.001
LD	81.8, [45.5 – 100.0]	92.6, [14.8 – 100.0]	0.875, [0.733 – 1.000], <.001
Volume	81.8, [36.4 – 100.0]	81.5, [11.1 – 96.3]	0.832, [0.671 – 0.992], <.001
pFactors[a]	*81.2, [45.5 – 100.0]*	*70.4, [33.3 – 92.6]*	*0.818, [0.712 – 0.923], 0.001*

[a]Logistic regression including histological subtype, molecular subtype and nuclear grade as factors in the regression.

Table 6.30 Area under the curve (AUC), sensitivity (%) and specificity (%) of absolute (A) and percentage (B) changes in DCE-MRI parameters after one cycle of NAC derived from multiple logistic regression models including the histological subtype, molecular subtype and grade as factors. Absolute changes were calculated as: $Parameter_{PC1} - Parameter_{Baseline}$. Percentage (%) changes were calculated as: $100\times(Parameter_{PC1} - Parameter_{Baseline})/Parameter_{Baseline}$.

	A. Absolute Changes		
	Sensitivity %	**Specificity** %	**AUC** AUC, [CI], *p*
K^{trans}	71.4, [14.3 – 100.0]	83.3, [41.6 – 95.8]	0.804, [0.593 – 1.000], 0.01
hs-K^{trans}	76.0, [69.9 – 82.5]	80.0, [77.7 – 82.5]	0.846, [0.744 – 0.949], <.001
k_{ep}	85.7, [42.8 – 100.0]	62.5, [12.5 – 95.8]	0.768, [0.545 – 0.990], 0.02
v_e	71.4, [14.3 – 100.0]	83.3, [25.0 – 100.0]	0.791, [0.577 – 1.000], 0.01
AFV	80.0, [30.0 – 100.0]	85.2, [37.4 – 96.3]	0.865, [0.712 – 1.000], <.001
LD	90.9, [54.6 – 100.0]	59.3, [37.0 – 88.9]	0.828, [0.666 – 0.990], <.001
Volume	70.0, [20.0 – 90.0]	85.1, [40.7 – 100.0]	0.822, [0.651 – 0.993], 0.001
pFactors[a]	*88.9, [69.2 – 100.0]*	*59.3, [40.0 – 73.2]*	*0.817, [0.712 – 0.923], <.001*

	B. Percentage Changes		
	Sensitivity %	**Specificity** %	**AUC** AUC, [CI], *p*
K^{trans}	85.7, [42.8 – 100.0]	58.3, [4.17 – 91.7]	0.732, [0.500– 0.964], 0.03
hs-K^{trans}	88.9, [44.4 – 100.0]	64.0, [16.0 – 80.0]	0.786, [0.576 – 0.960], 0.02
k_{ep}	85.7, [42.9 – 100.0]	62.5, [12.5 – 95.8]	0.768, [0.546 – 0.990], 0.02
v_e	85.7, [28.6 – 100.0]	70.8, [16.7 – 91.8]	0.760, [0.553 – 0.994], 0.01
AFV	80.0, [20.5 – 100.0]	80.8, [37.6 – 100.0]	0.865, [0.730 – 1.000], <.001
LD	81.8, [27.3 – 100.0]	92.6, [40.7 – 96.3]	0.831, [0.671 – 0.992], <.001
Volume	70.0, [20.0 – 90.0]	88.9, [40.7 – 100.0]	0.837, [0.672 – 1.000], <.001
pFactors[a]	*81.2, [45.5 – 100.0]*	*70.4, [33.3 – 92.6]*	*0.818, [0.712 – 0.923], 0.001*

[a]Logistic regression including histological subtype, molecular subtype and nuclear grade as factors in the model.

6.4 Discussion

Pathological response to neoadjuvant chemotherapy can indicate long-term outcome in primary breast cancer[6,45,46]. An accurate assessment of tumour response early during treatment may enable adjustment of therapy to the patient with the aim of increasing tumour response and improving patient outcomes. The main aim of this study was to investigate changes in quantitative and qualitative DCE-MRI parameters of breast cancers during neoadjuvant chemotherapy treatment and explore their relationship with tumour pathological response.

Previous studies have investigated and demonstrated the potential of the adjacent vessel sign in DCE-MRI for breast cancer diagnosis[38,39,47]. This chapter investigated the association between the number of tumour adjacent feeding vessels (AFV) – a qualitative feature of tumour vascularity – and pathological tumour response, also, the potential of this tumour feature to predict tumour response to therapy.

All DCE-MRI parameters decreased significantly during the course of treatment (with the exception of v_e) in all tumours. Lesions that showed pCR exhibited a larger percentage reduction per chemotherapy cycle than lesions with pPR. These results are in concordance with findings from previous studies[20,23,24,28,48] in which a reduction in tumour pharmacokinetic parameters from DCE-MRI was observed in patients who responded to NAC treatment. Some studies have reported a difference in K^{trans} between responders and non-responders before the commencement of treatment[20,49,50]. Overall, lower K^{trans} values were observed in cancers showing complete pathological response in comparison to tumours with partial response to NAC from baseline to end of treatment. This may reflect that cancers displaying pCR have reduced blood supply owing to the effect of cytotoxic therapy contributing to increased apoptosis and leading to a complete pathological response[51].

There was no significant reduction of v_e in cancers with pPR or pCR. O'Flynn et al[23]. reported an increase of v_e in breast tumours showing no response to treatment, whereas Yankeelov et al[48] observed a decrease of tumour v_e after treatment, although the study did not differentiate between responders and non-responders. Likewise, in a study by Cho et al[52], DCE-MRI parameters (K^{trans}, k_{ep} and v_e) did not lead to identification of pathological response to NAC after one cycle of chemotherapy. Results about correlations between DCE-MRI quantitative parameters and pathological response to NAC are controversial. Ah-See et al[46] showed that

K^{trans} and k_{ep} after two cycles of NAC were significantly related to pathologic response. Tudorica et al[53] presented that K^{trans}, k^{ep}, and v_e obtained after one cycle of NAC could be considered early predictors of pathologic response. In our study there were no non-responders, and this perhaps reflects the improvement in neoadjuvant chemotherapy over the past 10-15 years.

With respect to tumour volumes (ROI volumes), pre-treatment MRI evaluation of the 82 patients with advanced breast cancer showed tumour ROI volumes ranging from 0.5 to 106.6 cm^3. After 6 or 7 cycles of chemotherapy (end of treatment), tumour volumes in complete responder cancers ranged between 0.007 and 3.67 cm^3 and between 0.01 and 12.28 cm^3 in partial responders. Cancers that completely responded to NAC treatment presented smaller median volumes at baseline, in comparison to cancers that showed pathological partial response. Tumour ROI volumes decreased during the course of NAC in all cancers, as has been observed previously[46]. This morphological metric of tumour vascularity presented the biggest decline per treatment cycle, followed by AFVs and hs-K^{trans}. These observations were upheld when considering NST carcinomas alone. The reduction of tumour size during NAC has been previously identified as a good predictor of tumour pathological response and some researchers even consider that a reduction in tumour size is a better response predictor than DCE-MRI pharmacokinetic parameters[26,27]. In our study, the median number of adjacent feeding vessels of pCR cancers was lower than the median number of adjacent feeding vessels of cancers with pPR at baseline. Tumour volumes and the number of AFVs during NAC were significantly associated with pathological response. Previous studies have not reported the association of the number of adjacent feeding vessels with pathological tumour response. In the subset of NST cancers, hotspot K^{trans} and tumour longest diameters were significantly correlated to tumour pathological response. Overall, a baseline tumour size ≤20 mm was significantly associated with complete pathological response. Samuel et al[54]. also reported a significant correlation between tumour size and tumour pathological response. Other researchers differ, with tumour size failing to correlate to final pathological response in their study[46].

Absolute or percentage changes of DCE-MRI tumour parameters did not show significant correlations with pathological tumour response. Contrary to our findings, Pickles et al[28]. observed that tumour volume changes between pre-treatment and early treatment time points demonstrated differences between responders and non-responders with percentage changes

revealing the most significant result. Results from the I-Spy trial showed that k_{ep} could significantly differentiate between responders and non-responders after a single cycle of NAC[55]. We observed that NAC regimes did not affect the changes of DCE-MRI parameters, however, the sequence of taxanes' administration (taxanes first, taxanes second or taxanes throughout) did influence changes of K^{trans}.

There were not significant differences in changes (absolute or percentage) of parameters between pCR and pPR cancers from pre-treatment to post cycle 1. Interestingly, tumours having pPR showed bigger percentage changes between these two time points than cancers with pCR, however it should be noted that from the 37 cancers included in this evaluation of metrics' changes between baseline and post-cycle 1, 25 (68%) exhibited pPR. Furthermore, the fact that pPR cancers were bigger than pCR at baseline may have influenced on partial responder cancers presenting bigger percentage changes than pCR tumours after one cycle of NAC.

The association between patients' age and the number of AFV at baseline was statistically significant and independent of size/volume of the tumour, which means that there was an ~1% increase in the number of AFV per year of age and hence we would expect older women to have more AFVs than younger ones regardless of how big the tumour was. No other parameter showed a significant association with patients' age. Hotspot K^{trans} and AFVs were significantly associated with tumour size (LD and volume). Similarly, AFVs at baseline significantly correlated to hotspot K^{trans} and v_e at the same time-point. According to these results, the number of AFVs is a measure of tumour vascularity that can be related to PK estimates and given the correlations with volume, AFVs can be a surrogate marker of tumour volume and vice versa: i.e more AFVs, larger cancer and higher probability of developing pathological partial response (given the statistically significant differences in AFV observed between complete and partial responder cancers). The mixed effect statistical model revealed that the interaction between the number of chemotherapy cycles and tumour volume had a significant effect on hs-K^{trans}. Likewise, the interaction between the number of chemotherapy cycles and tumour longest diameters had a significant effect on AFVs.

With respect to the effect of tumour prognostic factors (histological and molecular subtype, grade and presence of in-situ carcinoma) on changes of DCE-MRI parameters, there was no effect of tumour histology or molecular subtype on changes of PK metrics, whereas tumour

histology and the interaction between the number of NAC cycles and histology influenced on the tumour size (LD and volume). NST cancers presented greater percentage changes of DCE-MRI PK parameters whereas NST and special type carcinomas presented greater percentage changes of DCE-MRI morphological parameters. Petruolo et al[56] also reported better pathological response to NAC in invasive ductal carcinomas (or NST) in comparison to invasive lobular cancers, which are unlikely to downstage[56].

There was a significant relationship between tumour grade and the pharmacokinetic parameter v_e, not seen with other DCE-MRI parameters. Similar to our study, previous research did not find a correlation between AFVs and tumour grade[38]. The interaction between the number of NAC cycles and nuclear grade had a significant effect on the number of AFVs. Changes in DCE-MRI parameters did not vary significantly between grade 2 and grade 3 cancers.

Tumour molecular subtypes showed a significant association with the number of AFVs, especially in NST cancers, and among all tumour prognostic factors, only tumour molecular subtype significantly influenced pathological response. This significant relationship between pathological response and receptor-based subtypes has been previously reported[57,58]. In our study, hormone receptor negative cancers had a more favourable pathological outcome than HR+ cancers, regardless of the NAC regime given. Similarly, DCE-MRI parameters in HR- cancers decreased at a faster rate than those in HR+ cancers during NAC. Our findings are in concordance with previous literature which states that a correlation between pCR and optimal clinical outcomes is stronger for patients with TNBC and HER2+ disease than for patients with HR+ cancers[56,59]. Other pathological features of the cancer such as tumour histology, grade and presence of in-situ carcinoma and NAC regime or schedule did not show a significant association with tumour pathological response. Conversely, previous studies[60,61] have reported that NAC therapy with taxanes (Docetaxel) or anthracyclines can influence pathological response by inducing a high pathological response rate.

Even though the presence or absence of in-situ carcinoma in all tumours did not show a significant relationship with pathological response, in NST cancers it could possibly allow differentiation between pCR and pPR cancers. Previous authors[62] have demonstrated high periductal vascularity around ducts involved by DCIS, and since most NST cancers in our study which were partial responders had DCIS, we could infer that this high periductal vascularity may have influenced the tumour response to NAC. The presence of in-situ carcinoma was

significantly associated with changes in hotspot K^{trans}, tumour LD and volume at mid-treatment (also in the NST subset) although in general, we did not observe significant differences in percentage changes of DCE-MRI parameters between tumours with in-situ carcinoma and tumours without in-situ carcinoma. As expected, tumours with no in-situ carcinoma responded better to NAC.

After assessing the ability of pathological features of breast cancer to predict pathological response, it was found that tumour receptor-based status was the only characteristic of the tumour which significantly predicted pathological response. Using baseline DCE-MRI parameters tumour volumes revealed the highest sensitivity (88.9%) and AUC (0.846) whereas hs-K^{trans} and v_e showed the highest specificity (80.0%) to predict pathological response. After one cycle of NAC, all PK metrics (K^{trans}, hs-$K^{trans,}$ K_{ep} and v_e) presented the highest sensitivity (88.9%) whereas the morphological parameters, AFVs and tumour longest diameter showed the highest specificity (92.6%) and AUC (0.874 and 0.875, respectively). Generally, cancers with lower values in DCE-MRI metrics at baseline or after one cycle of treatment were more likely to achieve pCR.

Absolute and percentage changes of DCE-MRI parameters after one cycle of neoadjuvant chemotherapy were also evaluated in order to know if they could predict tumour pathological complete response. Absolute changes in the tumour longest diameter after one cycle of therapy showed the highest sensitivity (90.9%) and absolute changes in tumour volumes revealed the highest specificity (85.1%). Post-cycle 1 absolute changes of AFVs had the highest area under the receiver operating characteristic curve (0.865). With respect to percentage changes of DCE-MRI parameters, changes in hs-K^{trans} showed the highest sensitivity (88.9%), changes in tumour LDs the highest specificity (92.6%) and changes in AFVs presented the highest AUC (0.865). In summary, changes in DCE-MRI derived tumour size and changes in the morphological biomarker of tumour vasculature, AFVs, were the best predictors of pathological complete response. Outcomes about the ability of DCE-MRI parameters to predict tumour response to NAC are controversial. Ah-See et al[46] reported that early changes in MRI-derived tumour size did not predict pathological response. They also found that an early change in K^{trans} was the best predictor of pathological non-response. Sharma et al[2], stated that a change of K_{ep} from the first to the second MRI during NAC could significantly differentiate between responder and non-responder cancers. By contrast, other studies [1,26,27,28] have reported that

tumour volume changes between the pre-treatment and early treatment time-points were the best predictors of tumour response to NAC.

Our study had several limitations. First, the problems presented during the acquisition or the post-processing of DCE-MR images for which some MRI evaluations needed to be excluded. Secondly, despite of having a variety of breast cancer types in our sample, the number of cancers within categories of histological and molecular subtypes was not the same, creating unbalance between groups. Likewise, our study participants were given different number of neoadjuvant chemotherapy cycles and drug regimens despite of sometimes having the same type of breast cancer, which it can be a plus point for oncologists in our health institution because as we know, cancer treatment should be individualised according to the patient's needs. There were no non-responders in the cohort making it difficult to compare our results with some of the other studies.

6.5 Conclusion

In this study, DCE-MRI qualitative parameters of the tumour were better correlated to pathological tumour response than pharmacokinetic parameters. Post-cycle 1 changes of DCE-MRI derived tumour size and the number of AFVs were the best predictors of pathological complete response We demonstrated the potential of the number of adjacent feeding vessels as a new parameter for assessing the tumour vascular function and, this parameter is immediately measurable by radiologists reporting the MRI examination. DCE-MRI parameters (with the exception of v_e) decreased during the course of NAC in cancers achieving pCR and pPR although the decline was more accelerated in pCR cancers. Hotspot K^{trans} showed better potential than whole lesion K^{trans} in differentiating complete pathological tumour response from partial response.

References

1. Loo, C. E. *et al.* Dynamic contrast-enhanced MRI for prediction of breast cancer response to neoadjuvant chemotherapy: Initial results. *Am. J. Roentgenol.* (2008). doi:10.2214/AJR.07.3567
2. Sharma, A. *et al.* DCE-MRI and parametric imaging in monitoring response to neoadjuvant chemotherapy in breast carcinoma: A preliminary report. *Polish J. Radiol.* (2018). doi:10.5114/pjr.2018.76271
3. Fisher, B. *et al.* Effect of preoperative chemotherapy on local-regional disease in women with operable breast cancer: Findings from national surgical adjuvant breast and bowel project B-18. *J. Clin. Oncol.* (1997). doi:10.1200/JCO.1997.15.7.2483
4. Kuerer, H. M. *et al.* Surgical conservation planning after neoadjuvant chemotherapy for stage II and operable stage III breast carcinoma. in *American Journal of Surgery* (2001). doi:10.1016/S0002-9610(01)00793-0
5. Fisher, B. *et al.* Effect of preoperative chemotherapy on the outcome of women with operable breast cancer. *J. Clin. Oncol.* (1998). doi:10.1200/JCO.1998.16.8.2672
6. Wolmark, N., Wang, J., Mamounas, E., Bryant, J. & Fisher, B. Preoperative chemotherapy in patients with operable breast cancer: nine-year results from National Surgical Adjuvant Breast and Bowel Project B-18. *J. Natl. Cancer Inst. Monogr.* (2001). doi:10.1093/oxfordjournals.jncimonographs.a003469
7. Van der Hage, J. A. *et al.* Preoperative chemotherapy in primary operable breast cancer: Results from the European Organization for Research and Treatment of Cancer Trial 10902. *J. Clin. Oncol.* (2001). doi:10.1200/JCO.2001.19.22.4224
8. Rastogi, P. *et al.* Preoperative chemotherapy: Updates of national surgical adjuvant breast and bowel project protocols B-18 and B-27. *Journal of Clinical Oncology* (2008). doi:10.1200/JCO.2007.15.0235
9. Bonadonna, G. *et al.* Primary chemotherapy in operable breast cancer: Eight-year experience at the Milan Cancer Institute. *J. Clin. Oncol.* (1998). doi:10.1200/JCO.1998.16.1.93
10. Bear, H. D. *et al.* The effect on tumor response of adding sequential preoperative docetaxel to preoperative doxorubicin and cyclophosphamide: Preliminary results from National Surgical Adjuvant Breast and Bowel Project Protocol B-27. *J. Clin. Oncol.* (2003). doi:10.1200/JCO.2003.12.005
11. Makris, A. *et al.* A reduction in the requirements for mastectomy in a randomized trial

of neoadjuvant chemoendocrine therapy in primary breast cancer. *Ann. Oncol.* (1998). doi:10.1023/A:1008400706949

12. Cocquyt, V. F. *et al.* Assessment of response to preoperative chemotherapy in patients with stage II an III breast cancer: The value of MRI. *Breast* (2002). doi:10.1054/brst.2002.0450
13. Feldman, L. D., Hortobagyi, G. N., Buzdar, A. U., Ames, F. C. & Blumenschein, G. R. Pathological Assessment of Response to Induction Chemotherapy in Breast Cancer. *Cancer Res.* (1986).
14. Gilles, R. *et al.* Locally advanced breast cancer: Contrast-enhanced subtraction MR imaging of response to preoperative chemotherapy. *Radiology* (1994). doi:10.1148/radiology.191.3.8184039
15. Trecate, G. *et al.* Locally advanced breast cancer treated with primary chemotherapy: Comparison between magnetic resonance imaging and pathologic evaluation of residual disease. *Tumori* (1999). doi:10.1177/030089169908500402
16. Drew, P. J. *et al.* Evaluation of response to neoadjuvant chemoradiotherapy for locally advanced breast cancer with dynamic contrast-enhanced MRI of the breast. *Eur. J. Surg. Oncol.* (2001). doi:10.1053/ejso.2001.1194
17. De Los Santos, J. *et al.* Accuracy of breast magnetic resonance imaging in predicting pathologic response in patients treated with neoadjuvant chemotherapy. *Clinical Breast Cancer* (2011). doi:10.1016/j.clbc.2011.06.007
18. Bansal, G. J. & Santosh, D. Accuracy of MRI for prediction of response to neo-adjuvant chemotherapy in triple negative breast cancer compared to other subtypes of breast cancer. *Indian J. Radiol. Imaging* (2016). doi:10.4103/0971-3026.195793
19. Padhani, A. R. Functional MRI for anticancer therapy assessment. *Eur. J. Cancer* (2002). doi:10.1016/S0959-8049(02)00388-X
20. Hayes, C., Padhani, A. R. & Leach, M. O. Assessing changes in tumour vascular function using dynamic contrast-enhanced magnetic resonance imaging. *NMR Biomed.* (2002). doi:10.1002/nbm.756
21. Hanahan, D. & Weinberg, R. A. The hallmarks of cancer. *Cell* (2000). doi:10.1016/S0092-8674(00)81683-9
22. Sarah M. Friedewald. *Breast Imaging, An Issue of Radiologic Clinics of North America*. (Elsevier, 2017).
23. O'Flynn, E. A. M. & deSouza, N. M. Functional magnetic resonance: Biomarkers of response in breast cancer. *Breast Cancer Research* (2011). doi:10.1186/bcr2815

24. O'Connor, J. P. B., Jackson, A., Parker, G. J. M. & Jayson, G. C. DCE-MRI biomarkers in the clinical evaluation of antiangiogenic and vascular disrupting agents. *British Journal of Cancer* (2007). doi:10.1038/sj.bjc.6603515
25. Padhani, A. R. *et al.* Prediction of clinicopathologic response of breast cancer to primary chemotherapy at contrast-enhanced mr imaging: Initial clinical results. *Radiology* (2006). doi:10.1148/radiol.2392021099
26. Yu, H. J., Chen, J. H., Mehta, R. S., Nalcioglu, O. & Su, M. Y. MRI measurements of tumor size and pharmacokinetic parameters as early predictors of response in breast cancer patients undergoing neoadjuvant anthracycline chemotherapy. *J. Magn. Reson. Imaging* (2007). doi:10.1002/jmri.21060
27. Martincich, L. *et al.* Monitoring response to primary chemotherapy in breast cancer using dynamic contrast-enhanced magnetic resonance imaging. *Breast Cancer Res. Treat.* (2004). doi:10.1023/B:BREA.0000010700.11092.f4
28. Pickles, M. D., Lowry, M., Manton, D. J., Gibbs, P. & Turnbull, L. W. Role of dynamic contrast enhanced MRI in monitoring early response of locally advanced breast cancer to neoadjuvant chemotherapy. *Breast Cancer Res. Treat.* (2005). doi:10.1007/s10549-004-5819-2
29. Teicher, B. A., Holden, S. A., Al-Achi, A. & Herman, T. S. Classification of Antineoplastic Treatments by Their Differential Toxicity toward Putative Oxygenated and Hypoxic Tumor Subpopulations in Vivo in the FSallC Murine Fibrosarcoma. *Cancer Res.* (1990).
30. Teicher, B. A., Lazo, J. S. & Sartorelli, A. C. Classification of Antineoplastic Agents by their Selective Toxicities toward Oxygenated and Hypoxic Tumor Cells. *Cancer Res.* (1981).
31. Lyng, H. *et al.* Assessment of tumor oxygenation in human cervical carcinoma by use of dynamic Gd-DTPA-enhanced MR imaging. *J. Magn. Reson. Imaging* (2001). doi:10.1002/jmri.10016
32. Zahra, M. A., Hollingsworth, K. G., Sala, E., Lomas, D. J. & Tan, L. T. Dynamic contrast-enhanced MRI as a predictor of tumour response to radiotherapy. *Lancet Oncology* (2007). doi:10.1016/S1470-2045(06)71012-9
33. Gaustad, J.-V. *et al.* DCE-MRI of Tumor Hypoxia and Hypoxia-Associated Aggressiveness. *Cancers (Basel).* **12**, 1979 (2020).
34. Graham, K. & Unger, E. Overcoming tumor hypoxia as a barrier to radiotherapy, chemotherapy and immunotherapy in cancer treatment. *International Journal of*

Nanomedicine (2018). doi:10.2147/IJN.S140462

35. Wouters, A., Pauwels, B., Lardon, F. & Vermorken, J. B. Review: Implications of In Vitro Research on the Effect of Radiotherapy and Chemotherapy Under Hypoxic Conditions. *Oncologist* (2007). doi:10.1634/theoncologist.12-6-690
36. Aomatsu, N. *et al.* Carbonic anhydrase 9 is associated with chemosensitivity and prognosis in breast cancer patients treated with taxane and anthracycline. *BMC Cancer* (2014). doi:10.1186/1471-2407-14-400
37. Banelli, B. *et al.* Pathological and molecular characteristics distinguishing contralateral metastatic from new primary breast cancer. *Ann. Oncol.* (2009). doi:10.1093/annonc/mdp470
38. Dietzel, M. *et al.* The adjacent vessel sign on breast MRI: New data and a subgroup analysis for 1,084 histologically verified cases. *Korean J. Radiol.* (2010). doi:10.3348/kjr.2010.11.2.178
39. Fischer, D. R. *et al.* The adjacent vessel on dynamic contrast-enhanced breast MRI. *AJR. Am. J. Roentgenol.* (2006). doi:10.2214/AJR.05.0377
40. Eisenhauer, E. A. *et al.* New response evaluation criteria in solid tumours: Revised RECIST guideline (version 1.1). *Eur. J. Cancer* (2009). doi:10.1016/j.ejca.2008.10.026
41. Rao, A. A., Feneis, J., Lalonde, C. & Ojeda-Fournier, H. A pictorial review of changes in the BI-RADS fifth edition. *Radiographics* (2016). doi:10.1148/rg.2016150178
42. ELSTON, C. W. & ELLIS, I. O. pathological prognostic factors in breast cancer. I. The value of histological grade in breast cancer: experience from a large study with long-term follow-up. *Histopathology* (1991). doi:10.1111/j.1365-2559.1991.tb00229.x
43. Hoon Tan, P. *et al.* The 2019 WHO classification of tumours of the breast. *Histopathology* (2020). doi:10.1111/his.14091
44. Pinder, S. E., Provenzano, E., Earl, H. & Ellis, I. O. Laboratory handling and histology reporting of breast specimens from patients who have received neoadjuvant chemotherapy. *Histopathology* (2007). doi:10.1111/j.1365-2559.2006.02419.x
45. Cleator, S. J., Makris, A., Ashley, S. E., Lal, R. & Powles, T. J. Good clinical response of breast cancers to neoadjuvant chemoendocrine therapy is associated with improved overall survival. *Ann. Oncol.* (2005). doi:10.1093/annonc/mdi049
46. Ah-See, M. L. W. *et al.* Early changes in functional dynamic magnetic resonance imaging predict for pathologic response to neoadjuvant chemotherapy in primary breast cancer. *Clin. Cancer Res.* (2008). doi:10.1158/1078-0432.CCR-07-4310
47. Zhao, S., Tan, R., Xiu, J., Yuan, X. & Liu, Q. Adjacent vessel sign and breast imaging

reporting and data system are valuable for diagnosis of benign and malignant breast lesions. *Biotechnol. Biotechnol. Equip.* (2014). doi:10.1080/13102818.2014.974016

48. Yankeelov, T. E. *et al.* Integration of quantitative DCE-MRI and ADC mapping to monitor treatment response in human breast cancer: initial results. *Magn. Reson. Imaging* (2007). doi:10.1016/j.mri.2006.09.006
49. George, M. L. *et al.* Non-invasive methods of assessing angiogenesis and their value in predicting response to treatment in colorectal cancer. *Br. J. Surg.* (2001). doi:10.1046/j.0007-1323.2001.01947.x
50. Yamashita, Y. *et al.* Dynamic contrast-enhanced MR imaging of uterine cervical cancer: Pharmacokinetic analysis with histopathologic correlation and its importance in predicting the outcome of radiation therapy. *Radiology* (2000). doi:10.1148/radiology.216.3.r00se07803
51. Nishida, N., Yano, H., Nishida, T., Kamura, T. & Kojiro, M. Angiogenesis in cancer. *Vascular Health and Risk Management* (2006). doi:10.2147/vhrm.2006.2.3.213
52. Cho, N. *et al.* Breast cancer: Early prediction of response to neoadjuvant chemotherapy using parametric response maps for MR imaging. *Radiology* (2014). doi:10.1148/radiol.14131332
53. Tudorica, A. *et al.* Early prediction and evaluation of breast cancer response to neoadjuvant chemotherapy using quantitative DCE-MRI. *Transl. Oncol.* (2016). doi:10.1016/j.tranon.2015.11.016
54. Olatoke, S., Agodirin, O., Rahman, G., Habeeb, O. & Akande, H. Relationship between tumour size and response to neoadjuvant chemotherapy among breast cancer patients in a tertiary center in Nigeria. *Malawi Med. J.* (2018). doi:10.4314/mmj.v30i1.3
55. Li, X. *et al.* DCE-MRI analysis methods for predicting the response of breast cancer to neoadjuvant chemotherapy: Pilot study findings. *Magn. Reson. Med.* (2014). doi:10.1002/mrm.24782
56. Petruolo, O. A. *et al.* Standard Pathologic Features Can Be Used to Identify a Subset of Estrogen Receptor-Positive, HER2 Negative Patients Likely to Benefit from Neoadjuvant Chemotherapy. *Ann. Surg. Oncol.* (2017). doi:10.1245/s10434-017-5898-z
57. Houssami, N., MacAskill, P., Von Minckwitz, G., Marinovich, M. L. & Mamounas, E. Meta-analysis of the association of breast cancer subtype and pathologic complete response to neoadjuvant chemotherapy. *Eur. J. Cancer* (2012). doi:10.1016/j.ejca.2012.05.023

58. Del Prete, S. *et al.* Clinical and pathological factors predictive of response to neoadjuvant chemotherapy in breast cancer: A single center experience. *Oncol. Lett.* (2019). doi:10.3892/ol.2019.10729

59. A., A. *et al.* Neoadjuvant therapy for breast cancer: Updates and proceedings from the seventh annual meeting of the canadian consortium for locally advanced breast cancer. *Curr. Oncol.* (2018). doi:10.3747/co.25.4153 LK - http://rug.on.worldcat.org/atoztitles/link/?sid=EMBASE&issn=17187729&id=doi:10.3747%2Fco.25.4153&atitle=Neoadjuvant+therapy+for+breast+cancer%3A+Updates+and+proceedings+from+the+seventh+annual+meeting+of+the+canadian+consortium+for+locally+advanced+breast+cancer&stitle=Curr.+Oncol.&title=Current+Oncology&volume=25&issue=5&spage=&epage=&aulast=Arnaout&aufirst=Angel&auinit=A.&aufull=Arnaout+A.&coden=CUONF&isbn=&pages=-&date=2018&auinit1=A&auinitm=

60. Amat, S. *et al.* Neoadjuvant docetaxel for operable breast cancer induces a high pathological response and breast-conservation rate. *Br. J. Cancer* (2003). doi:10.1038/sj.bjc.6600916

61. Chollet, P. *et al.* Clinical and pathological response to primary chemotherapy in operable breast cancer. *Eur. J. Cancer Part A* (1997). doi:10.1016/S0959-8049(97)00038-5

62. Teo, N. B. *et al.* Vascular density and phenotype around ductal carcinoma in situ (DCIS) of the breast. *Br. J. Cancer* (2002). doi:10.1038/sj.bjc.6600053

Chapter 7. Summary and future work

7.1 Introduction

This thesis provides insight into breast cancer pathophysiology using simultaneous PET and multi-parametric MRI. The relationships between imaging biomarkers of tumour vascularity measured by dynamic contrast-enhanced (DCE) MRI, markers of cellularity using diffusion-weighted imaging (DWI) and tumour hypoxic status using ^{18}F-fluoromisonidazole (^{18}F-FMISO) PET were explored. Correlations between functional PET-MRI parameters and immunohistochemical (IHC) biomarkers of hypoxia and vascularity as well as a new MRI morphological marker of tumour vascularity were presented.

7.2 Summary and future work

7.2.1. Relationship between hypoxia and vascularity in breast cancer by using PET-MRI

This work has been undertaken from a radiologist's perspective, imaging the relationship between vascularity and oxygenation in breast cancer. It is recognized that both processes are subject to temporal changes and most of the published data about these cancer hallmarks in breast has been acquired by performing two separate scans of the patient[1,2,3], a PET-CT and an MRI scan at different times. To remove the effect of temporal fluctuations in hypoxia and perfusion in breast cancer, this relationship was measured using combined PET-MR imaging with ^{18}F-fluoromisonidazole (^{18}F-FMISO). A significant negative relationship between ^{18}F-FMISO-PET K_i and DCE-MRI K^{trans}, the imaging parameters of tumour hypoxia and vascularity, respectively was found. Additionally, the relationship between DCE-MRI, DWI-MRI ADC and ^{18}F-FMISO-PET parameters was assessed.

In post-processed maps of tumour perfusion (K^{trans}) and hypoxia (K_i) intra-tumoral heterogeneity consistent with the dynamic changes of tumour blood flow and the hypoxic tumour micromilieu was demonstrated. A larger sample of breast carcinomas is needed in order to identify typical hypoxia-perfusion patterns in each molecular breast cancer subtype. Other MR techniques such as oxygen enhanced (OE)-MRI simultaneously to the PET could shed further understanding of this complex relationship.

This work allowed radiologists and oncologists to endorse the hypothesis of perfusion-driven hypoxia in breast cancer. I recommend the combined assessment of the hypoxic and vascular status of breast tumours (which could be achieved using simultaneous multi-modality imaging as reported here) because this needs to be considered for determining prognosis, treatment efficacy and therapy selection in breast cancer patients.

7.2.2. Relationship between tumour radiological features, whole-breast vascularity and PET/MR imaging parameters of hypoxia and vascular function

Previous authors have reported the diagnostic role of the "adjacent vessel sign" on DCE-MRI and so the total count of adjacent feeding vessels (AFVs) was investigated as a "new" imaging marker of the tumour vascular function. This is the first study in which correlations between ^{18}F-FMISO-PET/MRI and DCE-MRI morphological and quantitative features of the cancer were correlated to MR categories of signal-intensity curve and total number of adjacent feeding vessels in breast malignancies. The number of tumour adjacent feeding vessels (AFVs) showed a non-significant positive correlation with whole-breast vascularity scores. No significant correlations were observed between the number of adjacent feeding vessels and tumour histology, grade or molecular subtype.

Breast cancers with an MR type 3 curve showed higher hypoxic fractions on ^{18}F-FMISO-PET/MRI than breast cancers with kinetic curves type 1 and 2. This may be due to the shunting effect in immature neo-vasculature. DWI-MRI ADC from the darkest part of the cancer showed a significant association with the type of curve. Breast carcinomas of the lobular type and grade 2 presented the highest medians of AFVs and surprisingly, breast cancers with a kinetic curve type 1 showed higher median AFVs than breast cancers with kinetic curves type 2 and 3. Significant negative correlations were observed between AFVs and ^{18}F-FMISO derived parameters and significant positive correlations between DCE-MRI K^{trans}, v_e and AFVs. I encourage other researchers to continue exploring the role of the total number of tumour adjacent feeding vessels as a new imaging metric of tumour vascularity. Likewise, radiologists could use the total number of tumour feeding vessels on DCE-MRI evaluations as a good indicator of the quantitative parameter K^{trans} which is currently only calculated for research (AFVs and K^{trans} showed a significant positive correlation in this study).

7.2.3. Correlations between ^{18}F-FMISO-PET/MRI parameters and immunohistochemistry (IHC) biomarkers of tumour vascularity and hypoxia in breast cancer

After having proved that there was a correlation between tumour imaging biomarkers of vascularity and hypoxia in breast cancer, the next step was to confirm with immunohistochemical analysis the hypoxia and perfusion from imaging and to determine whether or not imaging biomarkers were associated to immunohistochemical biomarkers used to assess hypoxia and tumour vasculature. Only 19 breast cancers which were not treated with NAC were included for this analysis. Sixty-eight percent of breast cancers in the sample were positive for HIF-1 alpha immune-staining and 21% stained positive for CAIX. All cancers were CD31 positive. However, overall, non-significant negative correlations were shown between CD31 vascular markers and IHC hypoxic biomarkers. Similarly, I could not observe any significant association between HIF-1 alpha and CAIX expression.

Although there was a significant positive correlation between the ^{18}F-FMISO-PET parameter K_i mean and the immunohistochemical hypoxic marker, carbonic anhydrase IX (CAIX); there were no significant associations between ^{18}F-FMISO-PET hypoxic markers and HIF-1 alpha. HIF-1 alpha activation in these cancers may be influenced by either oestrogen receptors or 17 beta oestradiol rather than by hypoxia. A significant positive correlation was observed between K_i and the IHC parameter tumour vessel density. DCE-MRI pharmacokinetic parameters also showed positive correlations, although not significant, with CD31 derived vascular features (total count of tumour blood vessels, micro-vessel density and calibre).

In this same chapter, we also established correlations with other pathological features of the cancer such as tumour infiltrating lymphocytes (TILs, as evidence strengthens the clinical relevance of this immunological biomarker[4]) and the percentage of tumour cells. To the best of our knowledge, this work is the first one to reveal correlations between PET-MRI hypoxic and vascular biomarkers of breast cancer and immunological biomarkers. This work showed a significant negative correlation between ^{18}F-FMISO-PET parameter SUV (mean and max) and percentage of TILs. Similarly, we revealed a statistically significant negative correlation between tumour total count of vessels (obtained from CD31 staining) and TILs (%). There was a significant positive association between HIF-1 alpha expression and percentage of tumour

cells. However, further work on larger patient population is required to confirm the association between TILs and imaging markers of hypoxia and vascularity in breast cancer.

7.2.4. Correlations of breast cancer imaging vascular biomarkers with tumour response to neoadjuvant chemotherapy

The association between DCE-MRI tumour vascular features (pharmacokinetic and morphological), including total number of tumour AFVs, and pathological tumour response in different types of breast cancer was assessed in order to have a clearer understanding of breast cancer vascularity before and after neo-adjuvant chemotherapy. There was a significant decrease of almost all DCE-MRI parameters (with the exception of v_e) during the course of neoadjuvant chemotherapy in cancers with both, a complete and partial response. Tumour volumes showed the biggest decline after each treatment cycle, followed by AFVs and hotspot-K^{trans}. The last two were significantly related to tumour size.

Changes in tumour size and in the number of AFVs were the best predictors of pathological complete response. Furthermore, we observed that DCE-MRI qualitative metrics of the tumour vascular function correlated better to pathological tumour response than pharmacokinetic parameters which are more frequently used in research.

More research needs to be done in order to reliably demonstrate the potential of AFVs as a good predictor and indictor of breast cancer pathological response to neoadjuvant chemotherapy. We encourage other researchers to not underestimate qualitative DCE-MRI vascular features, since they may provide similar or better information than quantitative parameters.

7.3 Personal reflections upon my PhD

Reflecting upon my PhD, I have undertaken research across a variety of fields from breast PET-MRI to breast immunohistochemistry. When I arrived in Cambridge University, I had brought with me a general knowledge of radiology because I had studied the specialization in my native country. However, as soon as I arrived here, I had to confront my lack of knowledge on other scientific fields such as PET-MRI and breast MRI. I must admit that this created some fear on me at the beginning, however, in addition to my self-initiative for learning about new

subjects I received great support from both of my supervisors who had full expertise and experience on breast radiology and PET, respectively. At the end, I have now acquired a variety of new skills which are extremely useful for doing research and that clinical radiologists usually do not learn. I believe that I have shown the ability to move between fields acquiring relevant knowledge as I progressed, and this would not have been possible without the fantastic support from my supervisors Professor Fiona J. Gilbert and Dr Roido Manavaki.

In retrospect and reflecting on my work, if I were to start my PhD again having the experience that I have now, I would make the following adjustments:

- Knowing that a request of NHS research documents can take a while, I would start my request earlier in order to be able to recruit more patients into my studies. This would allow me to analyse a larger cohort of cancers of different histological and molecular types, such as more triple negative breast cancers.
- Instead of focusing myself on finding and brainstorming "new research ideas" I would start immediately working on my original plan and would spend more time extracting further information from the PET-MRI data already available and expanding the IHC analysis which could lead to more complex associations between biomarkers of breast cancer hallmarks.

I would also like to emphasize the value of supervisors' feedback, views, and advise, as being crucial to achieve and improve research goals.

References

1. C. Gaertner F, Souvatzoglou M, Brix G, J. Beer A. Imaging of Hypoxia Using PET and MRI. *Curr Pharm Biotechnol*. 2012. doi:10.2174/138920112799436267
2. Sun X, Niu G, Chan N, Shen B, Chen X. Tumor hypoxia imaging. *Mol Imaging Biol*. 2011. doi:10.1007/s11307-010-0420-z
3. Andrzejewski P, Wengert G, Helbich TH, et al. Sequential [18F]FDG-[18F]FMISO PET and Multiparametric MRI at 3T for Insights into Breast Cancer Heterogeneity and Correlation with Patient Outcomes: First Clinical Experience. *Contrast Media Mol Imaging*. 2019. doi:10.1155/2019/1307247
4. Dieci MV, Radosevic-Robin N, Fineberg S, et al. Update on tumor-infiltrating lymphocytes (TILs) in breast cancer, including recommendations to assess TILs in residual disease after neoadjuvant therapy and in carcinoma in situ: A report of the International Immuno-Oncology Biomarker Working Group on Bre. *Semin Cancer Biol*. 2018. doi:10.1016/j.semcancer.2017.10.003